

AD-A277 438



2

Fluid Dynamics Lagrangian Simulation Model

Final Report  
SAIC 94/1017

February 8, 1994



Science Applications International Corporation  
An Employee-Owned Company

This document has been approved  
for public release and sale; its  
distribution is unlimited

378

94-09512

94 3 18 064

1710 Goodridge Drive, P.O. Box 1303, McLean, Virginia 22102 (703) 821-4300

Other SAIC Offices Albuquerque, Boston, Colorado Springs, Dayton, Huntsville, Las Vegas, Los Angeles, Oak Ridge, Orlando, Palo Alto, San Diego, Seattle, and Tucson

**Fluid Dynamics Lagrangian Simulation Model**

**Final Report  
SAIC 94/**

**February 8, 1994**

**Submitted to:**

**Dr. William Sandberg  
Laboratory for Computational Physics and Fluid Dynamics  
Code 6400  
Naval Research Laboratory  
Washington, DC 20375-5000**

**Prepared by:**

**Ellis Hyman, Principal Investigator**

**Prepared Under:**

**Contract No. N00014-89-C-2106**

<b>Accesion For</b>	
NTIS	CRA&I
DTIC	TAB
Unannounced	
Justification .....	
<b>By</b> <i>ltr</i>	
Distribution /	
<b>Availability Codes</b>	
<b>Dist</b>	<b>Avail and / or Special</b>
<b>A-1</b>	

## TABLE OF CONTENTS

I.	Technical Discussion .....	1
II.	Simulation of Inviscid/Viscous Flows Over Complex Geometries .....	1
III.	Vortex Shedding and Lock-On .....	4
IV.	Turbulence Studies .....	5
V.	Numerical Simulations in Support of Narcotics Interdiction .....	8

**Appendix A** A Finite Element Solver for Axisymmetric Compressible Flows

**Appendix B** Simulation of Subsonic Viscous Flows Using Unstructured Grids and a Finite Element Solver

**Appendix C** Review -Vortex Shedding Lock-On and Flow Control in Bluff Body Wakes

**Appendix D** Vortex Shedding and Lock-On in a Perturbed Flow

**Appendix E** Interaction of Vorticity with a Free Surface in Turbulent Open Channel Flow

**Appendix F** Turbulence Modeling Near the Surface in an Open Channel Flow

**Appendix G** Length Scales of Turbulence Near a Free Surface

**Appendix H** The Enstrophy Balance During the Interaction of a Vortex Ring with a Shear-Free Boundary

**Appendix I** Three-Dimensional Vortex Interactions with a Free Surface

**Appendix J** Requirements Definition by Numerical Simulation

## **I. Technical Discussion**

The work performed by Science Applications International Corporation (SAIC) on this contract, "Fluid Dynamics Lagrangian Simulation Model," Contract Number N00014-89-C-2106, SAIC Project Number 01-0157-03-0768, focused on a number of research topics in fluid dynamics. The work was in support of the programs of NRL's Laboratory for Computational Physics and Fluid Dynamics and covered the period from 10 September 1989 to 9 December 1993. In the following sections we describe each of the efforts and the results obtained. Much of the research work has resulted in journal publications. These are included in Appendices of this report for which the reader is referred for complete details.

## **II. Simulation of Inviscid/Viscous Flows Over Complex Geometries**

The use of unstructured grids for the simulation of high-speed flows has been extensively reported in the literature (see references cited in Appendices A and B). In the present research effort, SAIC extended this technology to nearly incompressible flows, and applied the procedure to simulate inviscid as well as viscous flows past submarine configurations with all their appendages. One attractive feature of using triangular or tetrahedral meshes over structured meshes is that complex geometries can be easily represented. For example, constructing a structured mesh around a submarine with all its appendages will require a tedious task of decomposition of the domain. In the present work, unstructured grids are generated using the advancing front algorithm of Lohner. The governing equations of flow are solved using the finite-element version of the Flux-Corrected Transport algorithm (FEM-FCT). Details of the flow solver can be found in the Appendices referred to above.

As a first step, Euler and Navier-Stokes solutions were obtained for an axisymmetric flow. This provided an excellent case to validate the procedure employed and also a base to build models for predicting turbulent flows. The procedure was applied to solve a model problem of flow over a sphere; the computed results were found to be in good agreement with those found in the literature for both the potential flow case and the case of viscous flow at  $Re = 100$ . These results are included in the paper presented at the AIAA Fluid Dynamics Conference (Appendix A). Having established the correctness of the

procedure, it was then extended to compute flow over the submarine hull configuration. Grid refinement studies were conducted for the inviscid flow in order to establish the independence of the flow solution to the chosen grid. Also, a laminar viscous flow solution over this configuration was obtained for  $Re = 1000$ . The convergence rate for this problem deteriorated considerably, as would be expected, due to the presence of the small elements in the boundary layer that are needed to resolve the high gradients present in the flow variables. Hence, convergence acceleration of the numerical method was investigated by appropriately sub-stepping the viscous diffusion terms. It was found that this method of convergence acceleration does not yield substantial gain because the allowable time-step for the explicit scheme for low Mach numbers is limited by the speed of sound. Hence, this convergence acceleration procedure should be investigated with the barely-implicit correction (BIC) scheme.

The procedure was next extended to solve three-dimensional flows. Results were obtained for inviscid flow over the submarine with sail and stern appendages at various pitch angles of attack. This work was presented at the APS meeting in November 1989, and an abstract of this presentation follows.

**Study of Three-Dimensional Flows Past Complex Geometries Using a Finite-Element Method**, R. Ramamurti, SAIC & NRL and R. Lohner, GWU - The finite-element method of Lohner<sup>1</sup> has been advanced to study the flow past complex 3-D geometries. In the present investigation, the advancing front algorithm<sup>2</sup> is employed to generate the unstructured grids over a complete submarine configuration. A two-step Taylor-Galerkin procedure is used to discretize the Euler equations of motion. The procedure was tested via application to a model problem of inviscid flow past a sphere at  $M_\infty = 0.2$ . Comparison of the surface pressure distribution with potential flow is very good. The procedure is then extended for the simulation of 3-D flow past a submarine hull configuration and the results are compared with the axisymmetric solution. Flow past this configuration with sail and stern appendages is also investigated for various pitch angles of attack to study the asymmetric flow properties.

\* This work is supported by Naval Research Laboratory under a contract from DARPA.

<sup>1</sup> Lohner, R., Morgan, K. and Zienkiewicz, O.C., Int. J. Num. Meth. Fluids, No. 4, 1984.

<sup>2</sup> Lohner, R. and Parikh, P., AIAA Paper No. 88-0515, 1988.

In order to predict the formation of vortices and hence the noise generated by them, it is important to carry out a Navier-Stokes analysis.

Therefore, the viscous diffusion terms were incorporated into the 3-D version of the flow solver. In the numerical procedure, these terms were treated as a deferred correction in the second step of the Taylor-Galerkin procedure. Preliminary coarse grid results of the fully appended model at a pitch angle of attack of 10° show the presence of vortices at the junction of the sail and the hull and also at the tips of the stern planes. This configuration was also studied at a yaw angle of attack, in order to predict the forces and moments that will be involved in a maneuvering submarine. This is documented in the paper that was presented at the 29th AIAA Aerospace Sciences Meeting and is included as Appendix B.

In 1990, the research effort was directed towards simulating transient flow for resolving the D5 water-in-nozzle problem and to give better estimates of the transient forces acting on the nozzle. This research effort is part of the Trident related activities at NRL. It has been the primary research effort since January 1990. Work was also continued on the previous year's effort on simulating viscous flows past complex geometries such as the submarine hull with all its appendages.

The finite element method coupled with the adaptive remeshing algorithm was employed to predict the transient forces and the flow field in the nozzle. The interaction of the shock waves with the aft-shield was also investigated. Further, the rigid body motion of the aft-shield was integrated with the remeshing algorithm in order to study the effects of its movement. The effects of variable specific heat ratios on the dynamics of the flow was also investigated. The results of this effort were presented at the 43rd Annual APS meeting and the abstract follows.

**Numerical Simulation of Transient Flow in a Nozzle.\*** R. Ramamurti, SAIC & NRL, K. Kailasanath, NRL and R. Lohner, GWU - Unsteady flow in nozzles is studied in order to understand the dynamics of the flow field and to get better estimates on the forces acting on the nozzle. The numerical simulations have been performed using a finite-element method coupled with an adaptive remeshing algorithm. The scheme employed for the flow solver is a Finite-Element Method Flux-Corrected Transport scheme (FEM-FCT) which has shown excellent predictive capability for axisymmetric flow fields with strong and weak shocks. The effect of the presence of a barrier near the exit plane of the nozzle on the flow is studied by integrating the adaptive remeshing of the unstructured grid with the rigid body motion of the barrier. The movement of the barrier due to the interaction of the shock wave is calculated. The flow in the nozzle shows the presence of a recirculating

region which eventually exits the nozzle. The effect of variable ratio of specific heats is also investigated.

\*This work is supported by Naval Research Laboratory and SSPO.

Since March 1991, SAIC evaluated the newly developed incompressible flow code using unstructured meshes. This is done via application to several model problems such as flow over a flat plate, developing flow in a channel, laminar flow over a backward facing step, and flow past a circular cylinder.

### **III. Vortex Shedding and Lock-On**

SAIC conducted a study of a number of problems in the field of bluff body wakes. The study was carried out using a code obtained from Professor George Karniadakis at Princeton. This code, NEKTON, is a spectral element code and required substantial change to enable it to run on the computer at NRL. Once running we carried out an extensive numerical investigation of vortex shedding behind a circular cylinder.

The work consisted of determining the effect on the vortex street of superimposing a small perturbation on the incident mean flow upstream of the cylinder. Experimental work had suggested that for a range of frequencies and amplitudes, this perturbation could result in a phenomenon known as "lock-on", in which the frequency of vortex shedding in the wake was altered to match the frequency of the perturbation. For frequencies and amplitudes outside of a hypothetical frequency-amplitude curve, the vortex street could exhibit a variety of behaviors including quasi-periodic and chaotic shedding frequencies.

Two papers that were published jointly with Owen Griffin of NRL describe this work. The first paper to appear was a review article in which the experiments performed by various investigators were described and the results compared; a single numerical case in which lock-on was obtained was described in detail (cf. "Review-Vortex Shedding Lock-on and Flow Control in Bluff Body Wakes," ASME Journal of Fluid Engineering, December 1991.) This paper is included here as Appendix C.

The second paper (cf. "Vortex Shedding and Lock-on in Bluff Body Wakes," ASME Journal of Fluids Engineering, June 1993) contains the results of an extensive numerical investigation in which the shape of the frequency-

amplitude curve was defined, and a more complete analysis of the near-wake flow in cases of lock-on was done. In this analysis, quantities such as the drop in the time-averaged streamwise component of the velocity in the wake and the rms velocity fluctuations were examined, as well as the longitudinal vortex spacing and the length of the vortex formation region. The results were compared with experimental data and with data obtained numerically by other investigators, who had not attempted to define the frequency-amplitude curve, but had identified one or more individual cases of lock-on. This paper is included in this report as Appendix D.

#### **IV. Turbulence Studies**

This effort involved investigations of wall-bounded turbulent flows and free-surface turbulence. It included both the development of a new numerical code and the interpretation of the resulting simulation. The general approach was to use direct numerical simulations to generate a spatially and temporally accurate database for interrogation. The simulations were performed and analyzed on the NRL Cray X-MP. The major elements of these studies are described in the following.

1. *The structure of Turbulent Flows* - In wall bounded turbulent channel flow, the fluid flow is not entirely random, but exhibits a chaotic reoccurrence of organized events. A common feature of these events is an elongated region of low speed flow, or a low speed streak. A streak tracing algorithm has been developed which permits the detection and tracking of low speed structures in the boundary layer. The development of conditional sampling methodologies in conjunction with direct numerical simulations provides tools to obtain new insights into turbulent flows and turbulence-free surface interactions.
2. *Free-surface Turbulence* - The structure of turbulence near a free surface was examined by using results obtained from a direct simulation of flow between a no-slip wall and a shear free boundary, which serves as a model of a waveless free surface. The turbulence is generated at the no-slip boundary and convects to the free-surface.

- *Redistribution of Turbulence Kinetic Energy by Pressure-Strain*

An energy balance analysis shows that the pressure-strain term is the dominant producing term for the spanwise component of the turbulent kinetic energy at the free-surface. Two phenomenological models were developed for the redistribution, involving the interaction of turbulent eddies with the free-surface.

- *Enstrophy Production*

The total instantaneous enstrophy of a fluid is defined as the square of the instantaneous vorticity,  $\Sigma_i \Omega_i \Omega_i$ . As a result of the shear free nature of the top boundary, only normal vorticity may terminate on it. The vorticity components parallel to the top boundary must go to zero at the boundary. The time averaged fluctuating enstrophy balance equations, which are an indicator of the level of activity of the vorticity field are evaluated. Near the free surface the rate of production and destruction of enstrophy is set by the stretching and rotation of fluctuating vorticity by the fluctuating velocity field. The results of this study were presented at the 29th Aerospace Science Meeting, January 7-10, 1991, in Reno, Nevada. The associated paper is included here in Appendix E.

- *Length Scale and Modeling*

Two-point correlations, energy spectra, and length scales reveal important free surface induced effects. The length scales near the free surface are compared with the scales near the centerline of normal turbulent channel flow. This comparison reveals an increase by a factor of three in the streamwise length scales associated with the spanwise velocity fluctuations and an increase by a factor of two in the spanwise length scales for the streamwise velocity fluctuations. The length scales normal to the free surface are decreased for all velocity components. This indicates a more pancake-like eddy structure near the free surface compared to the structure near the centerline of a normal channel. The energy spectra show qualitative agreement with the Hunt-Graham model, though higher resolution calculations will be required to make more quantitative comparisons. In addition, the dissipation rates for the horizontal components of the

turbulence are reduced near the free surface while the dissipation of the vertical component remains approximately constant. Details were presented at the 29th Aerospace Science Meeting, January 7-10, 1991 in Reno, Nevada and are included in this report as Appendix F. A second paper on the subject was presented at the AIAA 22nd Fluid Dynamics, Plasmadynamics & Lasers Conference in June 1991 at Honolulu, Hawaii and is incorporated in this report in Appendix G.

### 3. *Vortex Reconnection*

A numerical simulation of the interaction of a vortex ring with a shear-free boundary was performed. The Reynolds number was 1000, based on the circulation and viscosity, and the ratio of the core diameter to the ring diameter was 0.4. In this simulation the vortex ring interacts with the shear-free boundary through the primary and secondary reconnection events resulting in a pair of vortex half rings attached to the boundary. The dynamics of the reconnection process are discussed using the enstrophy balances and an existing analytical model of the diffusion of a strained vortex pair. Based on these results, a physical description of the reconnection events was developed. This work is described in detail in a paper published in the Journal of the American Society of Mechanical Engineers (ASME) 1991 (AMD - Vo. 119, Dynamics of Bubbles and Vortices Near a Free Surface) and is included here in Appendix H. Additional description of the work appeared in an earlier paper presented at the Winter Annual Meeting of the ASME on Recent Advances and Applications in Computational Fluid Dynamics in November 1990 in Dallas, Texas. This is included here in Appendix I.

### 4. *Numerical Methods* - A code for the direct simulation of turbulence was developed. This code, THRDFS, is similar to the method of Kim, Moin, and Moser (1987). The primitive Navier-Stokes equations are rewritten as a fourth-order equation for the vertical velocity and a second-order equation for the vertical vorticity. The technique implicitly satisfies continuity, which allows decoupling of the pressure field from the viscous flow calculation. The pressure field is evaluated in a postprocessing calculation. Pressure and vertical velocity on the free-surface are coupled by requiring the normal momentum equation to be added to the free-surface boundary conditions.

The free-surface boundary conditions have been implemented in two forms. The boundary conditions are linearized in the first case, resulting in low amplitude waves and no mode coupling within the boundary conditions. The subsurface flow field, however, remains fully nonlinear and mode coupling is permitted. In the second implementation of the boundary conditions the application is for weakly nonlinear free-surfaces. The full nonlinearity of the boundary conditions is retained, but the conditions are still imposed on the mean free-surface.

## **V. Numerical Simulations in Support of Narcotics Interdiction**

We have been investigating the issues involved in requirements definition for narcotics interdiction. How much of a particular signature could be there, how does this amount change for different conditions, and what is the temporal relationship in various scenarios. Our approach has been to simulate numerically the conditions that arise during vapor or particulate transport. The advantages of this approach are that (1) a broad range of scenarios can be rapidly and inexpensively analyzed by simulation and (2) simulations can display quantities that are difficult or impossible to measure. The drawback of this approach is that simulations cannot include all of the phenomena present in a real measurement, and therefore the fidelity of the simulation results is always an issue.

A description of this work will be presented in San Diego, California in July 1993 at a meeting on Cargo Inspection Technologies, part of SPIE's International Symposium on Optics, Imaging, and Instrumentation.

We will discuss these issues and how they apply to the current problems. We will show the results of a 1D numerical simulation and compare these results with the analytical solution to show that the model is verifiable at this level. We will also present data of 3D simulations of vapor transport in a loaded cargo container and some of the materials issues present in this problem.

This work was also presented in June 1993 at the Contraband Detection Trace Chemical Phenomenology Workshop sponsored jointly by ARPA and the Office of National Drug Control Policy. A set of viewgraphs presented at the meeting and incorporated into the Proceedings of the Workshop are included in this report as Appendix J.

## **Appendix A**

### **A Finite Element Solver for Axisymmetric Compressible Flows**

**AIAA-89-1794**

**A Finite Element Solver for Axisymmetric  
Compressible Flows**

**Rainald Löhner**

**CMEC, The George Washington University,  
Washington, D.C.**

**Joseph D. Baum and Eric Loth**

**LCP&FD, Naval Research Laboratory, D.C.**

**Ravi Ramamurti**

**Science Applications Int. Corp. , MacLean, VA**

# A FINITE ELEMENT SOLVER FOR AXISYMMETRIC COMPRESSIBLE FLOWS

Rainald Löhner\*, Joseph D. Baum†, Eric Loth† and Ravi Ramamurti‡

\* CMEE, The George Washington University, Washington, D.C.

† LCP&FD, Naval Research Laboratory, Washington, D.C.

‡ Science Applications International Corp., McLean, VA

## Abstract

This paper describes an extension of previously developed Finite Element Euler and Navier-Stokes solvers on unstructured grids in Cartesian coordinate systems [1-5] to axisymmetric coordinate systems. It is shown how to arrive at a consistent, high-order formulation by a proper choice of interpolation for the unknowns. All integrals are derived in closed form, and the exact formulas are presented. Numerical examples simulating both transient and steady-state flows in the subsonic, transonic and supersonic regimes are given. The results demonstrate the accuracy and wide range of applicability of the method.

## Introduction

Many practical flow simulations require the solution of the equations describing axisymmetric compressible flows. Among these are flows in or past bodies of revolution at zero angle of attack, such as ducts, nacelles, fuselages, missiles, as well as certain types of explosions and detonations. For an axisymmetric coordinate system, the Navier-Stokes equations governing compressible flows may be written as:

$$\frac{\partial U}{\partial t} + \frac{\partial F_u}{\partial x} + \frac{1}{r} \frac{\partial F_r}{\partial r} = S_e + \frac{\partial F_u}{\partial x} + \frac{1}{r} \frac{\partial F_r}{\partial r} + \frac{S_v}{r}, \quad (1a)$$

where

$$U = \begin{Bmatrix} \rho \\ \rho u \\ \rho v \\ \rho e \end{Bmatrix}, \quad F_u = \begin{Bmatrix} \rho u \\ \rho u^2 + p \\ \rho uv \\ uH \end{Bmatrix}, \quad F_r = \begin{Bmatrix} \rho v \\ \rho uv \\ \rho v^2 + rp \\ rvH \end{Bmatrix}, \quad (1b-d)$$

$$H = \rho e + p, \quad S_e = \begin{Bmatrix} 0 \\ 0 \\ p \\ 0 \end{Bmatrix}, \quad (1e-f)$$

$$F_v = \begin{Bmatrix} 0 \\ \tau^{xx} \\ \tau^{rr} \\ u\tau^{xx} + v\tau^{rr} + q_s \end{Bmatrix}, \quad S_v = \frac{1}{Re} \begin{Bmatrix} 0 \\ 0 \\ \tau^{xx} \\ 0 \end{Bmatrix}, \quad (1g-h)$$

$$F_v = \begin{Bmatrix} 0 \\ \tau^{xx} \\ \tau^{rr} \\ u\tau^{xx} + v\tau^{rr} + q_s \end{Bmatrix}. \quad (1i)$$

Here  $x, r$  denote the axial and radial coordinates,  $\rho, p, e, H$  denote the density, pressure, energy and enthalpy,  $u, v$  denote the velocities in the  $x$  and  $r$  direction. Using Stokes hypothesis, the viscosity coefficient  $\mu$  and the bulk modulus  $\lambda$  are related by

$$\lambda = -\frac{2\mu}{3}, \quad (2)$$

and the viscous shear stresses and heat fluxes are given by

$$\tau^{xx} = 2\mu \frac{\partial u}{\partial x}, \quad \tau^{rr} = 2\mu \frac{\partial v}{\partial r}, \quad (3a, b)$$

$$\tau^{x\theta} = -2\mu \frac{v}{r}, \quad \tau^{r\theta} = \mu \left( \frac{\partial u}{\partial r} + \frac{\partial v}{\partial x} \right), \quad (3c, d)$$

$$q^x = k \frac{\partial T}{\partial x}, \quad q^r = k \frac{\partial T}{\partial r}, \quad (3e, f)$$

where  $T$  and  $k$  denote the temperature and thermal conductivity of the fluid respectively. The equation set is completed by the addition of the state equations

$$p = (\gamma - 1)\rho \left[ e - \frac{1}{2}(u^2 + v^2) \right], \quad (4a, b)$$

$$T = c_v \left[ e - \frac{1}{2}(u^2 + v^2) \right], \quad (4c)$$

which are valid for a perfect gas, where  $\gamma$  is the ratio of the specific heats and  $c_v$  is the specific heat at constant volume.

Multiplication of the system of Eqs. (1) with  $r$  yields

$$\frac{\partial rU}{\partial t} + \frac{\partial rF_u}{\partial x} + \frac{\partial rF_r}{\partial r} = S_e + \frac{\partial rF_u}{\partial x} + \frac{\partial rF_r}{\partial r} + S_v. \quad (5)$$

We will denote the form of the Euler equations as given by Eq.(1) as Form 1, and the form given by Eq.(5) as Form 2. Both forms have been used as

starting points for discrete approximations. Form 1 was used by Kutler, Chakravarthy and Lombard [6], who treated it as a system of equations in two dimensions. This straightforward use of Form 1 does not produce a conservative difference scheme, and therefore these authors employed a shock fitting scheme to trace the shocks. Form 2 was employed by Deese and Agarwal [7], Yu and Chen [8], and Woan [9]. These authors used this form in Jameson's two-dimensional cell-centered finite volume FLO52 code. Because the scheme is cell-centered, no problems appear at  $r = 0$  (no nodes are placed there). However, problems are expected at  $r = 0$  if a node-centered scheme is preferred.

### Two-Step Taylor-Galerkin

The two-step Taylor-Galerkin algorithm has been used extensively for the computation of both inviscid and viscous flows in two and three dimensions for Cartesian coordinate systems [3-5]. Given a system of partial differential equations of the form:

$$\frac{\partial U}{\partial t} + \frac{\partial F^i}{\partial x^i} = S_e + \frac{\partial F^i}{\partial x^i} + S_v, \quad (6)$$

where  $U, F^i$  and  $S$  denote the vectors of unknowns, fluxes and source terms, we proceed as follows:

#### a) First step : (Advective Predictor)

$$U^{n+\frac{1}{2}} = U^n + \frac{\Delta t}{2} \cdot \left( S_e \Big|^{n+\frac{1}{2}} - \frac{\partial F^i}{\partial x^i} \Big|^{n+\frac{1}{2}} \right) \quad (7)$$

#### b) Second step :

$$\begin{aligned} \Delta U^n = U^{n+1} - U^n = \Delta t \cdot & \left( S_e \Big|^{n+\frac{1}{2}} - \frac{\partial F^i}{\partial x^i} \Big|^{n+\frac{1}{2}} \right. \\ & \left. + S_v \Big|^{n+\frac{1}{2}} + \frac{\partial F^i}{\partial x^i} \Big|^{n+\frac{1}{2}} \right). \end{aligned} \quad (8)$$

In both substeps the spatial discretization is performed via the usual Galerkin weighted residual method [3-5]. However, we note that at  $t^{n+\frac{1}{2}} = t^n + \frac{1}{2}\Delta t$ , the quantities  $U, F, S$  are assumed as piecewise constant in the elements, whereas at  $t^n, t^{n+1}$ , the quantities  $U, F, S$  are assumed piecewise linear.

### Choice of Conservative Form and Interpolation

Having selected the time-marching algorithm, we are now faced with the choice of conservative form. We can either:

#### a) Take Conservative Form 1, and integrate consistently, e.g.,

$$\int_{\Omega} W \frac{\partial U}{\partial t} 2 \pi r dz dr, \quad (9)$$

which yields essentially Conservative Form 2, or

#### b) Take Conservative Form 2, interpret it as a two-dimensional Cartesian problem, and incorporate it 'as is' into an existing 2-D code.

It is interesting to note that whichever approach we take, we always require Conservative Form 2 in order to obtain a consistent, conservative scheme. The next question that arises is how to interpolate the unknowns involved in order to obtain a discretization scheme. We can:

- Interpolate  $(r\rho, r\rho u, r\rho v, r\rho e)$  by a piecewise linear approximation. This is the so-called 'group formulation'. It appears very economical and simple to implement, but for the limit as  $r \rightarrow 0$ , all derived quantities, such as the pressure, are not defined. They either have to be obtained using L'Hopital's rule (which involves taking derivatives), or the points lying on the axis  $r = 0$  have to be pushed to  $r = \epsilon$ , where  $\epsilon$  is a small number. We tried this option, but found that we always encountered numerical problems close to the axis  $r = 0$ .
- Interpolate  $(\rho, \rho u, \rho v, \rho e)$  and  $r$  by a piecewise linear approximation. This form yields a higher accuracy in the  $r$ -direction [10] and has no problems at  $r = 0$ . The integrals that appear in the weighted residual statement are more complicated to evaluate. However, they may still be derived in closed form. For these reasons we chose this second form for the spatial discretization of the Euler equations.

### The First Step

Evaluating all the integrals in the weighted residual statement of Eq.(7), denoting  $N_j^i$  as the derivative of the shape function  $N_j^i$  with respect to  $j$ , using the notation defined in Figure 1, and the expressions

$$r'_i = \frac{r_i}{\bar{r}_{el}}; \quad \bar{r}_{el} = \frac{r_A + r_B + r_C}{3}, \quad (10)$$

the following discretization for the Navier-Stokes equations results:

Continuity:

$$\begin{aligned} \bar{\rho}_{el} = \frac{1}{12} \sum_{j=1,3} (3 + r'_j) \rho_j & \\ - \frac{\Delta t}{2} \sum_{j=1,3} [N_{,x}^j(\rho u)_j + N_{,r}^j(\rho v)_j] & \quad (11) \\ - \frac{\Delta t}{2} \frac{1}{\bar{r}_{el}} \frac{1}{3} \sum_{j=1,3} (\rho v)_j & \end{aligned}$$

X-Momentum:

$$\begin{aligned}\bar{\rho}u_{el} = & \frac{1}{12} \sum_{j=1,3} (3 + r'_j)(\rho u)_j \\ & - \frac{\Delta t}{2} \sum_{j=1,3} [N'_{,s}(\rho u^2 + p)_j + N'_{,r}(\rho uv)_j] \\ & - \frac{\Delta t}{2} \frac{1}{\bar{r}_{el}} \frac{1}{3} \sum_{j=1,3} (\rho uv)_j\end{aligned}\quad (12)$$

R-Momentum:

$$\begin{aligned}\bar{\rho}v_{el} = & \frac{1}{12} \sum_{j=1,3} (3 + r'_j)(\rho v)_j \\ & - \frac{\Delta t}{2} \sum_{j=1,3} [N'_{,s}(\rho uv)_j + N'_{,r}(\rho v^2 + p)_j] \\ & - \frac{\Delta t}{2} \frac{1}{\bar{r}_{el}} \frac{1}{3} \sum_{j=1,3} (\rho v^2)_j\end{aligned}\quad (13)$$

Energy:

$$\begin{aligned}\bar{\rho}e_{el} = & \frac{1}{12} \sum_{j=1,3} (3 + r'_j)(\rho e)_j \\ & - \frac{\Delta t}{2} \sum_{j=1,3} [N'_{,s}(uH)_j + N'_{,r}(vH)_j] \\ & - \frac{\Delta t}{2} \frac{1}{\bar{r}_{el}} \frac{1}{3} \sum_{j=1,3} (vH)_j\end{aligned}\quad (14)$$

### The Second Step

For the second step, we again evaluate all the integrals exactly. Denoting as  $M_e$  the consistent mass matrix

$$M_e = \int N^i N^j r ds dr, \quad (15)$$

we obtain for the Euler equations:

Continuity:

$$M_e \Delta \rho = \Delta t \sum_{el} VOL_{el} \bar{r}_{el} \left[ N'_{,s} \bar{\rho} u_{el} + N'_{,r} \bar{\rho} v_{el} \right] \quad (16)$$

X-Momentum:

$$\begin{aligned}M_e \Delta \rho u = & \Delta t \sum_{el} VOL_{el} \bar{r}_{el} \left[ N'_{,s} ((\bar{\rho} u^2 + p)_{el} - r'^s_{el}) \right. \\ & \left. + N'_{,r} (\bar{\rho} uv_{el} - r'^r_{el}) \right]\end{aligned}\quad (17)$$

R-Momentum:

$$\begin{aligned}M_e \Delta \rho v = & \Delta t \sum_{el} VOL_{el} \bar{r}_{el} \left[ N'_{,s} (\bar{\rho} uv_{el} - r'^s_{el}) \right. \\ & \left. + N'_{,r} ((\bar{\rho} v^2 + p)_{el} - r'^r_{el}) \right] \\ & + \Delta t \sum_{el} VOL_{el} N^i (\bar{p}_{el} + r'^p_{el})\end{aligned}\quad (18)$$

Energy:

$$\begin{aligned}M_e \Delta \rho e = & \Delta t \sum_{el} VOL_{el} \bar{r}_{el} \left[ N'_{,s} (\bar{u} H_{el} - (u r'^s + v r'^r + q_s)_{el}) \right. \\ & \left. + N'_{,r} (\bar{v} H_{el} - (u r'^s + v r'^r + q_r)_{el}) \right]\end{aligned}\quad (19)$$

### Consistent Mass Matrices

A question that arises from the computational point of view is whether the consistent mass matrix, which is obtained by assembling, at element level, the following exact element matrices

$$M_e = \frac{VOL_{el}}{60} \left[ r_A \begin{pmatrix} 6 & 2 & 2 \\ 2 & 2 & 1 \\ 2 & 1 & 2 \end{pmatrix} + r_B \begin{pmatrix} 2 & 2 & 1 \\ 2 & 6 & 2 \\ 1 & 2 & 2 \end{pmatrix} + \right. \\ \left. r_C \begin{pmatrix} 2 & 1 & 2 \\ 1 & 2 & 2 \\ 2 & 2 & 6 \end{pmatrix} \right], \quad (20)$$

cannot be simplified by taking the average element radius in the integral (13). This would yield the element matrix

$$M_e = \frac{VOL_{el} \bar{r}_{el}}{12} \begin{pmatrix} 2 & 1 & 1 \\ 1 & 2 & 1 \\ 1 & 1 & 2 \end{pmatrix} = \bar{r}_{el} M_e^{2D}, \quad (21)$$

which is less expensive to evaluate. Our numerical experiments indicate that this simplification can be employed without loss of accuracy. The consistent mass

matrix is solved iteratively as in the Cartesian case [1-5], and again it is found that two to three passes over the elements are sufficient to raise the phase accuracy of the resulting scheme from second to essentially fourth order.

### Artificial Viscosities

a) **Modified Lapidus artificial viscosity:** The modified Lapidus artificial viscosity [11], which proved successful for Cartesian coordinate systems, can be extended to the axisymmetric case without any further modifications by multiplying the element contributions by their respective average element radius.

b) **Mass diffusion for the FEM-FCT algorithm:** The mass diffusion which is added to the high-order scheme to yield a monotonic low-order scheme as part of the FEM-FCT algorithm [5] can also be extended to the axisymmetric case by simply multiplying the Cartesian element contributions by their respective average element radius.

### Numerical examples

A number of numerical examples are given to illustrate the performance of the method when simulating transient and steady-state problems in the subsonic, transonic and supersonic flow regime. For all steady-state problems, local timestepping was used to accelerate the convergence.

1) **Supersonic flow past a sphere (steady state):** the case under consideration corresponds to a free-stream Mach Number of  $M_\infty = 3.0$ . For this steady-state solution, only the Lapidus artificial viscosity was employed to stabilize the solution. The exact stand-off distance for the shock should be of  $s = 1.216R$ , where  $R$  denotes the radius of the sphere [12]. The grid was adaptively remeshed three times [13]. The final solution is shown in Figures 2a-2c. The experimental stand-off distance is reproduced exactly by the solution.

2) **Shock impinging on a blunt body (transient):** The problem statement, as well as the solutions obtained at two different times are shown in Figures 3a-3f. A strong shock ( $M_s = 10$ ), moving from left to right, impinges on the concave body displayed in Figure 3a. An adaptive refinement scheme for transient problems [14] was employed to resolve accurately all flow features. The mesh was adapted every 7 timesteps, and two levels of refinement were allowed. The FEM-FCT option was invoked to maintain sharp shock-resolution. The main aim of this simulation was to demonstrate the good phase-accuracy and low numerical damping of the present scheme for this class of problems. As observed in earlier simulations of this class of problems [15-17] the concave shape of the

body affects the stability of the stand-off shock significantly. Figures 3g,h show the pressure time-histories at two stations along the axis of symmetry. Station 1 (Figure 3g) lies at the far right end of the domain, while station 7 lies shortly behind the final position of the shock. One can clearly observe a damped shock oscillation around its steady-state position. It takes many cycles for the shock to settle to its final position. This behaviour, which is not observed for convex bodies, was also seen in other numerical simulations and several wind-tunnel experiments [15-17].

3) **Flow in an Underexpanded Nozzle (steady state):** The nozzle geometry, adapted mesh and Mach number contours are shown in Figures 4a and 4b respectively. Several different runs were performed for this problem. Some had the FEM-FCT option switched on, others only employed the basic two-step scheme described above. All these runs showed the existence of the two shocks depicted in Figure 4b. The run reproduced here was done with a Lapidus artificial viscosity. Both shocks resulted from inadequate nozzle wall shape, as shown in the expanded Mach-number contour plot of the region near the throat (Fig. 4c). The pressure ratio across the shock is significantly lower than the pressure decrease through the throat, though the gradients are higher. During convergence to steady state, the grid was adaptively remeshed three times. The maximum stretching ratio for the elements was set to six. A comparison between the measured and predicted radial distribution of total pressure at the exit plane is shown in Fig. 4d. Significant scatter is shown in the experimental data, while no data is available in the region of the multiple shock system. Nonetheless, the results demonstrate very good agreement over most of the exit plane. Some deviation is shown near the wall. It stems from the existence of a third shock that starts at the wall just upstream of the exit plane of the nozzle.

4) **Flow past a sphere,  $Re = 100$  (steady, viscous):** Steady viscous flow past a sphere at a Mach-number of  $M_s = 0.1$  and Reynolds-number of  $Re = 100$  provides an important test example to evaluate the accuracy of the present scheme. No artificial viscosity was added for this subsonic case. The problem statement, as well as the results obtained, are shown in Figure 5. The grid employed for this case (Fig. 5a) consists of a structured portion divided into triangles in the boundary layer zone, and an unstructured mesh elsewhere. From Fig. 5d, it can be seen that the re-circulation zone extends 1.4 diameters into the wake, measured from the center of the sphere. This compares well with experimental results [17]. Figure 5e shows very good agreement of computed surface vorticity with earlier numerical results [18,19]. The flow separates at an angle of approximately  $123^\circ$ .

## Conclusions

We have described a Finite Element Solver for axisymmetric compressible flows. The Navier-Stokes equations are advanced forward in time using a two-step Taylor-Galerkin procedure. Due care was given to obtain a consistent integration of all variables. Although slightly more expensive than the equivalent Cartesian scheme, the current formulation is the only one that yields full second order accuracy for all the unknowns in both the axial and radial directions. A high-order, monotonicity preserving scheme is obtained by combining this basic two-step Taylor-Galerkin procedure with FEM-FCT techniques.

Future developments will center on extensions of the current explicit scheme to semi-implicit or implicit schemes.

## Acknowledgements

This work was partially funded by the Defense Nuclear Agency through the Laboratory for Computational Physics and Fluid Dynamics of the Naval Research Laboratory.

We would also like to thank Dr. Ronald Kostoff from ONR for his encouragement and interest.

## References

- [1] J. Donea - A Taylor Galerkin Method for Convective Transport Problems; *Int. J. Num. Meth. Engng.* 20, 101-119 (1984).
- [2] R. Löhner, K. Morgan and O.C. Zienkiewics - The Solution of Nonlinear Systems of Hyperbolic Equations by the Finite Element Method; *Int. J. Num. Meth. Fluids* 4, 1043-1063 (1984).
- [3] R. Löhner, K. Morgan, J. Peraire and O.C. Zienkiewics - Finite Element Methods for High Speed Flows; *AIAA-85-1531-CP* (1985).
- [4] R. Löhner, K. Morgan and O.C. Zienkiewics - An Adaptive Finite Element Procedure for High Speed Flows; *Comp. Meth. Appl. Mech. Eng.* 51, 441-465 (1985).
- [5] R. Löhner, K. Morgan, J. Peraire and M. Vahdati - Finite Element Flux-Corrected Transport (FEM-FCT) for the Euler and Navier-Stokes Equations; *Int. J. Num. Meth. Fluids* 7, 1093-1109 (1987).
- [6] P. Kutler, S.R. Chakravarthy and C.P. Lombard - Supersonic Flow Over Ablated Nozzles Using an Unsteady Numerical Procedure; *AIAA Paper 78-213* (1978).
- [7] J.E. Deese and R.K. Agarwal - Calculation of Axisymmetric Inlet Flowfields Using the Euler Equations; *AIAA Paper 83-1853* (1983).
- [8] N.J. Yu and H.C. Chen - Flow Simulations for Nacelle-Propeller Configurations Using Euler Equations; *AIAA Paper 84-2143* (1984).
- [9] C.J. Woan - Euler Solution of Axisymmetric Flows About Bodies of Revolution Using a Multi-grid Method; *AIAA Paper 85-0017* (1984).
- [10] P.L. Roe - Error Estimates for Cell-Vertex Solvers of the Compressible Euler Equations; *ICASE Rep. 87-6* (1987).
- [11] R. Löhner, K. Morgan, and J. Peraire - A Simple Extension to Multidimensional Problems of the Artificial Viscosity due to Lapidus; *Comm. Appl. Num. Meth.* 1, 141-147 (1985).
- [12] J. Zierep - *Theoretische Gasdynamik*; G. Braun, Karlsruhe (1976).
- [13] R. Löhner - An Adaptive Finite Element Solver for Transient Problems with Moving Bodies; *Comp. Struct.* 30, 303-317 (1988).
- [14] R. Löhner - An Adaptive Finite Element Scheme for Transient Problems in CFD; *Comp. Meth. Appl. Mech. Eng.* 61, 323-338 (1987).
- [15] R. Bastianon - Unsteady Solution of the Flowfield over Concave Bodies - *AIAA J.* 7, 531-533 (1969).
- [16] I.O. Bohachevsky and R.N. Kostoff - Supersonic Flow over Convex and Concave Shapes with Radiation and Ablation Effects; *AIAA J.* 10, 1024-1031 (1972).
- [17] M. Van Dyke - *An Album of Fluid Motion*, Parabolic Press; (1982).
- [18] R. Clift, J.R. Grace and M.E. Weber - *Bubbles, Drops and Particles*, Academic Press, (1978).
- [19] Y. Rimon and S.I. Cheng - Numerical Solution of a Uniform Flow over a Sphere at Intermediate Reynolds Numbers; *Phys. Fluids* 12,5, (1969).

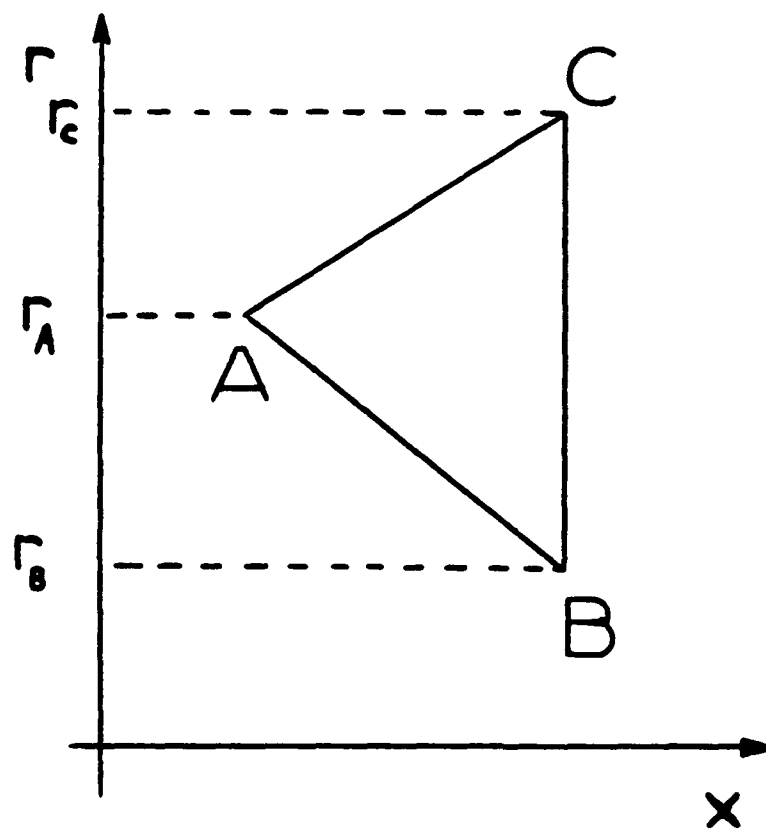


Figure 1: Notation used at element level

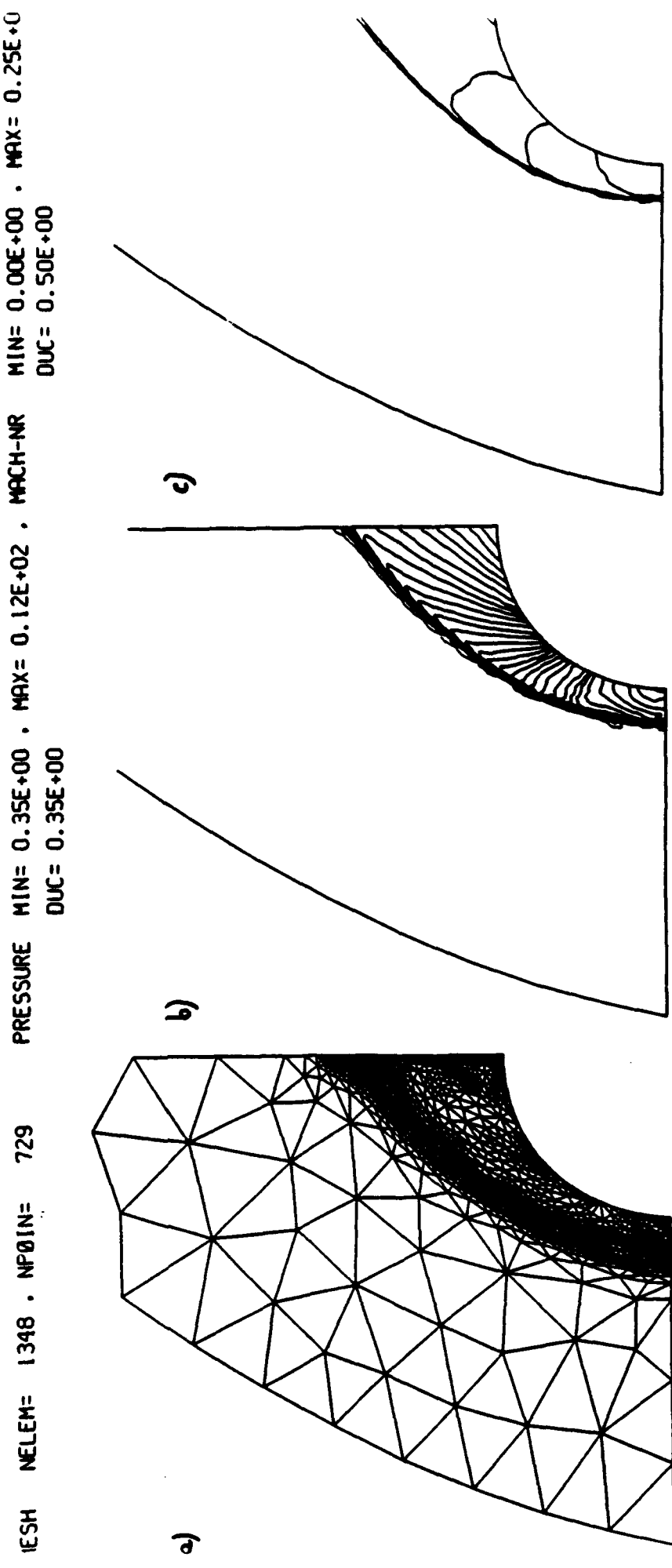


Figure 2: Supersonic Flow Past a Sphere

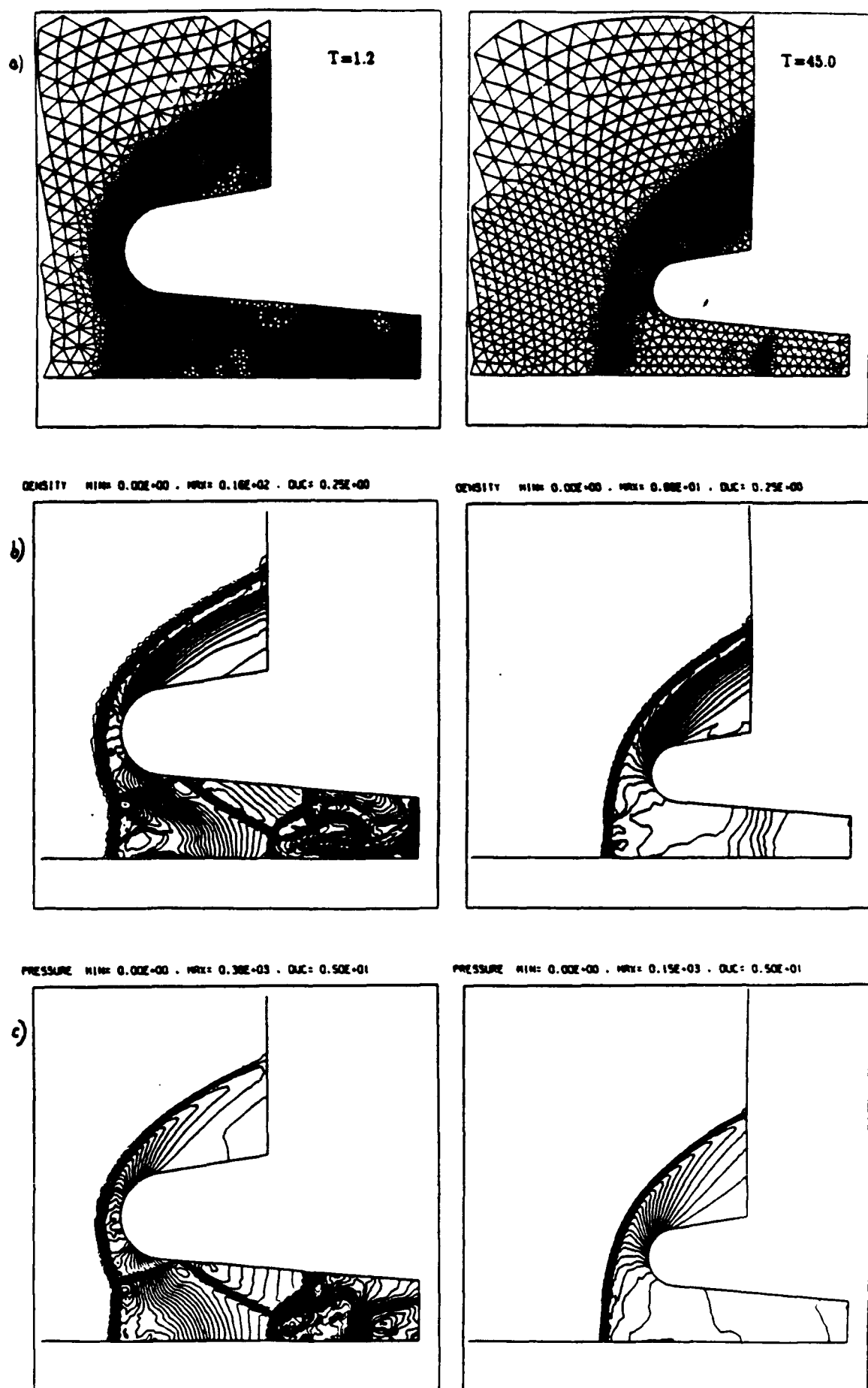


Figure 3: Shock-Concave Body Interaction

Figure 3g: Shock-Concave Body Interaction: Pressure History at Station 1

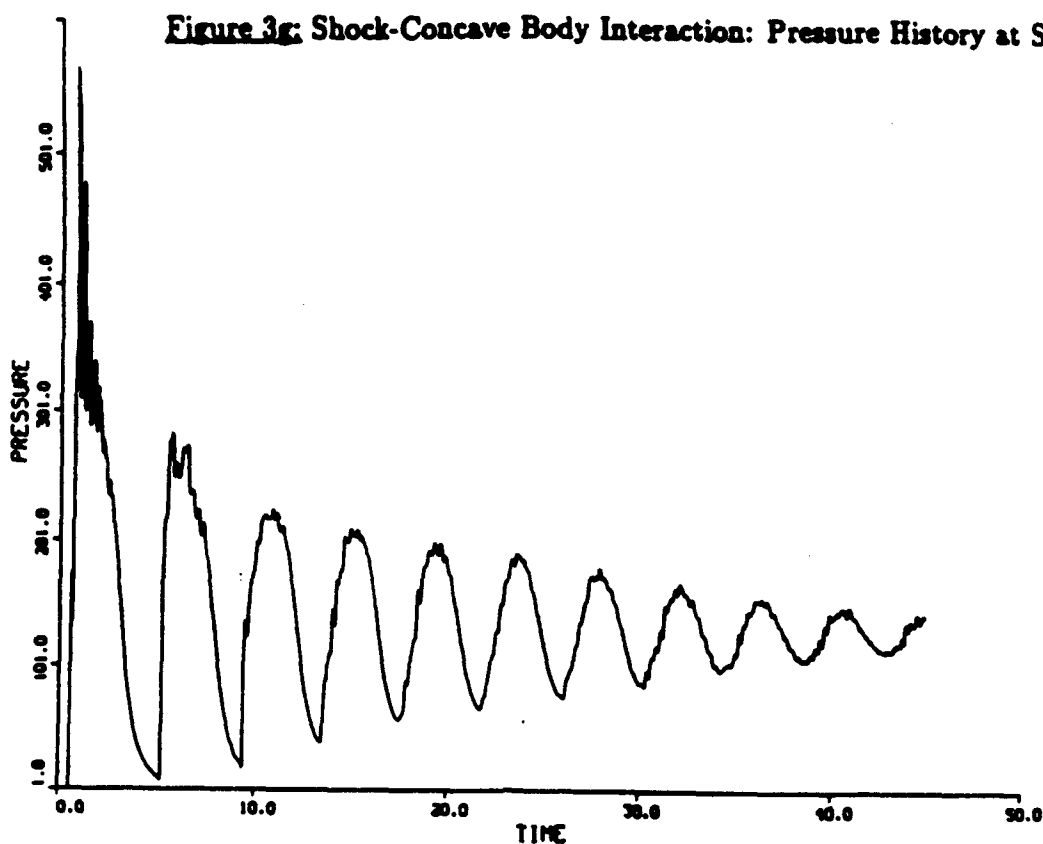
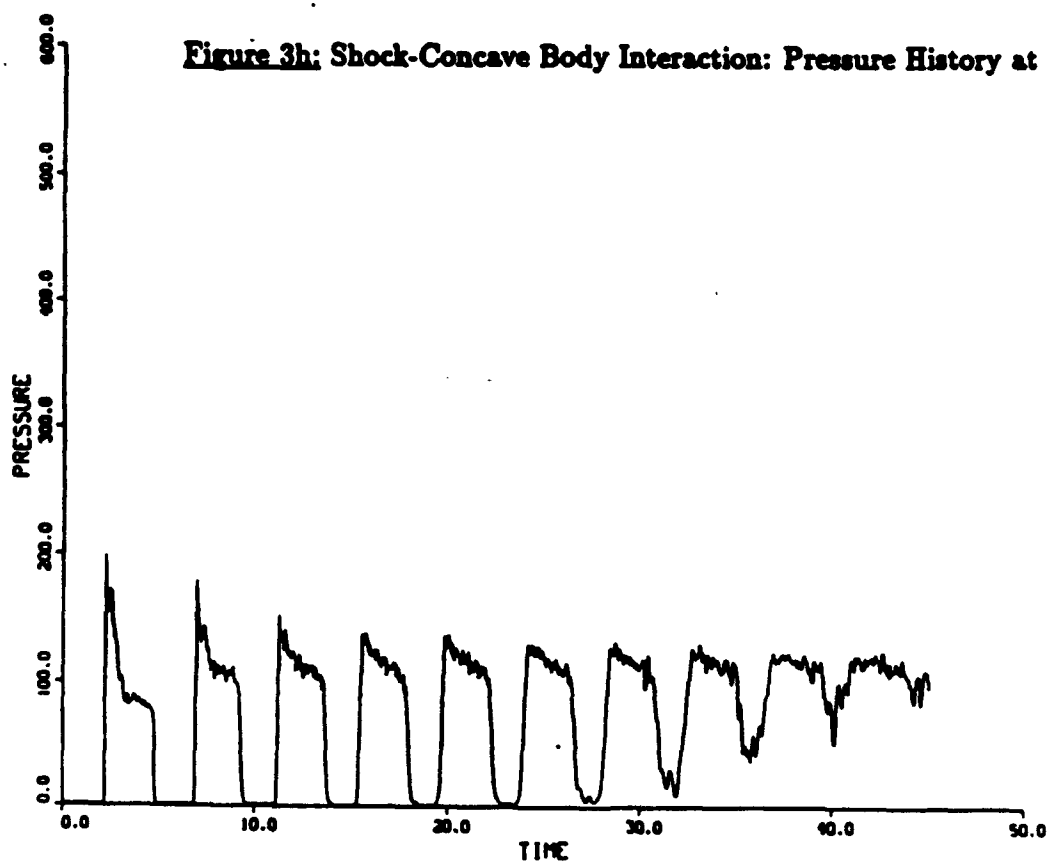


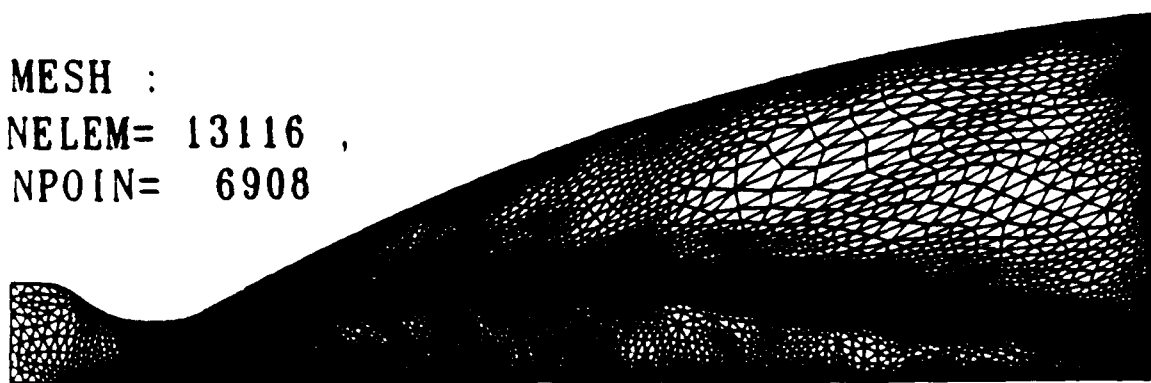
Figure 3h: Shock-Concave Body Interaction: Pressure History at Station 7



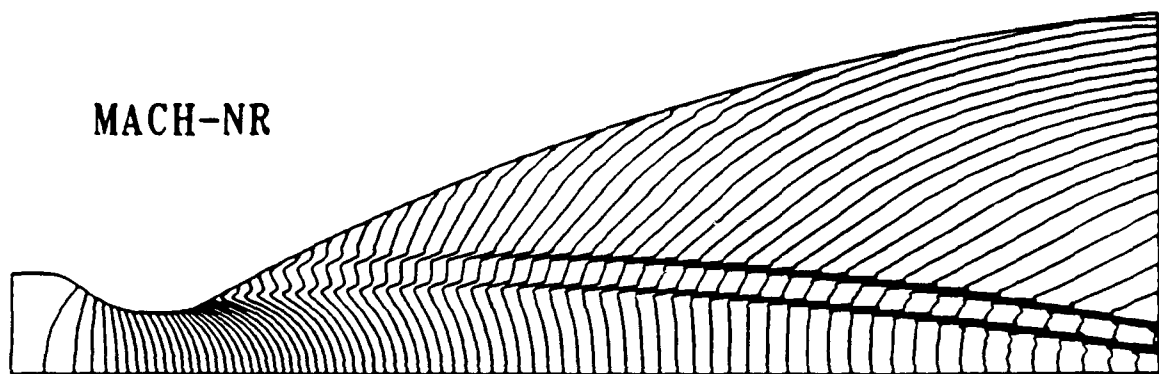
MESH :

NELEM= 13116 ,

NPOIN= 6908



MACH-NR



MACH-NR

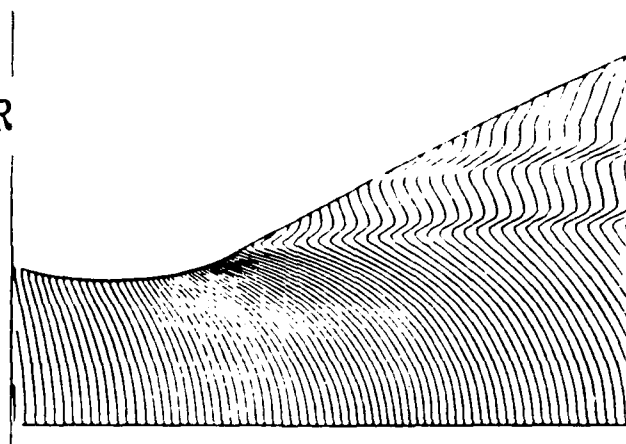


**Fig 4.** Mesh (a) and Mach Number Contours (b) for the Whole Nozzle and Expanded Mach Number Contours near the Throat.

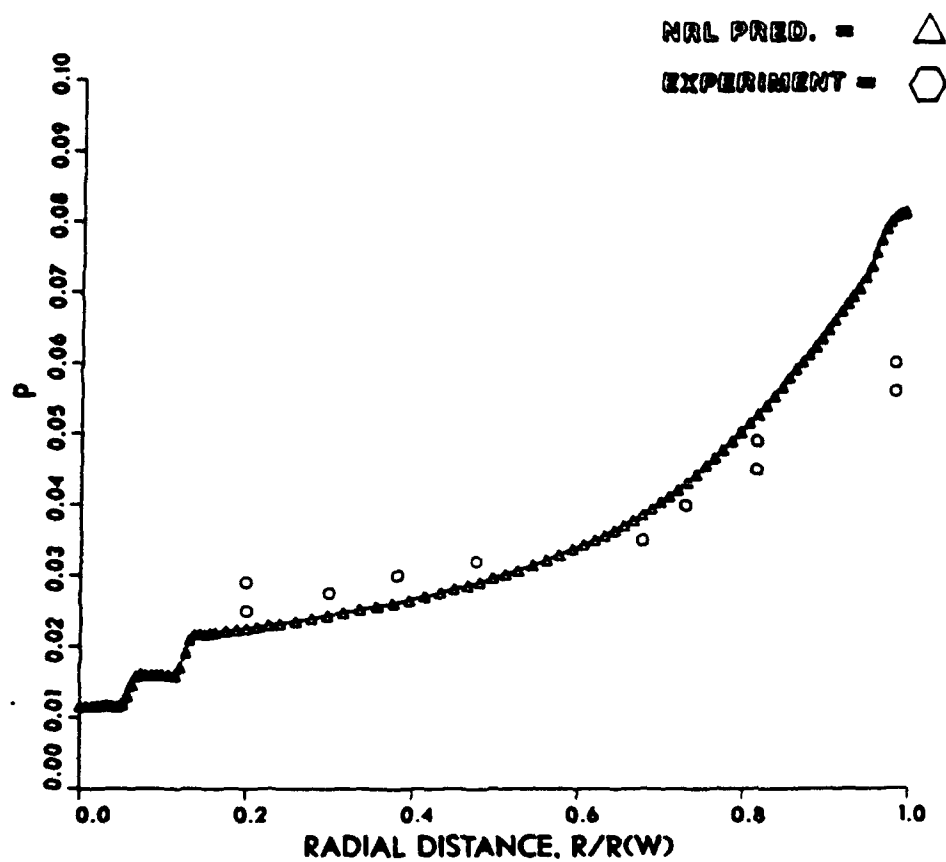
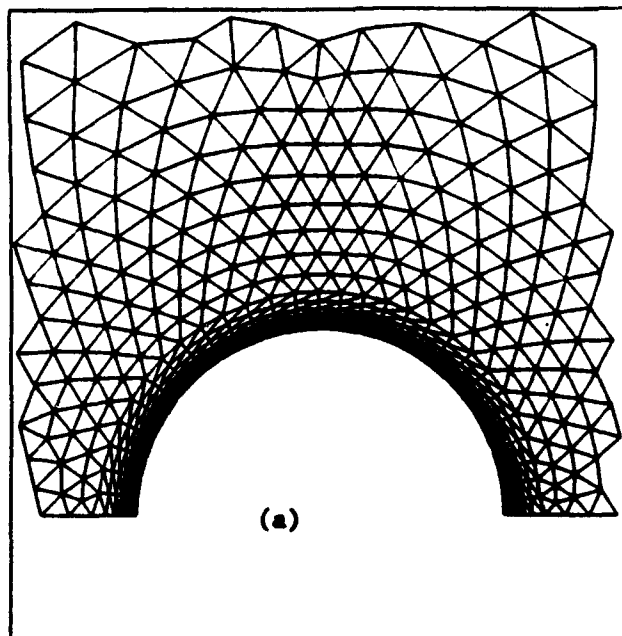
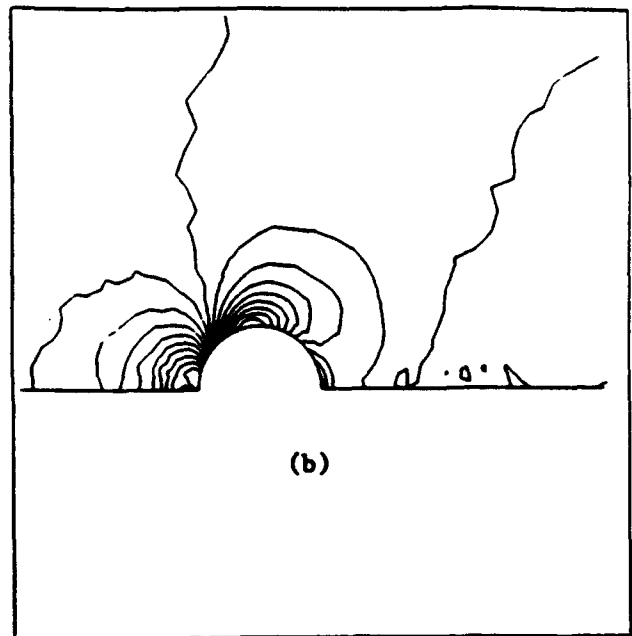


Figure 4d: Radial Distribution of Total Pressure at Exit Plane.

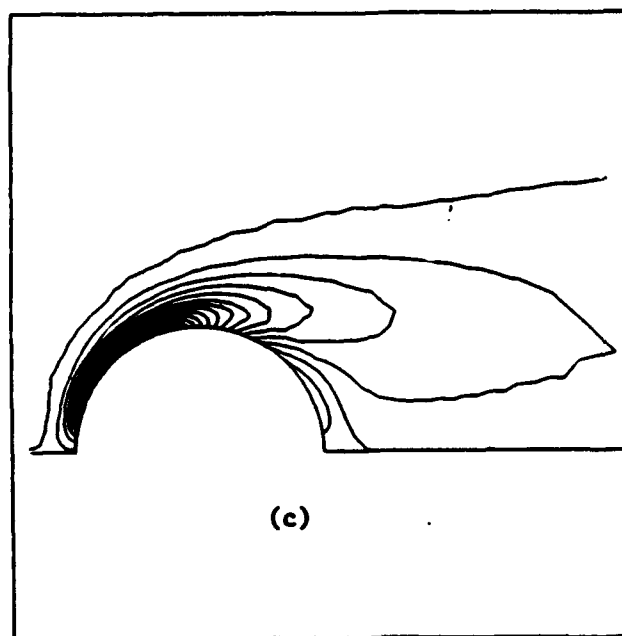
MESH : NELEM= 2029 , NPOINT= 1078



PRESSURE: MIN= 0.71E+02 , MAX= 0.72E+02 , DUC= 0.37E-01



VORTICITY: MIN=-0.90E+01 , MAX= 0.96E+00 , DUC= 0.53E+00



VELOCITY VECTORS

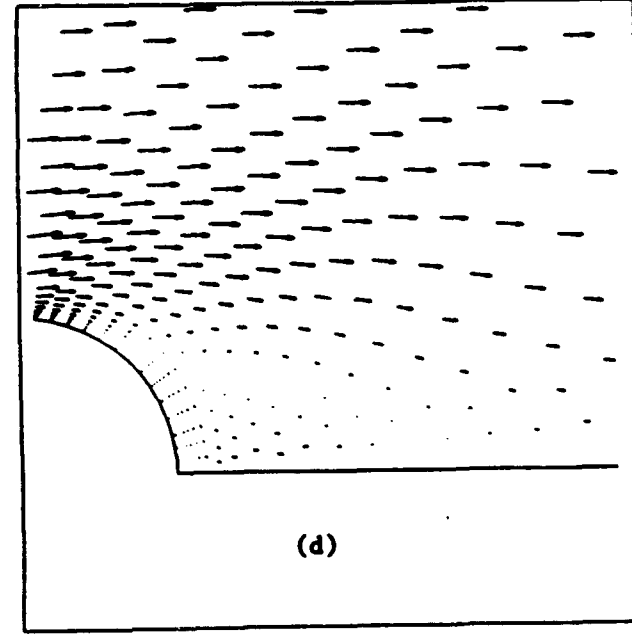


Figure 5: Flow past a Sphere:  $Ma=0.1$ ,  $Re=100$ .

(a) Grid; (b) Pressure Contours; (c) Vorticity Contours;  
(d) Velocity Vectors.

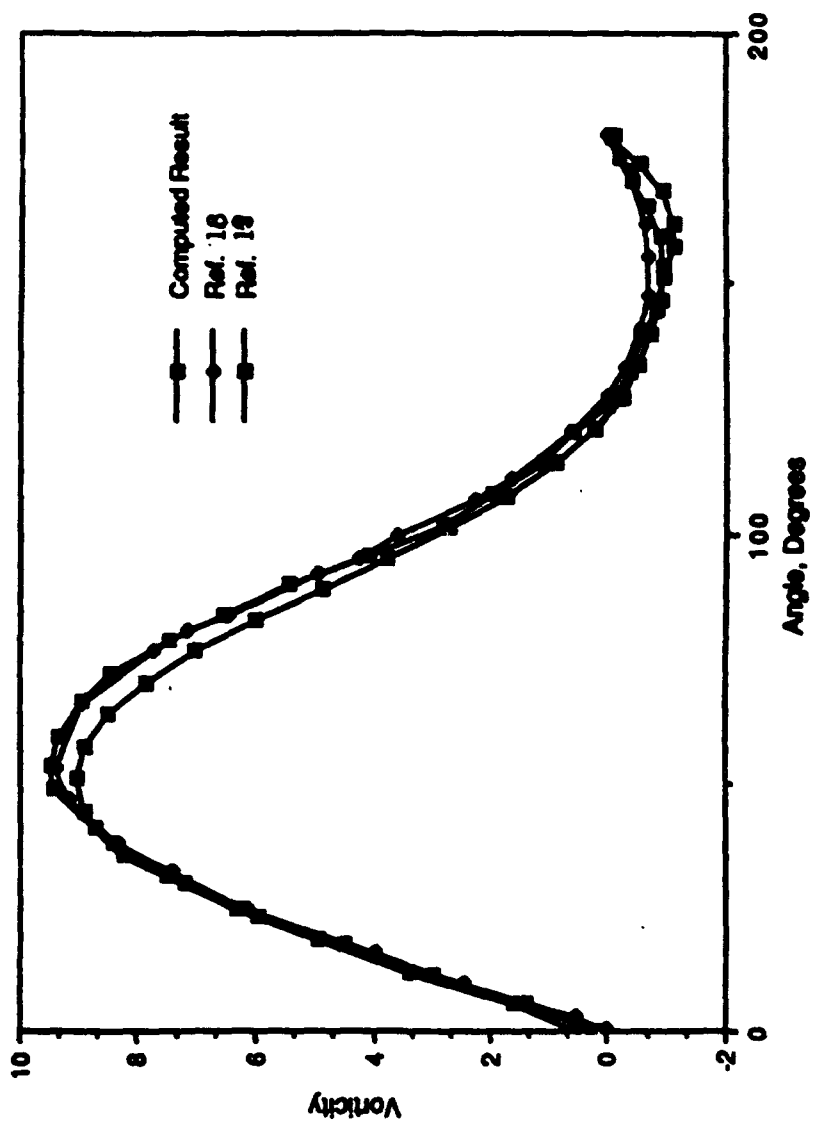


Figure 5e Comparison of Surface Vorticity Distribution on a Sphere.

## **Appendix B**

### **Simulation of Subsonic Viscous Flows Using Unstructured Grids and a Finite Element Solver**



**AIAA-90-0702**

**SIMULATION OF SUBSONIC VISCOUS FLOWS  
USING UNSTRUCTURED GRIDS AND A  
FINITE ELEMENT SOLVER**

**R. Ramamurti and R. Löhner\***

Science Applications International Corporation  
McLean, VA. 22102

and

Laboratory for Computational Physics and Fluid Dynamics  
Naval Research Laboratory  
Washington, D.C. 20375

\*The George Washington University  
Washington, D.C. 20052

**28th Aerospace Sciences Meeting**  
January 8-11, 1990/Reno, Nevada

# SIMULATION OF SUBSONIC VISCOUS FLOWS USING UNSTRUCTURED GRIDS AND A FINITE ELEMENT SOLVER

Ravi Ramamurti and Rainald Löhner\*

Science Applications International Corporation, McLean, VA 22102  
LCP&FD, Naval Research Laboratory, Washington, D.C. 20375

\* CMEE, School of Engineering and Applied Science  
The George Washington University, Washington, D.C. 20052

## Abstract

A finite element scheme [1,2] has been advanced for solving the Euler and Navier-Stokes equations with unstructured grids in both Cartesian and axisymmetric coordinate systems. The two-step Taylor-Galerkin procedure is employed to discretize the governing equations. The accuracy of the scheme is validated by comparing computed results for flow over a sphere with well known numerical results and via a grid-refinement study for an inviscid flow over an axisymmetric body. The procedure is extended to solve three-dimensional flows over submarine configurations with sail and stern appendages. Convergence acceleration for viscous flows by sub-stepping of the viscous terms is investigated.

## Introduction

Numerical solution of flow past complex geometries is an important tool for a fluid dynamicist. The use of unstructured grids consisting of triangular elements in two dimensions and tetrahedral elements in three dimensions together with a finite-element method has proven valuable in computing high-speed, compressible flows [1,2]. The advantage of using triangular or tetrahedral meshes over structured meshes is that complex geometries can be easily represented. For example, constructing a structured mesh around a submarine hull with its sail and stern appendages would require the tedious task of decomposing the domain. On the other hand, the advantage of the structured meshes is that they provide better resolution in the vicinity of the body and hence, allow better resolution of the strong gradients present in viscous flows. To accurately resolve these gradients, which are predominantly in the normal direction, it is necessary to have a fine mesh spacing in this direction while retaining a large spacing in the tangential direction. In the present work, a structured mesh is employed in the normal direction retaining unstructured mesh in the tangential direction. These structured meshes are then divided into triangular and tetrahedral elements in two and three dimensions respectively. The remainder of the unstructured grid is generated using the advancing front grid-generation algorithm [3].

In this paper the finite-element method is applied to solve low subsonic viscous flows both in axisymmetric and 3-D Cartesian coordinates. An explicit two-step Taylor-Galerkin procedure is employed to solve

This paper is declared a work of the U.S. Government and is not subject to copyright protection in the United States.

the governing equations. The convergence of the solution procedure to steady state depends on the speed of sound and the minimum cell-Reynold's number and is rather poor for low-speed, viscous flows. Therefore, two acceleration procedures are investigated in this paper. The first one tries to circumvent the timestep-limits imposed by cell Reynolds-numbers by using sub-stepping of the viscous fluxes. The second one tries to circumvent the timestep-limits imposed by the speed of sound by employing a semi-implicit technique, whereby the pressure-modes are integrated implicitly.

## Governing Equations

The equations governing the fluid flow are the Navier-Stokes equations which can be written as

$$\frac{\partial U}{\partial t} + \frac{\partial F_a^*}{\partial x} + \frac{1}{r^j} \frac{\partial F_a^*}{\partial r} + k \frac{\partial F_a^*}{\partial z} = j \frac{S_a}{r} + \frac{\partial F_v^*}{\partial z} + \frac{1}{r^j} \frac{\partial F_v^*}{\partial r} + k \frac{\partial F_v^*}{\partial z} + j \frac{S_v}{r}, \quad (1a)$$

where

- $j = 0, k = 0$ : 2-dimensional case,
- $j = 1, k = 0$ : axisymmetric case,
- $j = 0, k = 1$ : 3-dimensional case,

$$U = (\rho, \rho u, \rho v, \rho w, \rho e)^T,$$

$$F_a^* = \begin{Bmatrix} \rho u \\ \rho u^2 + p \\ \rho u v \\ \rho u w \\ u H \end{Bmatrix}, F_v^* = r^j \begin{Bmatrix} \rho v \\ \rho u v \\ \rho v^2 + p \\ \rho v w \\ v H \end{Bmatrix},$$

$$F_e^* = \begin{Bmatrix} \rho w \\ \rho u w \\ \rho v w \\ \rho w^2 + p \\ w H \end{Bmatrix}, H = \rho e + p, S_a = \begin{Bmatrix} 0 \\ 0 \\ 0 \\ 0 \\ 0 \end{Bmatrix},$$

$$F_v^* = \begin{Bmatrix} 0 \\ T_{zz} \\ T_{rz} \\ T_{sz} \\ u T_{zz} + v T_{rz} + w T_{sz} + q_s \end{Bmatrix},$$

$$F_v^r = r^j \begin{Bmatrix} 0 \\ \tau_{rs} \\ \tau_{rr} \\ \tau_{rs} \\ u\tau_{rs} + v\tau_{rr} + w\tau_{ss} + q_r \end{Bmatrix},$$

$$F_v^s = \begin{Bmatrix} 0 \\ \tau_{ss} \\ \tau_{rs} \\ \tau_{ss} \\ u\tau_{ss} + v\tau_{rs} + w\tau_{ss} + q_s \end{Bmatrix},$$

$$S_v = \frac{1}{Re} (0, 0, \tau_{ss}, 0, 0)^T. \quad (1b - 1k)$$

Here  $x, r$  and  $z$  denote the axial, radial and spanwise coordinates,  $\rho, p, e, H$  denote the density, pressure, energy and enthalpy and  $u, v, w$  denote the velocities in the  $x, r$  and  $z$  directions respectively. Using Stokes hypothesis, the viscosity coefficient  $\mu$  and the bulk modulus  $\lambda$  are related by

$$\lambda = -\frac{2\mu}{3}, \quad (2)$$

and the viscous shear stresses and heat fluxes are given by

$$\tau_{ss} = 2\mu \frac{\partial u}{\partial x}, \quad \tau_{rr} = 2\mu \frac{\partial v}{\partial r}, \quad \tau_{zz} = 2\mu \frac{\partial w}{\partial z},$$

$$\tau_{rs} = -2\mu \frac{v}{r}, \quad \tau_{rs} = \mu \left( \frac{\partial u}{\partial r} + \frac{\partial v}{\partial x} \right),$$

$$\tau_{rz} = \mu \left( \frac{\partial w}{\partial r} + \frac{\partial v}{\partial z} \right), \quad \tau_{zz} = \mu \left( \frac{\partial u}{\partial z} + \frac{\partial w}{\partial x} \right),$$

$$q_r = \kappa \frac{\partial T}{\partial x}, \quad q_r = \kappa \frac{\partial T}{\partial r}, \quad q_z = \kappa \frac{\partial T}{\partial z}, \quad (3a - 3i)$$

where  $T$  and  $\kappa$  denote the temperature and thermal conductivity of the fluid respectively. The equation set is completed by the addition of the state equation

$$p = (\gamma - 1)\rho \left[ e - \frac{1}{2} (u^2 + v^2) \right], \quad (4)$$

which is valid for a perfect gas, where  $\gamma$  is the ratio of the specific heats.

For the axisymmetric case, the system of Eqs. (1) is multiplied with  $r$  to yield

$$\frac{\partial rU}{\partial t} + \frac{\partial rF_a^s}{\partial x} + \frac{\partial F_a^r}{\partial r} = S_a + \frac{\partial rF_a^s}{\partial x} + \frac{\partial F_a^r}{\partial r} + S_v. \quad (5)$$

Using this form of the conservative equations can be shown to be the same as integrating the system of Eqs. (1) in a consistent manner. In the weighted residual framework, the use of conservative form represented by Eq. (5) in conjunction with separate interpolations for  $r$  and  $U$  avoids the problems encountered for  $r = 0$  using a node-centered scheme. Details of evaluating the integrals in the weighted residual statement and interpolation of the unknowns are given in Refs. [2,4].

### Two-Step Taylor-Galerkin Procedure

A two-step form of the one-step Taylor-Galerkin scheme is employed as the time advancing scheme. This belongs to the Lax-Wendroff class of schemes and has been used extensively for the computation of both inviscid and viscous flows in two and three dimensions for Cartesian coordinate systems [1,2]. Given a system of partial differential equations of the form

$$\frac{\partial U}{\partial t} + \frac{\partial F_a^i}{\partial x^i} = S_a + \frac{\partial F_v^i}{\partial x^i} + S_v, \quad (6)$$

where  $U, F_a^i$  and  $S_a$  denote the vector of unknowns, advective fluxes and advective source terms, and  $F_v^i$  and  $S_v$  denote viscous fluxes and viscous source terms, the two-step is as follows.

#### a) First step (Advection predictor):

$$U^{n+\frac{1}{2}} = U^n + \frac{\Delta t}{2} \cdot (S_a|_n - \frac{\partial F_a^i}{\partial x^i}|_n) \quad (7)$$

#### b) Second step :

$$\begin{aligned} \Delta U^n &= U^{n+1} - U^n \\ &= \Delta t \cdot (S_a|^{n+\frac{1}{2}} - \frac{\partial F_a^i}{\partial x^i}|^{n+\frac{1}{2}} + \frac{\partial F_v^i}{\partial x^i}|^n + S_v|_n). \end{aligned} \quad (8)$$

In both substeps the spatial discretization is performed via the usual Galerkin weighted residual method [1,2]. However, we note that at  $t^{n+\frac{1}{2}} = t^n + \frac{1}{2}\Delta t$ , the quantities  $U, F, S$  are assumed piecewise constant, whereas at  $t^n, t^{n+1}$ , the quantities  $U, F, S$  are assumed piecewise linear. Also, it should be noted that the viscous terms are added during the second-step of the procedure as a deferred corrector.

### Artificial Viscosities

For inviscid flows considered in the present paper, additional smoothing has been implemented in the flow-solver. Two post-smoothing artificial viscosities have been implemented. These are

- a) a modified Lapidus artificial viscosity, and
- b) a pressure-based artificial viscosity.

The modified Lapidus artificial viscosity has been described in [5]. The viscosity only acts in the direction  $l$ , and is of the form

$$k = h^2 \left| \frac{\partial(v \cdot l)}{\partial l} \right|, \quad l = \frac{\nabla|v|}{|\nabla|v||}. \quad (9)$$

Here  $h$  is the element-size, and  $\mathbf{v}$  denotes the velocity-vector.

The pressure-based artificial viscosity is a modification of that proposed by Morgan *et al.* [6]. The viscosity coefficient employed is of the form

$$k^i = \frac{|\sum_{el} (M_L - M_C)^{ij} p_j|}{\sum_{el} |(M_L - M_C)^{ij}| p_j + \epsilon \sum_{el} (M_L + M_C)^{ij} p_j} . \quad (10)$$

Here  $M_L$  and  $M_C$  again denote the lumped and consistent element matrices, while  $p_j$  denotes the pressure at node  $j$ . The terms following  $\epsilon$  are added to distinguish 'noise' from a true physical discontinuity. If  $\epsilon$  vanishes, the artificial viscosity is of first order, while for  $\epsilon > 0$  second order is achieved.

#### Barely-Implicit Correction Scheme

For low subsonic flows, the time-step for explicit schemes is limited by the largest eigenvalue of the system of equations. The idea behind BIC is to treat the 'speed of sound modes' implicitly and keep the treatment of the 'pure advection modes' explicit. The advantage of such a semi-implicit scheme is that the matrix to be inverted has a much simpler structure. A modal decomposition of the Jacobians of the advective fluxes into their 'speed of sound modes' and the 'pure advection modes' yields

$$A^i = \frac{\partial F_a^i}{\partial x_j} = A_u^i + A_p^i . \quad (11)$$

Based on this the advective fluxes can be written as

$$F_a^i = F_{uu}^i + F_{ap}^i . \quad (12)$$

Details of the modal analysis are given in Ref. [7]. The aim is to construct a time stepping scheme that is unconditionally stable for the 'speed of sound modes' contained in  $A_p^i$ , but only conditionally stable for the 'pure advection modes' contained in  $A_u^i$ . In order to achieve this goal, we integrate the  $F_{ap}^i$  terms implicitly, and the remaining  $F_{uu}^i$  terms explicitly:

$$\Delta U + \Theta \Delta t \frac{\partial \Delta F_{ap}^i}{\partial x_j} = \Delta \tilde{U} . \quad (13)$$

Here  $\Delta \tilde{U}$  denotes the increments that are obtained for the explicit, uncorrected scheme and  $\Theta$  is an implicitness parameter. Exploiting the sparse structure of the 'pressure fluxes'  $F_{ap}^i$ , we can reduce the system of coupled equations given in Eq. (13) to a single elliptic equation. This is achieved by combining the momentum and energy equations, and the equation of state. Note that this is different from the projection schemes widely used for the simulation of incompressible flows. These combine the continuity and momentum equations, and not the momentum and energy equations. The end result, after some algebra (see Ref. [7]), is the following elliptic equation for the pressure increment  $\Delta p$ :

$$\Delta p - \Theta^2 \Delta t^2 (\gamma - 1) \frac{\partial}{\partial x_j} \left( \frac{\rho e + p}{\bar{\rho}} \right) \frac{\partial \Delta p}{\partial x_j} = \Delta \tilde{p} + \Delta (\rho e + p) , \quad (14)$$

where

$$\Delta (\rho e + p) = -\Theta \Delta t (\gamma - 1) \frac{\partial}{\partial x_j} [(\rho e + p) \Delta \tilde{u}_j] . \quad (15)$$

The overall solution sequence then proceeds as follows:

First the solution is advanced explicitly yielding  $\Delta \tilde{U}$ . The pressure increment  $\Delta p$  is then obtained from Eq. (14). The velocities  $u_j$  are then corrected to get  $u_j^{n+1}$ . The new values for the energy  $(\rho e)^{n+1}$  are computed using Eq. (15).

The solution of the elliptic equation for pressure involves inversion of a large matrix. However, the bandwidth and condition-number of this matrix are much better than in the case of totally implicit schemes. Furthermore, because of its inherently elliptic character it is very well suited to any type of iterative solver. Numerical tests indicate that for the Mach-number range  $M_\infty = 0.05 - 0.1$ , only two to ten over-relaxed Jacobi passes are required.

#### Substepping of Viscous Fluxes

A Fourier stability analysis for the explicit scheme described above, shows that the scheme is stable provided

$$C \leq \frac{\sqrt{1 + Re_\Delta^2} - 1}{Re_\Delta} , \quad (16)$$

where  $C$  is the Courant number and  $Re_\Delta$  is the minimum cell Reynolds number. Convergence to steady state can be accelerated by local time-stepping. Although this local time-stepping strategy is efficient for inviscid flows, convergence is rather poor for viscous flows. One way to improve convergence is to treat the viscous terms in an implicit manner. Here we employ an alternative approach of sub-stepping the viscous terms. If the allowable time-step due to the viscous terms is much smaller than that for the advective terms, the use of substeps becomes a viable alternative. The implementation of the sub-stepping procedure is as follows:

During the second-step of the solution procedure, the inviscid fluxes are advanced with their allowable timestep  $\Delta t_a$ . The corresponding contribution to the right-hand side of Eq. (8) can be written as

$$R_a = \Delta t_a \cdot (S_a|^{n+\frac{1}{2}} - \frac{\partial F_a^i}{\partial x^i}|^{n+\frac{1}{2}}) . \quad (17)$$

Next, the ratio of allowable timesteps for the inviscid and viscous fluxes is computed as

$$r_{iv} = \frac{\Delta t_a}{\Delta t_v} . \quad (18)$$

Given  $r_{vv}$ , the required number of viscous substeps  $n_v$ , and the sequence of inviscid timesteps  $\Delta t_v^l, l = 1, n_v$  are computed. Next, the contribution of the viscous fluxes to the right-hand side is computed as

$$R_v^l = \sum_{m=1}^l \Delta t_v^m \cdot \left( \frac{\partial F_v^l}{\partial x^i} |^{n+1,m-1} + S_v |^{n+1,m-1} \right) . \quad (19)$$

Here, for  $m = 1$ , the flux contribution is computed at time-level  $n$ . The viscous contribution  $R_v^l$  is then added to the corresponding fraction of the inviscid right-hand side  $R_s$

$$R_{av}^l = R_v^l + \frac{\Delta t_v^l}{\Delta t_s} R_s . \quad (20)$$

Finally, the boundary conditions are applied to  $R_{av}^l$  and the unknowns are updated using

$$\Delta U^{n,l} = U^{n+1,l} - U^n = R_{av}^l . \quad (21)$$

Our numerical experiments indicate that:

- a) It is important to keep the viscosity of the fluid constant during substepping. Otherwise, the linear stability analysis is no longer valid.
- b) The advancement of viscous and inviscid fluxes must be accomplished in a time-accurate manner, as described by Eqs. (20) and (21). Otherwise, the critical balance of viscous and inviscid fluxes is destroyed, leading to numerical instability for large allowable timestep-ratios  $r_{vv}$ .

A simple timestep-sequence for substepping is to consider constant substeps

$$\Delta t_v^l = \frac{1}{n_v} \Delta t_s , l = 1, n_v . \quad (22)$$

### Results

#### Axisymmetric Flow

##### Flow past a Sphere, $Re = 100$

Steady viscous flow past a sphere at a Mach-number of  $M_\infty = 0.1$  and Reynolds-number of  $Re = 100$  provides an important test example to evaluate the accuracy of the present scheme. No artificial viscosity was added for this subsonic case. The problem statement, as well as the results obtained, are shown in Figure 1. The grid employed for this case (Fig. 1a) consists of a structured portion divided into triangles in the boundary layer zone, and an unstructured mesh elsewhere. From Fig. 1d, it can be seen that the recirculation zone extends 1.4 diameters into the wake, measured from the center of the sphere. This compares well with experimental results [8]. Figure 1e shows very good agreement of computed surface vorticity with earlier numerical results [9,10]. The flow separates at an angle of approximately  $123^\circ$ .

#### Flow past a Body of Revolution at Zero Angle of Attack

Having established the correctness of the procedure, the present scheme is then applied to solve flow past a hull-shaped body of revolution. First, the inviscid equations are solved on a coarse grid consisting of 988 points and 1807 elements. The results for  $M_\infty = 0.2$ , are shown in Fig. 2. In order to establish the reliability of the solutions, a grid refinement study is undertaken. The grid is refined using the classic h-refinement technique. The results in terms of pressure contours for the two grids are shown in Fig. 2b and c. Figure 2d shows the comparison of the surface pressure distribution, obtained employing the two grids. One can see that the effect of grid refinement is minimal on the quality of the solution. This indicates that the first mesh was already quite adequate.

Next, the procedure is applied to solve steady viscous flow past this configuration at  $M_\infty = 0.1$  and  $Re = 1000$ . The grid employed for this case consists of 7276 nodes and 14093 elements, and is shown in Fig. 3a. Results in terms of pressure and vorticity contours and velocity vectors are shown in Fig 3b-d. Correct trend in surface pressure distribution is observed. The vorticity contours show a tendency for the flow to separate in the afterbody region. This solution is obtained with local time-stepping but without sub-stepping of the viscous terms. For this case, convergence acceleration via substepping of the viscous terms with constant sub-step sizes did not yield substantial gain. This is due to the fact that the allowable time-step for the advective terms is already quite small at this low Mach number.

#### 2-D Flow Past Circular Cylinder Using BIC-FEM-FCT

For low subsonic flows, the barely-implicit scheme in conjunction with FEM-FCT is employed, so that the time-step limitation due to the speed of sound is eliminated. This procedure is applied for solving unsteady flow past a circular cylinder for  $Re = 100$  at a Mach-number of  $M_\infty = 0.1$ . This particular  $Re$ -number was chosen, because in this regime the experiments show the strongest variation of Strouhal-numbers as a function of Reynolds-number [11]. Figure 4 shows the grid employed, the velocity vectors and the entropy contours in the wake. The numerically obtained Strouhal-number was graphically indistinguishable from the experimental data. This is not surprising, as the grid close to the cylinder is extremely fine, allowing good boundary layer resolution, and the advection scheme is fourth-order accurate in phase-space. Four substeps for the viscous fluxes were employed. The savings occurred by this combination of semi-implicit scheme and the substepping as compared to an explicit solver were in excess of 1:50. The main ingredients for this high savings-factor stem from: a) elimination of the speed of sound limitation (1:10), b) low velocity in the boundary layer (1:5), c) substepping of the viscous fluxes (1:3).

### 3-Dimensional Flow

#### Inviscid Flow Past a Sphere, $M_\infty = 0.2$

Next, the procedure is extended to 3-D and an inviscid flow past a sphere was chosen as the test case, since axisymmetric results from the present study and earlier results are available for this case. Figures 5a and b show the grid employed and the pressure contours over the surface of the sphere. Figure 5c shows the comparison of the surface pressure distribution. From this figure, it is clear that the axisymmetric case compares very well with the potential flow solution; the agreement of the 3-D solution is fairly good except near the two stagnation points. This discrepancy may be due to the small artificial dissipation that was needed to stabilize the 3-D solution procedure.

#### Flow Past a Fully Appended Submarine

The procedure is applied to solve inviscid flow past a submarine with sail and stern appendages, at a Mach number  $M_\infty = 0.2$  and various pitch angles of attack  $\alpha$ , from  $0^\circ$  to  $10^\circ$ . The grid employed for this case consists of 383,956 tetrahedra and 70,222 nodes and is shown in Fig. 6a. Convergence to steady state was achieved in 1000 iterations, and the results in terms of surface pressure contours for  $\alpha = 0^\circ$  and  $10^\circ$  are shown in Fig. 6b and c respectively. Figure 6d shows that the variation of the lifting force due to pressure with angle of attack is linear. The non-zero force at  $\alpha = 0^\circ$  is due to the presence of the sail.

Next, viscous flow past the fully appended submarine configuration at  $\alpha = 10^\circ$  and  $Re = 10^6$  was considered. Results were obtained employing a coarse grid consisting of 410,162 tetrahedra and 71,524 nodes. At the time this calculation was performed, we did not have the capability to grid the boundary layers with semi-structured grids appropriately in 3-D. Thus, this run has to be viewed as an experiment as to what happens if Navier-Stokes boundary conditions are imposed on an Euler mesh. To our surprise, many viscous features were well reproduced on this coarse mesh, e.g. the necklace vortex at the junction of the sail and the hull, shown in Fig. 7a. From the vorticity contours at various cross-planes along the sail shown in figures 7b and c, it is clear that this vortex moves up along the sail. Also, a second vortex appears from the top of the sail and is shown in Fig. 7c. These vortices pass well above the stern planes controlling the motion of the submarine. The vorticity contours near the trailing-edge of the stern plane, Fig. 7d, show the presence of tip vortices.

#### Viscous Flow Past a Sphere Using Semi-Structured Grids

The three-dimensional viscous flow results presented so far show proper qualitative behaviour despite the relatively coarse mesh employed in the computation. In order to resolve the strong gradients present in viscous flows, a structured mesh is employed in the vicinity of the body. A typical grid consisting of 153,179 tetrahedra and 28,302 nodes is shown in Fig. 8a. The velocity vectors in the wake of the sphere show that the recirculation zone extends

upto one diameter into the wake measured from the center of the sphere.

### **Summary**

A finite element scheme has been employed to solve Euler and Navier-Stokes equations. Results were obtained for both axisymmetric and three-dimensional flows and the solution procedure was validated via application to a model problem of flow over a sphere. The validation was carried out for both Euler and Navier-Stokes solutions. Convergence acceleration for low-subsonic viscous flow cases was investigated by sub-stepping of the viscous terms when the time-step was limited predominantly by the minimum cell-Reynold's number and by employing the BIC-FEM-FCT when the time-step was limited by the speed of sound. Preliminary results were obtained for three-dimensional viscous flows past complex geometries. A 3-D semi-structured grid which combines structured grid in the normal direction in the vicinity of the body and unstructured grid in the remainder of the computational domain was developed for use with Navier-Stokes solver. Presently, fine grid results are being obtained for flow over a sphere at  $Re = 100$ . The convergence acceleration methods discussed in this paper will be incorporated in the 3-D solution procedure which will then enable efficient computation of unsteady viscous flows.

### **Acknowledgements**

This work was supported by a contract from DARPA through the Laboratory for Computational Physics and Fluid Dynamics of the Naval Research Laboratory. The authors wish to thank CRAY Research Inc., for letting us use their CRAY X-MP EA 4/64 computer.

### **References**

1. Löhner, R., Morgan, K., Peraire, J. and Zienkiewicz, O.C., "Finite Element Methods for High Speed Flows," AIAA-CP 854, pp. 403-410; AIAA Paper No. 85-1531, 1985.
2. Löhner, R., Morgan, K. and Zienkiewicz, O.C., "An Adaptive Finite Element Procedure for High Speed Flows," *Comp. Meth. Appl. Mech. Eng.*, Vol. 51, pp. 441-465, 1985.
3. Löhner, R. and Parikh, P., "Generation of Three Dimensional Unstructured Grids by the Advancing Front Method," *Int. J. Num. Meth. Fluids*, Vol. 8, pp. 1135-1149, 1988.
4. Löhner, R., Baum, J.D., Loth, E. and Ramamurti, R., "A Finite Element Solver for Axisymmetric Compressible Flows," AIAA Paper No. 89-1794, 1989.
5. Löhner, R., Morgan, K. and Peraire, J., "A Simple Extension to Multidimensional Problems of the Artificial Viscosity due to Lapidus," *Comm. Appl. Num. Meth.*, Vol. 1, pp. 141-147, 1985.
6. Morgan, K., Peraire, J., Theraja, R.R. and Stewart, J.R., "An Adaptive Finite Element Method

for Euler and Navier-Stokes Equations," AIAA CP-874, pp. 749-757; AIAA Paper No. 87-1172, 1987.

7. Löhner, R. and Patnaik, G., "BIC-FEM-FCT: An Algorithm for Low Mach-Number Flows," AIAA-CP 874, pp. 490-494; AIAA Paper No. 87-1126, 1987.

8. Van Dyke, M., "An Album of Fluid Motion," Parabolic Press, 1982.

9. Clift, R., Grace, J.R. and Weber, M.E., "Bubbles, Drops and Particles," Academic Press, 1978.

10. Rimon, Y. and Cheng, S.I., "Numerical Solution of a Uniform Flow over a Sphere at Intermediate Reynolds Numbers," *The Physics of Fluids*, Vol. 12, No. 5, 1969.

11. Schlichting, H., "Boundary-Layer Theory," McGraw-Hill, 1979.

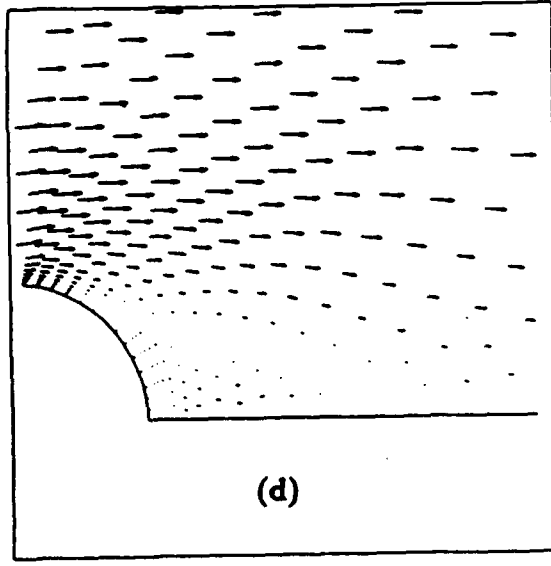
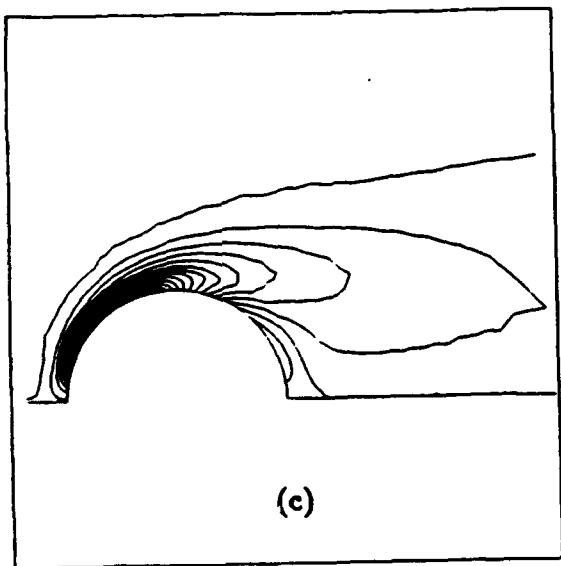
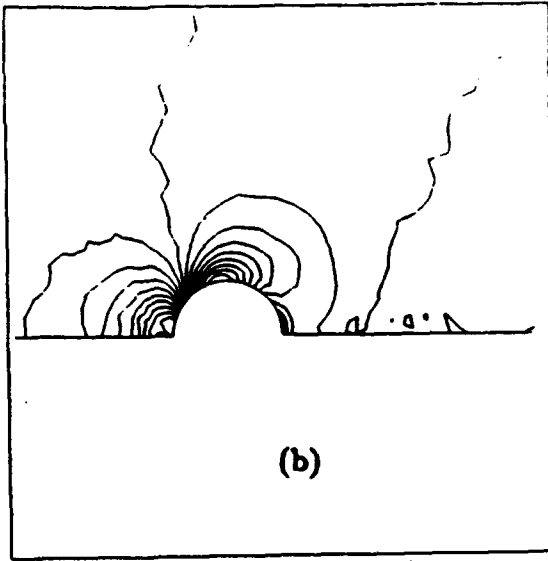
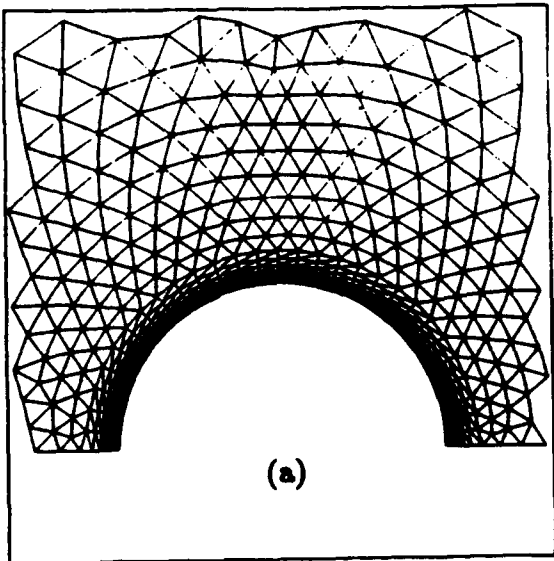
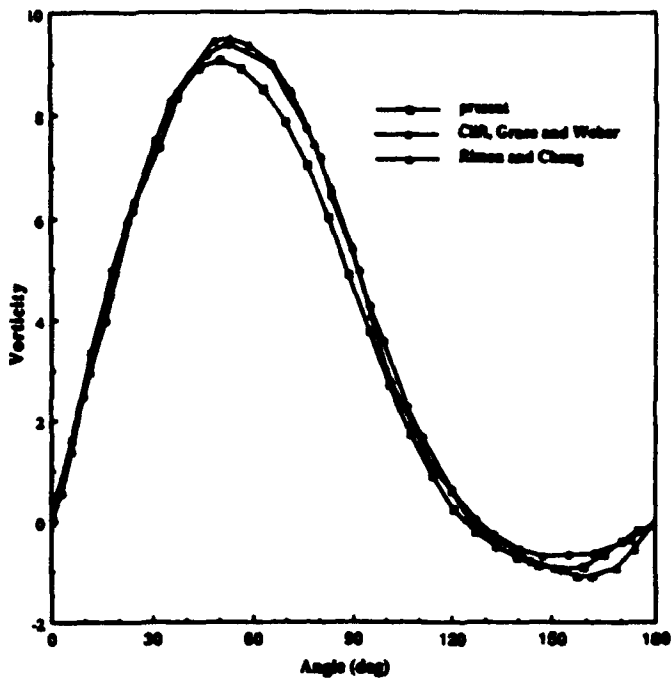
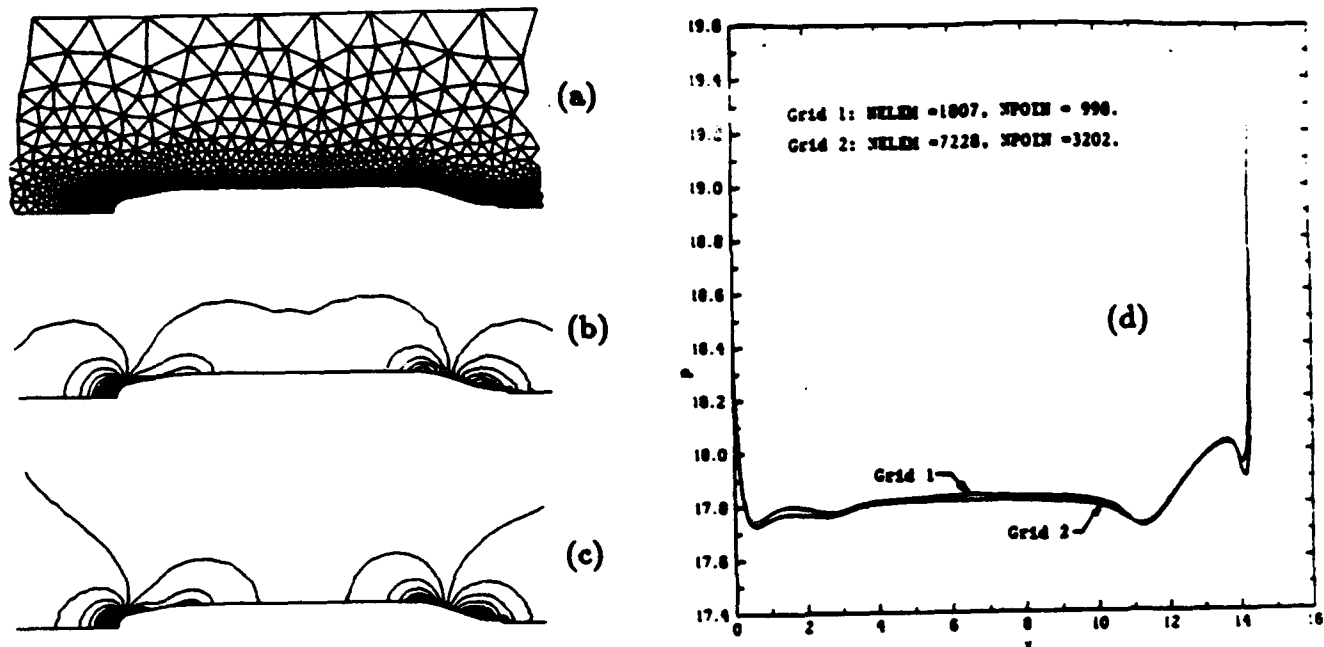


Fig. 1. Results for Flow Past a Sphere,  $Re = 100$ ,

(a) Grid; (b) Pressure Contours; (c) Vorticity Contours;  
 (d) Velocity Vectors.



**Fig. 1e. Comparison of Surface Vorticity Distribution on a Sphere.**



**Fig. 2. Results for Flow Past Axisymmetric Body,  $M_{\infty} = 0.2$ ,**  
**(a) Coarse Grid; (b) Pressure Contours; (c) Pressure Contours**  
**on Fine Grid; (d) Effect of Grid Refinement.**

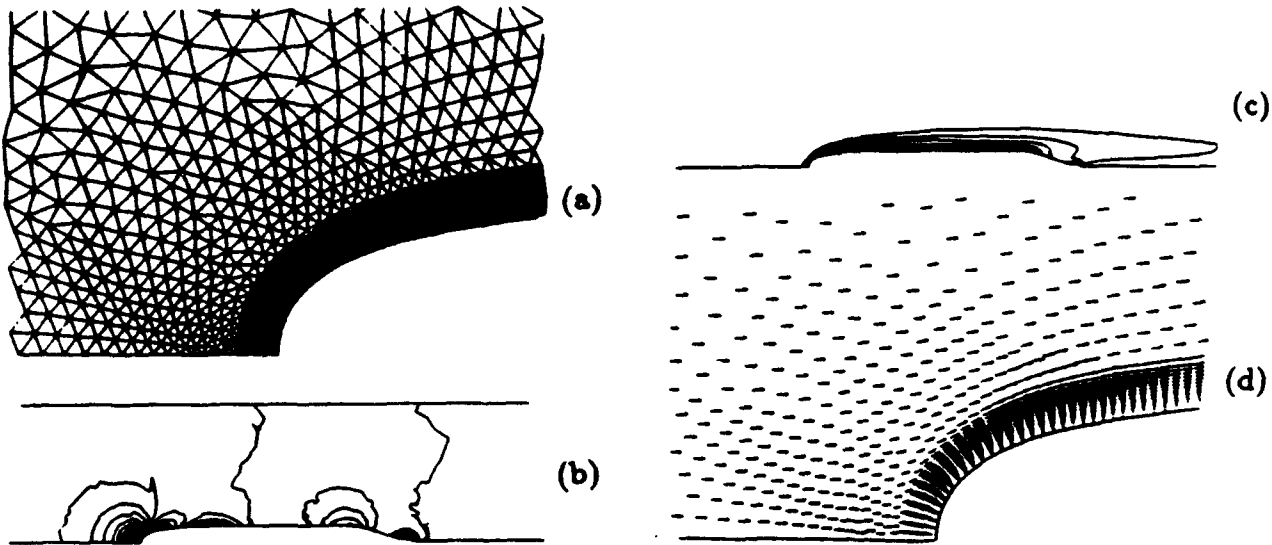


**Fig. 3. Results for Viscous Flow Past Axisymmetric Body,  $Re = 1000$ ,**  
**(a) Grid; (b) Pressure Contours; (c) Vorticity Contours;**  
**(d) Velocity Vectors.**

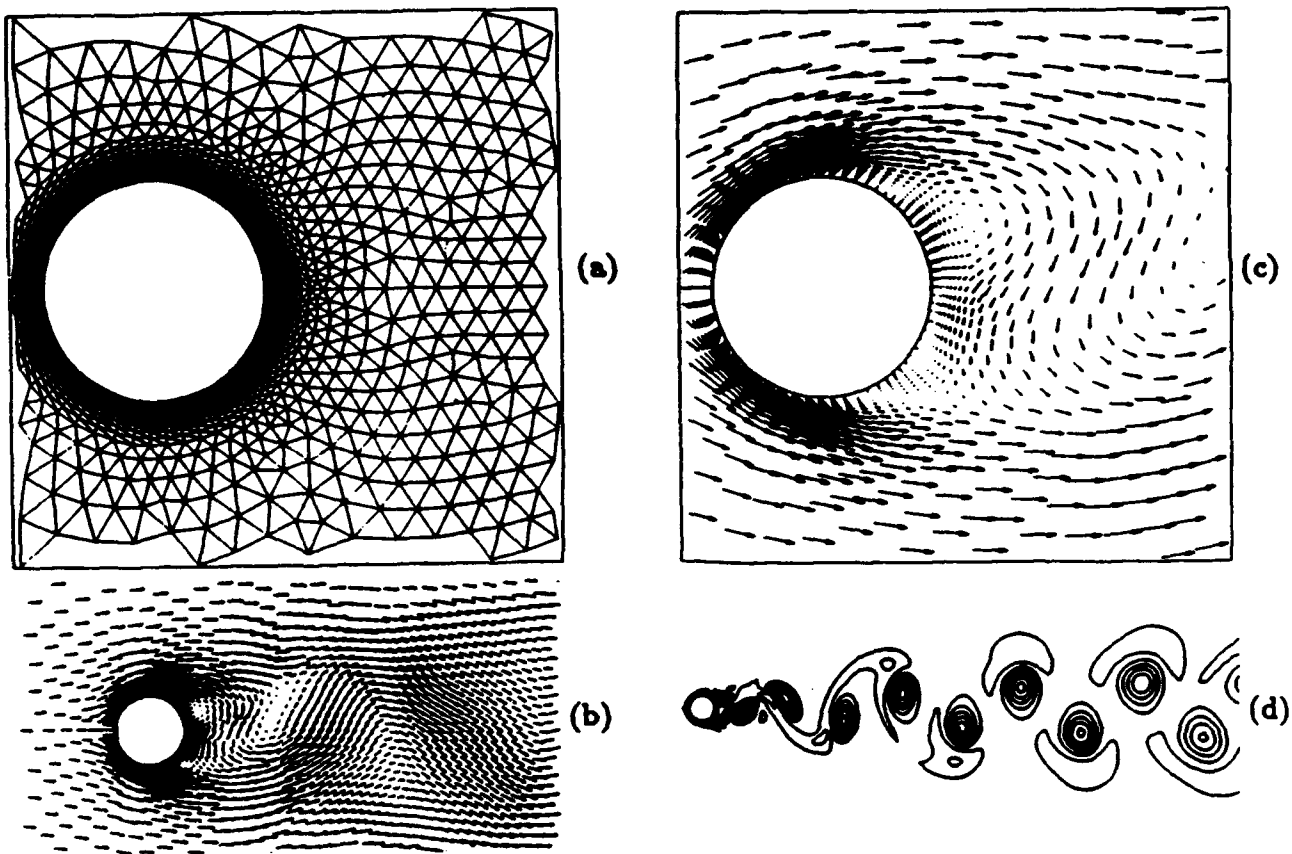
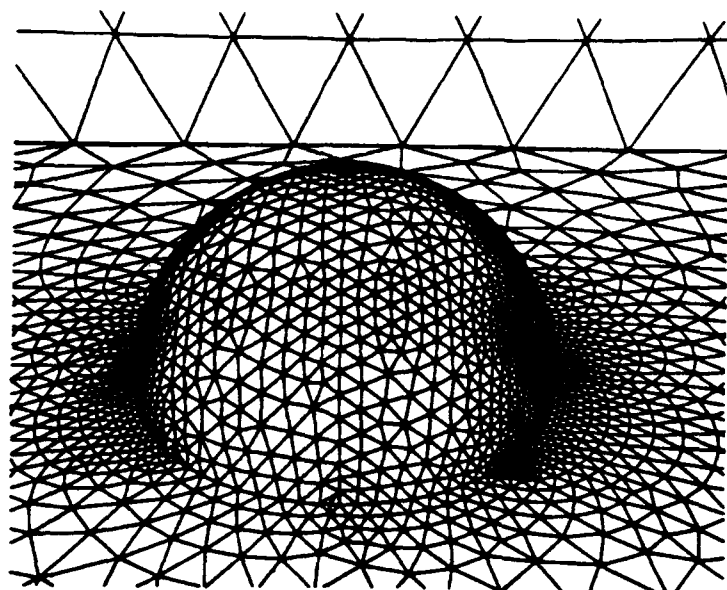
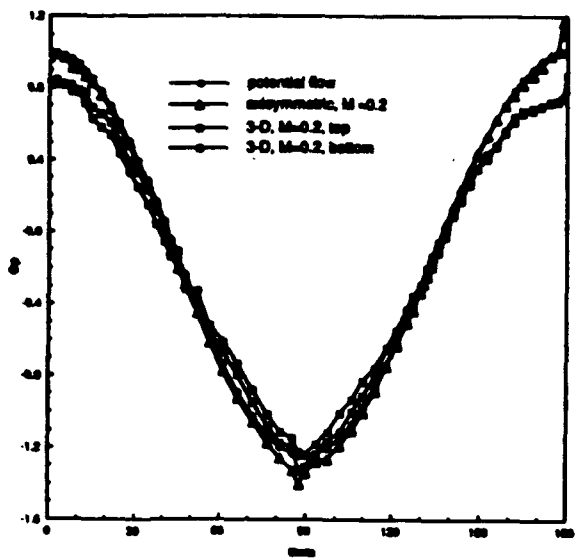


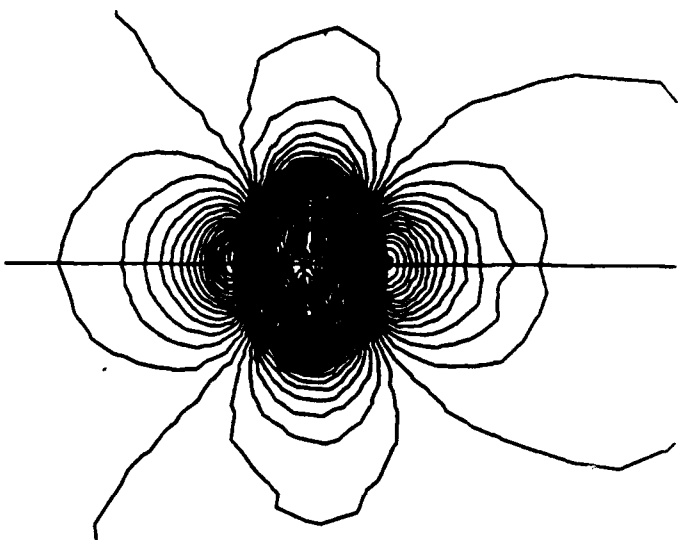
**Fig. 4. Flow Past a Circular Cylinder,  $M_\infty = 0.1$ ,  $Re = 100$**   
**(a) Grid; (b) Velocity Vectors; (c) Enlarged View;**  
**(d) Entropy Contours.**



(a)



(b)



(c)

**Fig. 5. Results for Inviscid Flow Past a Sphere,  $M_\infty = 0.2$ ,**  
**(a) Grid; (b) Comparison of Surface Pressure Distribution;**  
**(c) Pressure Contours.**

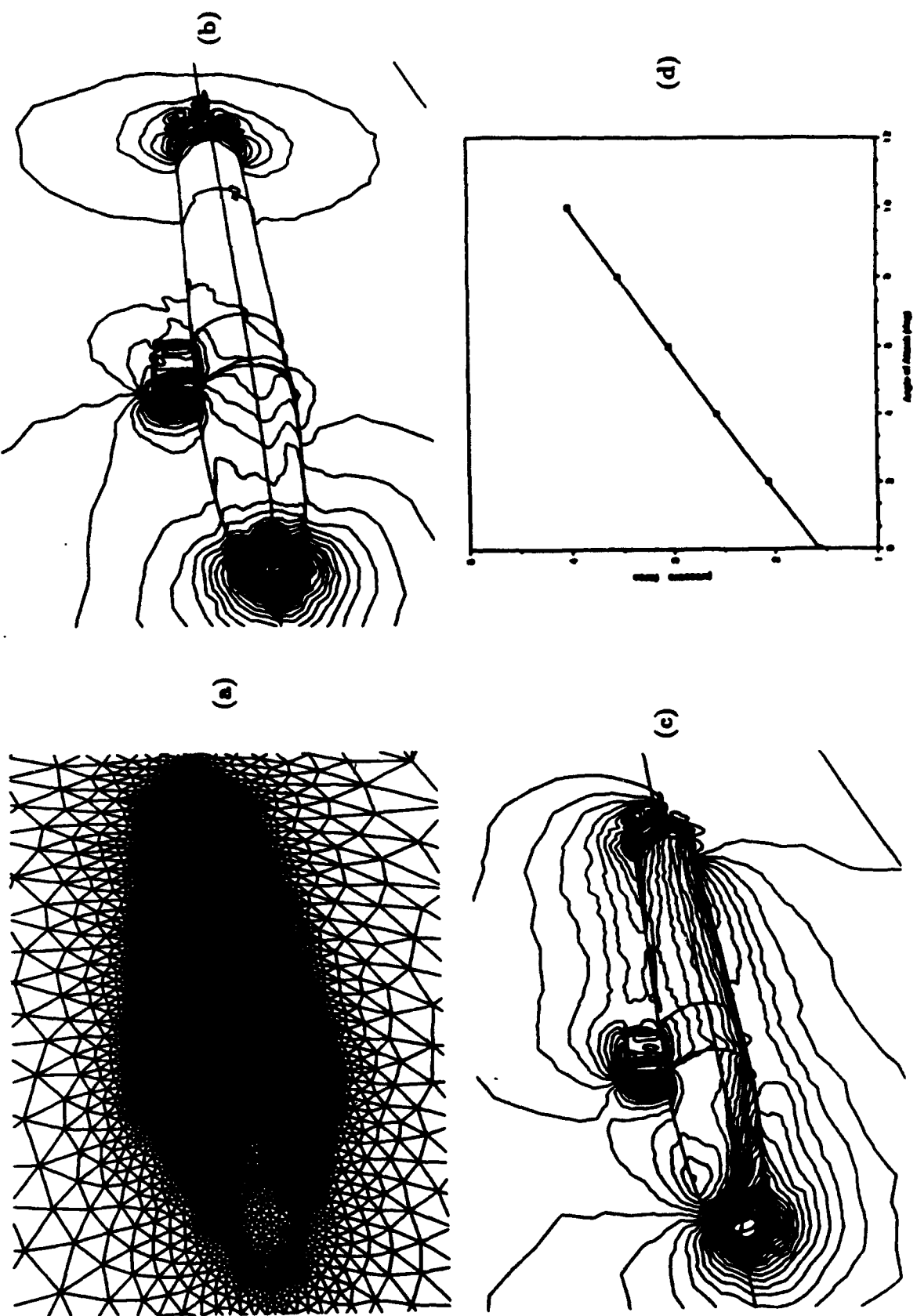


**Fig. 6. Results for Inviscid Flow Past Fully Appended Submarine,**  
 (a) Grid; (b) Pressure contours,  $\alpha = 0^\circ$ ;  
 (c) Pressure Contours,  $\alpha = 10^\circ$ ; (d) Lift vs  $\alpha$

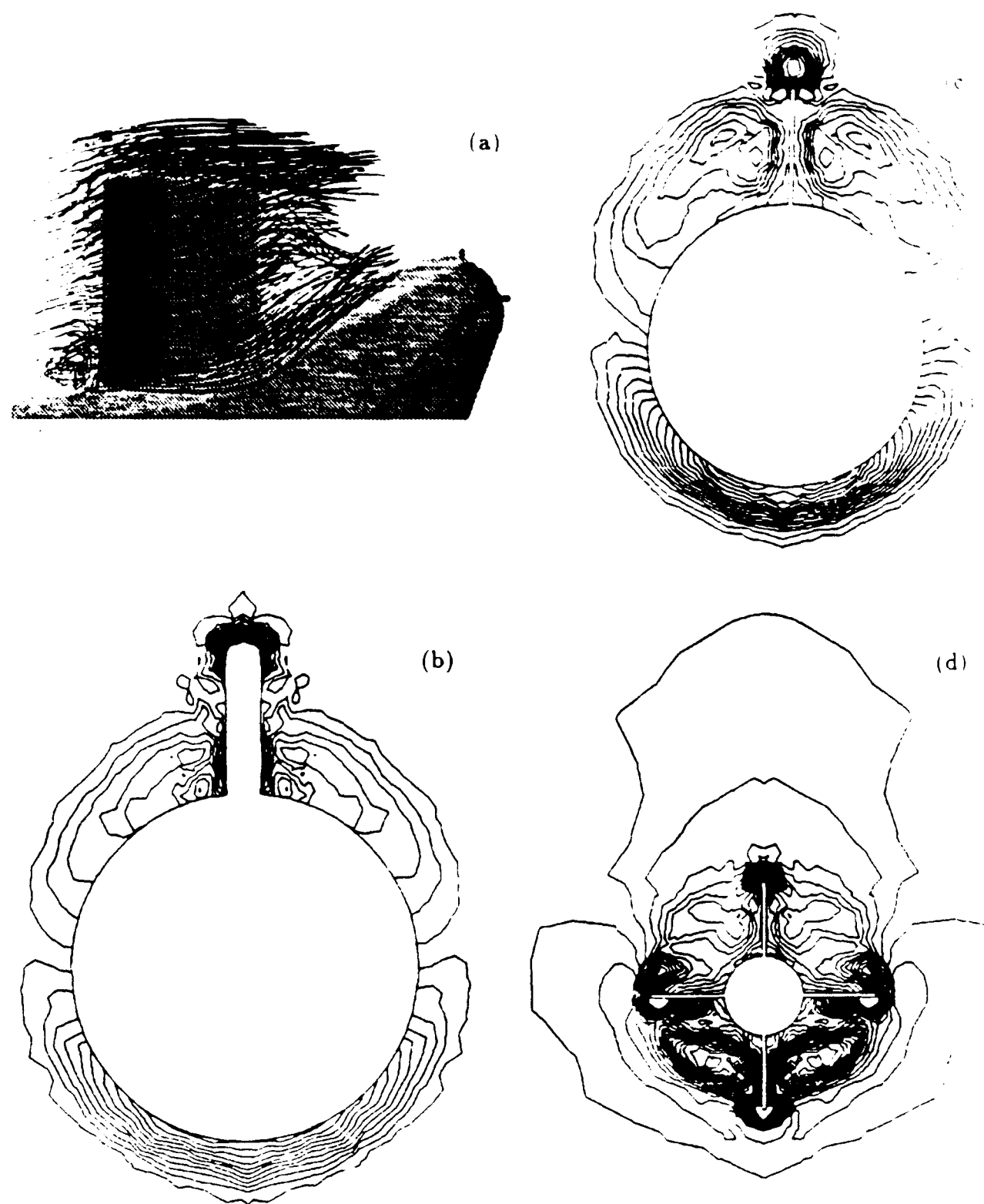


**Fig. 7. Results for Viscous Flow Past Fully Appended Submarine.**

- (a) Particle traces;
- (b) Vorticity Contours Near Leading-Edge of Sail;
- (c) Vorticity Contours Near Trailing-Edge of Sail;
- (d) Vorticity Contours Near Trailing-Edge of Stern Plane

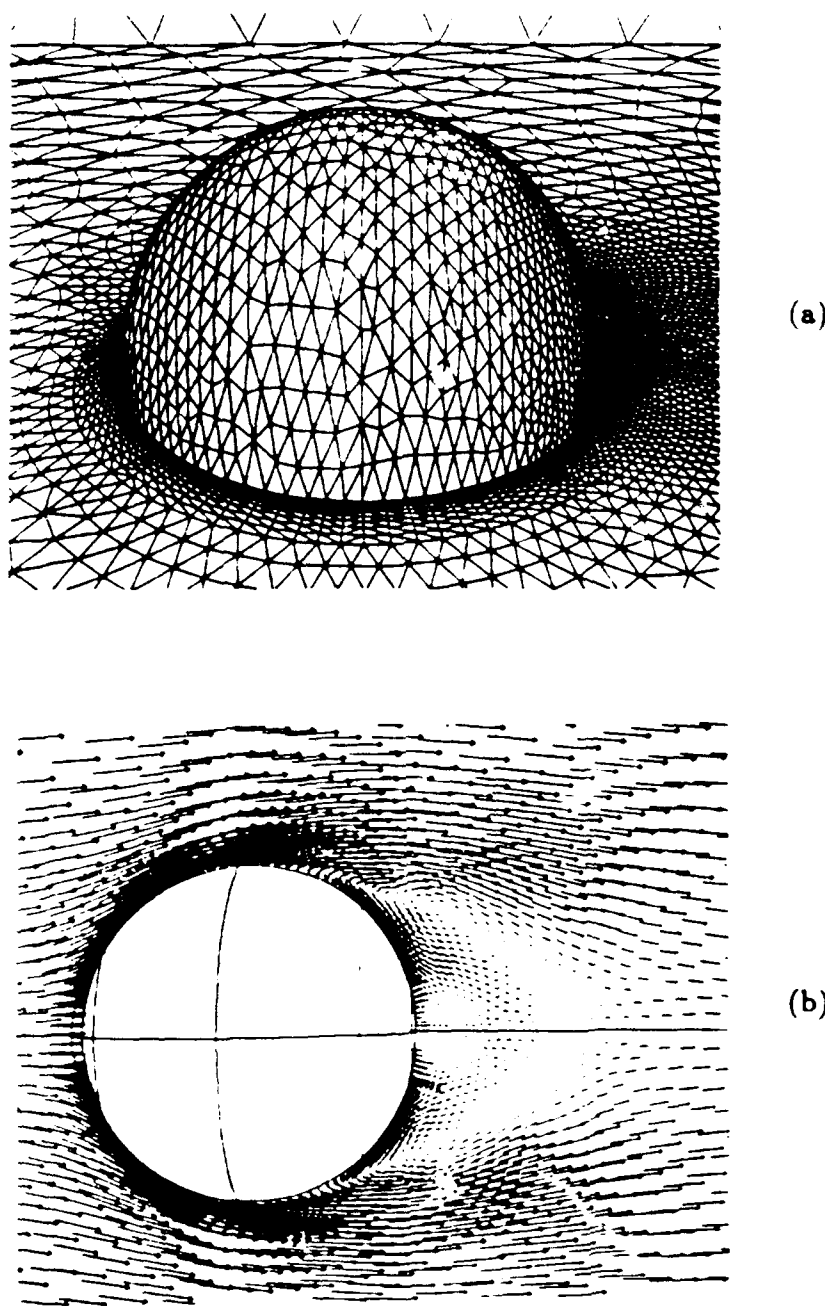


Fig. 8. Results for Flow Past a Sphere,  $Re = 100$ ,  
(a) Typical Semi-Structured Grid;  
(b) Velocity Vectors.

## **Appendix C**

### **Review -Vortex Shedding Lock-On and Flow Control in Bluff Body Wakes**

## Review—Vortex Shedding Lock-on and Flow Control in Bluff Body Wakes

O. M. Griffin

Naval Research Laboratory,  
Washington, DC 20375-5000.  
Fellow ASME

M. S. Hall

Science Applications International  
Corporation,  
McLean, VA 22102

*The results of recent experiments demonstrate that the phenomenon of vortex shedding resonance or lock-on is observed also when a bluff body is placed in an incident mean flow with a periodic component superimposed upon it. This form of vortex shedding and lock-on exhibits a particularly strong resonance between the flow perturbations and the vortices, and provides one of several promising means for modification and control of the basic formation and stability mechanisms in the near-wake of a bluff body. Examples are given of recent direct numerical simulations of the vortex lock-on in the periodic flow. These agree well with the results of experiments. A discussion also is given of vortex lock-on due to body oscillations both normal to and in-line with the incident mean flow, rotational oscillations of the body, and of the effect of sound on lock-on. The lock-on phenomenon is discussed in the overall context of active and passive wake control, on the basis of these and other recent and related results, with particular emphasis placed on active control of the circular cylinder wake.*

### Introduction

Vortex streets are formed in the wakes of bluff, or unstreamlined, bodies over a wide range of Reynolds numbers, from approximately 50 to  $10^6$  and even higher. The physics of vortex street formation and the near-wake flow have been the focal point for many past experimental studies, e.g., Roshko (1954, 1955), Gerrard (1966), Bearman (1965, 1967), Griffin and Ramberg (1974) and, most recently, Unal and Rockwell (1988a, b), Ongoren and Rockwell (1988a, b), and Williamson and Roshko (1988). One reason for this interest has been the importance of knowing how the mean and fluctuating fluid forces are generated on the body due to vortex shedding. Another reason is the perceived connection of the near-wake flow to the eventual evolution of the overall middle and far-wake vortex patterns (Cimbala et al., 1988; Browne et al., 1989). One of the most cogent descriptions of the physics of vortex streets and bluff body wakes was given by Morkovin (1964) as "a kaleidoscope of challenging fluid phenomena." This description is in many ways still true today. Modern high-speed computers and direct and large-eddy numerical simulation techniques now allow and, in the future, will further allow the vortex formation and wake modification and control processes to be studied computationally at high resolution (Karniadakis and Triantafyllou, 1989, 1990; Grinstein et al., 1990, 1991).

If a bluff cylinder is flexible and lightly damped, or rigid and flexibly mounted, then resonant oscillations can be excited by the incident flow. As a consequence of this flow-induced resonance, the body and wake oscillations have the same frequency

which is near one of the characteristic frequencies of the structures (Bishop and Hassan, 1964; Koopmann, 1967). Extensive recent reviews of vortex shedding from bluff bodies and vortex-induced oscillations have been given by Sarpkaya (1979) and Bearman (1984). This coincidence or resonance of the vortex and vibration frequencies is commonly termed lock-on. The term phase-locking also has been used in the literature (Rockwell, 1990). Lock-on or resonance occurs when the body is oscillated in-line with the incident flow (Griffin and Ramberg, 1976; Ongoren and Rockwell, 1988b), and the lock-on resonance also is induced when a cylinder is forced to oscillate normal to the flow over the appropriate range of imposed frequencies and amplitudes. Two recent studies (Tokomaru and Dimotakis, 1991; Filler et al., 1991) have shown that rotational oscillations of a circular cylinder can cause lock-on. The recent computations of Karniadakis and Triantafyllou show that a lock-on state can be reached when a small spatially and temporally varying periodic disturbance is introduced into the near-wake of the cylinder. The disturbance is analogous to a vibrating wire with the appropriate frequency and amplitude.

Vortex resonance, or lock-on, has been observed also when the incident mean flow has a sufficiently large periodic component superimposed upon it (Barbi et al., 1986; Armstrong et al., 1986, 1987). In this case the cylinder remains stationary, but the vortex lock-on resulting from the inflow perturbation modifies the character of the near-wake flow. There is a complete equivalence between this case and in-line oscillations of the cylinder when the acoustic wavelength is long compared to the cylinder's diameter. The introduction of an appropriate sound field also can cause lock-on to occur (Blevins, 1985). All of these external disturbances represent potential means

Contributed by the Fluids Engineering Division for publication in the JOURNAL OF FLUIDS ENGINEERING. Manuscript received by the Fluids Engineering Division March 19, 1991.

for active control of the bluff body near-wake flow (Rockwell, 1987, 1990). Active control of the vortex shedding in the wake of a stationary circular cylinder by means of acoustic feedback was demonstrated in the recent experiments of Ffowcs Williams and Zhao (1989). Passive control of the shedding process can be accomplished by geometric alterations such as a wake splitter plate (Bearman, 1965; Roshko, 1954, 1955; Mansingh, 1986). Recent discussions of the stability and control of separated flows in general are given by Oertel (1990) and Rockwell (1990).

Vortex lock-on and resonance phenomena have numerous practical engineering applications. These applications abound in offshore exploration and drilling, Naval and marine hydrodynamics, and underwater acoustics. Other areas of engineering practice impacted by these phenomena are civil and wind engineering, nuclear and conventional power generation, and electric power transmission. Modification and control of the flow can be employed to reduce the intensity of the wake in order to reduce the drag, for example. These same processes also can be used to intensify the wake flow in order to enhance heat transfer, mixing and combustion.

The emphasis of this review paper is on vortex shedding resonance and lock-on in the near-wakes of bluff bodies. Vortex shedding in a flow with a periodic component superimposed on the basic mean flow is introduced here as the first case for study. This is an interesting bluff body flow which has not been studied previously in detail. The more widely studied cases of vortex shedding resonance and lock-on due to body oscillations both normal to, in-line with the incident mean flow, and rotational are also discussed in some detail. The introduction of sound also is discussed for the relatively few contributions which are available. The discussion here is directed principally toward the circular cylinder, but limited discussion of other body configurations is introduced at places where it seems appropriate to do so.

### Near-Wake Flow Scaling

Roshko (1954, 1955) and Bearman (1967) originally showed that a characteristic group of nondimensional parameters for scaling of the wakes of bluff bodies could be derived by applying relatively simple physical arguments. The most recent formulation (Griffin, 1978, 1981, 1989) is a universal wake Strouhal number  $St^*$  for vortex shedding based upon measured parameters of the bluff body near-wake flow.

If one considers two shear layers a distance  $d'$  apart, with the velocity just outside the layers equal to  $U_b$ , the mean velocity at separation, then a wake Strouhal number can be defined as

$$St^* = \frac{f_{so}d'}{U_b} = St \left( \frac{U}{U_b} \right) \left( \frac{d'}{d} \right). \quad (1)$$

The characteristic frequency  $f_{so}$  associated with the flow is assumed to be proportional to the ratio  $U_b/d'$ . Here the classical Strouhal number of the vortex wake is

$$St = \frac{f_{so}d}{U}, \quad (2)$$

where  $d$  is the cylinder diameter and  $U$  is the incident flow velocity. When Bernoulli's equation is applied to the flow just outside the boundary layer at separation, the base pressure coefficient is

$$C_{pb} = \frac{2(p_b - p_\infty)}{\rho U^2} = 1 - \left( \frac{U_b}{U} \right)^2. \quad (3)$$

If the base pressure parameter or velocity ratio  $K = U_b/U$  is introduced, then

$$K^2 = 1 - C_{pb} \quad (4)$$

and

$$St^* = \frac{St}{K} \left( \frac{d'}{d} \right). \quad (4a)$$

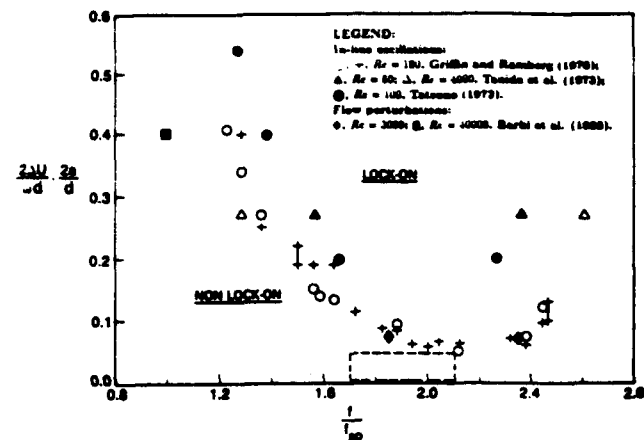


Fig. 1 Limits of the lock-on regime as a function of amplitude and frequency for in-line oscillations and flow perturbations. For the region enclosed by the dashed lines, see Fig. 2.

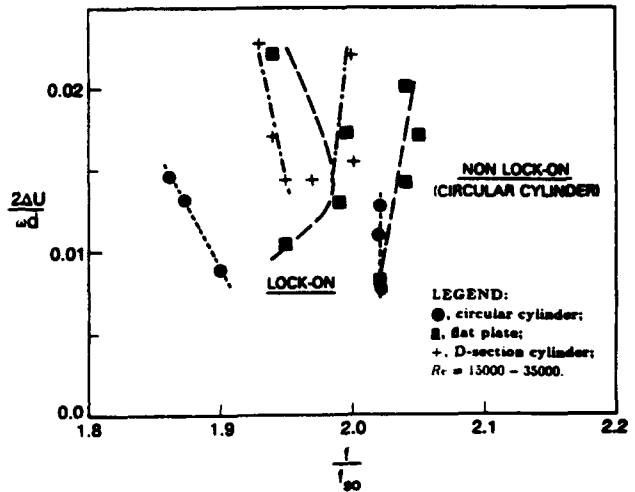


Fig. 2 Limits of the lock-on regime as a function of amplitude and frequency for in-line flow perturbations; data from Armstrong et al. (1986)

A wake Reynolds number  $Re^*$  is defined in a corresponding way as

$$Re^* = \frac{U_b d'}{\nu} = Re K \left( \frac{d'}{d} \right), \quad (5)$$

where  $Re = Ud/\nu$  is the usual free-stream Reynolds number. These scaling relations are employed later in the paper to correlate the near-wake flow properties with one another.

### Flow Perturbations and In-Line Oscillations

The recent experiments of Armstrong et al. (1986, 1987) and of Barbi et al. (1986) were conducted to examine the problem of vortex lock-on for a cylinder in a stream consisting of a steady flow with a periodic component superimposed upon it. In earlier experiments, Hatfield and Morkovin (1973) attempted to study the same problem, but the results were inconclusive because the flow perturbation amplitude and frequency were too low to cause lock-on. The results obtained by Barbi et al. and Armstrong et al. show some very basic similarities with the earlier experiments of Griffin and Ramberg (1976), which were conducted to examine vortex shedding lock-on for a cylinder oscillating in-line in a steady incident flow.

The vortex lock-on regime measurements by Barbi et al. are compared with those of Griffin and Ramberg in Fig. 1. The vertical axis represents two different measures of the perturbation amplitude. For the experiments of Griffin and Ram-

berg, the amplitude parameter is defined by the ratio of the peak-to-peak amplitude of cylinder displacement  $2a$  and the cylinder diameter  $d$ . And for the experiments of Barbi et al., the normalized "peak-to-peak" incident velocity perturbation is given by  $2\Delta U/\omega d$ . The horizontal axis is the ratio of the vibration frequency  $f$  and the Strouhal frequency  $f_{so}$  of a stationary cylinder. Also shown are the cylinder vibration results of Tanida et al. (1973) and of Tatsuno (1972), reproduced from the paper by Griffin and Ramberg. The dashed lines enclose the region occupied by the results of Armstrong et al. (1986, 1987) which are shown on an expanded scale in Fig. 2. Vortex lock-on and cross-flow oscillations usually occur near the Strouhal shedding frequency  $f_{so}$ . For in-line oscillations and flow perturbations, the lock-on is caused by frequencies which occur near twice the Strouhal frequency,  $f = 2f_{so}$ , since the fluctuating drag force is in the flow direction. However, in many cases the actual lock-on frequency is near the Strouhal frequency, or half the oscillation or perturbation frequency.

There is generally good agreement between the bounds of the lock-on regime for the two different types of external disturbance or flow control, though there is some scatter at the highest amplitudes. This is most likely due to Reynolds number effects, as noted by Barbi et al. The latter experiments were conducted at  $Re$  between 3,000 and 40,000, whereas the results of Tanida et al., Tatsuno, and of Griffin and Ramberg were conducted at  $Re$  between 80 and 4,000. The overall differences are relatively small in any case.

In Fig. 2 the vertical and horizontal axes have been scaled in the same way as in the previous figure. The original results of Armstrong et al. had been plotted in terms of the rms velocity  $u'$  and the reduced velocity  $U/f_{so}d$ . Three body shapes were investigated, i.e., a circular cylinder, a D-section cylinder, and a vertical flat plate. It is clear that the circular cylinder, with free separation points, has a lock-on range of about twice the breadth of the two bodies with fixed separation points. This basic difference in the lock-on behavior for these types of bluff bodies was previously discussed by Bearman and Davies (1975) and by Bearman (1984) for the case of body oscillations only. As shown by the former, the afterbody shape plays an important role in the character of the lock-on or resonance, e.g., in terms of the response of the base pressure and near wake flow to the forcing.

The base pressure coefficient  $C_{pb}$  is influenced by the flow perturbations in much the same manner as in the case of cylinder oscillations. For the stationary cylinder the base pressure coefficient is near  $C_{pb} = -1.44$ ; this value, though somewhat low for a circular cylinder, is in reasonable agreement with the results of West and Apelt (1982) for a comparable wind tunnel blockage ratio of nine percent. When the flow perturbation was largest, the base pressure was decreased to  $C_{pb} = -1.85$  at the point of maximum resonance, a reduced velocity of  $U/f_{so}d = 2.5$  (half the Strouhal value). The measured vortex formation region length  $l_f$  was reduced by this level of perturbation to  $0.9d$  from  $1.2d$ , the value measured for the unperturbed flow (Armstrong et al. 1987).

Lesser decreases in  $C_{pb}$  were measured for smaller levels of the flow perturbation, with an overall dependence upon reduced velocity  $U/f_{so}d$ . The mean drag coefficient  $C_D$  increased from 1.28 to 1.52 for the perturbed flow as compared to the unperturbed flow. The base pressures of the flat plate and D-section bodies also were decreased by the introduction of the incident flow perturbations. But the decrease was only half of that measured for the circular cylinder at the same perturbation amplitude, which further shows the effect of free versus fixed separation points on the vortex resonance. These experiments were conducted at Reynolds numbers between 15,000 and 35,000, and the base pressure coefficients of all three stationary bodies in the unperturbed flow were effectively constant over this range.

A recent experimental study of vortex resonance and lock-



Fig. 3 Time sequence of locked-on vortex shedding produced by cylinder oscillations in-line with the flow at an oscillation frequency of  $f = 2f_{so}$ ; from Ongoren and Rockwell (1988b)

on due to in-line oscillations of a circular cylinder was conducted by Ongoren and Rockwell (1988b). These experiments also included oscillations of the cylinder at inclination angles to the flow between  $\alpha = 0$  degrees (in-line) and  $\alpha = 90$  degrees (cross-flow), but the emphasis of the discussion here is on the in-line oscillations. The cross-flow oscillations (Ongoren and Rockwell, 1988a) are discussed in the next section. A wide range of vortex patterns was visualized by introducing pulsed hydrogen bubbles into the incident flow about a circular cylinder mounted vertically in a free-surface water channel.

Both symmetric and asymmetric vortex patterns were observed over a wide range of oscillation conditions. For the in-line oscillations, vortex lock-on was observed at  $f = 2, 3$ , and  $4 f_{so}$ , with an asymmetric street formed at twice the basic Strouhal frequency and a symmetric street formed at three times the Strouhal frequency. The asymmetric pattern was complex in that one row consisted of a line of single vortices, whereas the other row consisted of a line of oppositely rotating vortex pairs. The vortex lock-on at three times the Strouhal frequency resulted in the formation of a symmetric street of vortices. In these cases the basic patterns persist downstream over a large number of oscillation cycles. When the oscillation frequency is four times the Strouhal frequency, a symmetric pattern is formed but rapidly loses its coherence in the early wake.

A time sequence over a full in-line oscillation cycle is shown in Fig. 3 for the condition  $f = 2 f_{so}$ . Figure 3(a) was taken with the cylinder in its forwardmost position and shows a vortex shedding from one side of the cylinder as in Figs. 3(c) and (d). As the cylinder moves through its maximum downstream position and changes direction, a second vortex is formed and shed from the same side of the cylinder as in Figs. 3(e) and (f). Then a single vortex is formed from the other side of the cylinder as the motion cycle continues as shown in Fig. 3(g). Ongoren and Rockwell observed that the pattern persisted over 50 or more cycles of the oscillation, but often, if the flow was stopped and restarted, a mirror image of the pattern was formed. This is but one example of the complexity of the flow patterns which accompany the oscillations. In this case the

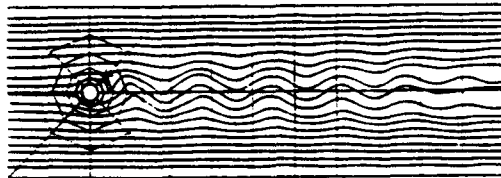


Fig. 4 Instantaneous streamlines, at  $Re = 200$ , of the forced wake response at  $t = 2.2f_{so}$  for vortex shedding from a cylinder in a perturbed flow. The wavelength  $\lambda$  of the vortex street is 4.66 cylinder diameters. The spectral element computational grid is superimposed on the streamline pattern.

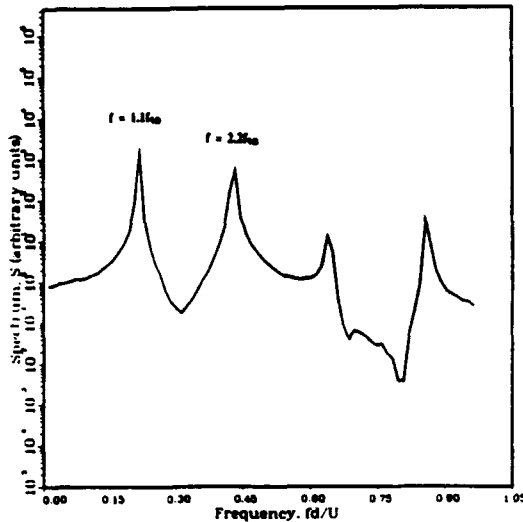


Fig. 5 A typical power spectrum of the flow velocity, at  $Re = 200$ , for the location ( $x = 2d$ ,  $y = 2d$ ) and the forcing conditions given in Fig. 4. Only the locked-on shedding frequency,  $f = 1.1f_{so}$ , the perturbation frequency,  $f = 2.2f_{so}$ , and their harmonics are dominant in the spectrum.

oscillation and vortex frequencies are phase-locked, but under other nonresonant conditions there was competition between the symmetric and asymmetric modes. Under these conditions, the lock-on persists in one mode over a specified number of cycles and then switches to the other mode. The mode competition also is influenced by the upstream feedback of disturbances from the near-wake of the cylinder. Complex patterns of three vortices such as these also were photographed by Griffin and Ramberg (1976) at similar frequencies during their wind tunnel experiments.

Numerical simulation provides yet another method of examining the effects of inflow perturbations and cylinder oscillations on the wake. This consists of superimposing an oscillatory component on the inflow boundary condition for a domain such as that shown by the spectral element grid in Fig. 4. The example given here was computed at NRL using a computer code similar to one employed extensively by Karniadakis and Triantafyllou (1989, 1990). The grid consists of 56 spectral elements, each of order  $N = 6$ . Results of the computation are shown in Figs. 4, 5, and 6, in which the lowest dominant frequency of the resulting vortex wake is near half the perturbation frequency when a boundary condition of the form

$$u = 1.0 + (0.8)\sin(4.4\pi f_{so} t)$$

$$v = 0.$$

is enforced at the inflow. This also represents an in-line oscillation, and is thus expected to result in a shedding frequency near  $f = 1.1f_{so}$  if lock-on occurs at one-half the perturbation frequency. The amplitude of the oscillatory component can be expressed as

$$a = 0.8 = 7.03\pi f_{so}.$$

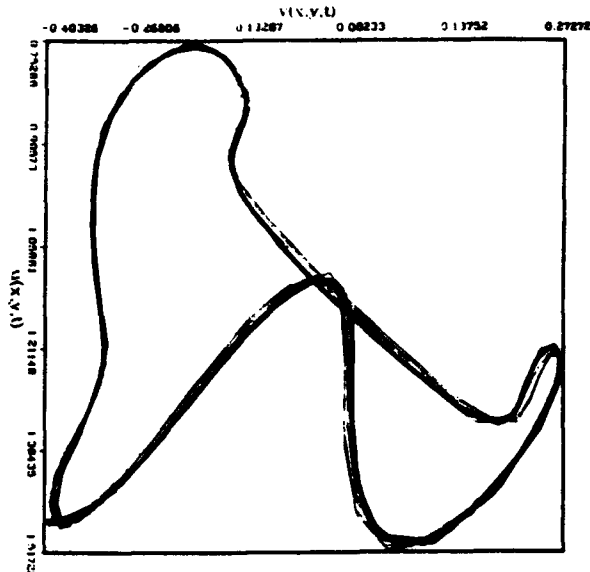


Fig. 6 Phase plane plot of the fluctuating velocity components, at  $Re = 200$ , for the location and forcing conditions given in Figs. 4 and 5. The regularity of the plot is demonstrative of the locked-on state of the vortex shedding.

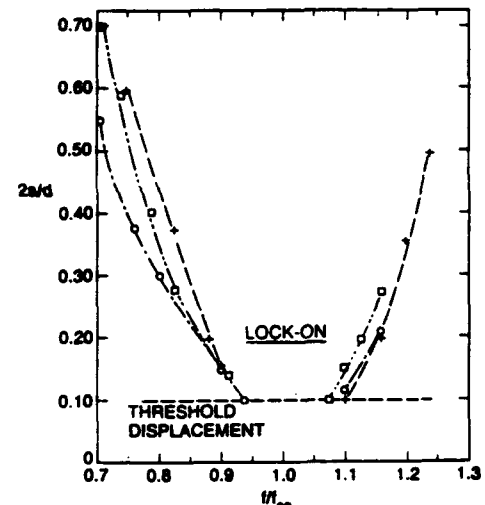


Fig. 7 Limits of the lock-on regime as a function of amplitude and frequency for cross-flow oscillations; from Koopmann (1987)

so that lock-on does occur and the results are in keeping with those shown in Fig. 1.

After an initial period of time corresponding to the quasi-steady stage in the forced perturbed flow calculation, the resulting streamwise velocity history at a point in the near wake is periodic. The corresponding power spectrum in Fig. 5 contains primary peaks at  $f = 1.1$  and  $2.2 f_{so}$  as expected, and secondary peaks at superharmonics of these values. No additional peaks appear in the spectrum. The phase plane plot corresponding to this case is shown in Fig. 6, and with the power spectrum gives evidence of lock-on in the fully developed flow. Streamlines corresponding to this case are also shown in Fig. 4. The vortex spacing here is approximately  $\lambda = 4.66d$ , representing a decrease of seven percent over the unforced value of  $\lambda = 5d$ . The normalized frequency  $\lambda/d(f/f_{so}) = 5.13$  for this case. These values compare well with the results of experiments which are discussed later in the paper. A more extensive discussion of the spectral element computations of the perturbed flow cylinder lock-on is given by Hall and Griffin (1991).



Fig. 8(a)



Fig. 8(b)



Fig. 8(c)

Fig. 8 Flow visualization of the vortex shedding from a circular cylinder oscillating in cross-flow at a Reynolds number of  $Re = 100$ . (a) stationary cylinder, unforced wake; (b)  $2y/d = 0.5$ ,  $\#f_{so} = 0.9$ ; (c)  $2y/d = 1.1$ ,  $\#f_{so} = 0.9$ .

### Cross-Flow Oscillations

The excellent reviews by Sarpkaya (1979) and by Bearman (1984) dealt with cross-flow oscillations of flexibly-mounted bluff bodies, bodies which were free to oscillate, and those which were forced. The purpose of the present paper is to complement these works, to compare with some pertinent past results, and to highlight more recent developments in the context of flow control and modification. The basic character of cross-flow lock-on due to forced oscillations can be represented by the measurements of Koopmann (1967) which are shown in Fig. 7. The appearance of the lock-on range is very similar overall to the corresponding cases of in-line oscillations and

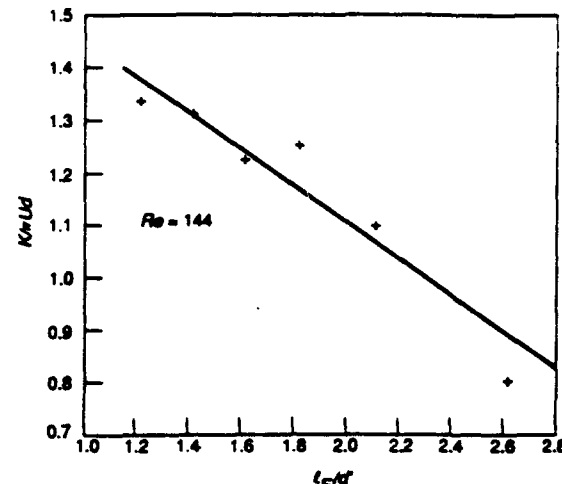


Fig. 9 The measured dependence between the initial circulation  $K$  of the vortices and the ratio of the formation region length  $l$ , and the wake width  $d'$  at formation. The Reynolds number is  $Re = 144$ ; from Griffin and Ramberg (1974).

flow perturbations shown in Figs. 1 and 2. However, the imposed oscillations are near the Strouhal frequency  $f_{so}$  rather than twice its value.

Many other effects of the cross-flow oscillations are also similar. For example, the longitudinal spacing of the vortex street adjusts in a similar manner to the example shown earlier; oscillation frequencies less than  $f_{so}$  expand the vortex street while frequencies greater than  $f_{so}$  contract the pattern. Increasing the amplitude of oscillation reduces the lateral spacing of vortices to the point of zero spacing, after which there is a drastic change in the appearance of the pattern as the flow adjusts to preclude the transition to a thrust-type vortex street. Three previously unpublished examples from experiments at NRL which demonstrate this effect are shown in Fig. 8. The street behind a stationary cylinder appears in Fig. 8(a) and shows the well-known geometry which has been visualized by numerous investigators. When the amplitude of oscillation is increased as shown in Fig. 8(b), the lateral spacing is much reduced. For still higher amplitudes of oscillation, beyond the limit of zero lateral spacing, a complex asymmetric pattern such as that shown in Fig. 8(c) emerges. These photographs were taken in a wind tunnel using an aerosol as the indicator. This emergence of the asymmetric pattern also has been observed by Ongoren and Rockwell (1988a) in water, using hydrogen bubbles as the flow indicator.

The formation region of the vortices as defined by the model of Gerrard (1966) also varies inversely with frequency in the resonance or lock-on regime (Griffin and Ramberg, 1974; Ongoren and Rockwell, 1988a), and is reduced in length by increasing amplitude of oscillation at any given constant frequency. These changes in the near wake vortex formation cause corresponding changes in the strength or circulation of the vortices. Reductions in the vortex formation length result in increasing the vortex strength by as much as 75 percent at a Reynolds number of 144. An example is shown in Fig. 9 where the nondimensional initial circulation of the vortices is plotted against the ratio of the formation length to the wake width at formation. The basic importance of the length scales to the near wake flow physics is discussed later in the paper. This increase in the vortex strength is accompanied by a corresponding increase in the rate of vorticity generation with amplitude of oscillation.

The base pressure coefficient  $C_{p0}$  also is reduced significantly by the oscillations in the lock-on or resonance regime (Stansby, 1976). As an example, the minimum base pressure on a circular cylinder at resonance was decreased by 33 percent as the am-

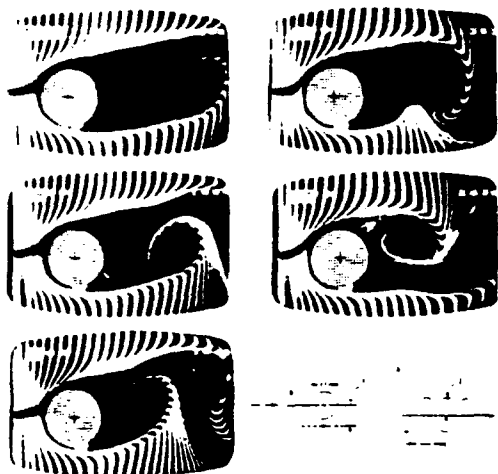


Fig. 10 Effect of the ratio of oscillation frequency  $f$  to the natural shedding or Strouhal frequency  $f_{st}$  on the vortex formation region of a circular cylinder; from Ongoren and Rockwell (1988a). All of the photographs were taken with the cylinder at its maximum negative position.

plitude of oscillation (measured in diameters from equilibrium) increased from  $0.1d$  to  $0.3d$ . The Reynolds number of the experiment was  $Re = 8600$ . As mentioned earlier herein, Armstrong et al. (1987) measured comparable decreases in the base pressure. However, the level of inflow perturbations was much less than the oscillation levels required to achieve the same level of base pressure modification. As noted earlier, the latter reduction in base pressure was accompanied by a reduction in the length of the vortex formation region from  $1.2d$  to  $0.9d$ .

The most comprehensive recent study of cross-flow oscillations is that of Ongoren and Rockwell (1988a). The Reynolds number range of the experiments was  $Re = 580$  to  $1300$ . They found that two fundamental types of lock-on take place; at a frequency of one-half of the Strouhal frequency, a subharmonic form of lock-on takes place whereby the shed vortex is always from one side of the body, whereas at frequencies near the Strouhal frequency the classical form of lock-on described above takes place as vortices are shed alternately from the body to form an altered Karman vortex street pattern.

It has been known for some time (Bearman and Currie, 1979; Zdravkovich, 1982) that a drastic change in the phase of the vortex shedding, relative to the body oscillations, occurs in the vicinity of the natural shedding frequency. However, Ongoren and Rockwell and, earlier, Bearman and Davies (1975) showed that the afterbody shape plays an important role in the phase shifting in that bodies with a short or nonexistent afterbody, i.e., a circular or triangular cylinder, experience a large phase shift, while a body such as a square or rectangular cylinder with a relatively large afterbody experiences little or no phase shift. This phase shift results in the switch of the initially shed vortex from the upper to the lower side of the cylinder or vice versa. The presence of the afterbody appears to induce reattachment of the initially shed vortex and to reduce the likelihood of the phase shifting. This is yet another indication of the importance of the vortex formation region and near-wake flow to the shedding process.

The changes in the vortex formation region with the frequency of the oscillations are shown by the photographs in Fig. 10 from Ongoren and Rockwell (1988a). The flow was visualized in water in the manner described in the previous section of the paper, and again the results are remarkably similar to the earlier wind tunnel photographs of Griffin and Ramberg (1974). All of the photographs were taken with the cylinder at its lowest position in the oscillation cycle, and the shift in phase of the shedding relative to the cylinder can be seen by comparing the wakes at  $f = 0.9 f_{st}$  and  $f = 1.05 f_{st}$ . The



Fig. 11 Flow visualization of synchronized vortex shedding due to rotational oscillation of a circular cylinder. Legend for data points: 0, -8;  $Re = 15,000$ ; (a)  $St = 0.3$ , (b)  $St = 0.5$ , (c)  $St = 0.7$ , (d)  $St = 0.9$ ; from Tokumaru and Dimotakis (1991).

substantial decrease in the length of the vortex formation region with frequency of oscillation also is evident from the photographs.

Other effects of the cross-flow oscillations observed by Ongoren and Rockwell included a large swinging motion of the circular cylinder wake about the body at frequencies less than the Strouhal frequency. This swinging motion is largest near the Strouhal frequency and then it abruptly disappears. There is evidence of some correlation between the phase shift in the shedding and the abrupt disappearance of the swinging motion. The swinging motion does not appear in the case of bodies with fixed separation points. There were numerous complex wake patterns observed at other frequencies. For instance, small-scale vortices were shed at superharmonic frequencies of  $n = 2, 3, 4$ , and higher nonharmonic frequencies, and the downstream wake eventually recovered to a lock-on and altered asymmetric pattern similar in form to the classical Karman vortex pattern. However, the altered pattern departed substantially from the classical Karman street, with the frequency taking the values  $f_a = f/n$ . An interesting aspect of the paper by Ongoren and Rockwell is the number of historical references, e.g., Meier-Windhorst (1939).

### Rotational Oscillations

Vortex lock-on and control of the near-wake flow also can be realized with small rotational oscillations of a circular cylinder. There are very few studies of this aspect of the problem, the most recent being those of Tokumaru and Dimotakis (1991) and of Filler et al. (1991). An important distinction between the two studies is that in the experiments of Tokumaru and Dimotakis the maximum rotational velocity of the cylinder was on the order of the velocity outside the boundary layer at separation (approximately  $1.4U$ ), whereas in the experiments of Filler et al. the maximum rotational velocity of the cylinder was only  $0.03U$ . These studies seem to show, however, that the range of lock-on frequencies, though still probably amplitude-dependent, is much reduced from what has been observed for imposed oscillations and flow perturbations as discussed earlier. There are essentially two types of forcing which can be introduced by rotational oscillations. The first is the classical form of lock-on or resonance which takes place

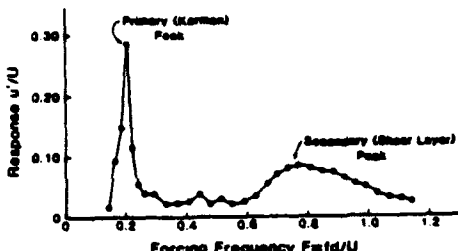


Fig. 12 A typical frequency response curve showing the normalized velocity response amplitude as a function of the forcing frequency for  $Re = 820$ , the vibration parameter  $\Omega_1 = 0.14$ , and  $d = 1.27$  cm; from Filler et al. (1991)

when the oscillations are near the Karman vortex shedding frequency. When the Reynolds number is greater than about  $Re = 500$ , oscillations of higher frequency also can excite the Bloor-Gerrard (Bloor, 1964) frequency of instability in the shear layers separating from the cylinder. This excitation of the B-G instabilities is likely to be caused by inflow perturbations and other types of imposed body oscillations as well.

A series of photographs of vortex lock-on at increasing values of the oscillation Strouhal number  $St_1$  are shown in Fig. 11. The oscillation parameter  $\Omega_1 = v_1/U$ , where  $v$  is the peak circumferential velocity, was kept fixed during the sequence of conditions shown in this figure, from Tokumaru and Dimotakis (1991). The experiments were performed in a CalTech water channel at a Reynolds number of  $Re = 5,000$ , and the flow was visualized by introducing a mixture of colored food dye into the water upstream of the cylinder. The dye mixture was made neutrally buoyant by diluting it with ethyl alcohol (P.E. Dimotakis, private communication). In all of the cases shown the vortex shedding is locked-on in the classical manner with the imposed rotational oscillations. When the oscillation Strouhal number was increased to  $St_1 = 1.5$ , the wake forcing went through a transition to the Bloor-Gerrard shear layer forcing. For a fixed value of oscillation Strouhal number of  $St_1 = 1$ , the transition to shear layer forcing takes place at an oscillation parameter of approximately  $\Omega = 16$ .

A plot of the velocity  $u'$  in the wake from Filler et al. (1991) as a function of the oscillation Strouhal number  $St_1$  is shown in Fig. 12. Here the oscillation parameter  $\Omega_1 = \omega_1 d/2U$ , where  $\omega_1$  is the frequency of the rotational oscillations. At the lower frequencies near the usual Karman shedding frequency a large resonant peak is seen when the oscillations are in that range. However, at the higher imposed frequencies there is a secondary broad peak in the range of the shear layer instability frequencies. In the Karman frequency range of vortex shedding the wake behaves like a nonlinear oscillator near resonance. This behavior is well known (Bishop and Hassan, 1964; Bearman, 1984) and has been explored by numerous investigators for the cases of cross-flow and in-line oscillations. The forced Bloor-Gerrard shear layer instabilities are simply convected downstream in the near wake. An important finding by Tokumaru and Dimotakis (1991) is that active control of the near-wake vortex formation and flow physics by rotational oscillations of the cylinder can reduce the drag on the cylinder by as much as a factor of six! This decrease in the drag coefficient  $C_D$  is accompanied by a comparable decrease in the wake displacement thickness  $\delta^*$  (a factor of five) as defined by an integral of the cross-stream wake velocity distribution over the height of the channel.

There are very few studies of rotational oscillations on wake flow control and vortex resonance or lock-on. Examples from the two most recent have been given here. For earlier examples the reader should refer to the work of Okajima et al. (1975) and of Taneda (1978). This is a new and potentially exciting approach to the active control of vortex formation and bluff body wake flows.

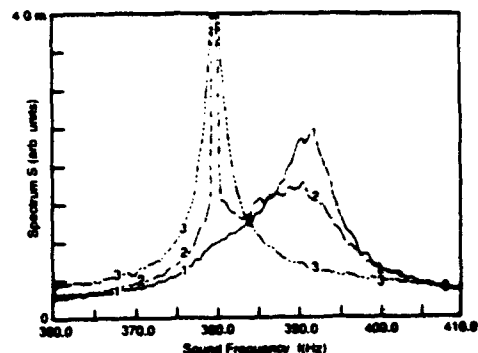


Fig. 13 Entrainment of natural or unforced vortex shedding at 392 Hz by sound at 380 Hz. The vertical scale is the same for all three spectra; from Blevins (1985).

### The Effects of Sound

The application of an appropriate sound field to the flow about a rigid cylinder can induce vortex lock-on and resonance in the wake. There are even fewer reported studies of the effect of sound than of rotational oscillations, the principal example of the former being that of Blevins (1985). The only other directly related work is that of Okamoto et al. (1981). As noted by Blevins, the effect on the vortex shedding of an acoustic wave propagating along the axis of a circular cylinder was examined by the latter. Only a minor influence was observed for sound excitation levels above 20 Pa.

The experiments performed by Blevins were at Reynolds numbers in the range  $Re = 20,000$  to  $40,000$  in a wind tunnel that allowed a transverse sound field to be applied such that the cylinder was located at the node of the acoustic pressure field. This is the point of maximum induced velocity due to the sound. It was observed by Blevins that the vortex lock-on was induced by the velocity rather than the pressure.

An example of the results reported by Blevins (1985) is shown in Fig. 13. The frequency of the vortex shedding was  $f_s = 392$  Hz, and the frequency of the applied sound field was  $f = 380$  Hz. Thus the lock-on occurred at a frequency less than the Strouhal frequency. The average spectral output from a flush-mounted hot-film probe mounted on the cylinder is plotted for the three test runs. The spectrum labeled 1 shows the typical averaged spectrum for a rigid cylinder in a uniform flow, with the broad peak in this case centered at the vortex shedding frequency of 392 Hz. When a 100 Pa sound field is applied two peaks are present—a sharp peak at 380 Hz induced by the applied sound, and a broader reduced and shifted peak due to vortex shedding. An increase in the applied sound field to 250 Pa produces a typical lock-on spectrum with a single sharp peak at the frequency of the sound. The lock-on frequency here is less than the Strouhal frequency, and it was observed by Blevins that the induced resonance always was stronger at the reduced frequencies as compared to frequencies higher than the Strouhal frequency. The sound field and the vortex shedding were phase locked over a range of phase angles which varies nearly linearly with the applied sound frequency.

An additional observation by Blevins (1985) was that turbulence in the free stream suppressed the influence of sound on the vortex shedding. The results suggest that the induced sound field velocity must exceed the turbulence velocities in order for the sound to influence the vortex shedding. Also, the introduction of sound substantially increased the coherence of the vortex shedding along the span of the cylinder as is usually found when a circular cylinder is oscillated.

### The Near-Wake Flow Field

There is a physical dependence between the wake width  $d'$  at the end of the vortex formation region of a bluff body and

Table 1 Legend for data plotted in Fig. 14

Symbol	Bluff body type	Method	Investigators
•	Half cylinder (D-section)	Wind tunnel experiment	Armstrong et al. (1986, 1987)
—	Flat plate	Wind tunnel experiment	Armstrong et al. (1986, 1987)
•	Circular cylinder	Wind tunnel experiment	Armstrong et al. (1986, 1987)
•	Circular cylinder	Wind tunnel experiment	Barbi et al. (1986)
□ □ □	Wide splitter plate (D-section)	Computation	Grinstein et al. (1991)
—	Hydrofoil	Wind tunnel experiment	Blake et al. (1977)
+	D-section cylinder	Wind tunnel experiment	Simmons (1975)
— ▽	D-section cylinder with and w/o splitter plate	Wind tunnel experiment	Bearman (1965)

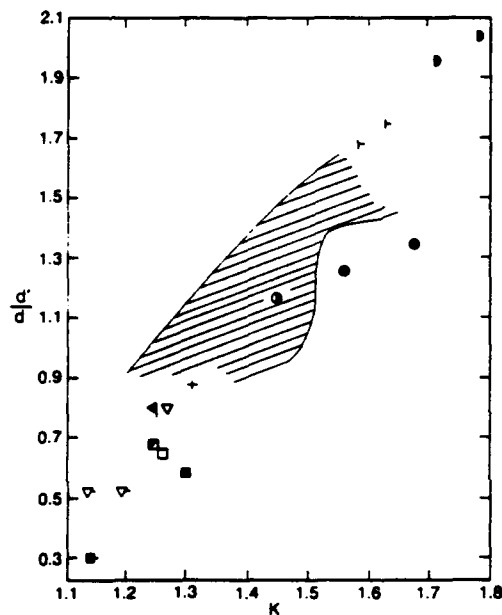


Fig. 14 Wake width  $d'/d$  as a function of the base pressure parameter or velocity ratio  $K$ . The legend is given in Table 1. The shaded area in the figure corresponds to a variety of body geometries and flow conditions given in Griffin (1989).

the base pressure coefficient  $-C_{pb}$  or the related velocity ratio  $K$ . As discussed earlier, these are important characteristic physical parameters of the bluff body wake. In general, the bluffness of a given body shape is represented by a wider wake, and corresponding lower base pressure or higher velocity ratio. For a cylinder vibrating normal to the incident flow, the variation of both the measured base pressure and wake width with the frequency ratio  $f/f_{so}$  over the lock-on regime show the same resonant behavior (Griffin, 1989). Both  $-C_{pb}$  and  $d'$  increase to a maximum value and then gradually decrease as the upper limit of the lock-on range of frequencies is reached. Only the base pressure variation was measured by Armstrong et al., but the wake width can be estimated as a function of  $U/f_{so}d$ , using the wake similitude relationships summarized earlier in the paper and measured values of  $St$  and  $C_{pb}$  (or  $K$ ). For the range of Reynolds numbers corresponding to the experiments of Armstrong et al., the wake Strouhal number  $St^*$  is essentially constant at a value of 0.16, so that

$$d'/d = (St^*/St)K$$

from Eq. (4a).

The wake widths for several cylinders and flow conditions are plotted as a function of  $K$  in Fig. 14. The legend for the data in the figure is given in Table 1. This range of the base

pressure parameter or separation velocity ratio  $K$  represents the entire regime over which vortex shedding takes place over bluff bodies, whether the shedding is natural or unforced, or the shedding is controlled or modified by some means such as oscillations, in-flow perturbations, sound, and wake splitter plates. The shaded area represents a host of results for oscillating circular cylinders, D-section cylinders, and flat plates under a wide variety of conditions (Griffin, 1989). There is generally good agreement between the new perturbed and steady flow results and the earlier data, except for the two circular cylinder results from Armstrong et al. which are displaced to the right of the overall trend of the data set. This departure from the overall trend of the results is due to the much reduced base pressure measured on the circular cylinder in those experiments, as previously mentioned. In the experiments of Armstrong et al. the circular cylinder and flat plate base pressures were virtually the same under otherwise unvarying conditions of blockage, incident flow, axial uniformity, etc. One might expect the base pressure coefficient for a circular cylinder at the Reynolds numbers studied to be closer to the values of  $C_{pb} = -1$  to 1.1 measured by Barbi et al. and others at the same Reynolds numbers.

The wake widths for flow over a D-section cylinder computed by Grinstein et al. (1990, 1991) are also plotted in Fig. 14. The results shown represent a two-dimensional computation using the flux-corrected transport (FCT) algorithm, but comparable results were obtained with companion three-dimensional computations described by Grinstein et al. (1990). These computations were made for compressible flows with freestream Mach numbers in the range 0.3 to 0.6 at standard temperature and pressure conditions. However, for these Mach numbers compressibility effects are relatively small and reasonable comparisons can be made with incompressible flow experiments. The wake widths plotted in Fig. 14 were obtained directly from computed contour plots of rms velocity  $u'$  at the end of the vortex formation region. The results shown represent flow over the body both with and without a splitter plate attached and they agree remarkably well with the experimental results of Blake et al. (1977), Simmons (1975) and Bearman (1965). The D-section bluff body results overall represent the lowest regime of  $K$  which has been observed thus far.

A comprehensive experimental study of the effects of wake splitter plates on vortex shedding from a circular cylinder was made recently by Unal and Rockwell (1988b). The experiments were conducted in the Reynolds number range  $Re = 140$  to 5000, and the primary objective was to study the effects of the passive wake interference on the formation region of the vortices. An unusual aspect of these experiments was the ratio of the plate thickness  $h$  to the cylinder diameter  $d$ , which was approximately 0.5. Also, the plate length was approximately  $l_p = 24d$  cylinder diameters, in contrast to the splitter plate

Table 2 Longitudinal vortex spacing or wavelength in the near-wake of a circular cylinder vibrating in-line with an incident uniform flow

Vibration frequency, $f$ (Hz)	Frequency ratio, $f/f_{s_0}$	Vortex spacing, $\lambda/d$	Relative change, $\Delta\lambda/\lambda$	Vortex convection speed, $1/2\lambda/U$
Reynolds number = 190				
69.2	1.88	5.2	+0.07	0.94
73.6	2.00	4.9	0	0.93
75.6	2.06	4.7	-0.05	0.91
78.9	2.14	4.7	-0.04	0.96
80.4	2.18	4.4	-0.09	0.92
Average = 0.93				

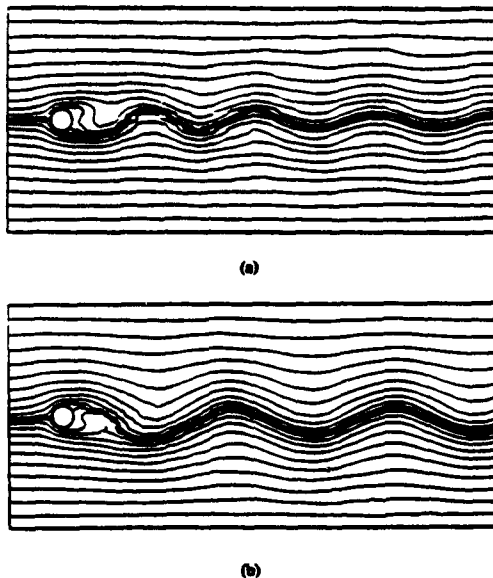


Fig. 15 (a) Instantaneous streamlines at  $Re = 100$  for natural shedding. (b) Instantaneous streamlines at  $Re = 100$  and near-wake forcing at the excitation frequency,  $f_e = 0.75 f_s$  (a lock-in state); from Karniadakis and Triantafyllou (1989).

geometries discussed above. The leading edge of the plate had a tapered and sharply pointed configuration.

These experiments yielded several important conclusions and reinforced those previously reached by other investigators. The first is a reiteration of the importance of the dynamics of the formation region to the overall near-wake flow and the possibility of control and modification of the vortex wake. Second, the wake formation is dominated by an absolute instability and there is a close relation between the vortex formation process and the dynamics of the near-wake Karman vortex street. Other conclusions are the importance of Reynolds number to the wake formation, at least over the range examined, but that no locking-on or vortex resonance occurs in the presence of the passive wake interference. Nonetheless, the results of these and the other experiments and computations discussed here have demonstrated the potential importance of both passive and active control to the flow physics of bluff body wakes.

The downstream vortex spacing or wavelength is a valuable and important diagnostic parameter for the state of the spatial structure and development of the near-wake. Measurements of the spacing for a variety of in-line and cross-flow oscillations, and also for the unforced wakes of stationary cylinders were reported originally by Griffin and Ramberg (1976). These can be compared to the direct numerical simulations of Karniadakis and Triantafyllou (1989) and our recent NRL simulations (Hall and Griffin, 1992). The vortex spacing or longitudinal wavelength can be employed as a measure of the spatial state of the flow as compared to phase plane diagrams

of the streamwise and cross stream components of the wake velocity fluctuations which can be employed comparably to assess the temporal state of the near-wake.

Two examples from Karniadakis and Triantafyllou are shown in Fig. 15. The upper instantaneous streamline pattern corresponds to the unforced wake at  $Re = 100$  while the lower pattern corresponds to a wake forced by a spatially localized acceleration which varied with time in the near-wake vortex formation region with normalized amplitude and frequency, respectively, of  $A = 0.10$  and  $f/f_{s_0} = 0.75$ , and which decayed exponentially in the far field. The center of the disturbance was located at  $x = 2$ ,  $y = 0$ , measured in multiples of cylinder diameter. This is a unique form of control disturbance which had not been investigated in any previous work. For the unforced wake  $\lambda = 5d$  and for the forced wake  $\lambda = 7d$ , an increase of forty percent. A similar example from the NRL perturbed flow computations is given in Fig. 6.

Comparable measurements were made at  $Re = 190$  by Griffin and Ramberg (1976). The results are summarized in Table 2. The cylinder oscillations were in-line with the flow over a range of frequencies near twice the Strouhal frequency (as in Fig. 1) and, for the cases shown, a single vortex was shed during each oscillation cycle. Thus this basic forced wake pattern shared many of the same overall features of the wake forced with the cross-flow oscillations. The measured changes in the forced wake vortex spacing correspond directly with those from the direct numerical simulations; for  $f < 2f_{s_0}$  the wavelength is increased while for  $f > 2f_{s_0}$  the wavelength is decreased as shown in Table 2. Extrapolating the measured results in the table to the case shown in Fig. 15 using a least-squares straight line given by Griffin and Ramberg (1976), the vortex spacing is  $\lambda = 6.2d$ . This compares reasonably well with the computed results of  $\lambda = 7d$ . The measured vortex spacing for the stationary cylinder at  $Re = 190$  ( $\lambda = 4.9d$ ) is virtually identical to the computed value at  $Re = 100$  ( $\lambda = 5d$ ).

The vortex street wavelengths computed by Karniadakis and Triantafyllou and more recently at NRL are compared further with measured street wavelengths for both forced and unforced conditions in the range of Reynolds numbers from 100 to 2000 in Fig. 16. The computations fit well with the overall trend of the measured data, which show only a very slight dependence on Reynolds number in this range. The vertical scale in the figure essentially is a normalized form of the convection speed of the vortices, or the downstream speed of the vortex cores. The constant phase or convection speed is representative of a non-dispersive physical system.

Several measurements of the vortex phase or convection speed, i.e., the speed at which the vortex cores travel downstream, are given in Table 2. Though there is some scatter, the data generally are grouped around the average value of  $U_c = 0.93U$ . This gives some evidence that both forced and unforced or natural periodic vortex wakes have the same basic non-dispersive properties.

The experiments of Tokumaru and Dimotakis (1991) also included measurements of the vortex street wavelength  $\lambda$  over a wide range of the oscillation Strouhal number  $St_s = f_s d/U$ .

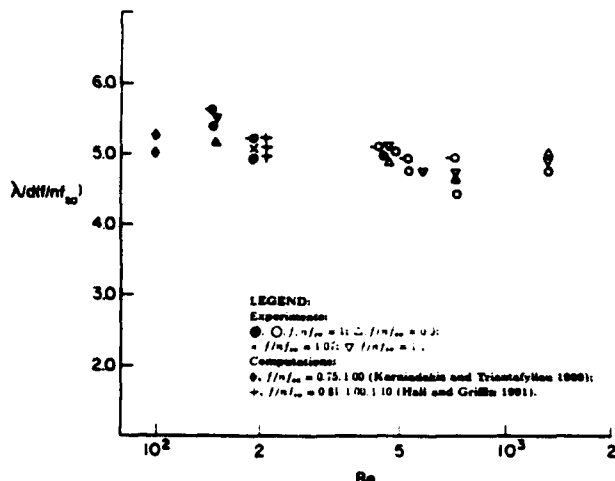


**Fig. 16** Longitudinal vortex spacing  $\lambda/d$  ( $\#f_{\infty}$ ) as a function of Reynolds number  $Re$ . All of the measurements were made in the wakes of stationary and oscillating cylinders. Data points at  $Re = 190$  and  $200$  correspond to in-line oscillations and flow perturbations with  $n = 2$ ; all other results correspond to cross-flow oscillations (experiments) and near-wake perturbations (computations) with  $n = 1$ .

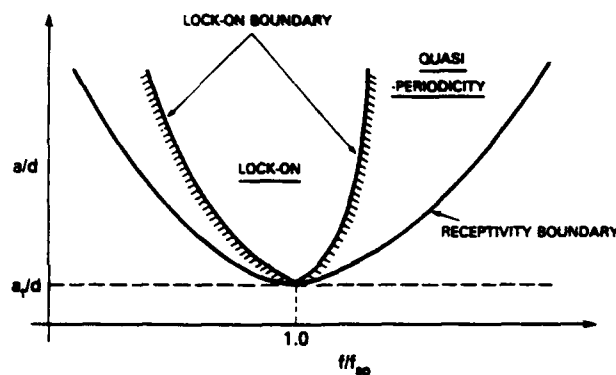


Fig. 17 State selection (amplitude versus frequency) diagram for laminar wakes. The plot should only be interpreted in a qualitative sense; from Karniadakis and Triantafyllou (1988).

For the observed range of lock-on where  $St_f = 0.3$  to 1.0, the geometry of the vortex street adjusted in terms of the wavelength  $\lambda$  and the frequency  $f$  to form yet again an essentially non-dispersive street pattern, though there is some slight scatter in the measurements. The lateral spacing of the near-wake vortex street also decreased with increasing  $St_f$  over this lock-on range. The Reynolds number for these experiments was  $Re = 15,000$ , and some complementary smooth cylinder experiments were conducted at a lower Reynolds number of  $Re = 3,300$  and with surface roughness added to the cylinder at the higher Reynolds number. The results were similar in both cases. These observations for the case of active control with rotational oscillations confirm and extend the conclusions drawn earlier for both forced and unforced wakes.

## Near-Wake Flow Stability

The introduction of the absolute/convective theory of fluid dynamic stability has led to a promising new approach and a new theoretical framework for understanding the physics of vortex formation and near-wake flow development (Koch, 1985; Triantafyllou et al., 1986, 1987; Monkewitz and Nguyen, 1987; Rockwell, 1987; Chomaz et al., 1988; Unal and Rockwell, 1988a, b; Ongoren and Rockwell, 1988a, b; Karniadakis and Triantafyllou, 1989; Oertel, 1990; Huerre and Monkewitz, 1990; Rockwell, 1990). A flow is said to be absolutely unstable

when an initial infinitesimally small disturbance grows exponentially in place at the location where it is introduced. In the case of a convective instability the initially small disturbance is transported or convected away from the point of its introduction, leaving behind an undisturbed region of flow. Chomaz et al. (1988) have introduced the term *global instability*. They note that the existence of a local absolute instability is only a necessary, but not sufficient, condition for the existence of a global instability in a shear flow, and that the localized region of absolute instability must physically grow to a large size to become globally unstable.

Recent stability calculations based upon computed and measured mean velocities in the wakes of stationary circular cylinders suggest that the vortex formation region is absolutely unstable while the fully-formed vortex street is convectively unstable. The vortex formation region is thought to be a complex global region of upstream and downstream propagating vorticity waves, self-excitation of the flow, and modal competition and interaction (Rockwell, 1990). This region of self-excited oscillations and flow resonance plays an important role in frequency selection, and thus in programming and control of the flow separation and the overall unsteady flow. More extensive stability calculations of this nature may also lead to better understanding of bluff body wakes, and their active control and modification by any of the means discussed here. A better understanding of passive wake control and modification, e.g., by splitter plates and base bleed, may be achieved in the same manner. The most recent and comprehensive discussions of absolute/convective and local/global instabilities for spatially developing shear flows, including bluff body wakes, are given by Huerre and Monkewitz (1990), Oertel (1990), and Rockwell (1990).

Karniadakis and Triantafyllou (1989) conducted a linear stability analysis of the time-averaged flow in the near-wake which was derived from their direct numerical simulation of the cylinder wake at  $Re = 100$ . The flow was assumed to be locally parallel and slowly varying in the downstream direction. The averaged flow was found to be absolutely unstable for approximately 2.5 diameters downstream from the cylinder. This corresponds generally to the length scale of the vortex formation region at subcritical Reynolds numbers below  $10^4$  (Bloor and Gerrard, 1966), a wide range of Reynolds numbers. At greater downstream distances the flow is convectively unstable. Thus the continuous formation of the vortex street is thought to be sustained by the near-wake absolute instability. Good global agreement was found between the stability analysis and the computation in that the Strouhal number was  $St = 0.179$  in both cases. This is slightly higher than most experiments (Roshko, 1954; Williamson, 1988), which may be due partly to finite grid size and the extent of the computational domain, and to the three-dimensional effects which invariably exist in a cylinder wake. Williamson (1988) has shown the importance of the spanwise variation of the cylinder wake flow.

### Summary and Concluding Remarks

Previous observations of vortex resonance or lock-on for bluff body near-wakes which have been accumulated by numerous researchers over the years now have been extended to several additional types of imposed disturbances of both fundamental and practical importance—a bluff body in a perturbed incident flow consisting of a mean flow with a periodic component superimposed upon it, rotational oscillations of the body, and sound. And the first of these cases has been shown to be fundamentally identical, under appropriate conditions, to the lock-on or vortex resonance of a cylinder oscillating in line with an incident uniform flow. The vortex lock-on results from the periodic flow exhibit a particularly strong form of resonance, with a relative perturbation amplitude of  $2\Delta U/\omega D = 0.014$  resulting in a reduction in base pressure from

$C_{p0} = -1.44$  to  $-1.85$ , or 22 percent, for a circular cylinder (Armstrong et al., 1986, 1987). For a circular cylinder oscillating in cross-flow, as noted earlier, a peak-to-peak vibration amplitude of  $2a/d = 0.20$  to 0.30 is required to provide a comparable reduction in  $C_{p0}$  (Stansby, 1976). Conditionally-averaged wake velocity measurements by Armstrong et al. (1987) have indicated that the strength of the vortices was increased by 29 percent and the spacing was decreased by 25 percent for the largest perturbation levels of their experiments.

These are quite remarkable modifications of the near-wake flow for such a relatively small perturbation amplitude. Thus, seemingly small perturbations of the basic wake flow can produce large changes in vortex strength, base pressure and drag on a bluff circular cylinder or other cross-section. Modification and control of the basic formation or instability mechanisms of the wake thus can provide a means for making substantial changes in the near-wake vortex pattern, and possibly even the middle- and far-wake patterns as well (Cimbala et al., 1988, Browne et al., 1989).

Karniadakis and Triantafyllou (1989) have characterized the state of both the forced and unforced vortex wakes by means of a state diagram as sketched in Fig. 17. At a small but finite amplitude the transitions corresponding to the upper and lower limits of the lock-on are given by two bounding frequencies; within these limits only periodic lock-on states exist. Two quasi-periodic regions are thought to develop at frequencies well above and below the lock-on regime, together with chaotic states in narrow regions immediately adjacent to the lock-on boundaries. These are conceptually similar in overall appearance to the vortex resonance or lock-on measurements of Koopmann (1967) for cross-flow oscillations of a cylinder, reproduced here in Fig. 7, and for the in-line flow perturbations and cylinder oscillations shown in Figs. 1 and 2.

As the threshold amplitude  $a$ , is approached, these finite regions shrink to a single frequency  $f_c$ . For cross flow oscillations of the cylinder  $f_c = f_{s0}$  while for in-line oscillations of the body and periodic perturbations of the mean flow  $f = 2f_{s0}$  as shown in Fig. 2. The small amplitude perturbations introduced by Armstrong et al. (1986, 1987) correspond qualitatively to those discussed by Karniadakis and Triantafyllou. The relatively large amplitude cylinder oscillations and flow perturbations investigated by Koopmann (1967), Griffin and Ramberg (1974, 1976) and Barbi et al. (1986) and shown in Figs. 1 and 7 introduce nonlinearities and complex changes in the near-wake flow field as shown by the flow visualization studies of Griffin and Ramberg (1974, 1976), Williamson and Roshko (1988), and Ongoren and Rockwell (1988a, b). At the largest amplitudes of oscillation, highly complex vortex flow patterns were observed; and a more extensive kaleidoscope of complex vortex patterns over an even wider range of frequencies and amplitudes was observed experimentally by Williamson and Roshko (1988).

Further research based upon these new analytical and computational approaches described herein is likely to lead to new and more complete fundamental understanding of the near-wake vortex dynamics and vortex lock-on, which until now have been studied mostly by using the more traditional modeling approaches combined with experiments. The results discussed in this paper suggest that modification and control of the basic instability or formation mechanisms of the wake by imposed oscillations, i.e., cross-flow, in-line and rotational, incident flow perturbations, and an imposed sound field provide a means for making substantial alterations to the near-wake vortex pattern, and possibly to the middle- and far-wake flow patterns as well which exist relatively far downstream from the wake-generating body.

### Acknowledgments

This study was conducted as part of a research program in

fluid dynamics and bluff body flows supported by the Naval Research Laboratory and the Office of Naval Research. We are grateful to Dr. George Karniadakis of Princeton University for several helpful discussions on the spectral element computations and absolute/convective stability concepts. We are also grateful to our colleagues who provided figures and photographs from their research, and to the referees and editors who made numerous constructive and helpful comments to us.

### References

Armstrong, B. J., Barnes, F. H., and Grant, I., 1986, "The Effect of a Perturbation on the Flow Over a Cylinder," *Phys. Fluids*, Vol. 29, pp. 2095-2102.

Armstrong, B. J., Barnes, F. H., and Grant, I., 1987, "A Comparison of the Structure of the Wake Behind a Circular Cylinder in a Steady Flow With That in a Perturbed Flow," *Phys. Fluids*, Vol. 30, pp. 19-26.

Barbi, C., Favier, D. P., Maresca, C. A., and Telionis, D. P., 1986, "Vortex Sheding and Lock-On of a Circular Cylinder in Oscillatory Flow," *J. Fluid Mech.*, Vol. 170, pp. 527-544.

Bearman, P. W., 1963, "Investigation of the Flow Behind a Two Dimensional Model With a Blunt Trailing Edge and Fitted With Splitter Plates," *J. Fluid Mech.*, Vol. 21, pp. 241-255.

Bearman, P. W., 1967, "On Vortex Street Wakes," *J. Fluid Mech.*, Vol. 28, pp. 625-641.

Bearman, P. W., 1984, "Vortex Sheding From Oscillating Bluff Bodies," *Ann. Rev. Fluid Mech.*, Vol. 6, pp. 195-222.

Bearman, P. W., and Currie, I. G., 1979, "Pressure Oscillation Measurements on an Oscillating Circular Cylinder," *J. Fluid Mech.*, Vol. 91, pp. 661-677.

Bearman, P. W., and Davies, M. E., 1975, "The Flow About Oscillating Bluff Structures," *Proc. 4th Int. Conf. Wind Eff. Build. Struct.*, ed. K. J. Eaton, pp. 285-295, Cambridge Univ. Press.

Bishop, R. E. D., and Hassan, A. Y., 1964, "The Lift and Drag Forces on a Circular Cylinder," *Proc. R. Soc., London, Series A*, Vol. 277, pp. 51-75.

Blevins, R. D., 1985, "The Effect of Sound on Vortex Sheding From Cylinders," *J. Fluid Mech.*, Vol. 161, pp. 217-237.

Blake, W. K., Maga, L. J., and Finkenstein, G., 1977, "Hydrodynamic Variables Influencing Propeller and Hydrofoil Singing," *Noise and Fluids Engineering*, ASME: New York, pp. 191-199.

Bloor, M. S., 1964, "Transition to Turbulence in the Wake of a Circular Cylinder," *J. Fluid Mech.*, Vol. 19, pp. 290-304.

Bloor, M. S., and Gerrard, J. H., 1966, "Measurements on Turbulent Vortices in a Cylinder Wake," *Proc. Roy. Soc., Lond., Series A*, Vol. 294, pp. 319-342.

Browne, L. W. B., Antonia, R. A., and Shah, D. A., 1989, "On the Origin of the Organized Motion in the Turbulent Far-Wake of a Cylinder," *Exp. Fluids*, Vol. 7, pp. 475-480.

Chomaz, J. M., Huerre, P., and Redekopp, L. T., 1988, "Bifurcations to Local and Global Modes in Spatially Developing Flows," *Phys. Rev. Lett.*, Vol. 60, pp. 25-28.

Cimbala, J. M., Nagib, H. M., and Roshko, A., 1988, "Large Structure in the Far Wakes of Two-Dimensional Bluff Bodies," *J. Fluid Mech.*, Vol. 190, pp. 265-298.

Flows Williams, J. E., and Zhao, B. C., 1989, "The Active Control of Vortex Sheding," *J. Fluids Struct.*, Vol. 3, pp. 115-122.

Filler, J. R., Marston, P. L., and Mih, W. C., 1991, "Response of the Shear Layers Separating From a Circular Cylinder to Small Amplitude Rotational Oscillations," *J. Fluid Mech.*, Vol. 231, pp. 481-499.

Gerrard, J. H., 1966, "The Mechanics of the Formation Region of Vortices Behind Bluff Bodies," *J. Fluid Mech.*, Vol. 25, pp. 401-413.

Griffin, O. M., 1978, "A Universal Strouhal Number for the 'Locking-On' of Vortex Sheding to the Vibrations of Bluff Cylinders," *J. Fluid Mech.*, Vol. 85, pp. 591-606.

Griffin, O. M., 1981, "Universal Similarity in the Wakes of Stationary and Vibrating Bluff Structures," *ASME JOURNAL OF FLUIDS ENGINEERING*, Vol. 103, pp. 52-58.

Griffin, O. M., 1989, "Flow Similitude and Vortex Lock-On in Bluff Body Near-Wakes," *Phys. Fluids A*, Vol. 1, pp. 697-703.

Griffin, O. M., and Ramberg, S. E., 1974, "The Vortex Street Wakes of Vibrating Cylinders," *J. Fluid Mech.*, Vol. 66, pp. 553-576.

Griffin, O. M., and Ramberg, S. E., 1976, "Vortex Sheding From a Cylinder Vibrating in Line With an Incident Uniform Flow," *J. Fluid Mech.*, Vol. 75, pp. 257-271.

Grinstein, F. F., Boris, J. P., Griffin, O. M., Hussain, F., and Oran, E. S., 1990, "Coherent Structure Dynamics in Spatially Evolving Near Wakes," *28th Aerospace Sciences Meeting (Reno)*, AIAA Paper 90-0507.

Grinstein, F. F., Boris, J. P., and Griffin, O. M., 1991, "A Numerical Study of Passive Pressure-Drag Control in a Plane Vortex Street Wake," *AIAA J.*, Vol. 29, in press.

Hall, M. S., and Griffin, O. M., 1992, "Vortex Sheding and Lock-On in a Perturbed Flow," in preparation.

Hatfield, H. M., and Morkovin, M. V., 1973, "Effect of an Oscillating Free Stream on the Unsteady Pressure on a Circular Cylinder," *ASME JOURNAL OF FLUIDS ENGINEERING*, Vol. 95, pp. 249-254.

Huerre, P., and Monkewitz, P., 1990, "Local and Global Instabilities in Spatially Developing Flows," *Ann. Rev. Fluid Mech.*, Vol. 22, pp. 473-537.

Karniadakis, G. E., and Triantafyllou, G. S., 1989, "Frequency Selection and Asymptotic States in Laminar Wakes," *J. Fluid Mech.*, Vol. 199, pp. 441-469.

Karniadakis, G. E., and Triantafyllou, G. S., 1990, "Direct Numerical Simulation of the Three-Dimensional Vortex Street," 28th Aerospace Sciences Meeting (Reno), AIAA Paper 90-0113.

Koch, W., 1985, "Local Instability Characteristics and Frequency Determination of Self-Excited Wake Flows," *J. Sound Vib.*, Vol. 99, pp. 53, 83.

Kooppmann, G. H., 1967, "The Vortex Wakes of Vibrating Cylinders at Low Reynolds Numbers," *J. Fluid Mech.*, Vol. 28, pp. 501-512.

Mananah, V., 1986, "Experimental Investigation of the Effects of Splitter Plates on the Flow Behind a Rectangular Cylinder," Ph.D. thesis, Queen's University, Kingston, Ontario, Canada.

Meier-Windhors, A., 1939, "Flatterschwingungen von Zylindern im gleichmassigen Flüssigkeitsstrom," *Mitteilungen des Hydraulischen Instituts der Technischen Hochschule, München*, Heft 9, pp. 9-39.

Munkewitz, P. A., and Nguyen, L., 1987, "Absolute Instability in the Near-Wakes of Two-Dimensional Bluff Bodies," *J. Fluid Struct.*, Vol. 1, pp. 165-184.

Morkovin, M. V., 1964, "Flow Around Circular Cylinders. A Kaleidoscope of Challenging Fluid Phenomena," *ASME Symposium on Fully Separated Flows*, ASME, New York.

Oertel, H., 1990, "Wakes Behind Bluff Bodies," *Ann. Rev. Fluid Mech.*, Vol. 22, pp. 539-564.

Okajima, A., Takata, H., and Asanuma, T., 1975, "Viscous Flow Around a Rotaionally Oscillating Circular Cylinder," *Inst. Space and Aero. Sci. (U. Tokyo)*, Report No. 532.

Okamoto, S., Hirose, T., and Adachi, T., 1981, "The Effect of Sound on the Vortex Shedding From a Circular Cylinder," *Bull. Japan Soc. Mech. Engrs.*, Vol. 24, pp. 45-53.

Ongoren, A., and Rockwell, D., 1988a, "Flow Structure From an Oscillating Cylinder. Part I: Mechanisms of Phase Shift and Recovery in the Near Wake," *J. Fluid Mech.*, Vol. 191, pp. 197-223.

Ongoren, A., and Rockwell, D., 1988b, "Flow Structure From an Oscillating Cylinder. Part II: Model Competition in the Near Wake," *J. Fluid Mech.*, Vol. 191, pp. 225-245.

Rockwell, D., 1987, "Unpublished Manuscript: A View of Hypotheses and Issues on Bluff Body Near-Wake Instabilities," Lehigh University.

Rockwell, D., 1990, "Active Control of Globally-Unstable Separated Flows," *ASME International Symposium on Nonsteady Fluid Dynamics (Proceedings)*, FED-Vol. 92, pp. 379-394.

Roshko, A., 1954, "On the Drag and Shedding Frequency of Two-Dimensional Bluff Bodies," *Natl. Adv. Comm. for Aero., Washington, DC*, Technical Note 3169.

Roshko, A., 1955, "On the Wake and Drag of Bluff Bodies," *J. Aero. Sci.*, Vol. 22, pp. 124-132.

Sarpkaya, T., 1979, "Vortex Induced Oscillations: A Selective Review," *ASME Journal of Applied Mechanics*, Vol. 46, pp. 241-258.

Simmons, J. E. L., 1975, "Effect of Separation Angle on Vortex Streets," *Proc. ASCE, J. Eng. Mech.*, Vol. 101, pp. 649-661.

Stansby, P. K., 1976, "Base Pressure of Oscillating Cylinders," *Proc. ASCE, J. Eng. Mech.*, Vol. 104, pp. 591-600.

Taneda, S., 1978, "Visual Observations of the Flow Past a Circular Cylinder Performing a Rotatory Oscillation," *J. Phys. Soc. Japan*, Vol. 45, pp. 1038-1043.

Tanida, Y., Okajima, A., and Watanabe, Y., 1973, "Stability of a Circular Cylinder Oscillating in Uniform Flow or in a Wake," *J. Fluid Mech.*, Vol. 61, pp. 769-784.

Tatsuura, M., 1972, "Vortex Streets Behind a Circular Cylinder Oscillating in the Direction of Flow," *Bull. Res. Inst. Appl. Mech.*, Kyushu University, Vol. 36, pp. 25-37 (in Japanese).

Tokumaru, P. T., and Dimotakis, P. E., 1991, "Rotary Oscillation Control of a Cylinder Wake," *J. Fluid Mech.*, Vol. 224, pp. 77-90.

Triantafyllou, G., Triantafyllou, M., and Christoumidis, C., 1986, "Stability Analysis to Predict Vortex Street Characteristics and Forces on Circular Cylinders," *ASME J. Offshore Mech. and Arctic Engineering*, Vol. 109, pp. 148-154.

Triantafyllou, G., Kupfer, K., and Bers, A., 1987, "Absolute Instabilities and Self-Sustained Oscillations in the Wakes of Circular Cylinders," *Phys. Rev. Lett.*, Vol. 59, pp. 1914-1917.

Unal, M. F., and Rockwell, D., 1988a, "On Vortex Formation From a Cylinder. Part 1. The Initial Instability," *J. Fluid Mech.*, Vol. 190, pp. 491-512.

Unal, M. F., and Rockwell, D., 1988b, "On Vortex Formation From a Cylinder. Part 2. Control by Splitter Plate Interference," *J. Fluid Mech.*, Vol. 190, pp. 513-529.

West, G. S., and Apte, C. J., 1982, "The Effects of Tunnel Blockage and Aspect Ratio on the Mean Flow Past a Circular Cylinder With Reynolds Numbers Between  $10^4$  and  $10^5$ ," *J. Fluid Mech.*, Vol. 114, pp. 361-377.

Williamson, C. H. K., and Roshko, A., 1988, "Vortex Formation in the Wake of an Oscillating Cylinder," *J. Fluid Struct.*, Vol. 2, pp. 355-381.

Williamson, C. H. K., "Defining a Universal and Continuous Strouhal-Reynolds Number Relationship for the Laminar Vortex Shedding of a Circular Cylinder," *Phys. Fluids*, Vol. 31, pp. 2742-2744.

Zdravkovich, M. M., 1982, "Modification of Vortex Shedding in the Synchronization Range," *ASME JOURNAL OF FLUIDS ENGINEERING*, Vol. 104, pp. 513-517.

## **Appendix D**

### **Vortex Shedding and Lock-On in a Perturbed Flow**

# Vortex Shedding and Lock-On in a Perturbed Flow

**Mary S. Hall**

Science Applications International Corporation, McLean, VA 22102

**Owen M. Griffin**

Naval Research Laboratory, Washington, DC 20375-5351  
Fellow ASME.

*Vortex shedding resonance or lock-on is observed when a bluff body is placed in an incident mean flow with a superimposed periodic component. Direct numerical simulations of this flow at a Reynolds number of 200 are compared here with experiments that have been conducted by several investigators. The bounds of the lock-on or resonance flow regimes for the computations and experiments are in good agreement. The computed and measured vortex street wavelengths also are in good agreement with experiments at Reynolds numbers from 100 to 2000. Comparison of these computations with experiments shows that both natural, or unforced, and forced vortex street wakes are nondispersive in their wave-like behavior. Recent active control experiments with rotational oscillations of a circular cylinder find this same nondispersive behavior over a three-fold range of frequencies at Reynolds numbers up to 15,000. The vortex shedding and lock-on resulting from the introduction of a periodic inflow component upon the mean flow exhibit a particularly strong resonance between the imposed perturbations and the vortices.*

## Introduction

Vortex streets are formed in the wakes of circular cylinders and other bluff, or unstreamlined, bodies over a wide range of Reynolds numbers from approximately 50 to  $10^6$  and even higher. The physics of vortex street formation has been the focal point for many past experimental studies, e.g., Roshko (1954, 1955), Gerrard (1966), Bearman (1965, 1967), Griffin and Ramberg (1974) and, more recently, Ongoren and Rockwell (1988a, b), and Williamson and Roshko (1988), because of the importance of the near-wake flow to the eventual evolution of the overall middle and far-wake vortex patterns. Modern high-speed computers and direct numerical simulation techniques have allowed the vortex formation and modification processes to be studied numerically at high resolution (Karniadakis and Triantafyllou, 1989, 1992; Grinstein et al., 1991).

When a bluff cylinder is excited into resonant oscillations by an incident flow, the cylinder and its shed vortices have the same frequency near one of the characteristic frequencies of the body (Koopmann, 1967; Sarpkaya, 1979; Bearman, 1984; Griffin and Hall, 1991). This coincidence or resonance of the shedding and vibration frequencies is commonly termed lock-on, and such a state emerges when the body is oscillated externally in various orientations relative to the incident flow over the appropriate range of imposed frequencies and amplitudes (Koopmann, 1967; Griffin and Ramberg, 1974, 1976; Ongoren and Rockwell, 1988a,b; Nuzzi et al., 1992). Two recent experimental studies (Tokomaru and Dimotakis, 1991; Filler et al., 1991) have shown that rotational oscillations of a circular cylinder cause lock-on and result in marked changes in the geometry of the near-wake flow.

Vortex resonance or lock-on is observed experimentally when

the incident mean flow has a sufficiently large periodic component superimposed upon it (Barbi et al., 1986; Armstrong et al., 1986, 1987). The cylinder remains stationary in the flow, but the vortex lock-on or resonance produced by the inflow perturbation modifies the character of the near-wake flow. This is equivalent to the in-line oscillations when the acoustic wavelength is long compared to the cylinder diameter.

The introduction of an appropriate sound field also can cause lock-on to occur (Blevins, 1985). And control of the vortex formation and shedding by periodic mass injection into the cylinder's boundary layer prior to separation has been demonstrated by Williams et al. (1992). All of these external disturbances are potential means for active control of the bluff body near-wake flow (Oertel, 1990; Rockwell, 1990).

Vortex lock-on and resonance phenomena have numerous practical engineering applications in addition to their importance in a fundamental physical sense. Applications abound in offshore exploration and drilling, Naval and marine hydrodynamics, and underwater acoustics. Other areas of engineering practice where these phenomena play important roles are civil and wind engineering, nuclear and conventional power generation, and electric power transmission.

The main topic of this paper is a particular case of vortex shedding resonance and lock-on in the near-wakes of bluff bodies. Vortex shedding in an incident flow with a periodic component superimposed on the basic mean flow is computed here to high resolution using the spectral element method. This is an interesting bluff body flow which has not been studied either computationally or experimentally in detail up to this time.

## Flow Perturbation and In-Line Oscillation Experiments

The experiments of Armstrong et al. (1986, 1987) and of

Contributed by the Fluids Engineering Division for publication in the JOURNAL OF FLUIDS ENGINEERING. Manuscript received by the Fluids Engineering Division January 17, 1992; revised manuscript received November 4, 1992. Associate Technical Editor: F. T. Dodge.

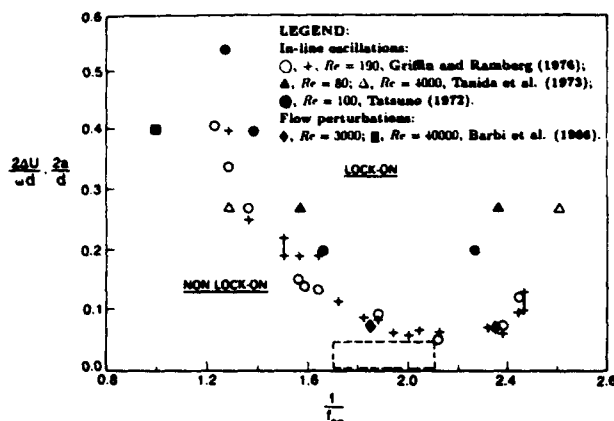


Fig. 1 Limits of the lock-on regime as a function of amplitude and frequency for in-line oscillations and inflow perturbations; from Griffin and Hall (1991)

Barbi et al. (1986) were conducted to examine vortex lock-on for a cylinder in a stream consisting of a steady uniform flow with a superimposed periodic component. The results of both studies show some very basic similarities with the earlier experiments of Griffin and Ramberg (1976), which are conducted to examine vortex shedding lock-on for a cylinder oscillating in-line with an incident flow. More recent experiments with in-line oscillations have been conducted by Ongoren and Rockwell (1988a,b).

The vortex lock-on measurements by Barbi et al. are compared with those of Griffin and Ramberg in Fig. 1. The vertical axis represents two different measures of the perturbation amplitude. For the experiments of Griffin and Ramberg the peak-to-peak amplitude of cylinder displacement is given by  $2a/d$ . And for the experiments of Barbi et al. the normalized "peak-to-peak" incident velocity perturbation is given by  $2\Delta U/\omega d$ . The horizontal axis is the ratio of the vibration frequency  $f$  and the Strouhal frequency  $f_{s0}$  of a stationary cylinder. The two types of external disturbance are essentially identical for the case shown. Also shown are the cylinder vibration results of Tanida et al. (1973) and of Tatsuno (1972), reproduced from the paper by Griffin and Ramberg. The dashed lines enclose the results of Armstrong et al. (1986, 1987). Vortex lock-on and cross-flow oscillations usually occur near the Strouhal shedding frequency  $f_{s0}$ . For in-line oscillations and flow perturbations the lock-on is caused by frequencies near twice the Strouhal frequency,  $2f_{s0}$ , since the forcing fluctuations in the drag force are in the flow direction. However, in many cases the actual lock-on frequency is near the Strouhal frequency, or half the oscillation or perturbation frequency.

There is generally good agreement between the bounds of the lock-on regime for the two different types of external disturbance or flow control, though there is some scatter at the highest amplitudes. This is most likely due to Reynolds number effects, as noted by Barbi et al. The latter experiments were conducted at  $Re$  between 3000 and 40,000, whereas the results of Tanida et al., Tatsuno, and of Griffin and Ramberg were conducted at  $Re$  between 80 and 4000. The overall agreement is good.

The base pressure coefficient  $C_{pb}$  is influenced by the flow perturbations in much the same manner as in the case of cylinder oscillations. For the stationary cylinder the base pressure coefficient is near  $C_{pb} = -1.44$ ; this value, though somewhat low for a circular cylinder, is in reasonable agreement with the results of West and Apelt (1982) for a comparable wind tunnel blockage ratio of nine percent. At the largest flow perturbation, the base pressure was decreased to  $C_{pb} = -1.85$  at the point of maximum resonance, a reduced velocity of  $U/f_{s0}d = 2.5$  (or

half the Strouhal value). The measured vortex formation region length  $l_f$  was reduced by this level of perturbation to  $0.9d$  from  $1.2d$ , the value measured for the unperturbed flow (Armstrong et al., 1987). The mean drag coefficient  $C_D$  increased from 1.28 to 1.52 for the perturbed flow as compared to the unperturbed flow.

### The Numerical Method

Recent advances in computational fluid dynamics permit new approaches to examining the effects of inflow perturbations and cylinder oscillations on the bluff body near-wake. One of these methods, which we employ herein, consists of superimposing an oscillatory component on the inflow boundary condition for a domain such as the spectral element grid (see Fig. 4). The computational results presented in this and the following section were obtained by means of direct numerical simulation of two-dimensional flow past a circular cylinder at sub-critical Reynolds numbers. The equations solved are the incompressible Navier-Stokes equation

$$\partial_t v + (v \cdot \nabla) v = -\nabla p/\rho + \nu \nabla^2 v$$

together with the continuity equation

$$\nabla \cdot v = 0$$

A no-slip boundary condition is imposed on the surface of the cylinder, a Neumann boundary condition is used at the outflow, and periodic boundary conditions are imposed in the longitudinal or downstream direction at the cross-stream boundaries of the domain. At the inflow, a uniform stream with a superimposed time-periodic small amplitude perturbation is used in most of the cases presented in the section on computational results. In the first case discussed, that of natural or unforced vortex shedding, the inflow consists solely of a uniform stream.

The computer code employed here is a variation of the spectral element formulation used by Karniadakis and Triantafyllou (1989, 1992). Modifications of the code performed at NRL have not altered the basic spectral-element methodology, which is described in some detail in the above-mentioned references. However, numerous variations have been made in the computational grid and in the computed flow quantities over the grid in order to examine the details of the flow history and development, the velocity spectra, and the flow geometry of the near-wake of the cylinder. Briefly, a time-splitting algorithm is employed in the usual way, with the nonlinear term being solved first using a third-order explicit Adams-Basforth scheme with a Courant stability condition. Incompressibility is enforced when the pressure term is solved in the second step, and boundary conditions are imposed in the third step, when the new velocity is found by implicit solution of the viscous term. In the second and third steps, intermediate values obtained from the previous steps are used as the "old" values. Although it is not possible to say formally what the resulting overall order of the splitting scheme is, the lowest order step is the third, implicit backward Euler step, which is order  $O(\Delta t)$ .

The spatial resolution of the computed flow can be affected in two ways: by choice of the size and number of elements and by choice of the order of Lagrangian interpolating polynomials used within the elements. In the present work, the fifty-six element grid was essentially the same as that shown in Karniadakis and Triantafyllou (1989), and can be seen in Fig. 4. Within each two-dimensional element sixth-order interpolating polynomials were used in both the streamwise and cross-stream directions, for a total of  $7 \times 7$  or 49 Gauss-Lobatto collocation points within each element. This resulted in very fine resolution in that portion of the domain surrounding the cylinder, and a more coarse resolution in the far wake. Clustering of the collocation points near the element boundaries resulted in smooth solutions across these boundaries.

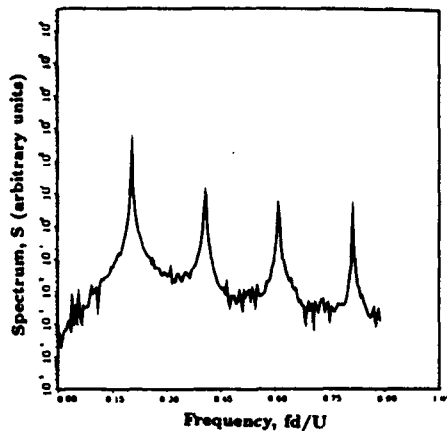


Fig. 2 (a) The spectrum corresponding to the  $x$ -component of the velocity  $U_x$  at the history point located at  $(x,y) = (2,2)$ . This is the natural shedding case (no perturbation) at  $Re = 200$ .

As with all spectral methods, a weighted residual technique is used to generate the discrete equations, and the system of discrete equations then is solved using a conjugate-gradient algorithm. A benchmark case demonstrates the ability of the code to accurately predict the important flow parameters involved in the simulation of vortex shedding from bluff bodies, using the shedding frequency and the vortex street wavelength as diagnostics. For this we chose natural or unforced shedding at Reynolds number  $Re = 100$  based on cylinder diameter, since this case was also studied by Karniadakis and Triantafyllou (1989) and extensive results are available in their paper. Our predicted natural shedding frequency of  $St = 0.176$  differs from the value of 0.179 predicted by Karniadakis and Triantafyllou (1989) by only 1.67 percent, which is insignificant owing to the fact that the  $St = 0.179$  value overestimates recent experimentally determined values, e.g., Williamson (1989), by approximately eight percent.

No asymmetry is needed in the initial or boundary conditions in order to initiate the asymmetric vortex shedding in this simulation of natural shedding, as well as all of the Reynolds number  $Re = 200$  simulations discussed in the next section. Rather, asymmetries due to computer truncation are sufficient to cause the vortex shedding to develop naturally as it does in any laboratory flow due to the presence of infinitesimal ambient disturbances. The asymmetry is not due to any numerical instability, but rather to the highly unstable nature of the symmetric flow that is realized briefly early-on in the computations. We refer to this early symmetric solution as the quasi-steady state of the flow.

### Computation of the Flow

The first case for which we present numerical results is natural or unforced vortex shedding at a Reynolds number of 200. For this condition the inflow boundary condition at the left of the domain is a uniform flow, and the near-wake and vortex shedding patterns develop without forcing. We include this case for comparison with the perturbed flow results.

The spectrum corresponding to the  $x$ -component of the velocity  $U_x$  at a point  $(x,y) = (2,2)$  is shown in Fig. 2, where the units are scaled by the cylinder diameter. The highest peak in the spectrum is located at the natural shedding frequency  $f_{s0}$  corresponding to  $St = 0.195$ , and other peaks can be seen at higher harmonics of this shedding frequency. Approximately 2000 time intervals were used to produce this spectrum and all of the computed spectra discussed in this paper. Each time interval represents ten time steps in the calculation, and 2000 time intervals correspond to approximately thirty shedding cycles.

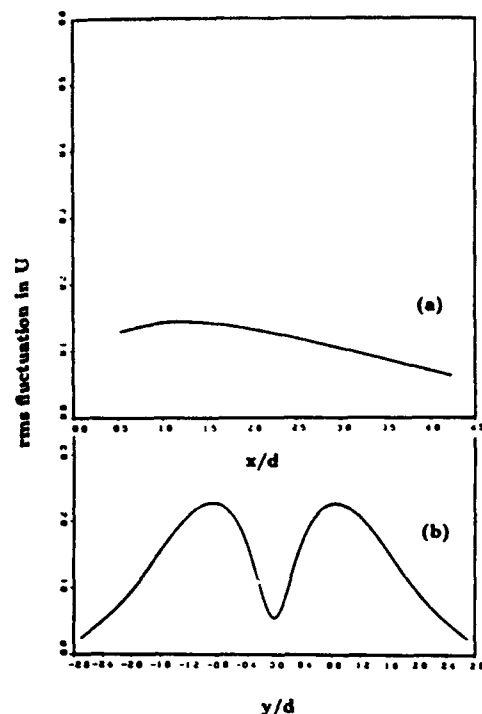
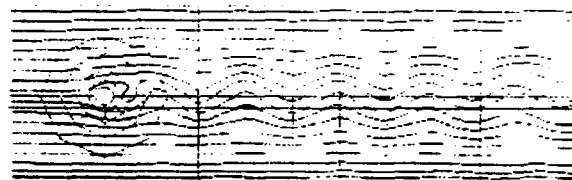


Fig. 3 (a) The rms fluctuation in the  $x$ -component of the velocity  $U_x$  along the wake centerline and (b) the rms fluctuation across the wake at  $x = 5$  diameters downstream



Natural shedding;  $Re = 200$

Fig. 4 Instantaneous streamlines for natural shedding at  $Re = 200$ . The spectral element grid employed in the computations is shown superimposed on the spectrum.

The cylinder base-region flow in the vortex formation region is important to the development of the near-wake flow (Bearman, 1965; Gerrard, 1966), and to the ensuing physical evolution of the wake. One measure of the downstream extent of the formation region is the maximum in the fluctuating velocity which occurs just downstream of the cylinder on the wake centerline. The formation region length also can be measured in terms of the minimum of the local pressure coefficient  $C_p$  on the wake centerline (Roshko, 1954, 1955). The fluctuation  $u_{rms}$  of the  $x$ -component of velocity on the wake centerline is plotted in Fig. 3 as a function of distance downstream from the cylinder, as measured in multiples of the cylinder diameter. The computed peak in  $u_{rms}$  is located at about 1.25 cylinder diameters downstream, which is comparable with measurements from laboratory experiments which have been reported in the literature (Bloor and Gerrard, 1966; Griffin, 1971).

A cross-wake distribution of the velocity fluctuation  $u_{rms}$  at  $x = 5d$  is plotted in Fig. 3(b). The same quantity at  $x = 3d$  is shown in Fig. 9(a) where it is superimposed on a perturbed flow case. The corresponding mean velocities are shown in Fig. 8. The deficit in the mean velocity is apparent as well as

the approach to the free stream condition as the distance from the centerline is increased. The peaks in the rms velocity at the two downstream locations also show the usual concentrated off-wake effects of the passing vortex pairs. The computed fluctuations in the wake are slightly less than comparable wind tunnel measurements near this Reynolds number (Griffin and

Ramberg, 1974), probably owing to differences between the two-dimensional computations and the three-dimensional experiments.

The final result for the natural shedding case is the instantaneous streamline pattern shown in Fig. 4. Here the streamlines are spaced evenly across the computational domain at the inflow, and the spreading of the streamlines in the near wake gives some evidence of the deficit in the mean flow in the cross-wake direction, as was shown in Fig. 3(b). The wavelength of the vortex street for this unforced flow is  $\lambda = 5d$ , which is typical of the results shown in Fig. 12.

Next a perturbed boundary condition of the form

$$U_x = 1.0 + \Delta u \sin \omega t, \\ U_y = 0.$$

was enforced at the inflow, where  $U_x$  and  $U_y$  denote the  $x$ - and  $y$ -components of the velocity, respectively. Here  $\Delta u = \alpha \omega$ , where  $\omega = 2\pi f$ , and the perturbation frequency  $f = 2\alpha f_{so}$ . The parameter  $\alpha$  varied from 0.05 to 0.25, while  $\omega$  was varied to give values of the perturbation frequency ranging from  $1.4f_{so}$  to  $2.8f_{so}$  (Fig. 5). Each closed circle or cross in this figure represents a direct numerical simulation. Those that represent lock-on behavior are indicated by the closed circles.

The shaded regions in Fig. 5 indicate regions across which breakdown occurs, from a periodic, locked-on flow to a non-periodic or quasi-periodic flow in which the primary frequency is the natural shedding frequency rather than the perturbation frequency. We have not attempted to define precisely the width of this region, but only to bracket it. As will be shown in the

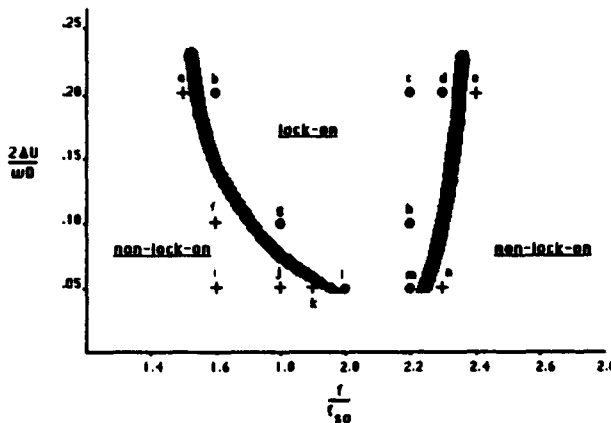


Fig. 5 Limits of the lock-on regime for perturbed flow at  $Re = 200$ . Each closed circle or cross represents a numerical simulation. Those simulations in which lock-on occurred are indicated by closed circles. The shaded region forms the approximate boundary between the lock-on and non-lock-on regimes.

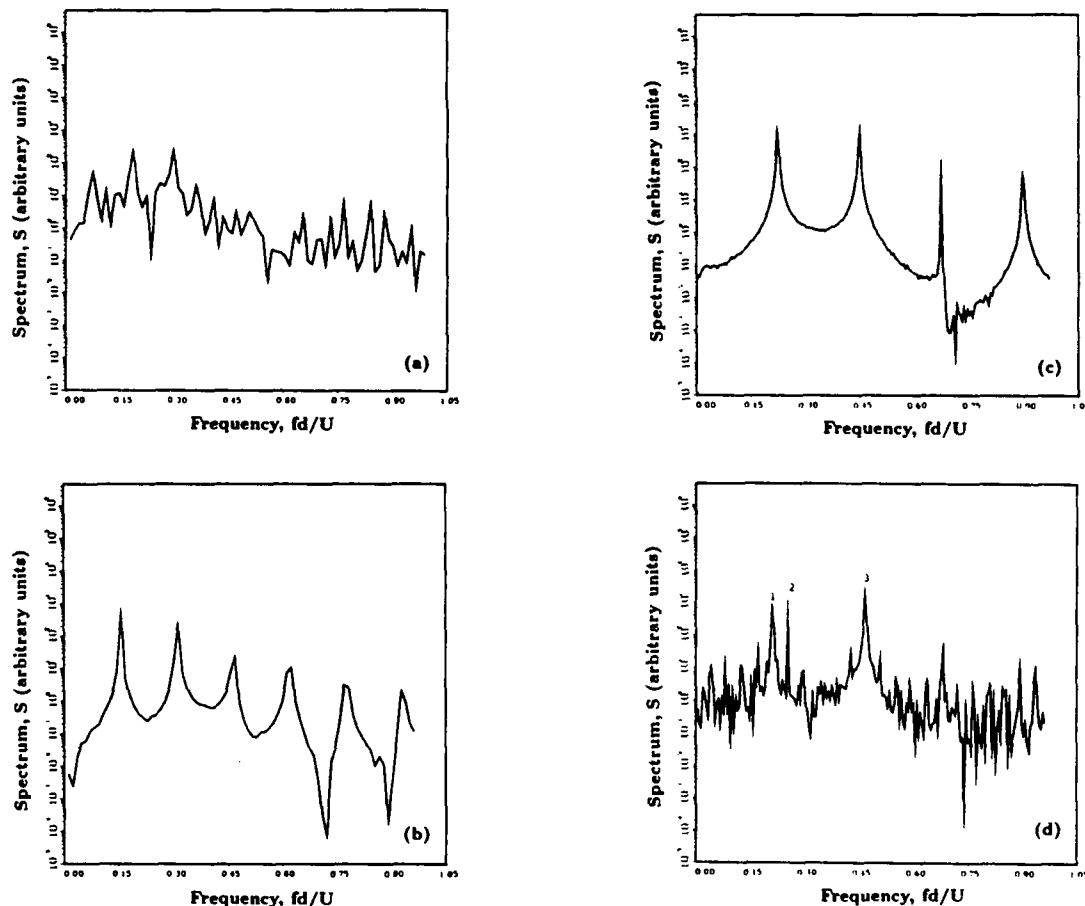


Fig. 6 The spectrum of the  $x$ -component of the velocity  $U$ , at the history point located at  $(x, y) = (2, 2)$ ; (a) case a in Fig. 5, (b) case b, (c) case d, and (d) case e

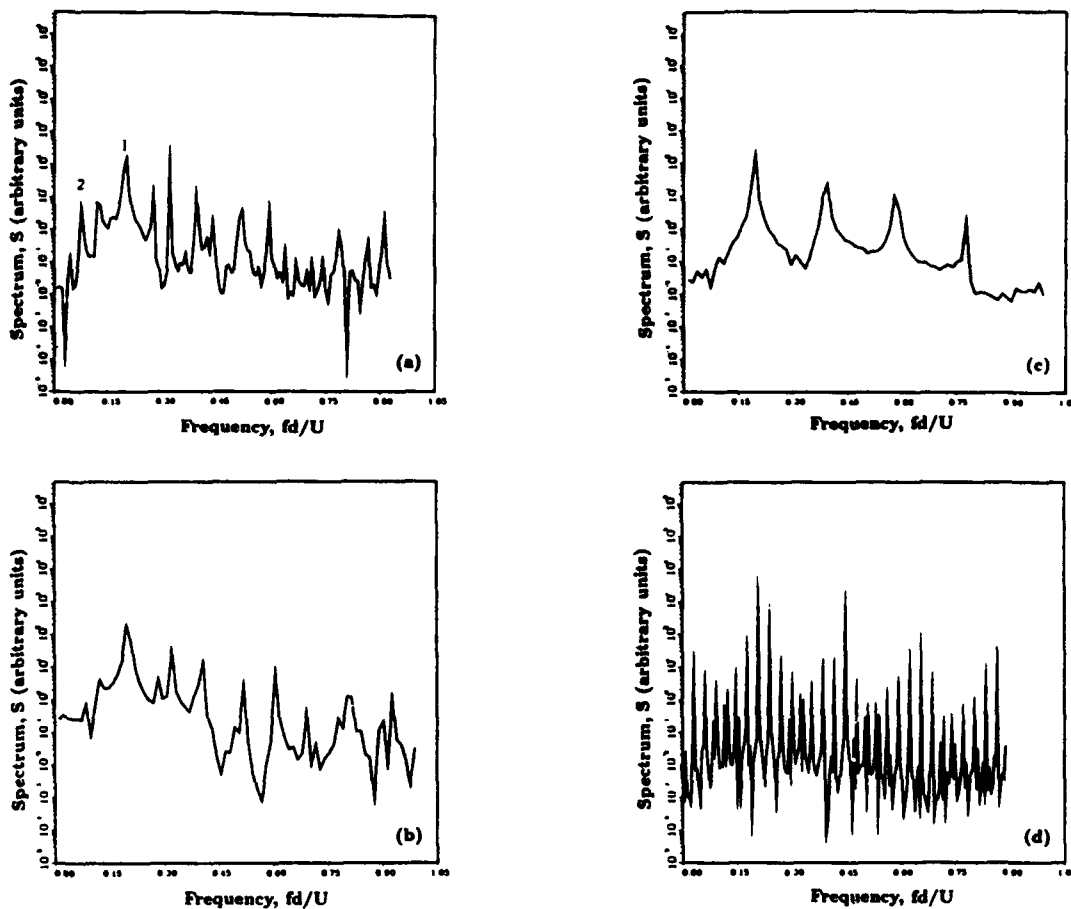


Fig. 7 The spectrum corresponding to  $U$ , at  $(x,y) = (2,2)$ ; (a) case  $f$  in Fig. 5, (b) case  $i$ , (c) case  $l$ , and (d) case  $n$

following, in all of the cases lying outside of the lock-on region, the flow continues to be strongly influenced by the perturbation, as evidenced by the chaotic nature of the flow in contrast with the regular, periodic natural shedding case. However, we have chosen to define non-lock-on cases as those for which the highest peak in the spectrum occurs at the natural shedding frequency or at a frequency corresponding to neither the perturbation nor the natural shedding frequency.

We first examine cases  $a$ ,  $b$ ,  $d$ , and  $e$  in Fig. 5. For these four cases, the amplitude of the perturbation is held fixed while the frequency is increased from  $1.5f_{so}$  (case  $a$ ) to  $2.4f_{so}$  (case  $e$ ). A forcing frequency of  $1.5f_{so}$  results in a nonperiodic velocity history with the spectrum in Fig. 6(a), which shows clearly the chaotic nature of the flow. The highest peak in the spectrum occurs just below the natural shedding frequency of  $St = 0.195$ . Increasing the forcing frequency from  $1.5f_{so}$  to  $1.6f_{so}$  results in case  $b$  in Fig. 5. The flow is periodic, with shedding frequency equal to  $0.8f_{so}$ , and thus lock-on has occurred. The flow pattern is more complex than that of the unperturbed case, and we see from the spectrum in Fig. 6(b) that there is now significantly more energy in the higher harmonics of the perturbation frequency than occurred in higher harmonics of  $f_{so}$ . The wavelength of the vortex pattern is  $\lambda = 5.7d$ , an increase of fourteen percent from the unforced value of  $\lambda = 5d$ .

Moving farther to the right in Fig. 5, we again increase the perturbation frequency to  $2.3f_{so}$  for case  $d$ . Lock-on again takes place, this time at a frequency of  $1.15f_{so}$ . The spectrum corresponding to this case is shown in Fig. 6(c).

The results from case  $e$  demonstrate that we have crossed over the shaded region and are once again outside of the lock-

on region. The dominant peak in the spectrum (Fig. 6(d)) occurs at neither the natural shedding frequency nor the perturbation frequency. The three highest peaks in the spectrum are labeled. Peak number 1 occurs just above the natural shedding frequency at approximately  $St = 0.2$ , peak number 2 occurs at half the perturbation frequency or  $St = 0.23$ , and peak number 3 occurs at the sum of these, or  $St = 0.43$ . Thus peak 3, the highest, is a higher harmonic of neither the natural shedding frequency nor the perturbation frequency, but of the average of the two. This case is indicative of a wider transitional region than we have shown in Fig. 5, in which the dominant frequency in the flow is neither the perturbation nor the natural frequency. Indeed, the presence of two nearby peaks in the spectrum suggests intermittency in the shedding frequency.

We next examine case  $f$  in Fig. 5, which lies just to the left of the lock-on region. Here the frequency of the perturbation is the same as in case  $b$ , but the amplitude has been decreased from 0.2 to 0.1 nondimensional units. Referring to the spectrum for case  $b$  in Fig. 6(b), we see the dramatic change brought about in the flow due to this change in amplitude. The peak in the spectrum for case  $f$ , labeled number 1 on Fig. 7(a), is at the natural shedding frequency of  $St = 0.195$ . The peak labeled number 2 occurs at half of the perturbation frequency, or approximately  $St = 0.078$ . When the amplitude of the perturbation is reduced further to 0.05 in case  $i$ , the spectrum in Fig. 7(b) shows that now the natural shedding frequency is clearly dominant, and thus this condition is farther outside the lock-on region than the previous result.

At this value of perturbation amplitude, we now examine the effects of increasing the perturbation frequency by pre-

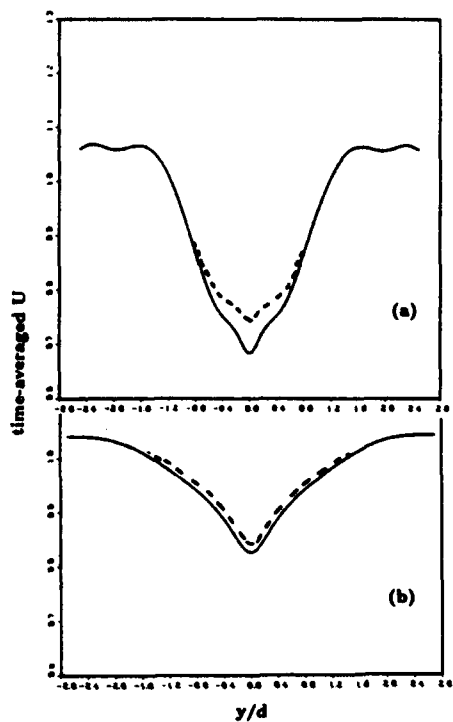


Fig. 8 The cross-stream distribution of mean velocity  $U_x(y)$  at (a)  $x = 3d$  and (b)  $x = 5d$  downstream from the cylinder, case g. The results for the natural shedding case (dashed lines) are superimposed.

senting results for cases *l* and *n*. A dramatic change occurs as the perturbation frequency is increased to  $2.0f_{so}$  (case *l*). While the resulting flow resembles the natural shedding case, the frequency of the oscillation is lower than the natural shedding frequency obtained in the unforced case by approximately five percent (Fig. 7(c)), and higher harmonics correspond to multiples of this latter value. The reason for this discrepancy has not yet been determined conclusively; our original estimate of the natural shedding frequency at Reynolds number 200 was approximately five percent lower than that of Karniadakis and Triantafyllou (1989), while their estimate was judged to overestimate the experimentally determined value by approximately eight percent. Thus the present computed result is within an acceptable range.

A change again occurs as we increase the perturbation frequency to  $2.3f_{so}$  for the final case *n*. The flow pattern again becomes complex as shown by the spectrum in Fig. 7(d), with the first dominant peak occurring at the natural shedding frequency of  $St = 0.195$ . A second peak of nearly equal height occurs at a frequency equal to approximately  $St = 0.45$ , or twice the perturbation frequency. Thus again we see the perturbation frequency having a greater effect on the higher harmonics of the flow.

For a more complete analysis of the near-wake flow in a lock-on condition, we further examine case *g*. As in the natural shedding case, we first measured the drop in the time-averaged  $x$ -component of the velocity across the wake at two different downstream locations. Time averaging again was done over approximately thirty shedding cycles. We see from Fig. 8(a), which shows computed velocities three diameters downstream from the cylinder, that the drop in mean velocity across the wake is approximately 35 percent. Comparing this with an approximately 30 percent drop in the natural shedding case (superimposed), indicates that the effect of the perturbation is to slightly decrease the mean flow along the centerline. However, the rms fluctuation corresponding to this mean flow is greater than that seen in the natural shedding case, with a

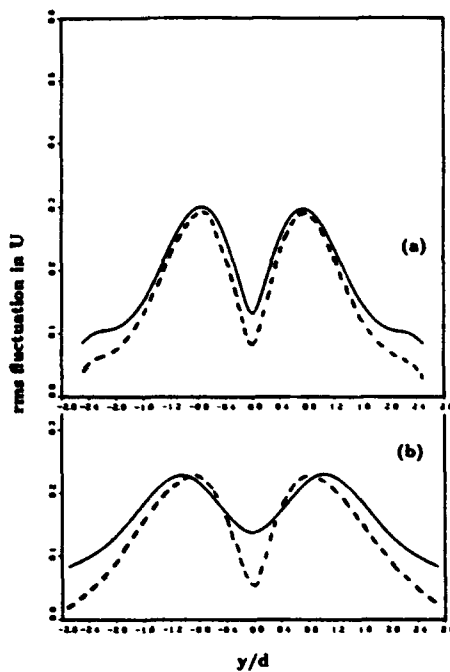


Fig. 9 The cross-stream distribution of rms velocity fluctuations corresponding to the mean velocities for case *g* in Fig. 8. The results for the natural shedding case (dashed lines) are superimposed.

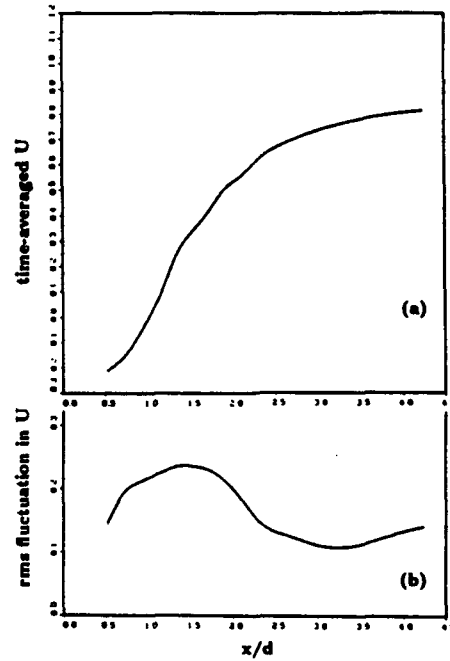


Fig. 10 The (a) mean flow and (b) rms fluctuation in the velocity along the wake centerline, for case *g*

proportionately greater fluctuation along the centerline. In the natural shedding case there was a nearly 70 percent drop in the rms fluctuation across the wake three diameters downstream from the cylinder. By comparison, the rms fluctuation in the perturbed flow exhibits an approximately 57 percent drop across the wake (Fig. 9(a)). Farther downstream at  $x = 5d$  the time-averaged flows of the natural shedding perturbed cases are nearly identical (Fig. 8(b)). At this same downstream lo-

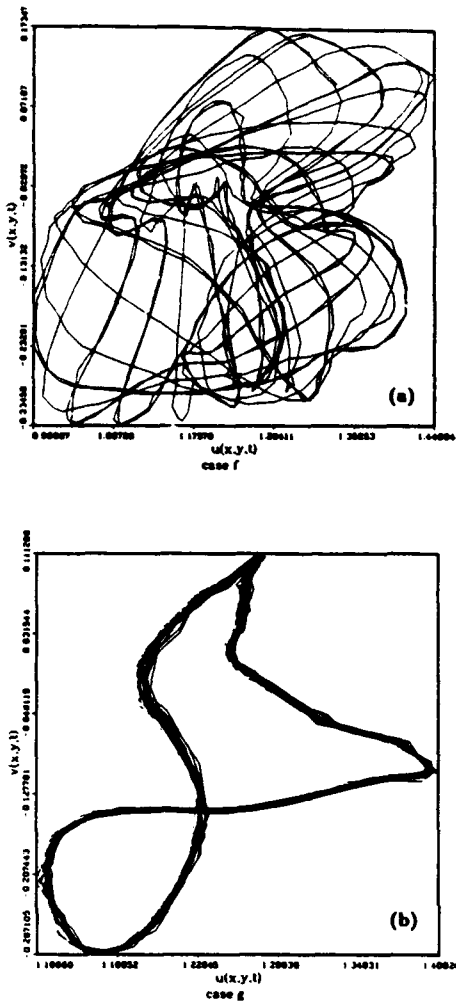


Fig. 11 Phase plane plots of  $U_x$  versus  $U_y$  for (a) case  $f$ , and (b) case  $g$

cation, the maximum rms fluctuation of the perturbed flow has decayed approximately to that of the natural shedding case, but the fluctuation remains greater at the wake edges and along the wake centerline (Fig. 9(b)). The corresponding  $u_{rms}$  for the natural shedding case is shown in Fig. 3(b).

The mean flow and the rms fluctuation in the velocity along the centerline behind the cylinder are shown in Fig. 10. Comparing the rms fluctuation with the natural shedding case (Fig. 3(a)) we see that the peak of the fluctuation, which marks the end of the vortex formation region, has moved from its natural shedding position approximately one diameter downstream from the cylinder to a point approximately one and a half diameters downstream. This is an expansion of the vortex formation region with perturbation frequency when  $f < 2f_{so}$ . Comparably, the downstream extent of the formation region is contracted when  $f > 2f_{so}$ . Both of these modifications in the shedding are analogous to those observed when a circular cylinder undergoes both in-line and crossflow oscillations under lock-on conditions (Griffin and Ramberg, 1974, 1976; Ongoren and Rockwell, 1988a, b).

A zone of reversed mean flow is found adjacent to the cylinder as shown in Fig. 10, followed by a stagnation point ( $\bar{U} = 0$ ) and the transition to positive mean flow at approximately one diameter downstream. The extent of the reversed flow region is controlled by the perturbations in much the same way as the overall formation region.

The  $U_x$  versus  $U_y$  phase plane plots for cases  $f$  and  $g$  are

Table 1 Longitudinal vortex spacing or wavelength in the near-wake of a circular cylinder vibrating in-line with an incident uniform flow; adapted from Griffin and Ramberg (1976)

Vibration frequency, $f$ (Hz)	Frequency ratio, $f/f_{so}$	Vortex spacing, $\lambda/d$	Relative change, $\Delta\lambda/\lambda$	Vortex convection speed, $1/2\lambda/U$
Reynolds number = 190				
69.2	1.88	5.2	+ 0.07	0.94
73.6	2.00	4.9	0	0.93
75.6	2.06	4.7	- 0.05	0.91
78.9	2.14	4.7	- 0.04	0.96
80.4	2.18	4.4	- 0.09	0.92
Average = 0.93				

shown in Fig. 11. The history point in both cases is once again located in the separated flow just outside the wake at  $(x, y) = (2, 2)$ . These phase plane representations of the velocity demonstrate most graphically the periodic nature of the forced or lock-on state of the flow, as opposed to the chaotic state of the non-lock-on state.

## Discussion of Results

The longitudinal vortex spacing or wavelength is a valuable physical diagnostic for the state of the spatial structure and development of the fully-developed vortex street. Measurements of the spacing for a variety of in-line and cross-flow oscillations, and also for the unforced wakes of stationary cylinders have been reported by Griffin and Ramberg (1976). These can be compared to the direct numerical simulations of Karniadakis and Triantafyllou (1989) and our recent NRL simulations that are discussed here. The wavelength of the pattern can be employed as a measure of the spatial state of the flow, as compared to phase plane diagrams of the streamwise and cross stream velocities, which can be employed in a comparable way to assess the temporal state of the near-wake.

One example given by Karniadakis and Triantafyllou (1989) is that of a wake forced by a localized spatially and temporally varying disturbance in the vortex formation region, with normalized amplitude and frequency, respectively, of  $a = 0.10$  and  $f/f_{so} = 0.75$ . The center of the disturbance was located at  $x = 2$ ,  $y = 0$ , measured in multiples of the cylinder diameter. This is a unique form of control disturbance which had not been investigated previously. For the unforced wake  $\lambda = 5d$ , while for the forced wake  $\lambda = 7d$ , an increase of forty percent in the wavelength.

Comparable measurements were made at  $Re = 190$  by Griffin and Ramberg (1976) and the results are summarized in Table 1. The cylinder oscillations were in-line with the flow over a range of frequencies near twice the Strouhal frequency as in Fig. 1. The measured changes in the forced vortex spacing correspond directly with those achieved in the direct numerical simulations, since for  $f < 2f_{so}$  the wavelength increases while for  $f > 2f_{so}$  the wavelength decreases. Extrapolating the results in the table to the condition  $f = 1.6f_{so}$  in the present case and to  $f = 0.75f_{so}$  from Karniadakis and Triantafyllou using a least-squares fit given by Griffin and Ramberg, the vortex spacing is  $\lambda = 6.2d$ . This compares reasonably well with both computations. The measured vortex spacing for the stationary cylinder at  $Re = 190$  ( $\lambda = 4.9d$ ) is very nearly equal to the wavelength computed here at  $Re = 200$ , namely  $\lambda = 5d$ .

The computed vortex street wavelengths are compared further with measurements for both forced and unforced conditions for Reynolds numbers from 100 to 2000 in Fig. 12. The computations agree well overall with the experiments, which show only a very slight dependence on Reynolds number in this range. The vertical scale is a normalized form of the vortices' convection speed, or the downstream translational speed of the vortex cores. The constant phase or convection

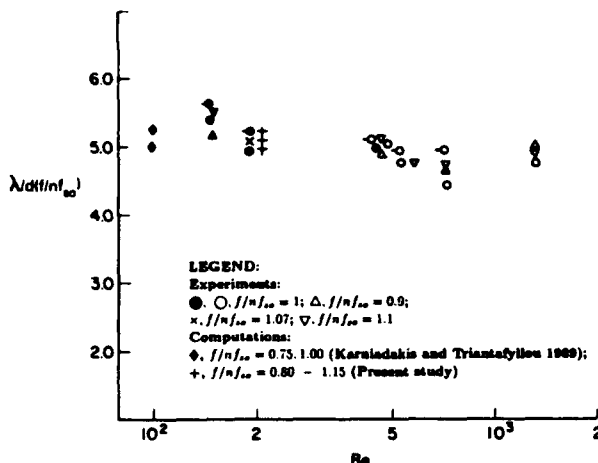


Fig. 12 Longitudinal vortex spacing  $\lambda/d (in f_0)$  as a function of Reynolds number  $Re$ . All of the measurements were made in the wakes of stationary and oscillating cylinders. The data points at  $Re = 100$  and  $200$  correspond to in-line oscillations and inflow perturbations (composite of six) with  $n = 2$ ; all other data correspond to cross-flow oscillations (experiments) and near-wake perturbations (computations) with  $n = 1$ .

speed is representative of a nondispersive physical system, as compared to the many dispersive, complex physical systems which occur in nature, e.g. surface water waves and mixing layers under certain conditions, where the phase speed depends on the wavelength or wavenumber and the frequency.

Several measurements of the pattern's convection speed also are given in the table. Though there is some scatter, the average value is  $U_* = 0.93U$ . Tokumaru and Dimotakis (1991) also found that the convection speed remained nearly constant at a similar value in a lock-on state produced by rotational oscillations at a Reynolds number of 15,000, even as both the imposed frequency of the oscillations varied over a three-fold range and the street wavelength underwent similarly marked changes. This gives some additional evidence that both forced and unforced or natural periodic vortex wakes have the same basic nondispersive character over a wide range of externally imposed disturbances.

These modifications of the near-wake flow are achieved by the imposition of relatively small inflow perturbations. Thus, seemingly small perturbations of the wake flow are capable of producing large changes in vortex strength and shed vorticity, base pressure and drag on a bluff circular cylinder or body of other cross-section. Modification and control of the basic formation or instability mechanisms of the wake can lead to substantial changes in the near-wake vortex pattern, and possibly even the middle- and far-wake flow as well as found by Cimbala et al. (1988), and by Browne et al. (1989).

### Summary and Concluding Remarks

Several issues pertaining to bluff body near-wake flow control and modification have been investigated for a bluff body in a flow consisting of a basic mean flow with a superimposed periodic component. Direct numerical simulations of perturbed flow about a circular cylinder are in good agreement with experimental results, particularly in reproducing the vortex shedding resonance or lock-on regime boundaries at  $Re = 200$ . The lock-on regime defines the frequency range over which perturbations in the incident flow cause vortices to be shed at the forcing frequency rather than at the natural shedding frequency. At an amplitude of  $2\Delta U/wd = 0.2$ , perturbation frequencies in the range  $1.6f_0$  to  $2.3f_0$  result in lock-on, and the extent of this frequency range decreases with decreasing perturbation amplitude. The change in the lock-on boundary

was more rapid at frequencies less than  $2f_0$ , which is in qualitative agreement with experiments from Fig. 1 and Koopmann (1967).

Computations of the near-wake flow show that in flow perturbations causing lock-on can control the location and extent of the vortex formation region and the level of velocity fluctuation both along and across the wake. Some typical results at  $f < f_0$  show a shift downstream of the vortex formation region, as identified by the peak rms velocity fluctuation along the wake centerline, and an increased fluctuation level along the centerline that extends to at least five cylinder diameters downstream. These modifications to the near-wake flow are indicative of selectively increased vortex strength and shed vorticity in the near-wake as a result of the locking-on.

The computed values of the vortex wavelength  $\lambda$  in the perturbed flow are in good agreement with measurements in both unforced, or natural, and forced wakes for Reynolds numbers between 100 and 2000. The predominant vortex street frequency and wavelength adjust in such a way that a constant phase or convection speed of the pattern is achieved over a wide range of conditions which cause lock-on. Recent active control experiments with rotational oscillations of a circular cylinder at a Reynolds number of 15,000 show that the wake adjusts in the same way over a three-fold range of imposed frequencies. The essentially constant vortex phase or convection speed is indicative of the basic nondispersive physical character of forced and unforced, or natural, bluff body near-wakes.

### Acknowledgments

This work was conducted as part of a research program in fluid dynamics and bluff body flows supported by the Naval Research Laboratory and the Office of Naval Research. We are grateful to Dr. George Karniadakis of Princeton University for numerous helpful discussions on both the spectral element method and the computations reported here.

### References

- Armstrong, B. J., Barnes, F. H., and Grant, I., 1986, "The Effect of a Perturbation on the Flow Over a Cylinder," *Physics of Fluids*, Vol. 29, pp. 2095-2102.
- Armstrong, B. J., Barnes, F. H., and Grant, I., 1987, "A Comparison of the Structure of the Wake Behind a Circular Cylinder in a Steady Flow With That in a Perturbed Flow," *Physics of Fluids*, Vol. 30, pp. 19-26.
- Barbi, C., Favier, D. P., Maresca, C. A., and Telionis, D. P., 1986, "Vortex Shedding and Lock-on of a Circular Cylinder in Oscillatory Flow," *Journal of Fluid Mechanics*, Vol. 170, pp. 527-544.
- Bearman, P. W., 1963, "Investigation of the Flow Behind a Two Dimensional Model with a Blunt Trailing Edge and Fitted with Splitter Plates," *Journal of Fluid Mechanics*, Vol. 21, pp. 241-255.
- Bearman, P. W., 1967, "On Vortex Street Wakes," *Journal of Fluid Mechanics*, Vol. 28, pp. 625-641.
- Bearman, P. W., 1984, "Vortex Shedding from Oscillating Bluff Bodies," *Annual Review of Fluid Mechanics*, Vol. 16, pp. 195-222.
- Blevins, R. D., 1985, "The Effect of Sound on Vortex Shedding from Cylinders," *Journal of Fluid Mechanics*, Vol. 161, pp. 217-237.
- Bloor, M. S., and Gerrard, J. H., 1966, "Measurements of Turbulent Vortices in a Cylinder Wake," *Proceedings of the Royal Society of London, Series A*, Vol. 294, pp. 319-342.
- Browne, L. W. B., Antonia, R. A., and Shah, D. A., 1989, "On the Origin of the Organized Motion in the Turbulent Far-Wake of a Cylinder," *Experiments in Fluids*, Vol. 7, pp. 475-480.
- Cimbala, J. M., Nagib, H. M., and Roshko, A., 1988, "Large Structure in the Far Wakes of Two-Dimensional Bluff Bodies," *Journal of Fluid Mechanics*, Vol. 190, pp. 265-298.
- Filler, J. R., Marston, P. L., and Mih, W. C., 1991, "Response of the Shear Layers Separating from a Circular Cylinder to Small Amplitude Rotational Oscillations," *Journal of Fluid Mechanics*, Vol. 231, pp. 461-489.
- Gerrard, J. H., 1966, "The Mechanics of the Formation Region of Vortices Behind Bluff Bodies," *Journal of Fluid Mechanics*, Vol. 25, pp. 401-413.
- Griffin, O. M., 1971, "The Unsteady Wake of an Oscillating Cylinder at Low Reynolds Number," *ASME Journal of Applied Mechanics*, Vol. 38, pp. 729-738.
- Griffin, O. M., and Ramberg, S. E., 1974, "The Vortex Street Wakes of Vibrating Cylinders," *Journal of Fluid Mechanics*, Vol. 66, pp. 553-576.
- Griffin, O. M., and Ramberg, S. E., 1976, "Vortex Shedding from a Cylinder

Vibrating in Line with an Incident Uniform Flow," *Journal of Fluid Mechanics*, Vol. 73, pp. 257-271.

Griffin, O. M., and Hall, M. S., 1991, "Vortex Shedding Lock-On and Flow Control in Bluff Body Wakes," *ASME JOURNAL OF FLUID ENGINEERING*, Vol. 113, pp. 526-537.

Grinstein, F. F., Boris, J. P., and Griffin, O. M., 1991, "A Numerical Study of Passive Pressure-Drag Control in a Plane Vortex Street Wake," *AIAA Journal*, Vol. 29, pp. 1436-1442.

Karniadakis, G. E., and Triantafyllou, G. S., 1989, "Frequency Selection and Asymptotic States in Laminar Wakes," *Journal of Fluid Mechanics*, Vol. 199, pp. 441-469.

Karniadakis, G. E., and Triantafyllou, G. S., 1992, "Three Dimensional Dynamics and Transition to Turbulence in the Wake of Bluff Objects," *Journal of Fluid Mechanics*, Vol. 238, pp. 1-30.

Koopmann, G. H., 1967, "The Vortex Wakes of Vibrating Cylinders at Low Reynolds Numbers," *Journal of Fluid Mechanics*, Vol. 28, pp. 501-512.

Nuzzi, F., Magness, C., and Rockwell, D., 1992, "Three-Dimensional Vortex Formation from an Oscillating, Non-Uniform Cylinder," *Journal of Fluid Mechanics*, Vol. 238, pp. 31-54.

Oertel, H., 1990, "Wakes Behind Blunt Bodies," *Annual Review of Fluid Mechanics*, Vol. 22, pp. 539-564.

Ongoren, A., and Rockwell, D., 1988a, "Flow Structure from an Oscillating Cylinder. Part I: Mechanisms of Phase Shift and Recovery in the Near Wake," *Journal of Fluid Mechanics*, Vol. 191, pp. 197-223.

Ongoren, A., and Rockwell, D., 1988b, "Flow Structure from an Oscillating Cylinder. Part II: Mode Competition in the Near Wake," *Journal of Fluid Mechanics*, Vol. 191, pp. 225-245.

Rockwell, D., 1990, "Active Control of Globally-Unstable Separated Flows," *ASME International Symposium on Nonsteady Fluid Dynamics (Proceedings)*, FED-Vol. 92, pp. 379-394.

Roshko, A., 1954, "On the Drag and Shedding Frequency of Two-Dimensional Bluff Bodies," *National Advisory Committee for Aeronautics, Washington, DC, Technical Note 3169*.

Roshko, A., 1955, "On the Wake and Drag of Bluff Bodies," *Journal of the Aeronautical Sciences*, Vol. 22, pp. 124-132.

Sarpkaya, T., 1979, "Vortex Induced Oscillations: A Selective Review," *ASME, Journal of Applied Mechanics*, Vol. 46, pp. 241-258.

Stansby, P. K., 1976, "Base Pressure of Oscillating Circular Cylinders," *Proceedings of ASCE, Journal of Engineering Mechanics*, Vol. 104, pp. 591-600.

Tanida, Y., Okajima, A., and Watanabe, Y., 1973, "Stability of a Circular Cylinder Oscillating in Uniform Flow or in a Wake," *Journal of Fluid Mechanics*, Vol. 61, pp. 769-784.

Tatsuno, M., 1972, "Vortex Streets Behind a Circular Cylinder Oscillating in the Direction of Flow," *Bulletin of the Research Institute for Applied Mechanics of Kyushu University*, Vol. 36, pp. 25-37.

Tokumaru, P. T., and Dimotakis, P. E., 1971, "Rotary Oscillation Control of a Cylinder Wake," *Journal of Fluid Mechanics*, Vol. 224, pp. 77-90.

West, G. S., and Apelt, C. J., 1982, "The Effects of Tunnel Blockage and Aspect Ratio on the Mean Flow Past a Circular Cylinder with Reynolds Numbers Between  $10^3$  and  $10^5$ ," *Journal of Fluid Mechanics*, Vol. 114, pp. 361-377.

Williams, D. R., Mansy, H., and Amato, C., 1992, "The Response and Symmetry Properties of a Cylinder Wake Subjected to Localized Surface Excitation," *Journal of Fluid Mechanics*, Vol. 234, pp. 71-96.

Williamson, C. H. K., and Roshko, A., 1988, "Vortex Formation in the Wake of an Oscillating Cylinder," *Journal of Fluids and Structures*, Vol. 2, pp. 355-381.

Williamson, C. H. K., 1989, "Defining a Universal and Continuous Strouhal-Reynolds Number Relationship for a Laminar Vortex Shedding of a Circular Cylinder," *Physics of Fluids*, Vol. 31, pp. 2742-2744.

## **Appendix E**

### **Interaction of Vorticity with a Free Surface in Turbulent Open Channel Flow**



**AIAA 91-0236**  
**Interaction of Vorticity**  
**with a Free Surface**  
**in Turbulent Open Channel Flow**

R.I. Leighton<sup>†</sup>, T.F. Swean, Jr., R.A. Handler,  
and J.D. Swearingen

Center for Advanced Space Sensing,  
Naval Research Laboratory,  
Washington, D.C.

<sup>†</sup>Science Applications International Corp.,  
McLean, Va.

**29th Aerospace Sciences Meeting**  
**January 7-10, 1991/Reno, Nevada**

# INTERACTION OF VORTICITY WITH A FREE SURFACE IN TURBULENT OPEN CHANNEL FLOW

R.I. Leighton\*, T.F. Swean, Jr.†, R.A. Handler,‡ J.D. Swearingen\*

Center For Advanced Space Sensing  
Naval Research Laboratory  
Washington, D.C. 20375-5000

## Abstract

The interaction between vorticity and a free surface, modeled as a shear free boundary is studied using a direct numerical simulation of an open channel flow at low Reynolds number ( $Re_{f_s} = U_{f_s}h/\nu = 2340$  where  $h$  is the channel depth and  $U_{f_s}$  is the mean free-surface velocity). As a result of the shear free nature of the top boundary, only normal vorticity may terminate on it. The vorticity components parallel to the top boundary must go to zero as the boundary is approached. The time averaged fluctuating enstrophy balance equations, which are an indicator of the level of activity of the vorticity field are evaluated. Near the free surface the rate of production and destruction of enstrophy is set by the stretching and rotation of fluctuating vorticity by the fluctuating velocity field. The transport of enstrophy by the fluctuating velocity has a minor role. Of the the production terms, the three involving the stretching of vorticity along its axis are the most important, and a simple model explaining this is presented.

$u_i^+ = u_i/u^*$	Non-dimensional velocity
$l_i^+ = l_i/l^*$	Non-dimensional length
$t^+ = t/t^*$	Non-dimensional time
$\langle a(x) \rangle = \sum_{\text{ensemble}} a(x)$	Averaging operator
$h = L_s$	Channel height
$L_{s_1}$	Streamwise box length
$L_{s_2}$	Transverse box length
$\nu$	Kinematic viscosity
$\rho$	density
$F_n = U_{f_s}/\sqrt{gh}$	Froude number
$Re = Uh/\nu$	Reynolds number
$Re^* = u^*h/\nu$	Wall Reynolds number
$Re_{f_s} = U_{f_s}h/\nu$	Free surface Reynolds no.

## 1. Introduction

The total instantaneous enstrophy of a fluid is defined as the square of the instantaneous vorticity,  $\sum_i \Omega_i \Omega_i$ . Enstrophy can be determined as well from the mean vorticity,  $\bar{\Omega}_i \Omega_i$ , and the fluctuating vorticity,  $\bar{\omega}_i \omega_i$ . This paper will be limited to an analysis of the fluctuating vorticity. The dominate motivation for studying the enstrophy balance equations is the natural interpretation of enstrophy as a measure of vortical activity. The no-slip boundary, where the majority of the fluctuating vorticity is produced is the source of the turbulent kinetic energy. Much of the turbulent kinetic energy is believed to be associated with coherent structures and a quasi-regular turbulent burst cycle. If it is assumed that coherent vorticity is an important feature of these structures, then enstrophy is a good tool for analysis. Although a clear connection between vorticity and coherent structures or events has yet to be developed, the concept of the vortex loop has often invoked to explain the visualization of the results of experiments or direct numerical simulations (DNS). The connection between vorticity and turbulent structures may be equally valid at the free-surface. As will be discussed below, the conditions at the free-surface require that vorticity tangential to the surface vanish as the surface is approached. Simultaneously, the surface-normal gradient of the component of vorticity perpendicular to the surface must vanish. These are reflectional boundary conditions, and are significantly different than the

## Nomenclature

$U_i$	Instantaneous velocity
$u_i$	Fluctuating velocity
$\Omega_i$	Instantaneous vorticity
$\omega_i$	Fluctuating vorticity
$u_i' = \sqrt{\sum_{s_1, s_2} u_i^2}$	RMS fluctuating velocity
$\omega_i' = \sqrt{\sum_{s_1, s_2} \omega_i^2}$	RMS fluctuating vorticity
$\bar{U}_i(x_2)$	Mean velocity
$U_{f_s} = \bar{U}_1(x_2 = 0.0)$	Mean free surface velocity
$u^* = \sqrt{\tau_{\text{wall}}/\rho}$	Friction velocity
$l^* = \nu/u^*$	Viscous lengthscale
$t^* = \nu/u^{*2}$	Viscous timescale

\*Research Scientist, SAIC, McLean, VA, 22102

†Research Mechanical Engineer, NRL, Member AIAA  
+Mechanical Engineer, NRL

This paper is declared a work of the U.S. Government and is not subject to copyright protection in the United States.

condition of rotational symmetry about the  $x_1$ -axis (aligned with the channel centerline) that occurs in the closed channel case.

Another important interpretation of enstrophy can be made through its relation to the isotropic dissipation function. The isotropic dissipation function, commonly used in  $k - \epsilon$  turbulence models, is defined as:

$$\epsilon = \nu \frac{\partial u_i}{\partial x_j} \frac{\partial u_j}{\partial x_i}, \quad (1)$$

for homogeneous turbulence. However, the following can be shown

$$\begin{aligned} \frac{\partial u_i}{\partial x_j} \frac{\partial u_j}{\partial x_i} &= \frac{1}{2} \frac{\partial u_i}{\partial x_j} \frac{\partial u_i}{\partial x_j} + \frac{1}{2} \frac{\partial u_j}{\partial x_i} \frac{\partial u_j}{\partial x_i} \\ &= \frac{1}{2} \left( \frac{\partial u_i}{\partial x_j} - \frac{\partial u_j}{\partial x_i} \right) \left( \frac{\partial u_i}{\partial x_j} - \frac{\partial u_j}{\partial x_i} \right) \\ &= \overline{\omega_k \omega_k}. \end{aligned} \quad (2)$$

In Eq. 2 the identity for homogeneous incompressible turbulence,

$$\begin{aligned} \frac{\partial u_i}{\partial x_j} \frac{\partial u_j}{\partial x_i} &= \frac{\partial}{\partial x_j} \left( \overline{u_i \frac{\partial u_i}{\partial x_j}} \right) - \overline{u_i} \left( \frac{\partial}{\partial x_j} \frac{\partial u_i}{\partial x_j} \right) \\ &= 0, \end{aligned} \quad (3)$$

has been used<sup>1</sup>. Therefore the isotropic dissipation function is related to the fluctuating enstrophy as

$$\epsilon = \nu \overline{\omega_k \omega_k}. \quad (4)$$

Consequently, the study of the enstrophy balance can be viewed as the study of the creation and destruction of the isotropic dissipation function. The enstrophy balance equation may be a more convenient tool to study the dissipation because its terms have better physical interpretations. Furthermore the component equations  $\omega_k \omega_k$  (no implied summation) can be examined individually. As mentioned above, while the isotropic dissipation is not the local dissipation of turbulent kinetic energy, it is relevant for turbulence modeling.

## 2. The Numerical Simulation

The incompressible three-dimensional Navier-Stokes equations are solved for initial and boundary conditions approximating a turbulent open-channel flow of water at a Reynolds number of 2340, where  $Re_h = U_f h / \nu$  and  $h$  is the channel depth and  $U_f$ ,

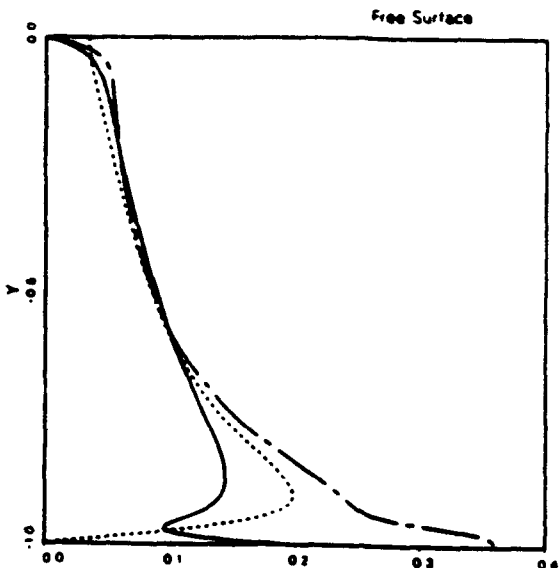


Fig. 1 RMS Fluctuating Vorticity. Symbols: —,  $\omega_1$ ; - - -,  $\omega_2$ ; - - - - ,  $\omega_3$ .

is the mean free-surface velocity. Based on the friction velocity,  $u_* = \sqrt{\frac{\tau_{wall}}{\rho}}$ , the Reynolds number is  $Re_* = 134$ . The governing equations are recast into a 4<sup>th</sup> order equation for the vertical velocity and a 2<sup>nd</sup> order equation for the vertical vorticity and the continuity equation is solved explicitly in the recovery of the streamwise velocity. This formulation was first discussed by Orszag and Patera<sup>2</sup> and later implemented in a simpler form in the large scale direct simulations by Kim, Moin and Moser<sup>3</sup>. It is the latter formulation that will be used. This method involves the use of the homogeneous solutions of the time discretized 4<sup>th</sup> order equation to satisfy all the required boundary conditions. The equations are numerically solved after they are Fourier transformed in the streamwise ( $x_1$ ) and spanwise ( $x_3$ ) directions and Chebychev transformed in the vertical direction ( $x_2$ ). The  $x_2$  axis, scaled by the channel height has its origin at the free surface. The channel bottom is  $x_2 = -1$ . The calculations are performed on a grid of  $48 \times 65 \times 64$  nodes in  $x_1, x_2, x_3$ , respectively, for a resolution of  $26.3l_*$  in the streamwise direction and  $13.2l_*$  in the spanwise direction ( $l_* = \nu \sqrt{\frac{\rho}{\tau_{wall}}}$ ). The total box size is  $1684l_* \times 134l_* \times 632l_*$ . With the geometry scaled by the channel height, the height, length and width of the channel are  $1, 4\pi$  and  $3\pi/2$ , respectively.

In the free-surface problem the nonlinear and time-dependent boundary conditions must be satisfied on an unknown surface elevation,  $\eta$ . The boundary conditions can be simplified considerably if the surface is not allowed to deflect ( $\eta \equiv 0$ ). The rigid

lid approximation is equivalent to

$$\omega_2 = 0 \text{ at } x_2 = 0. \quad (5)$$

To further simplify the boundary conditions, the usual balance of normal stresses<sup>6</sup> is replaced by

$$\frac{\partial^2 u_2}{\partial x_2^2} = 0 \text{ at } x_2 = 0. \quad (6)$$

Eq. 6 can be derived from the zero tangential stress conditions, the continuity equation, and the rigid lid assumption. These conditions and the definition of vorticity can also be combined to form the remaining free-surface boundary condition,

$$\frac{\partial \omega_2}{\partial x_2} = 0 \text{ at } x_2 = 0, \quad (7)$$

where the vorticity is non-dimensionalized by  $U_0/h$ ,  $U_0$  is the initial ( $t = 0$ ) free-surface velocity.

At the bottom wall of the channel, the no-slip velocity boundary conditions are composed. The no-slip velocity condition sustains the shear layer which is responsible for maintaining the turbulence. The boundary conditions are periodic on all dependent variables in the streamwise and spanwise directions.

After the wall shear stress achieved a statistically steady state at the correct value, and the total stress across the channel was linear, turbulent flow data was acquired. Forty-two realizations of the turbulent flow were saved during an interval of approximately  $4000t^*$  ( $t^* = \nu/u^*$ ). We have compared single point statistics and spectra with from the closed channel calculation performed at the Naval Research Laboratory<sup>7</sup> and, where possible, results from the high resolution NASA Ames closed channel computation<sup>3</sup>. In general, the single point statistics in the wall and buffer regions are very similar to the closed channel results. The effects of the upper boundary are apparent in the range of  $0.0 \leq x_2 \leq -0.3$  as compared to similar data from the closed channel calculations.

### 3. Fluctuating Vorticity

The near wall behavior of the rms vorticity,  $\omega'_1$  in Fig. 1 is similar to the prior results of Kim, Moin and Moser<sup>3</sup>. Near the free surface the horizontal components of vorticity vanish, while the vertical component approaches a constant value of  $\omega'_2 \nu/u^{*2} = 0.035$ . This can be compared to 0.057 at the centerline for a low resolution closed channel simulation performed at NRL and 0.042 for the results Kim, Moin and Moser<sup>3</sup>. A Taylor series expansion about the top boundary indicates that  $\omega'_1$  and  $\omega'_3$  both approach zero linearly. A physical explanation of why  $|\frac{d\omega'_1}{dx_2}| > |\frac{d\omega'_3}{dx_2}|$  as the free surface is being approached can be developed by examining the  $\overline{\omega_i \omega_i}$  balance equations.

### 4. Balance Equations

The relationship of enstrophy to fluctuating vorticity is similar to the relationship of turbulent kinetic energy to fluctuating velocity. The balance equations are derived in the same manner as the balance equations for the components of the Reynolds stress tensor. The equations for the mean and instantaneous vorticity are multiplied the mean and instantaneous vorticity, respectively. These equations are time averaged resulting in equations for the mean enstrophy and the mean equation of the instantaneous enstrophy. Subtracting the latter from the former yields the equation of the mean fluctuating enstrophy. As in the case of the Reynolds stress tensor, the equations for the individual components of the enstrophy,  $\overline{\omega_1 \omega_1}, \overline{\omega_2 \omega_2}, \overline{\omega_3 \omega_3}$  can be formulated. The details of the derivation of the balance equation for the fluctuating enstrophy are contained in Balint, Vukoslavcevic and Wallace<sup>4</sup>. The steady state balance equations are:

$$\begin{aligned} \overline{U_j} \frac{\partial}{\partial x_j} \left( \frac{1}{2} \overline{\omega_i \omega_i} \right) &= - \overline{u_j} \frac{\partial}{\partial x_j} \left( \frac{1}{2} \omega_i \omega_i \right) - \overline{u_j \omega_i} \frac{\partial \overline{\Omega_i}}{\partial x_j} \\ &+ \overline{\omega_i \omega_j} \frac{\partial \overline{U_i}}{\partial x_j} + \overline{\omega_i \omega_j} \frac{\partial \overline{u_i}}{\partial x_j} \\ &+ \overline{\Omega_j \omega_i} \frac{\partial \overline{u_i}}{\partial x_j} + \nu \frac{\partial^2 \frac{1}{2} \overline{\omega_i \omega_i}}{\partial x_j^2} - \nu \frac{\partial \overline{\omega_i}}{\partial x_j} \frac{\partial \overline{\omega_i}}{\partial x_j}, \end{aligned} \quad (8)$$

with  $i = 1, 2$  or, 3 for the component equations and an implied summation for the total fluctuating enstrophy.

According to Tennekes and Lumley<sup>5</sup> and Balint<sup>4</sup>, et al., the eight terms of the enstrophy balance equation have the following interpretation:

- (1)  $\overline{U_j} \frac{\partial}{\partial x_j} \left( \frac{1}{2} \overline{\omega_i \omega_i} \right)$ : The convection of the fluctuating enstrophy,
- (2)  $-\overline{u_j} \frac{\partial}{\partial x_j} \left( \frac{1}{2} \omega_i \omega_i \right)$ : Transport of fluctuating enstrophy by fluctuating velocity,
- (3)  $-\overline{u_j \omega_i} \frac{\partial \overline{\Omega_i}}{\partial x_j}$ : Gradient production of enstrophy,
- (4)  $\overline{\omega_i \omega_j} \frac{\partial \overline{U_i}}{\partial x_j}$ : production by mean velocity gradient,
- (5)  $\overline{\omega_i \omega_j} \frac{\partial \overline{u_i}}{\partial x_j}$ : production by fluctuating velocity gradient.
- (6)  $\overline{\Omega_j \omega_i} \frac{\partial \overline{u_i}}{\partial x_j}$ : Mixed production,
- (7)  $\nu \frac{\partial^2 \frac{1}{2} \overline{\omega_i \omega_i}}{\partial x_j^2}$ : Viscous diffusion,
- (8)  $\nu \frac{\partial \overline{\omega_i}}{\partial x_j} \frac{\partial \overline{\omega_i}}{\partial x_j}$ : Viscous dissipation.

The interpretation of terms 1 - 6 can be expanded by examining the non-linear term of the vorticity equation from which they were derived:

$$\nabla \times \mathbf{u} \times \boldsymbol{\omega} = (\boldsymbol{\omega} \cdot \nabla) \mathbf{u} - (\mathbf{u} \cdot \nabla) \boldsymbol{\omega}. \quad (10)$$

The first term is the amount of instantaneous stretching or rotation of the vorticity by the gradient of the velocity field. Following Batchelor<sup>6</sup>, if P and Q are two local points on a vortex line, then

$$(\omega \cdot \nabla)u = |\omega| \lim_{PQ \rightarrow 0} \frac{\delta u}{PQ}, \quad (11)$$

where  $\delta u$  is the variation  $u$  over the distance  $PQ$ . That component of  $\delta u$  which is aligned with  $\omega$  acts to stretch or compress the vorticity while the component perpendicular to  $\omega$  causes the vortex line to undergo instantaneous rigid body rotation. For example if we assume the vorticity is aligned in the  $z_3$  direction then

$$\omega_3 \frac{\partial u_1}{\partial z_3}$$

is the rotation of the vorticity vector from the  $\omega_3$  component to the  $\omega_1$ . A similar interpretation holds for  $\omega_3 \frac{\partial u_2}{\partial z_3}$ . In the remaining direction the vorticity and the velocity gradient are aligned and stretching or compressing of the vorticity occurs. This is shown in Fig. 2. The second term on the right hand side of equation (10) is the convective part of the substantial derivative.

Terms (1), (2), and (3) of Eq. 8 can be identified with the convective part of the nonlinear terms: (1) and (2) can be considered as transport terms and (3) being a gradient production term. For the geometry under study term (1), transport by the mean velocity is zero. Terms (4), (5) and (6) are stretching/compression/rotation terms. Term (4) accounts for the production of  $\bar{\omega}_1 \omega_1$  due to the rotation of  $\omega_2$  into  $\omega_1$  by  $\frac{\partial u_1}{\partial z_2}$ . This term, which is non-zero only for  $i = 1$ , and  $j = 2$  represents the action of the mean velocity on the fluctuating vorticity. Term (5) is the production of enstrophy due to the stretching/compression and rotation of fluctuating vorticity by the fluctuating velocity field. As will be shown later, this is an important term near the free-surface. Term (6), the so-called mixed production term accounts for the production of enstrophy due to the stretching and rotation of the mean vorticity field,  $\bar{\omega}_3$ , by the fluctuating velocity fields,  $u_i$ . This term represents the action of the fluctuating velocity field on the mean vorticity field. The last two terms are interpreted as viscous diffusion and viscous dissipation of fluctuating enstrophy.

### 5. The Enstrophy Balances

The terms of Eq. (8) have been calculated and are shown in Fig. 3. They are normalized by the initial free-surface velocity and the channel height. The balance for the total enstrophy and its components near the free surface are in Figs. 4 a-d. Gains in enstrophy are indicated on the right hand side of these

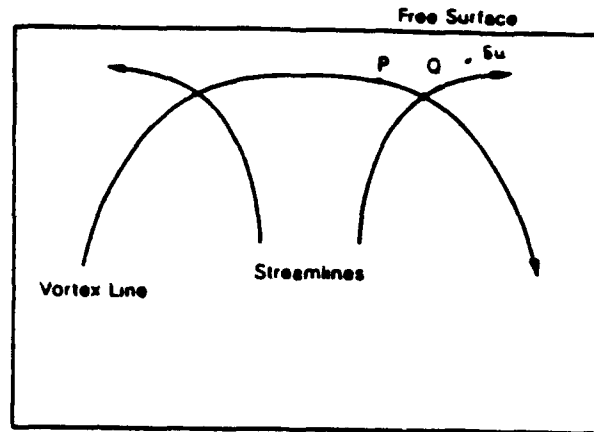


Fig. 2. A schematic of vortex stretching and rotation by the fluctuating velocity.

figures. The individual terms give a better indication of the mechanisms by which the enstrophy is generated and destroyed. Note that the scale of the abscissa has been changed between Fig. 4a and Figs. 4b-d.

#### 5.1 Balance Near the Wall

The majority of the production and dissipation of vorticity fluctuations occurs near the wall where the mean velocity gradient and the mean spanwise vorticity are large. In a very thin region near the wall the diffusion and dissipation of enstrophy are in balance. In the region  $(-0.8 \geq z_2 \geq -0.95)$  the mixed production term (6), the production by the mean velocity gradient term (4), and the turbulent production terms (5) are the dominate sources for fluctuating enstrophy, in increasing importance away from the wall. These terms are the rotation/stretching terms of the balance equations. The gains are almost completely balanced by the viscous dissipation. The transport/convection related terms are all small. With the exception of near the free surface, the terms of the individual balances decrease with increasing distance from the wall. Near the free-surface there is a thin region ( $z_2 \geq -0.10$ ) of significant change. Details of the individual balances near the wall can be found in Leighton, et al.<sup>7</sup>.

#### 5.2 Balance Near the Surface

As can be seen in Fig. 4a, the viscous dissipation of enstrophy (8) and the turbulent production (5) dominate in the region  $-0.10 \geq z_2 \geq -0.33$ . In this region there is still some production of fluctuating enstrophy by the mean velocity gradient. Since the mean velocity gradient must approach zero at the shear free surface, the enstrophy production due to the mean gradient must go to zero. Turbulent production of enstrophy, the dominate production mechanism for the upper 1/3 of the channel decays rapidly

for  $z_2 > -0.05$ . Viscous diffusion and turbulent transport act to increase the enstrophy in the region  $z_2 > -0.10$ . Enstrophy dissipation balances the production and diffusion near the top boundary. In the thin region  $y \geq -0.08$  the significant changes in the terms of Eq. 8 can be understood by examining the component terms.

Figs. 4b-d show the level of gain or loss for each component of enstrophy near the surface. In the upper 1/3 of the channel the transport term becomes relatively more important, albeit the term is still small. The fluctuating normal velocity field transports  $\omega_1 \omega_1$  and  $\omega_3 \omega_3$  towards the surface. As the gradients in  $\omega_1'$  and  $\omega_3'$  increase near the surface, there is a corresponding increase in the enstrophy transport (see Fig. 1). The action of the transport term of  $\omega_2 \omega_2$ , while always small, is to reduce the level of normal vorticity near the surface.

Figs. 4b and 4c show that the mixed production terms do play a role in the top of the channel, but approach zero as the shear-free surface is approached. It is interesting to note that the mixed production term for the  $\overline{\omega_1 \omega_1}$  balance equation is negative in the region  $(0.0 \geq y \geq -0.33)$  and almost completely balanced by the production due to the mean velocity gradient. In the case of  $\overline{\omega_1 \omega_1}$ , this term expresses the effect of the rotation of the mean vorticity vector by the fluctuating velocity field to cancel the fluctuating axial vorticity. This is done at nearly the same rate at which vorticity is being rotated out of the mean vorticity into the fluctuating normal vorticity by the fluctuating normal velocity.

The dissipation and diffusion curves in Figs. 4b-d indicate a strong dependence of the diffusion and dissipation process on the orientation of the vorticity. Viscous diffusion, which has been negligible in the region  $-0.1 \geq y \geq -0.85$  becomes the dominate source for the horizontal components of enstrophy ( $\omega_1 \omega_1$  and  $\omega_3 \omega_3$ ) near the surface, ( $y \geq -0.05$ ). Due to the reflective nature of the shear free boundary, the horizontal components of vorticity go to zero at the boundary and any such vorticity near the boundary will be influenced by the anti-parallel image vorticity. The effect of the image vorticity or equivalently the shear-free boundary is to increase diffusion of the vorticity in the fluid towards its image, and in the process increase the dissipation of enstrophy. For the normal component ( $\omega_2 \omega_2$ ) the process of dissipation and diffusion are entirely different. In this case the image vorticity is not anti-parallel vorticity promoting diffusion, but simply a continuation of the physical vorticity across the shear-free interface. The dissipation of the mean square fluctuating normal vorticity in Fig. 4c is related to the radial diffusion of normal vorticity.

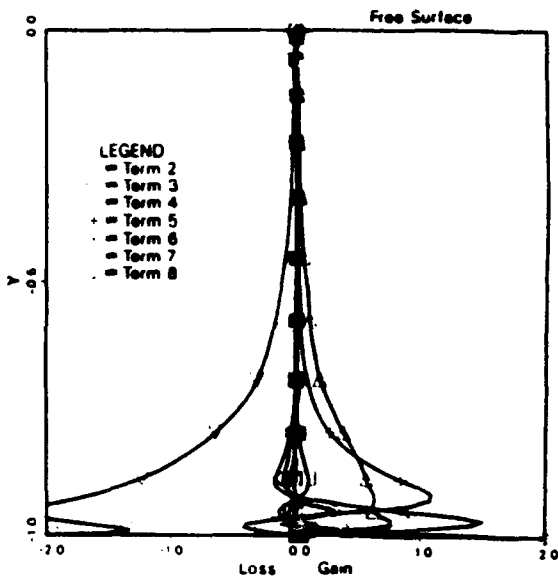


Fig. 3. The terms of Eq. 8.

Also apparent in Figs. 4b-d are the differences in the characteristics of the turbulent production and the transport of enstrophy between the cases of the horizontal vorticity and the vertical vorticity. With the exception of the mean and mixed production, terms (4) and (6) the horizontal terms are similar. In the upper 1/3 of the channel, the turbulent production of enstrophy contributes positively, exhibiting a generally slow decline with increasing distance from the solid wall. However in the layer  $-0.05 \geq y \geq -0.1$  the decline stops, and at least for the transverse component of enstrophy, there is a slight increase in production. Since  $\Omega_1$  and  $\Omega_3$  approach zero at the shear-free boundary, the production of these components of enstrophy must also approach zero. The non-zero turbulent production of the normal component of enstrophy at the surface is a result of the shear-free boundary and a normal strain field, which will be discussed later.

The production term (5) is further separated into the various stretching and rotation components in Fig. 5. For all three enstrophy components the production due to stretching dominates. For the stretching terms to be relevant, there must be some strain aligned with the vorticity. While this strain is not accounted for by the existence of the anti-parallel image vortex, numerical experiments involving interacting vortex rings or vortex tubes indicate a rapid increase in the component of strain aligned with the vorticity during the vortex reconnection. A similar

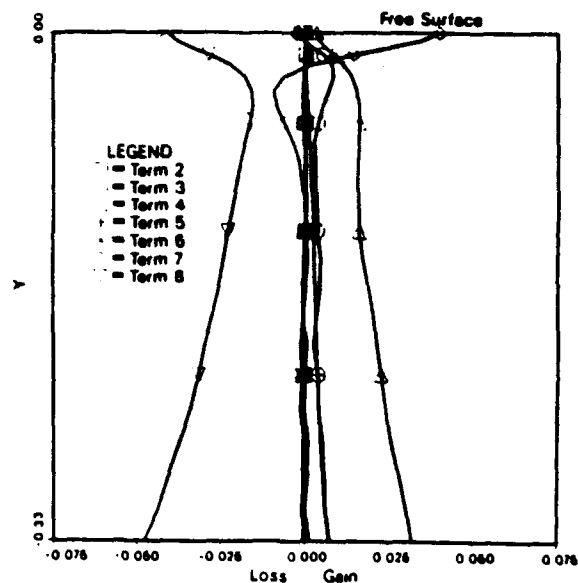


Fig. 4a. Enstrophy balance in a turbulent open channel flow near the free surface.

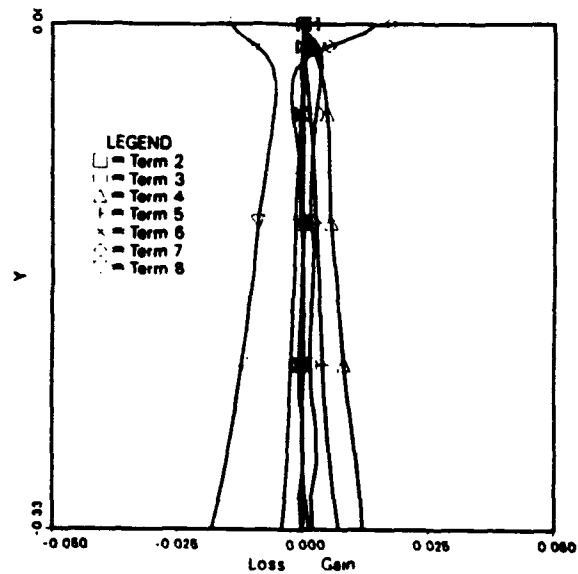


Fig. 4b. Mean square fluctuating axial vorticity balance in a turbulent open channel flow near the free surface.

process may be relevant when the horizontal components of vorticity approach the top surface. The flow field transporting the vorticity to the free surface may also be responsible for the strain.

Although the rotation terms are small and declining as the surface is approached, the terms representing the rotation of vorticity from the axial to the transverse direction and from the transverse to the axial have small increases near the boundary. This may be due to the rotation of small eddies, having vorticity components parallel to the surface by large eddies.

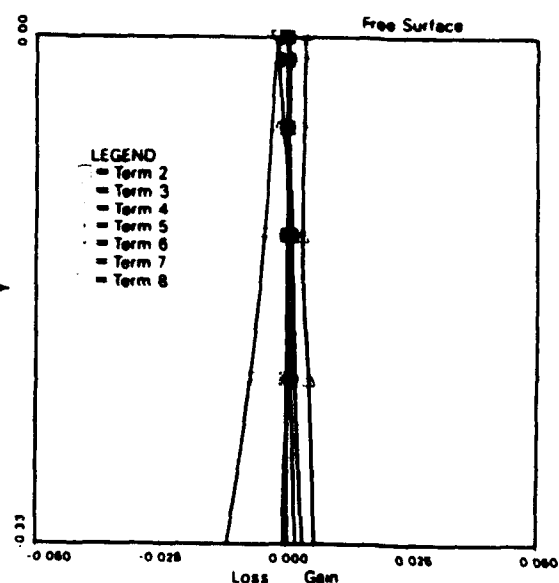


Fig. 4c. Mean square fluctuating normal vorticity balance in a turbulent open channel flow near the free surface.

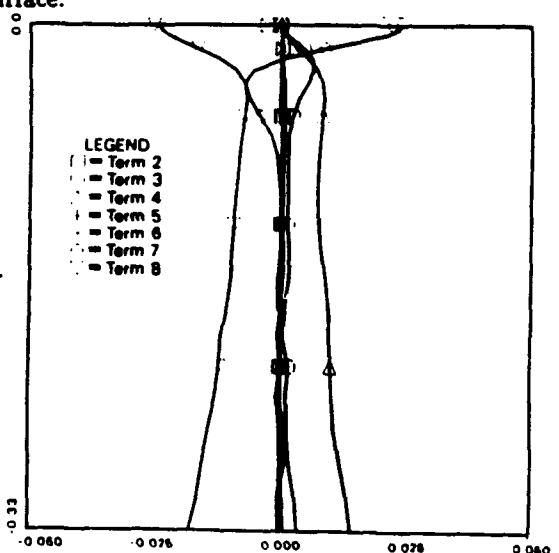


Fig. 4d. Mean square fluctuating transverse vorticity balance in a turbulent open channel flow near the free surface.

The enstrophy balance in the vertical ( $x_2$ ) direction shows the effect of attachment of the normal vorticity to the free surface. The turbulent production of  $\overline{\omega_2 \omega_2}$  varies slightly in the upper 1/3 of the channel. However, as can be seen in Fig. 5 the production mechanism changes with increasing distance from the shear-free boundary. Near the surface,  $x_2 \geq -0.08$ , the stretching of the vorticity is important. Below ( $x_2 \leq -0.08$ ) the gain in enstrophy is due to rotation of the fluctuating vorticity field, and stretching has become negligible. The source of the strain near the free-surface is probably the flow induced by the low pressure within the vorticity attached to the surface.

## 6. Vortical Events At The Free Surface

From figure 5, it is apparent that the term in Eq. 8 most responsible for the production of enstrophy is transverse stretching of transverse vorticity,  $\omega_3 \frac{\partial \omega_3}{\partial x_3}$ . Figure 6 is a plot of this property for the plane  $x_2 = -0.05$ . The turbulent structures or events responsible for generating this component of the enstrophy are localized and intense. The contour intervals are  $10\omega_3 \frac{\partial \omega_3}{\partial x_3}$ . To more clearly identify the structures associated with the localized production, histograms of the level of production by turbulent stretching have been determined and are contained in Leighton<sup>7</sup>, et.al. From the histograms it was determined that, at this plane ( $x_2 = -0.05$ ) that approximately 3–6% of the area was responsible for 30–60% of the turbulent enstrophy production. This behavior is typical for all nine components of term (5), Eq. 8. This conclusion was verified by calculating the skewness and flatness for these production terms. For each of the nine cases the skewness and flatness factors were large ( $10 - 10^2$  for skew and  $10^2 - 10^4$  for flatness).

Based on the observation of production events local in space, and the behavior of the average fluctuating vorticity, two models of the interaction of vorticity with the surface were developed.

### 6.1 Two models for the production events

The two proposed models of the interaction of vorticity with the free surface can be described as 'the spin model' and 'the splat model'. These models are similar to and have been influenced by the models presented by Koh and Bradshaw<sup>8</sup> and Hunt<sup>9</sup>. Although the names are meant to be suggestive of the kinematics of the enstrophy producing events, the models are similar to the models by the same name for the pressure source terms described in Ref. 9.

In the 'spin' model, a vortical structure originating in the buffer layer, tilts downstream and is attached to the free surface in a quasi-stable configuration. This model is relevant when discussing the vertical component of enstrophy. These structures, which can be liken to vortex tubes connected to the free surface have been observed in flow visualizations of the DNS dataset of the open channel flow. Within these vortex tubes there is a significant 'down draft'. It is conjectured that this down draft is responsible for the transport of enstrophy away from the surface and provides the strain necessary to maintain these structures. Were it not for these down drafts, and the vorticity intensification they provide, these vortical structures would eventually diffuse and cancel.

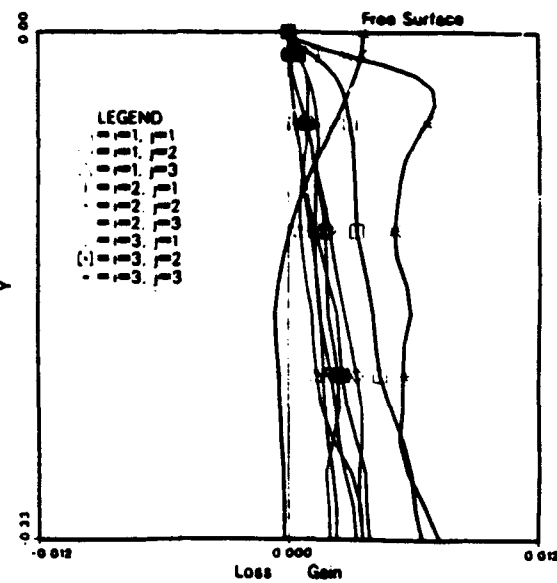


Fig. 5. Turbulent production of fluctuating enstrophy by stretching (heavy lines) and rotation (light lines),  $\overline{\omega_i \omega_j} \frac{\partial \omega_k}{\partial x_k}$ .

The eventual diffusion has been seen in a simulation of vortex reconnection in which there was no down draft.<sup>10</sup> In this case there was radial diffusion of vorticity from the core near the intersection of the vortex ring and the shear-free surface.

In the 'splat' model a volume of fluid 'containing' vorticity impacts the free surface, leading to stretching, intensification and cancellation of vorticity. The fluctuating normal velocity field promotes the increase of horizontal component enstrophy near the free surface by two mechanisms: transport and vortex stretching. Due to the large gradient in  $\overline{\omega_1 \omega_1}$  and  $\overline{\omega_3 \omega_3}$  near the top boundary, the vertical velocity fluctuations provide an efficient means of transporting vorticity to the free surface. As the turbulent eddy approaches the top boundary the vertical momentum is deflected into the horizontal direction. During this 'splat' event, the vorticity contained in a turbulent eddy interacting with the top surface will be rotated parallel to the boundary and stretched. The vorticity in the fluid near the free surface will be subjected to a large strain and will have a large gradient due to the proximity of its reflected image. This leads to increased production of fluctuating enstrophy by the fluctuating velocity fields and to large enstrophy dissipation or vorticity cancellation. Other details about this type of model can be found in Ref. 9.

## 7. Conditional Sampling and Ensemble Averaging

To verify that the two models are qualitatively correct, the open channel flow was conditionally sampled on the plane  $z_3 = -0.05$ . The condition used was that the local value of the enstrophy production by vortex stretching ( rotation was not considered ) exceeded the mean value by a factor of ten, and that the production was a local maximum. The enstrophy production at the locations determined by the first condition accounted for approximately 50% of the production by stretching and rotation, but only about 2% of the area. For the spanwise component,  $\omega_3 \omega_3 \frac{\partial u_3}{\partial z_3}$ , only detected events with negative vorticity were considered. There were approximately an order of magnitude more events with negative vorticity contributing to the turbulent production of spanwise enstrophy than events with positive vorticity. For the remaining components, only events with positive vorticity were considered. In this case there were as many positive as negative vortical events detected.

Certain properties associated with these events have been ensemble averaged and are shown in figures 7 – 10. The properties are averaged on a vertical line through the detected events. The ensemble averaged vorticity, shown in Fig. 7 are larger than those shown in Fig. 1, almost by a factor of ten, an indication that these events are substantial contributors to the rms vorticity.

### 7.1 The Splat Event

As discussed above the spin model involves a vortical structure, like a vortex tube attached to the free

surface and extending into the buffer layer. The existence of substantial ensemble-averaged vertical vorticity in regions far from the free surface, as seen in Fig. 7 supports the conceptual model of an attached vortex tube.

Fig. 8 is the ensemble-averaged vertical velocity. In the case of the normal component of enstrophy, the negative velocity will stretch the attached vertical vorticity. This is the down-draft within the vortex tube mentioned earlier. The peak negative velocity occurs at  $z_2 \approx -0.15$ . The strain rates  $\frac{\partial u_3}{\partial z_2}$  are shown in Fig. 9. The peak in the normal strain occurs at the surface, again consistent with the proximity of the vortex stretching with the free surface. The strain and the resulting vortex stretching are negative for  $z_2 < -0.15$ . This may be due in part to the tilting of the vortical structure in the main part of the flow.

The final figure is the rate of dissipation of enstrophy for each of the components. The normal vorticity is largely unaffected by its image and has a low level of dissipation. Due to this small dissipation, it is conjectured that these events will have a longer duration than the 'splat' events.

### 7.2 The Splat Event

Although the conditionally sampled results are consistent with both the model and the RMS vorticity distributions, they do not explain the greater intensity of the  $\omega_3$  components. The location of the maximum transverse vorticity is above the conditioning plane,  $y = -0.05$  while the maximum for the axial vorticity is below. This characteristic and the amplitude of the maximum are consistent with their rms values.

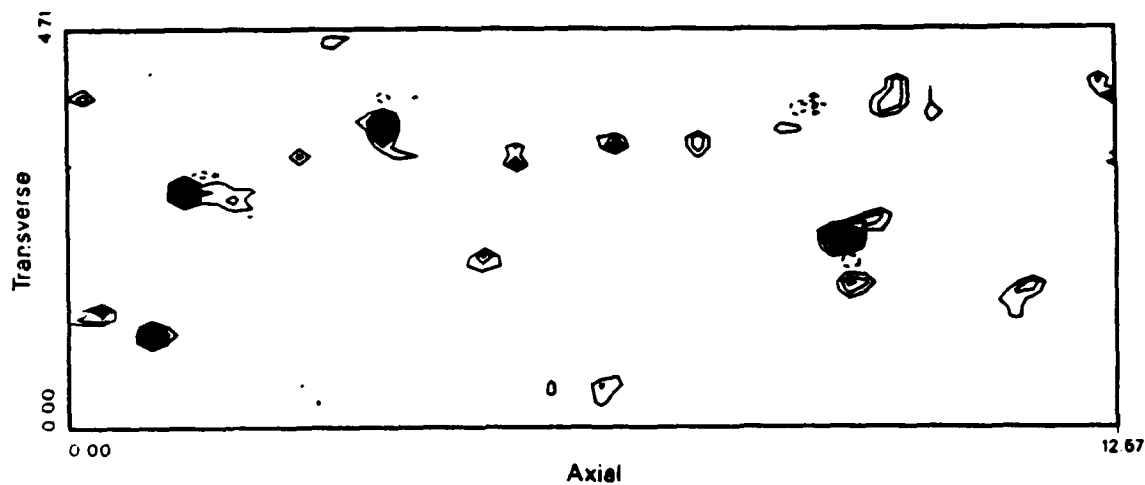


Fig. 6. Enstrophy production due to transverse stretching of transverse vorticity ( $\omega_3 \omega_3 \frac{\partial u_3}{\partial z_3}$ ). Planview of plane  $y = -0.05$ . Contours are for  $\omega_3 \omega_3 \frac{\partial u_3}{\partial z_3} = 10 \omega_3 \omega_3 \frac{\partial u_3}{\partial z_3}$ .

Fig. 8 is the vertical velocity associated with these events. For the rising turbulent eddy of the model the vertical velocity is positive, resulting in a 'splat' at the surface. The strain rates  $\frac{\partial u_i}{\partial x_i}$  are shown in figure 9. The transverse strain is larger than the axial strain. This is consistent with the larger transverse turbulent production and vorticity.

Fig. 10 is the rate of dissipation of enstrophy for each of the components. The terms in  $x_1$  and  $x_3$  direction are similar. The dissipation occurs very close to the boundary and is very intense: approximately an order of magnitude larger than the mean value. Due to the reflective nature shear-free boundary there exists an image vorticity across the boundary resulting in annihilation of vorticity near the shear-free boundary.

### 8. Conclusions

The enstrophy balance equations have been evaluated for a direct numerical simulation of turbulent open channel flow. The free surface has been modeled as a shear-free boundary. Near the free surface there are two dominate sources of enstrophy: Transport due to velocity fluctuations and production due to the vortex stretching and rotation by the velocity fluctuations. At the free surface, diffusion is the dominate source of enstrophy. The gains in enstrophy are balanced by enstrophy dissipation. When the components of the total enstrophy are considered individually, the components parallel to the surface, ( $\bar{\omega}_1 \omega_1$  and  $\bar{\omega}_3 \omega_3$ ) are found to be responsible for the variation in the balances near the surface. The balance equations for  $\bar{\omega}_2 \omega_2$  show little variation near the surface.

Two models, referred to as the 'spin' and 'splat'

models can be used to explain this behavior. The splat model is similar to the model discussed in Hunt<sup>8</sup> in which an eddy is swept to the surface. The resulting redistribution of normal momentum into horizontal momentum will stretch and intensify any vorticity transported in the eddy. Due to the image vorticity resulting from the reflective nature of the free surface, the intense vorticity will quickly cancel with its image and the enstrophy dissipation will be enhanced.

Fundamental to the 'spin' model is a stable vortical structure originating in the buffer layer and extending to the free surface. The mild variation of the normal balance is a result of the quasi-stable nature of the attached structure. Without close anti-parallel image vorticity, these structures do not dissipate quickly. The downflow within these vortical structures result in sufficient strain to maintain the vorticity against the effects of viscous diffusion.

A large portion of the production of enstrophy near the free surface is due to these highly localized intense events. The area responsible for this production is very small. Approximately 3 - 6% of the area on the plane  $x_2 = -0.05$  is responsible for 30 - 60% of the production. Conditionally sampling and ensemble averaging the production events verified that their characteristics are consistent with the proposed models.

### Acknowledgements

This work is supported by the Naval Research Laboratory as part of the Fluid Dynamics Task Area. The simulations were performed at the Naval Research Laboratory.

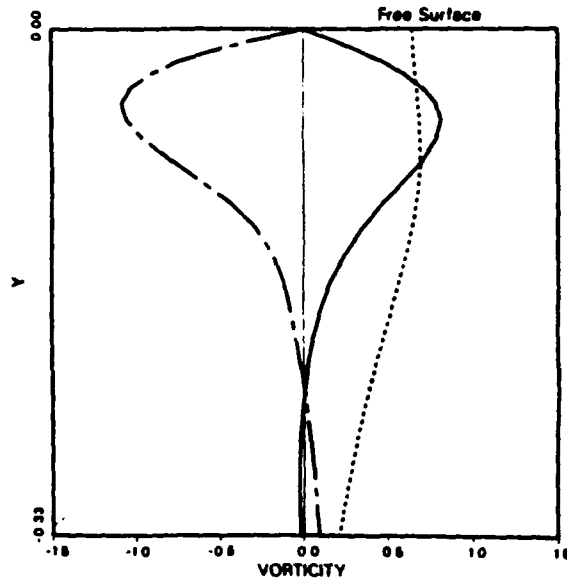


Fig. 7. Ensemble averaged vorticity, conditioned by the requirement that  $\omega_i \omega_i \frac{\partial u_i}{\partial x_i} \geq 10 \omega_i \omega_i \frac{\partial u_i}{\partial x_i}$ .  
 —,  $\langle \omega_1 \rangle$ ; ---,  $\langle \omega_2 \rangle$ ; ----,  $\langle \omega_3 \rangle$ .

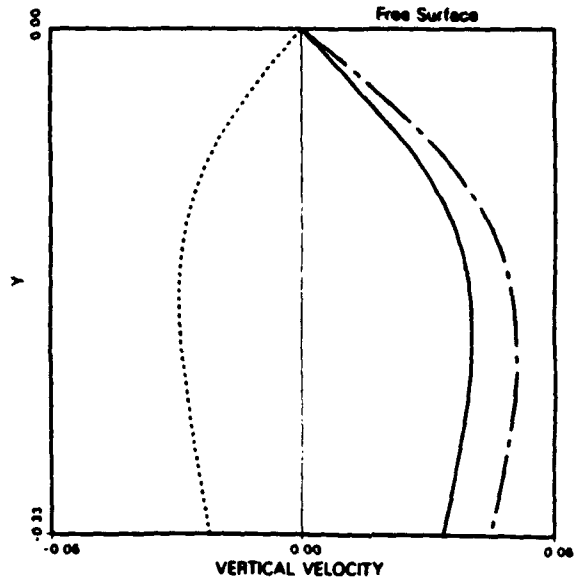


Fig. 8. Ensemble averaged vertical velocity.  
 —,  $\langle u_1 \rangle$ ; ---,  $\langle u_2 \rangle$ ; ----,  $\langle u_3 \rangle$ .

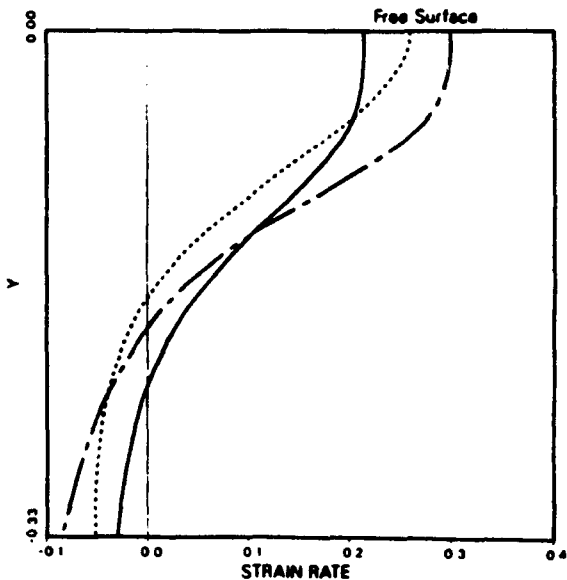


Fig. 9. Ensemble averaged strain.  
 —,  $\langle \frac{\partial u_1}{\partial x_1} \rangle$ ; - - -,  $\langle \frac{\partial u_2}{\partial x_2} \rangle$ ; - - - - ,  $\langle \frac{\partial u_3}{\partial x_3} \rangle$ .

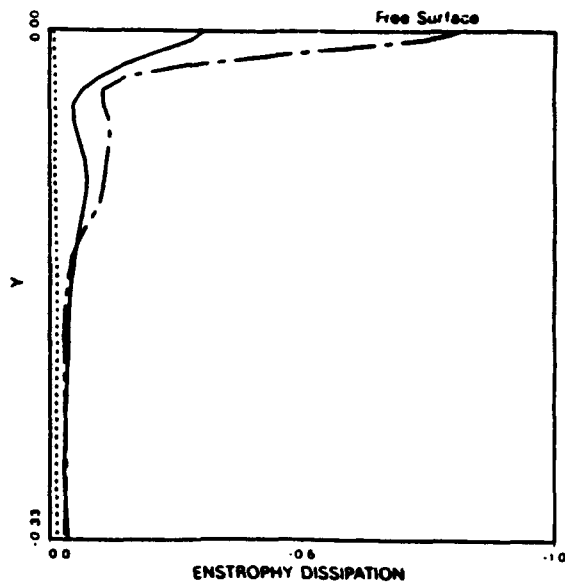


Fig. 10. Ensemble averaged dissipation of enstrophy.  
 —,  $i = 1$ ; - - -,  $i = 2$ ; - - - - ,  $i = 3$ .

#### References

- [1] Hinze, J.O., 1975 *Turbulence*. McGraw-Hill, New York
- [2] Orszag, S.A., and Patera, A.T., 1981 Subcritical Transition to Turbulence in Planar Shear Flows in *Transition and Turbulence*. Academic Press, London.
- [3] Kim, J., Moin, P., and Moser, R., 1987 Turbulence statistics in a fully developed channel flow at low Reynolds number. *J. Fluid Mech.* 177, 133.
- [4] Balint, J.-L., Vukoslavcevic, P. and Wallace, J.M., 1988 The transport of enstrophy in a turbulent boundary layer. In *Proceedings of the Zarif Memorial International Seminar on Wall Turbulence*.
- [5] Tennekes, H. and Lumley, J.L., 1972 *A First Course In Turbulence*. The MIT Press, Cambridge, Mass.
- [6] Batchelor, G.K., 1967 *An Introduction To Fluid Dynamics*. Cambridge University Press, Cambridge, England.
- [7] Leighton, R.I., Swean, T.F., Handler, R.A. and Swearingen, J.D., 1991 Direct simulation of low Reynolds number open channel flow. In preparation for submittal to *Physics of Fluids*.
- [8] Bradshaw, P. and Koh, Y.M., 1981 A note on Poisson's equation for pressure in a turbulent flow. *Physics of Fluids*. 24, 777.
- [9] Hunt, J.C.R. 1984 Turbulence structure and turbulent diffusion near gas-liquid interfaces. in *Gas Transfer at Water Surfaces*. D. Reidel Pub. Co.
- [10] Leighton, R.I. and Swean, T.F., 1991 The interaction of a vortex ring with a shear-free boundary. In preparation for submittal to *Physics of Fluids*.

## **Appendix F**

### **Turbulence Modeling Near the Surface in an Open Channel Flow**



**AIAA 91-0613**  
**Turbulence Modeling**  
**Near the Free Surface**  
**in an Open Channel Flow**

T.F. Swean, Jr., R.I. Leighton<sup>†</sup>, R.A. Handler,  
and J.D. Swearingen

Center for Advanced Space Sensing,  
Naval Research Laboratory,  
Washington, D.C.

<sup>†</sup>Science Applications International Corp.,  
McLean, Va.

**29th Aerospace Sciences Meeting**  
**January 7-10, 1991/Reno, Nevada**

# TURBULENCE MODELING NEAR THE FREE SURFACE IN AN OPEN CHANNEL FLOW

T.F. Swean, Jr.,<sup>†</sup> R.I. Leighton,<sup>\*</sup> R.A. Handler,<sup>†</sup> J.D. Swearingen<sup>†</sup>

Center For Advanced Space Sensing  
Naval Research Laboratory  
Washington, D.C. 20375-5000

## Abstract

The velocity data from a direct numerical simulation of low Reynolds number turbulence in an open channel have been used to compute the terms in the budget equations for the turbulence kinetic energy, the dissipation of turbulence kinetic energy and the Reynolds stresses. The budget data show that the dissipation rates of the horizontal components of the turbulence are reduced near the surface while the dissipation of the vertical component remains approximately constant. The data also show that the pressure-strain term is the dominant producing term for the spanwise component of energy in the near surface region. A model for this behavior valid for flows exhibiting homogeneity in the spanwise and streamwise directions is proposed and tested against the data. In general the model is found to work well but wider testing is necessary.

## Nomenclature

$a_{ij}$	= Reynolds stress anisotropy
$A_a, A, A'$	= functions of $a_{ij}$
$a_a, b_a, \text{etc.}$	= terms in Eqs. (5)
$C_a$	= model constants
$g$	= gravitational constant
$h$	= channel height
$k$	= turbulence kinetic energy
$\ell^*$	= $\nu/u_r$ , viscous length scale
$p$	= fluctuating pressure
$p^{(a)}$	= defined in Eqs (8a,b)
$Re_h$	= $\bar{U}_1 h / \nu$ , Reynolds number
$R^*$	= $u_r h / \nu$ , wall Reynolds number
$S_{ij}$	= mean strain rate
$t^*$	= $\nu/u_r^2$ , viscous timescale
$\mathbf{U}$	= instantaneous velocity vector
$U_i$	= instantaneous velocity component
$u_i$	= fluctuating velocity component
$u_r$	= $\sqrt{\tau_w / \rho}$ , friction velocity
$u^+$	= $\bar{U}_1 / u_r$

<sup>†</sup> Research Mechanical Engineer, NRL, Member AIAA

<sup>\*</sup> Research Scientist, SAIC, McLean, VA, 22102

<sup>†</sup> Mechanical Engineer, NRL

This paper is declared a work of the U.S. Government and is not subject to copyright protection in the United States.

$z_i$	= coordinate direction
$z_3^+$	= $z_3 u_r / \nu$
$y$	= $1 - z_3$
$\delta_{ij}$	= Kronecker's delta
$\epsilon$	= isotropic dissipation function
$(\bar{\theta})$	= averaged quantity
$\nu$	= kinematic viscosity
$\Phi_{ij,a}^p$	= decomposed pressure strain, Eq. (9)
$\rho$	= density
$\tau$	= shear stress
$\Omega$	= instantaneous vorticity vector
$\Omega_i$	= instantaneous vorticity component
$\Pi_a^p$ , etc.	= terms in Eqs. (6,7)

## Subscripts

$i$	= 1, 2, 3, coordinate directions
$s$	= value at free surface
$w$	= value at wall

## 1. Introduction

The turbulent flow below a gas-liquid interface plays an important role in diverse areas ranging from environmental flows and industrial mixing processes to the remote sensing of ship wakes. The near-boundary influences upon transfer and diffusion at the interface are of primary concern in environmental and industrial applications, whereas remote sensing issues ultimately involve any surface motions that may be detectable. For example, the two most common and persistent features seen in synthetic-aperture-radar images of ship wakes are bright "narrow vees" and long dark "scars", which may be a result of surface Bragg wave generation or modification through interactions with near surface turbulence. Common to all of these problems is the need for a better understanding of the structure of turbulence below a free surface

For several decades it has been realized that the presence of a free surface influences the evolution of mean velocity and turbulence but the mechanisms have not been completely described. Early observations of Nikuradse<sup>1</sup> showed the flow in straight open channels to be three-dimensional and that the maximum of the streamwise mean velocity occurs below rather than coincident with the free surface. More recently, the studies of Ueda<sup>2</sup> and Komori et al.<sup>3</sup> for open channel flows showed that the eddy viscosity is significantly attenuated by the presence of the free

surface. In the latter paper it is also shown that in a region near the free surface the surface-normal velocity fluctuations are diminished while the fluctuations in the plane of the surface are increased. The largest increase in the near-surface region is in the spanwise component. This paper also indicates that the viscous dissipation,  $\epsilon$ , has vanishingly small normal gradient near the free surface. A similar redistribution of the turbulence intensities was observed by Thomas and Hancock.<sup>4</sup> In their work a moving wall experiment was devised such that the wall moved at the velocity of the adjacent turbulent fluid so that no velocity gradients and shear stresses were present at the wall, conditions similar to those at an uncontaminated, waveless free surface. Damping of the velocity fluctuations in the wall-normal direction accompanied by an increase in the streamwise fluctuations was observed. The spanwise fluctuations were only slightly increased. In recent experimental studies by Ramberg et al.<sup>6</sup> and Swean et al.<sup>6,7</sup> single-point hot-film measurements of the velocity correlations were obtained near the free surface in a jet flow. These measurements also showed the existence of a thin layer near the free surface wherein the redistribution of turbulence energy occurred rapidly with most of the vertical component transferring into the spanwise component, an observation similar to that of Komori et al. referenced above.

All of the above experiments experienced problems in acquiring data very near the surface. The hot-film studies suffer from the effects of probe contamination and bio-kage brought about by the intrusive sensor near the boundary. Laser doppler velocimetry methods have problems due to reflection and refraction at the free surface. As a result of the experimental problems associated with obtaining reliable measurements near an air-water interface, the situation is that considerably less is known about the characteristics of turbulence near a free surface as opposed to flow near to solid walls.

Due to the interest and relevance of the problem, a direct numerical simulation of turbulent open channel flow has been performed by Leighton et al.<sup>8</sup> This paper is an analysis of time-averaged data from Leighton's calculation with the goal of evaluating and improving turbulence models for use in practical calculations of the near-surface flow. In the next section a brief description of the calculation is given.

## 2. Direct Numerical Simulation

The incompressible 3D Navier-Stokes equations were solved for initial and boundary conditions approximating a turbulent open-channel flow of water at  $Re_h = 2340$  based on the channel depth,  $h$ , and the mean steady velocity at the free surface,

$\bar{U}_s = \bar{U}_2(z_3 = h)$ . The governing equations were re-cast in the manner suggested by Orsag and Patera<sup>9</sup> and implemented by Kim, Moin and Moser<sup>10</sup> for closed channel flow. The final equation system, in which the pressure has been eliminated, consists of a 4<sup>th</sup> order equation for the vertical velocity,

$$\left( \frac{\partial \nabla^2}{\partial t} - \frac{\nabla^4}{Re_h} \right) U_2 = \left( \frac{\partial^2}{\partial z_1^2} + \frac{\partial^2}{\partial z_3^2} \right) (\mathbf{U} \times \boldsymbol{\Omega})_2 - \frac{\partial}{\partial z_2} \left( \frac{\partial}{\partial z_1} (\mathbf{U} \times \boldsymbol{\Omega})_3 + \frac{\partial}{\partial z_3} (\mathbf{U} \times \boldsymbol{\Omega})_1 \right), \quad (1)$$

and a 2<sup>nd</sup> order equation for the vertical vorticity,

$$\left( \frac{\partial}{\partial t} - \frac{\nabla^2}{Re_h} \right) \boldsymbol{\Omega}_2 = \frac{\partial}{\partial z_2} (\mathbf{U} \times \boldsymbol{\Omega})_1 - \frac{\partial}{\partial z_1} (\mathbf{U} \times \boldsymbol{\Omega})_3, \quad (2)$$

where all variables are non-dimensionalized by  $h$  and  $\bar{U}_s$ , and bold-face type indicates vector quantities with  $\boldsymbol{\Omega} = (\nabla \times \mathbf{U})$ . Following solution of Eqs. (1,2), the streamwise and spanwise velocity components ( $U_1, U_3$ ) are recovered from the incompressibility condition and the definition of vorticity.

The equations are solved after they are Fourier transformed in the streamwise ( $z_1$ ) and spanwise ( $z_3$ ) directions and Chebyshev transformed in the vertical direction ( $z_2$ ). The calculations were performed on a  $48 \times 65 \times 64$  grid in  $z_1, z_2, z_3$  respectively, which allows the resolution of all essential turbulent scales without resort to subgrid models. With the geometry scaled by the channel height, the vertical, streamwise and transverse dimensions of the channel are 1,  $4\pi$  and  $3\pi/2$ , respectively. In wall units the domain is  $134\ell^* \times 1684\ell^* \times 632\ell^*$ , where  $\ell^* = h/R^*$  with  $R^* = 134$ . For comparison purposes a companion calculation was performed for a closed channel flow. For reasons of economy this calculation was at half the wall-normal resolution of the open channel case and was at a lower Reynolds number,  $R^* = 125$ . Nevertheless the qualitative behavior of the data for all aspects examined was identical to that reported by Mansour, Moin and Kim (henceforth MKM).<sup>11</sup> As such these closed channel data can serve in certain instances to compare qualitatively the different behavior in the open and closed channel simulations.

The boundary conditions are periodic on all dependent variables in the streamwise and spanwise directions. No slip conditions are used at the channel bottom while the free surface is approximated as a rigid free slip surface with vanishing shear. The shear-free rigid lid condition is an approximation to the exact free surface condition which is valid at low Froude number ( $\bar{U}_s(gh)^{-1/2}$ ) for a surface free of any contaminants. Leighton et al.<sup>8</sup> have estimated the surface displacement *a posteriori* from the results of

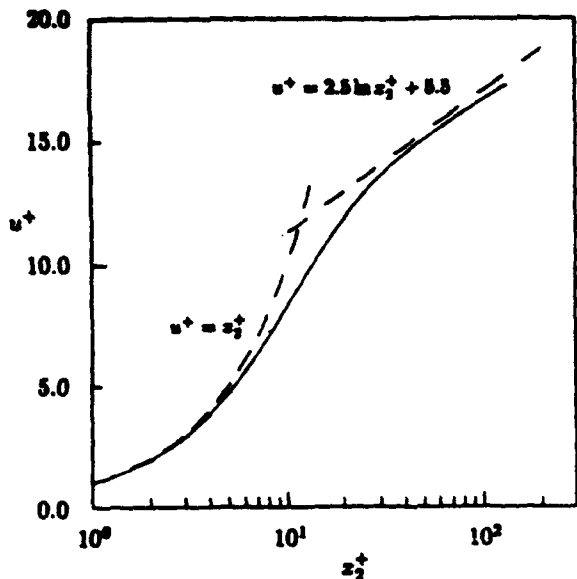


Fig. 1 Mean velocity profile across the channel.

the simulation and using the channel height,  $h = 0.04\text{m}$ , from the experiments of Komori et al.<sup>3</sup> For these conditions the rms surface deflections could be expected to be approximately  $1.6 \times 10^{-4}\text{m}$  ( $0.004h$ ) and negligible as observed in the laboratory experiments. For later reference the boundary values of the dependent and derived variables at the wall ( $z_2 = 0$ ) and free surface ( $z_2 = 1$ ) are:

$$U_1 = U_2 = U_3 = \Omega_2 = \frac{\partial U_2}{\partial z_2} = 0; z_2 = 0. \quad (3)$$

and

$$\frac{\partial U_1}{\partial z_2} = \frac{\partial U_3}{\partial z_2} = U_2 = \frac{\partial \Omega_2}{\partial z_2} = \frac{\partial^2 U_2}{\partial z_2^2} = 0; z_2 = 1. \quad (4)$$

The derivative conditions on  $U_2$  arise from continuity considerations at the respective boundaries.

The computer code used in the simulation was designed and developed to run on the CRAY X-MP/24 at the Naval Research Laboratory. Approximately  $10^{-5}$  seconds per timestep per grid point were required for the simulation. After the wall shear stress achieved a statistically steady behavior, 42 realizations of the instantaneous velocity data were saved during a time interval of approximately  $4000t^*$  where  $t^* = \nu/u_r^2$ . Statistics were obtained by averaging in the streamwise and spanwise directions and in time.

### 3. Discussion of Results

The mean velocity normalized by  $u_r$  is shown in Fig. 1. Also shown by the dashed lines are the

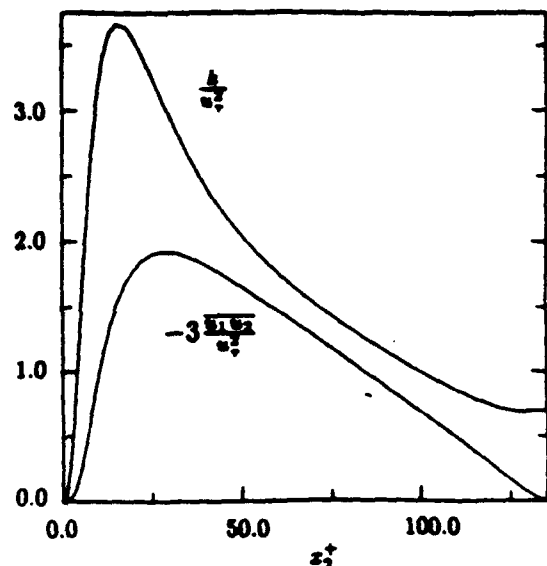


Fig. 2 Profiles of turbulence kinetic energy and Reynolds stress across the channel.

wall laws  $u^+ = z_2^+$  and  $u^+ = 2.5 \ln z_2^+ + 5.5$ . A best fit of the present data for the logarithmic region is  $u^+ = 2.4 \ln z_2^+ + 5.6$ . The lower slope is consistent with the value of 2.43 found by Nezu and Rodi<sup>12</sup> for open channel flows over a Reynolds number range  $439 \leq R^* \leq 6139$ . The intercept is near the upper bound ( $5.29 \pm 0.47$ ) found in their experiments and is probably a low Reynolds number effect.<sup>11</sup> The notable difference between the velocity data in Fig. 1 and closed channel behavior is the absence of a clearly defined wake region in the outer flow, rather the log law is maintained until very close to the free surface when the velocity adjusts to the vanishing gradient condition.

Figure 2 shows the normalized turbulence kinetic energy  $k = \frac{1}{2}(u_1^2 + u_2^2 + u_3^2)$  and the Reynolds shear stress,  $\bar{u}_1 \bar{u}_2$ , which has been further scaled for plotting by a factor as shown. According to the boundary conditions given by Eqs. (3,4) the velocity components and pressure can be expanded about the free surface as,

$$\begin{aligned} u_1 &= a_1 + c_1 y^2 + O(y^3) \\ u_2 &= b_2 y + d_2 y^3 + O(y^4) \\ u_3 &= a_3 + c_3 y^2 + O(y^3) \\ p &= a_p + c_p y^2 + O(y^3) \end{aligned} \quad (5)$$

where  $y$  is defined with the origin at the free surface. Use of these expansions and averaging results in  $k = \frac{1}{2}(a_1^2 + a_3^2) + O(y^2)$  near the surface and  $\partial k / \partial y = 0$  at the surface which is evident in the figure.

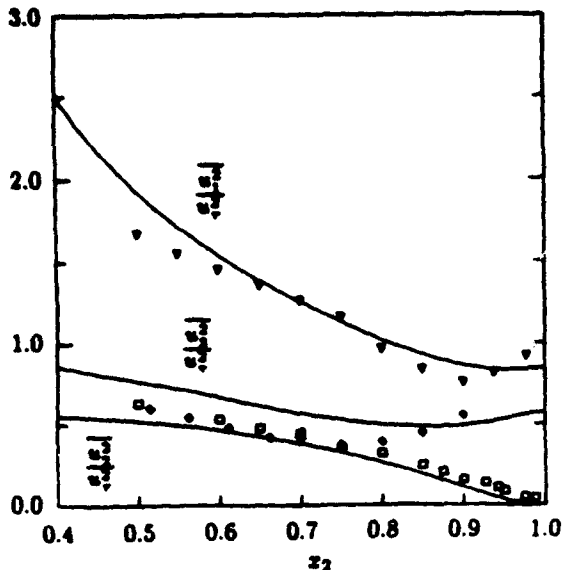


Fig. 3 Profiles of normal stresses across the channel and comparison with data of Komori et al.<sup>3</sup>

Figure 3 shows the three components of  $k$  from the simulation. The symbols are the experimental results of Komori et al.<sup>3</sup> which were taken at  $Re_h \approx 3100$ . There is qualitative agreement between the experimental and numerical results. Both exhibit an increase in the horizontal components as the free surface is approached and the increase is greatest for the spanwise component. The computed local minimum of the spanwise component occurs further from the free surface than in the streamwise component which is also consistent with the experiments. This behavior is more easily recognisable in Fig. 4 which contains the distributions of the three components of the turbulence kinetic energy made non-dimensional by the local value of  $k$ . Also shown in this figure are the data from the closed channel calculation referenced in the previous section and, as noted, these data are presented for qualitative comparison only. For the closed channel calculation the  $z_2 = 1$  boundary corresponds to the channel centerline. Figure 4 shows that near the free surface,  $z_2 > 0.7$ , most of the energy from the vertical component is transferred to the spanwise component with only a small increase in the horizontal component. This contrasts with the behaviors of the various components of turbulence energy in the closed channel simulation where the relative interchange of energy appears to be primarily from the streamwise component to the vertical in the region near the channel centerline. In order to understand this behavior, the budget equations of the individual velocity correlations have been examined.

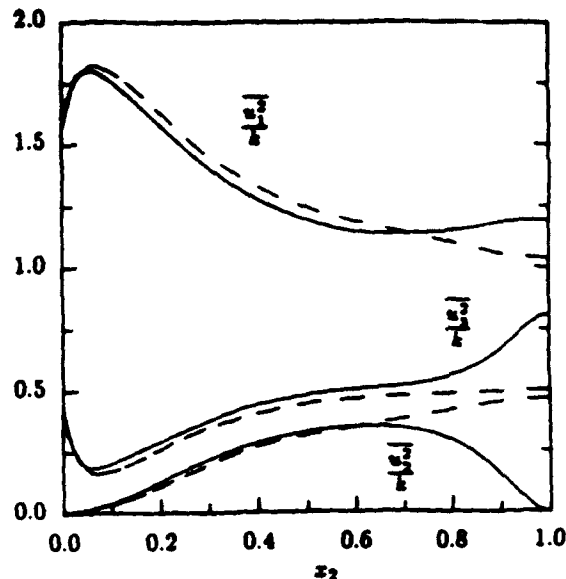


Fig. 4 Profiles of normal stresses normalized by the local value of turbulence kinetic energy. Dashed lines are from a closed channel simulation.

For the flow under consideration, which is statistically steady and homogeneous in the spanwise and streamwise directions, the transport equations for the one-point velocity correlations are,

$$\frac{D\bar{u}_i\bar{u}_j}{Dt} = 0 = P_{ij} + \Pi_{ij} + T_{ij} + \Phi_{ij} + D_{ij} - \epsilon_{ij}. \quad (6)$$

The symbols on the right-hand side of Eq. (6) denote the rates of production, pressure diffusion, turbulent transport, pressure strain, viscous diffusion and dissipation, respectively. The explicit representations of these terms are:

$$\begin{aligned} P_{ij} &= -\bar{u}_i\bar{u}_k \frac{\partial \bar{U}_j}{\partial x_k} - \bar{u}_j\bar{u}_k \frac{\partial \bar{U}_i}{\partial x_k}, \\ \Pi_{ij} &= -\frac{1}{\rho} \left( \frac{\partial p\bar{u}_i}{\partial x_j} + \frac{\partial p\bar{u}_j}{\partial x_i} \right), \\ T_{ij} &= -\frac{\partial}{\partial x_k} \bar{u}_i\bar{u}_j\bar{u}_k, \\ \Phi_{ij} &= \frac{1}{\rho} p \left( \frac{\partial \bar{u}_i}{\partial x_j} + \frac{\partial \bar{u}_j}{\partial x_i} \right), \\ D_{ij} &= \nu \frac{\partial^2 \bar{u}_i\bar{u}_j}{\partial x_k \partial x_k}, \\ \epsilon_{ij} &= 2\nu \frac{\partial \bar{u}_i}{\partial x_k} \frac{\partial \bar{u}_j}{\partial x_k}. \end{aligned}$$

The equation obtained by taking half the trace of Eq. (6) is the equation for the turbulence kinetic energy,  $k$ . The equation for the trace of the dissipation rate tensor,  $\epsilon = (\epsilon_{11} + \epsilon_{22} + \epsilon_{33})/2$ , is given by Hanjalic and Launder<sup>13</sup> as,

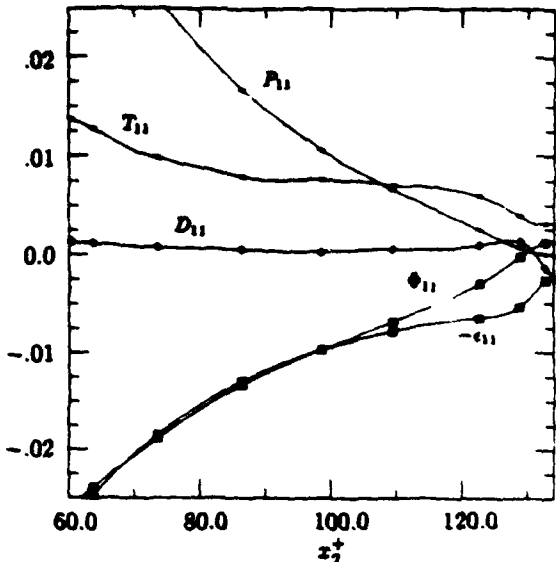


Fig. 5 Distribution of the terms in the budget of  $\bar{u}_1^2$  in the upper half of the channel.

$$\begin{aligned}
 \frac{D\epsilon}{Dt} = 0 = & -2\nu \left( \frac{\partial u_i}{\partial x_i} \frac{\partial u_k}{\partial x_k} \right) \frac{\partial \bar{U}_i}{\partial x_i} - 2\nu \left( \frac{\partial u_i}{\partial x_i} \frac{\partial u_k}{\partial x_k} \right) \frac{\partial \bar{U}_i}{\partial x_k} \\
 & - 2\nu u_k \frac{\partial u_i}{\partial x_i} \frac{\partial^2 \bar{U}_i}{\partial x_k \partial x_i} - 2\nu \frac{\partial u_i}{\partial x_i} \frac{\partial u_k}{\partial x_i} \frac{\partial u_k}{\partial x_i} \\
 & - \frac{2\nu}{\rho} \frac{\partial}{\partial x_k} \left( \frac{\partial p}{\partial x_i} \frac{\partial u_k}{\partial x_i} \right) - \nu \frac{\partial}{\partial x_k} u_k \left( \frac{\partial u_i}{\partial x_i} \frac{\partial u_i}{\partial x_k} \right) \\
 & + \nu \frac{\partial^2 \epsilon}{\partial x_k^2} - 2 \left( \nu \frac{\partial^2 u_i}{\partial x_k \partial x_i} \right)^2. \quad (7)
 \end{aligned}$$

The first four terms are production terms ( $P_i^1$  to  $P_i^4$ ), while terms five through eight are pressure transport ( $\Pi_i$ ), turbulent transport ( $T_i$ ), viscous diffusion ( $D_i$ ), and dissipation ( $\epsilon$ ), respectively.

The terms in the budget equations for the three normal stresses and the dissipation rate are shown in Figs. 5-8. All terms in Eqs. (6,7) have been normalized by  $u_i^4/\nu$  and the budgets are displayed only for the upper half of the channel nearest the free surface. Since the production of turbulence is much lower than in the high shear region close to the solid wall, the individual terms in the equations are typically an order of magnitude lower than their corresponding values near the wall. The near-wall data are available in Leighton et al.<sup>8</sup> and are very similar to the data of MKM.<sup>11</sup>

Figure 5 shows that away from the surface all terms in the  $\bar{u}_1^2$  budget have the same relative importance except  $D_{11}$ , the viscous diffusion. Moving toward the surface, the production rate vanishes with the mean velocity gradient. At the wall, the viscous

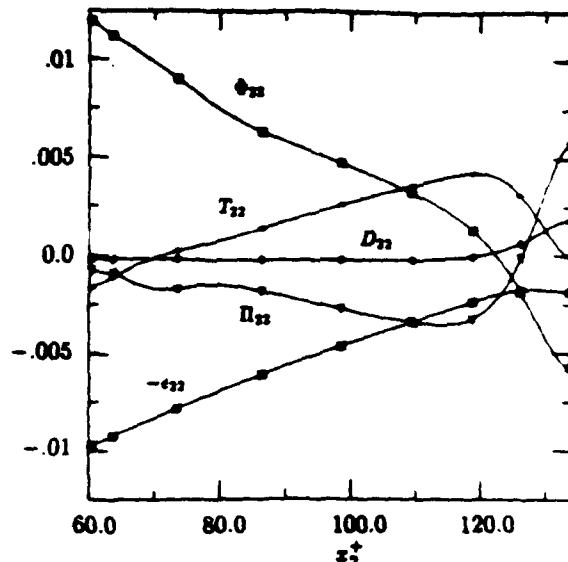


Fig. 6 Distribution of the terms in the budget of  $\bar{u}_3^2$  in the upper half of the channel.

terms balance the turbulence transport and the pressure strain, the latter having become a slight positive contributor to the budget very near the wall. The  $\bar{u}_3^2$  balance in Fig. 6 is relatively more complex than that for  $\bar{u}_1^2$ . For this component the magnitude of the budget terms near the free surface are only reduced by about one-half from their values near the solid wall. Near the free surface, the asymptotic behavior of the various terms can be determined by using Eqs. (5) as

$$\begin{aligned}
 T_{22} &= -3\bar{b}_2^3 y^2 + \dots \\
 \Pi_{22} &= -2\bar{a}_p \bar{b}_2 - 6(\bar{c}_p \bar{b}_2 + \bar{a}_p \bar{d}_2) y^2 + \dots \\
 \Phi_{22} &= 2\bar{a}_p \bar{b}_2 + 2(\bar{c}_p \bar{b}_2 + 3\bar{a}_p \bar{d}_2) y^2 + \dots \\
 D_{22} &= 2\bar{b}_2 \bar{b}_2 + 24\bar{b}_2 \bar{d}_2 y^2 + \dots \\
 \epsilon_{22} &= 2\bar{b}_2 \bar{b}_2 + 12\bar{b}_2 \bar{d}_2 y^2 + \dots
 \end{aligned}$$

It is seen that at the free surface  $\epsilon_{22}$  balances  $D_{22}$  and the two pressure-velocity terms cancel. Note that the pressure strain has rapidly become a consuming term in the near-surface region whereas it had been a major producer in the budget equation in the outer flow. This is in contrast to the behavior shown in Fig. 7 for the  $\bar{u}_3^2$  component. In this case  $\Phi_{33}$  increases near the surface and at the surface is considerably more of a source for  $\bar{u}_3^2$  than is  $\Phi_{11}$  in the  $\bar{u}_1^2$  budget. This largely explains why the transverse component of turbulence kinetic in Fig. 4 is increased relatively more so than the streamwise component as  $\bar{u}_3^2$  approaches zero at the free surface. In the next section a model for this behavior is proposed.

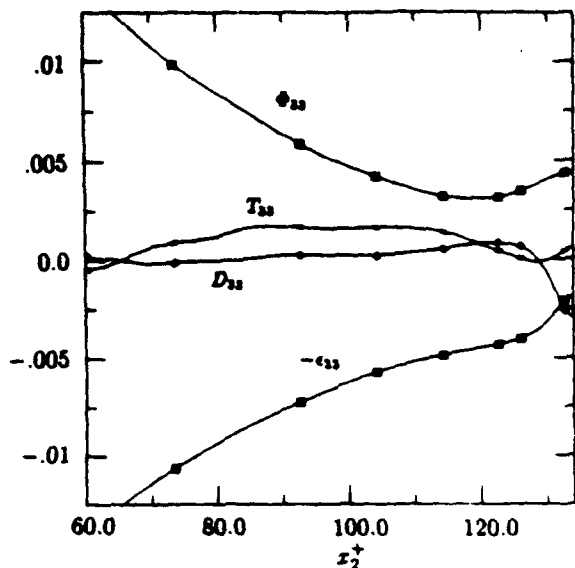


Fig. 7 Distribution of the terms in the budget of  $u_2^2$  in the upper half of the channel.

A curious feature contained in Figs. 5 and 7 is the behavior of  $\epsilon_{ii}$  as the surface is approached. Moving toward the free surface the dissipation rates exhibit a sharp drop in magnitude in the upper 5-10% of the channel. The  $\epsilon_{22}$  on the other hand shows a very slight increase in magnitude and could well be approximated as constant in this region. This behavior is contrary to standard modeling assumptions near the free surface. Hossain and Rodi<sup>14</sup> and later Naot and Rodi<sup>15</sup> have assumed that in most respects other than the vanishing of the surface-normal velocity component, the free surface behaves like a symmetry plane. The exception is the presumed behavior of the dissipation rate for turbulence kinetic energy which is expected to increase near the surface. This is based on the assumption that the macro-length scale of the turbulence ( $L \propto k^{1.8}/\epsilon$ ) is reduced by the presence of the boundary. This scale does not become zero since it reflects the fluctuating motion in all three directions and the horizontal extent of the eddies is not restricted.

The terms in the budget equation for the dissipation rate are shown in Figure 8. In the upper portion of the channel the first three production terms in Eq. (7) are small and have been lumped together as shown. Until very near the free surface the production by turbulence,  $P_t^4$ , largely balances the dissipation term. Very near the surface the dominant terms are the viscous diffusion and the dissipation, each exhibiting very large gradients of opposite sign near the boundary. Reconsidering Figs. 5 and 7, it is seen that in these cases also the rapid variation in

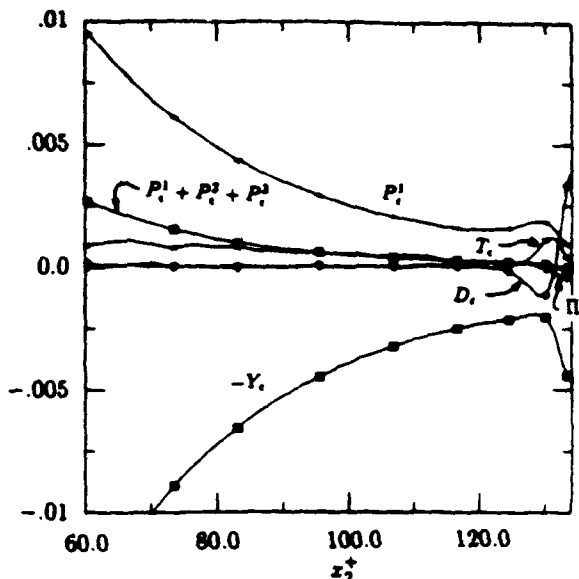


Fig. 8 Distribution of the terms in the budget of the turbulence kinetic energy dissipation rate in the upper half of the channel.

the dissipation term appears to be at least partially offset by the variation in the diffusion term. It should be remembered that  $\epsilon_{ii}$  (or  $\epsilon$ ) is not the actual dissipation of turbulent energy for inhomogeneous flows although it does approximate the total dissipation for high Reynolds number. The particular terms  $D_{ii}$  and  $\epsilon_{ii}$  have arisen from the combination of the actual dissipation rate with the rate of work by the viscous shear stresses of the turbulence.<sup>16</sup> In flows far from solid walls the viscous diffusion is generally neglected and as such the modeled dissipation rate implicitly models the work term. Figure 9 shows the balance of turbulence kinetic energy obtained from the trace of Eq. (6). The viscous terms have been added and together they balance the transport terms at the wall. It is seen that the total viscous term varies only slightly near the boundary and might be easier to model. Future work will re-process the velocity data to determine the actual dissipation term separately from the work term.

#### 4. Pressure-Strain Rate Model

The above data show that the pressure-strain term is a key contributor to the redistribution of normal stresses near the boundaries. Leighton et al<sup>8</sup> have decomposed the fluctuating pressure into a 'slow' pressure,  $p^{(1)}$ , a 'fast' pressure,  $p^{(2)}$ , and a Stokes pressure,  $p^{(3)}$ , in the manner suggested by MKM.<sup>11</sup> These components satisfy the equations:

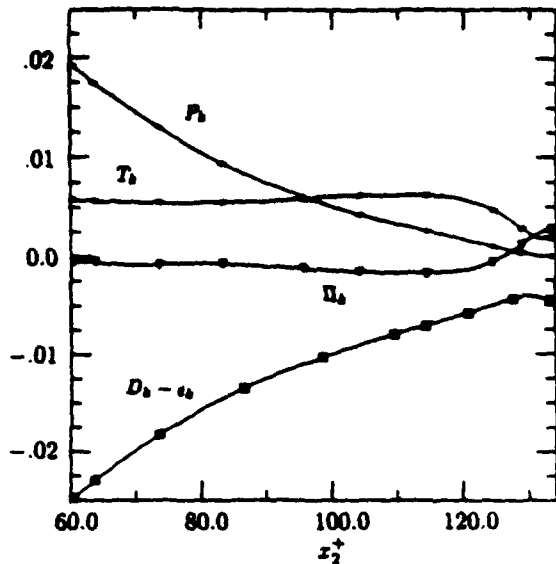


Fig. 9 Distribution of the terms in the budget of turbulence kinetic energy in the upper half of the channel.

$$\begin{aligned}\nabla^2 p^{(1)} &= -\left(\frac{\partial u_i}{\partial x_j} \frac{\partial u_j}{\partial x_i} - \frac{\partial u_i}{\partial x_i} \frac{\partial u_j}{\partial x_j}\right), \\ \nabla^2 p^{(2)} &= -2 \frac{\partial \bar{U}_1}{\partial x_2} \frac{\partial u_2}{\partial x_1}, \\ \nabla^2 p^{(s)} &= 0,\end{aligned}\quad (8a)$$

with boundary conditions,

$$\begin{aligned}\frac{\partial p^{(1)}}{\partial x_2} &= 0 : x_2 = 0, 1 \\ \frac{\partial p^{(2)}}{\partial x_2} &= 0 : x_2 = 0, 1 \\ \frac{\partial p^{(s)}}{\partial x_2} &= \frac{1}{Re_h} \frac{\partial^2 u_2}{\partial x_2^2} : x_2 = 0, 1.\end{aligned}\quad (8b)$$

The pressure data from the solution of Eqs. (8a-b) have been used to decompose the pressure-strain term into

$$\Phi_{ii} = 2p \frac{\partial u_i}{\partial x_i} = \Phi_{ii}^{(1)} + \Phi_{ii}^{(2)} + \Phi_{ii}^{(s)}.$$

Figure 10 shows this splitting in the upper portion of the channel for each of the components. The Stokes term is only of consequence very near the solid wall and is not plotted. It is seen that the slow or return terms are dominant in the region plotted. Only in the  $\Phi_{33}$  component is the fast term the larger of the two and for the  $\Phi_{22}$  term the fast component is nearly zero over the whole domain shown.

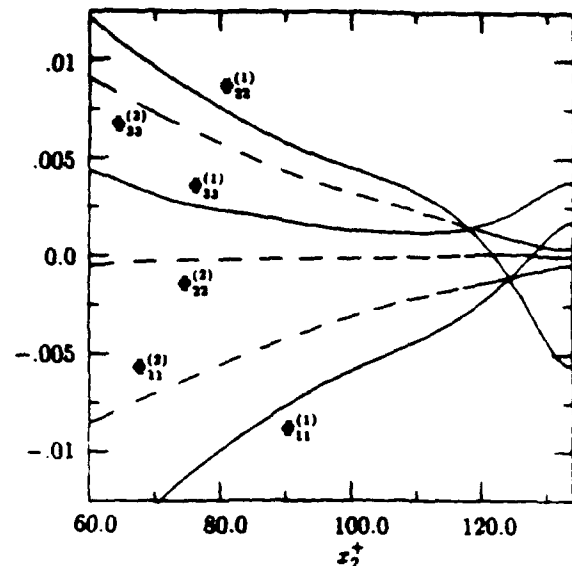


Fig. 10 Distribution of the rapid and return contributions to the pressure-strain rate for each diagonal component.

The distributions of  $\Phi_{ij}$  shown in Fig. 10 differ markedly at the free surface relative to their behavior at a solid wall.<sup>11</sup> Most importantly they do not vanish in any component. Clearly some sort of surface proximity effect is needed in order to model the rapid variations exhibited. Generally the total term is modeled,

$$\Phi_{ij} = \Phi_{ij}^{(1)} + \Phi_{ij}^{(2)} + \Phi_{ij,w}^{(1)} + \Phi_{ij,w}^{(2)} \quad (9)$$

where  $\Phi_{ij}^{(1)}$  is some variant of Rotta's<sup>17</sup> model,

$$\Phi_{ij}^{(1)} = -C_1 \epsilon a_{ij}, \quad (10)$$

and the rapid term includes at least the isotropization of production term,  $(P_{ij} - \frac{2}{3} P_k \delta_{ij})$ . Typical of these models and one that is borrowed from in the current study, is that due to Launder, Reece and Rodi.<sup>18</sup>

$$\begin{aligned}\Phi_{ij}^{(2)} &= -\frac{(C'_2 + 8)}{11} (P_{ij} - \frac{2}{3} P_k \delta_{ij}) \\ &- 2 \frac{(30C'_2 - 2)}{55} k S_{ij} - \frac{8(C'_2 + 8)}{11} (B_{ij} - \frac{2}{3} P_k \delta_{ij}),\end{aligned}\quad (11)$$

where,

$$B_{ij} = -\bar{u}_i \bar{u}_k \frac{\partial \bar{U}_k}{\partial x_j} - \bar{u}_j \bar{u}_k \frac{\partial \bar{U}_k}{\partial x_i},$$

and  $C'_2 = 0.4$ . The wall terms are usually modeled in a form analogous to Eqs. (10,11) but with different coefficients and including a damping function. The Launder, Reece and Rodi form is,

$$\Phi_{ij,w}^{(1)} + \Phi_{ij,w}^{(2)} = (0.125 \epsilon a_{ij} + 0.015 (P_{ij} - B_{ij})) \frac{k^{\frac{3}{2}}}{\epsilon x_2}.$$

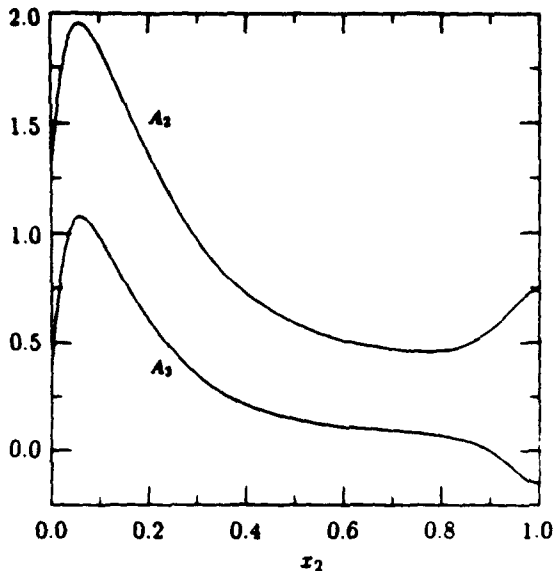


Fig. 11 Distribution of the second and third invariants of the Reynolds stress anisotropy tensor across the channel.

This particular damping function is singular at a free surface since  $k$  does not vanish. A virtual origin could be used and has been employed by Naot and Rodi<sup>15</sup>. An alternative is to use a term based on the surface-normal velocity such as  $f_w \sim (u_2^2)^{5/3} k / \epsilon x_2$ , which does not become singular and is more appealing on physical grounds. However, the approach taken in this study is to make use of the properties of the second and third invariants,  $A_2$  and  $A_3$  of the stress anisotropy tensor,  $a_{ij}$ .

$$A_2 \equiv a_{ij} a_{ij} ; A_3 \equiv a_{ij} a_{jk} a_{ki}. \quad (12)$$

As pointed out by Lumley<sup>19</sup>, if one component of velocity vanishes, then the difference,  $A_2 - A_3$ , becomes the constant value  $8/9$  irrespective of the behavior of the other two velocity components. In this case the function  $A \equiv 1 - 9(A_2 - A_3)/8 = 0$  in the regions where the turbulence becomes locally two-dimensional. At the free surface the pressure-strain rates do not vanish so it is necessary to modify this approach. Figure 11 shows the variation of  $A_2$  and  $A_3$  computed from the simulation data. Near both boundaries  $A_2 - A_3 = 8/9$  as  $a_{22} \rightarrow -2/3$ . Near the free surface it is observed that  $A_3$  becomes negative. This is very close to the  $x_2$  location where  $a_{33}$  becomes positive (see Fig. 4). For flows in which the non-zero velocity components remain uncorrelated as the third component vanishes, the vanishing of  $A_3$  corresponds exactly to the vanishing of one of the remaining remaining  $a_{ii}$ . Equation (12) shows that for such a flow  $A_3$  reaches a minimum of  $-2/9$  when  $a_{11} = a_{33}$ . It is plausible to assume that in the absence of boundaries

the horizontal components will tend to approach this state at a free surface. The available experimental data as well as the current simulation data support this conjecture. If this is the case then the vanishing of  $A_3$  can be used as a detector for free surface proximity effects.

A model based on Lumley's suggestion and used as the basis of the current model is that due to Launder and Shima.<sup>20</sup> In their model  $\Phi_{ij}^{(1)}$  is given by Eq. (10) with the coefficient,

$$C_1 = 2.58 A A_2^{25} \{1 - \exp((0.0067 k^2 / \nu \epsilon)^2)\}. \quad (13)$$

The rapid term is given by the first term in Eq. (11) with the coefficient,  $8(C'_2 + 8)/11$ , replaced with  $C_2 = 0.75 A^{5/3}$ . The Launder and Shima model also contains additional explicit expressions for the wall terms in Eq. (9) that are not repeated here since they are not used.

In the current work an effort has been made to construct a model with a minimum of parameters. In Eq. (13), both the coefficient,  $A$ , and the term in braces containing the Reynolds number act to damp the pressure-strain rate near a solid wall. Equations (8a,b) are only dependent upon viscosity thru the boundary condition on the equation for  $p^{(s)}$  and MKM have shown that for low Reynolds flows of the type under study here,  $\Phi_{ij}^{(s)}$  is small even near the wall. The term in braces has thus been omitted in the current study. Exploratory calculations retaining the term, and using the statistics from the simulation have shown that the term has little effect on model performance and in fact the pressure-strain rate data are better correlated with its omission. Although the concern here has not been model performance near the solid wall, this study has also retained the third term in Eq. (11) since its inclusion substantially improves the behavior in the  $\Phi_{22}$  component near the wall. The basic form of the current model then becomes,

$$\Phi_{ij}^{(1)} = -C_1 A \epsilon a_{ij} ; C_1 \equiv 1.3 A_2^{25}. \quad (14)$$

$$\Phi_{ij}^{(2)} = A_2^{5/3} \left( -\frac{(C'_2 + 8)}{11} (P_{ij} - \frac{2}{3} P_k \delta_{ij}) - \frac{8(C'_2 + 8)}{11} (B_{ij} - \frac{2}{3} P_k \delta_{ij}) \right). \quad (15)$$

The numerical value in the definition of  $C_1$  above has been adjusted from its former value to account for the factor of approximately  $1/2$  that the retention of the exponential term of the original model would have contributed in the outer flow. The form adopted for the free surface region is,

$$\Phi_{ij,s}^{(1)} = -C_1 (A - A') \epsilon (2.2 a_{ij} + 9.8 (a_{ik} a_{ki} - A_2/3)). \quad (16)$$

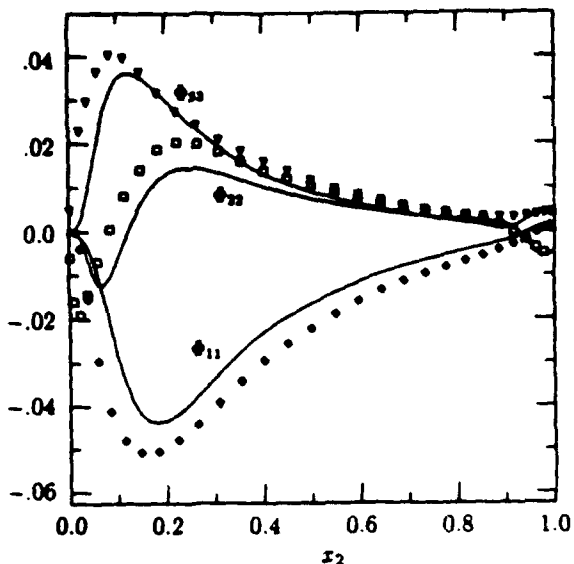


Fig. 12 Comparison of the modeled pressure-strain rate with the data from the simulation.

where  $C_1$  is given by Eq. (14) and  $A' \equiv 1 - 9/8(A_2 - |A_3|)$ . As discussed earlier this term will only become active when the anisotropy in one of the horizontal components vanishes while the vertical velocity is damped near the free surface. The constants 2.2 and 9.8 have been determined so as match the overall level of the data in the surface region. The 2<sup>nd</sup> order term has been shown by Speziale et al.<sup>21</sup> to occur in a formal expansion for  $\Phi_{ij}$ , and it is used in the current formulation to achieve more closely the separation in  $\Phi_{33}$  and  $\Phi_{11}$  observed in the simulation. Near the free surface the anisotropy in the  $u_3$  component of velocity is relatively small compared to  $a_{11}$  so to first order in anisotropy the model predicts that  $\Phi_{11} > \Phi_{33}$ . The second order term is small in both components but has a much greater relative effect on the  $u_3$  component.

Figure 12 shows the model performance when computed with the simulation data which are represented by the symbols. The lines are computations with Eqs. (14-16). The incorrect near-surface asymptotic behavior is mostly due to the sharp variation in  $\epsilon$  discussed in the previous section. Incorporating the proper asymptotic behavior near the free surface will be a topic for further research. Near the solid wall the current model performs reasonably well and markedly better than the original Launder, Reece and Rodi model which was analyzed by MKM.<sup>11</sup> The asymptotic behavior near the wall is not correct and this must be examined as well. Without the inclusion of the term containing  $B_{ij}$  in Eq. (15) the change in sign in the near wall region for  $\Phi_{22}$  is not achieved but

rather the modeled distribution is uniformly positive until vanishing at the wall.

### 5. Concluding Remarks

The simulation data show that there is a preferential redistribution of turbulence energy to the spanwise component of energy as the normal component is damped at the free surface. This is in accordance with the still-limited experimental observations. The budget equations show that the pressure-strain rate term, particularly the return term, is a key contributor to this behavior. The budgets also show that the isotropic part of the dissipation of turbulence energy decreases rapidly very near the free surface which is contrary to current modeling assumptions which assume it to increase to account for reduced levels of eddy viscosity observed near the free surface. A model for the near-surface pressure-strain term has been proposed and shown to correlate the simulation data fairly well. In its current form the model is limited to flows in which the correlation of the horizontal velocity components is small while the vertical component vanishes. Much wider testing is necessary to determine when this condition exists. Future efforts will consider this point along with questions raised regarding the dissipation of turbulence at the surface.

### Acknowledgements

This work is supported by the Naval Research Laboratory under the Core fluid mechanics program and the Office of Naval Research under the Surface Ship Wake Detection Program. Many of the calculations were performed under an NRL Cray Grant. The authors acknowledge the many fruitful discussions with Dr. Jeff Crouch.

### References

- <sup>1</sup>Nikuradse, J., "Turbulente Strömung im Innern des rechteckigen offenen Kanals", *Forschungsarbeiten*, Heft 281, 1926, pp. 36-44.
- <sup>2</sup>Ueda, H., "Eddy Diffusivity Near the Free Surface of Open Channel Flow", *International Journal of Heat and Mass Transfer*, Vol. 20, No. 11, 1977, pp. 1127-1136.
- <sup>3</sup>Komori, S., Ueda H., Ogino, F. and Mizushima, T., "Turbulence Structure and Transport Mechanism at the Free Surface in an Open Channel Flow", *International Journal of Heat and Mass Transfer*, Vol. 25, No. 4, 1982, pp. 513-521.
- <sup>4</sup>Thomas, S.M. and Hancock, P.E., "Grid Turbulence Near a Moving Wall", *Journal of Fluid Mechanics*, Vol. 82, 1977, pp. 481-496.
- <sup>5</sup>Ramberg, S.E., Swean, T.F., Jr. and Plesniak, M.W., "Turbulence Near a Free Surface in a Plane Jet", *NRL Memorandum Report No. 6367*, 1989.
- <sup>6</sup>Swean, T.F., Jr., Ramberg, S.E., Plesniak, M.W. and Stewart, M.B., "Turbulent Surface Jet in

Channel of Limited Depth", *ASCE Journal of Hydraulic Engineering*, Vol. 115, No. 12, 1989, pp. 1587-1606.

<sup>7</sup>Swean, T.F., Jr., Ramberg, S.E. and Miner, E.W., "Anisotropy in a Turbulent Jet Near a Free Surface" *ASME Journal of Fluids Engineering*, to appear 1991.

<sup>8</sup>Leighton, R.I., Swean, T.F., Jr., Handler, R.A. and Swearingen, J.D. "Direct Simulation of Low Reynolds Number Open Channel Flow", NRL Memorandum Report, 1991.

<sup>9</sup>Orszag, S.A. and Patera, A.T., "Subcritical Transition to Turbulence in Planar Shear Flows" in *Transition and Turbulence*, ed. by R.E. Myer, Academic Press, London, New York, 1981, pp. 127-146.

<sup>10</sup>Kim, J., Moin, P. and Moser, R., "Turbulence Statistics in a Fully Developed Channel Flow at Low Reynolds Number", *Journal of Fluid Mechanics*, Vol. 177, 1987, pp. 133-136.

<sup>11</sup>Mansour, N.N., Moin, P. and Kim, J., "Reynolds-Stress and Dissipation-Rate Budgets in a Turbulent Channel Flow", *Journal of Fluid Mechanics*, Vol. 194, 1988, pp. 15-44.

<sup>12</sup>Nezu, I. and Rodi, W., "Open-Channel Flow Measurements With a Laser Doppler Anemometer", *ASCE Journal of Hydraulic Engineering*, Vol. 112, No. 5, 1986, pp. 335-355.

<sup>13</sup>Hanjalić, K. and Launder, B.E., "Contribution Towards a Reynolds-Stress closure for Low-Reynolds-Number Turbulence", *Journal of Fluid Mechanics*, Vol. 74, 1976, pp. 593-610.

<sup>14</sup>Hossain, M.S. and Rodi, W., "Mathematical Modelling of Vertical Mixing in Stratified Channel Flow", *Proceedings, Second Symposium on Stratified Flows*, Trondheim, Norway, 1980.

<sup>15</sup>Naot, D. and Rodi, W., "Calculation of Secondary Currents in Channel Flow", *ASCE Journal of Hydraulic Engineering*, Vol. 108, No. HY8, 1982, pp. 948-968.

<sup>16</sup>Hinze, J.O., *Turbulence*, McGraw-Hill, New York, 1975.

<sup>17</sup>Rotta, J.C., "Statistical Theorie Nichomogener Turbulenz", *Zeitschrift für Physik*, Vol. 129, 1951, p.547.

<sup>18</sup>Launder, B.E., Reece, G.J. and Rodi, W., "Progress in the Development of a Reynolds-Stress Turbulence Closure", *Journal of Fluid Mechanics*, Vol. 68, 1975, pp. 537-565.

<sup>19</sup>Lumley, J.L., "Computational Modeling of Turbulent Flows", *Advances in Applied Mechanics*, Vol. 18, 1978, p.123-176.

<sup>20</sup>Launder, B.E. and Shima, N., "Second-Moment Closure for the Near-Wall Sublayer: Development and Application", *AIAA Journal*, Vol. 27, No. 10, 1989, p.1319-1325.

<sup>21</sup>Speziale, C.G., Sutcu, S. and Gatski, T.B., "Modeling the Pressure-Strain Correlation of Turbulence - An Invariant Dynamical Systems Approach", NASA Contractor Report 181979, ICASE Report No. 90.5, 1990.

## **Appendix G**

### **Length Scales of Turbulence Near a Free Surface**



**AIAA-91-1775**

**Length Scales of Turbulence  
Near a Free Surface**

R. Handler, J. Swearingen, T. Swean  
Naval Research Laboratory  
Washington, DC

R. Leighton  
Science Applications, Inc.  
McLean, VA

**AIAA 22nd Fluid Dynamics,  
Plasmadynamics & Lasers Conference  
June 24-26, 1991 / Honolulu, HI**

## LENGTH SCALES OF TURBULENCE NEAR A FREE SURFACE

R.A. Handler,<sup>†</sup> J.D. Swearingen,<sup>†</sup> T.F. Swean, Jr.,<sup>††</sup> R.I. Leighton\*

Center For Advanced Space Sensing

Naval Research Laboratory

Washington, D.C. 20375-5000

## ABSTRACT

Two-point correlations, energy spectra, and length scales are examined in the vicinity of a free surface, modeled as a shear-free boundary in a direct numerical simulation of open channel flow. The length scale results indicate that a typical eddy is flattened as it interacts with the surface. The scales associated with the vertical component of velocity seem to determine the extent of the source layer described in the Hunt-Graham model. The energy spectra show qualitative agreement with the model, though higher resolution calculations will be required to make more quantitative comparisons. Additionally, the proximity of the free surface to the bottom solid wall of the channel evidences itself as a wall-layer streaky structure which persists to a noticeably greater distance away from the wall. Some speculations are offered to explain this effect.

## NOMENCLATURE

$h$	= channel height
$k$	= turbulent kinetic energy
$\ell^*$	= $\nu/u_r$ , viscous length scale
$Re_h$	= $\bar{U}_h h/\nu$ , Reynolds number
$R^*$	= $u_r h/\nu$ , wall Reynolds number
$R_\theta$	= $U_\infty \theta/\nu$ , momentum thickness Reynolds number
$t^*$	= $\nu/u_r^2$ , viscous timescale
$\mathbf{U}$	= instantaneous velocity vector
$U_i$	= instantaneous velocity component
$u_i$	= fluctuating velocity component
$u_r$	= $\sqrt{\tau_w/\rho}$ , friction velocity
$\lambda_{ij}$	= turbulent microscale
$\Lambda_{ij}$	= turbulent macroscale
$R_{ij}$	= two-point correlation tensor
$x_i$	= coordinate direction
$x_i^+$	= $x_i u_r/\nu$

<sup>†</sup>Mechanical Engineer, NRL,<sup>††</sup>Research Mechanical Engineer, NRL, Mem. AIAA

\*Research Scientist, SAIC, McLean, VA, 22102

This paper is declared a work of the U.S. Government and is not subject to copyright protection in the United States.

$\overline{(\ )}$	= averaged quantity
$\Phi_{ij}$	= spectral density
$\kappa_1$	= streamwise wavenumber
$\nu$	= kinematic viscosity
$\rho$	= density
$\theta$	= momentum thickness
$\tau_w$	= shear stress
$\Omega$	= instantaneous vorticity vector
$\Omega_i$	= instantaneous vorticity component

## Subscripts

$i$	= 1, 2, 3, coordinate directions
$s$	= value at free surface
$\infty$	= value in free stream
$w$	= value at wall

## 1. INTRODUCTION

The study of the structure of turbulence near a free surface is obviously important to our understanding of the complex interaction of the atmosphere and upper ocean. It is also of fundamental relevance to the wall-bounded turbulence problem, since it isolates the boundary influence on turbulent fluctuations from the turbulence production mechanism at the wall. The first detailed experiment which addressed itself to this particular problem was that of Uzkan and Reynolds<sup>1</sup> (UR). They passed grid generated homogeneous turbulence over a wall which moved with the mean flow and therefore generated no mean shear at the boundary. They found that the streamwise turbulence intensity near the shear-free boundary did not peak as it does near a stationary solid wall, but instead decreased monotonically from its free stream value to zero at the boundary. Later, Thomas and Hancock<sup>2</sup> (TH) performed a similar experiment at a Reynolds number about 20 times greater than that of UR and found that the intensity of the streamwise component increases as the boundary is approached.

The discrepancy between these two results was explained satisfactorily by Hunt and Graham<sup>3</sup> (HG) who proposed a two layer model for the interaction. At high turbulent Reynolds numbers there exists a thin viscous layer near the wall embedded in a larger source layer. The source layer should be roughly the size of the integral length scale of the free stream turbulence and exists essentially because of the no mass-flux condition at the boundary. Their theory predicts a redistribution of turbulent energy in the source layer

from the vertical component of velocity to the streamwise and spanwise components. The UR result was easily explained since, at the low Reynolds number of their experiment, the viscous layer dominated the region near the surface and the turbulence was accordingly damped. At the higher Reynolds number of the TH experiment, the source layer dominated and the redistribution of the turbulence behaved according to the HG model. Many of these results were later confirmed by the large eddy simulations of Biringen and Reynolds<sup>4</sup>. Recently, Brumley and Jirka<sup>5</sup> (BJ) presented results for experiments in which homogeneous turbulence interacted with a free surface. Their results agreed reasonably well with a modified form of the HG model.

The simulations performed here were designed to represent as closely as possible the physics of free surface/turbulence interaction in which the effects of surface waves can be safely neglected. For this purpose, fully developed turbulence between a solid wall and a free surface is simulated. The physical processes represented by these simulations differ in some important respects from processes involved in the physical experiments noted above. First, in these simulations, no viscous layer can develop since  $u_1$  and  $u_3$ , the fluctuating streamwise and spanwise velocity components, are not forced to zero as in the UR and TH experiments. In fact, even in the BJ experiments a viscous layer developed near the surface due to the presence of surface contaminants. Secondly, in these simulations, the turbulence impinging on the free surface is not isotropic since it is being generated at a solid wall. It is evident that the solid wall is acting as a generator of anisotropic turbulence which is then convected toward the free surface. Lastly, it is possible to examine the question of the influence, if any, of the free surface on the turbulent structure at the solid surface boundary. In this work two-point correlations, energy spectra, and turbulent length scales will be examined in an effort to investigate the turbulent structure near a free surface in the absence of surface waves.

## 2. DIRECT NUMERICAL SIMULATION

The incompressible three-dimensional Navier-Stokes equations are solved for initial and boundary conditions approximating a turbulent open channel flow of water at a Reynolds number,  $Re_h$ , based on the channel height,  $h$ , and the mean velocity at the free surface,  $\bar{U}_s$ , of 2340. The notation  $x_1$ ,  $x_2$ , and  $x_3$  is used to denote the streamwise, wall-normal, and spanwise coordinates respectively. The governing equations, formulated in the manner suggested by Orszag and Patera<sup>6</sup> and later implemented in a simpler form by Kim, Moin and Moser<sup>7</sup>, consist of a

fourth order equation for the vertical velocity,  $U_2$  :

$$\left( \frac{\partial \nabla^2}{\partial t} - \frac{\nabla^4}{Re_h} \right) U_2 = \left( \frac{\partial^2}{\partial x_1^2} + \frac{\partial^2}{\partial x_3^2} \right) (\mathbf{U} \times \boldsymbol{\Omega})_2 - \frac{\partial}{\partial x_2} \left( \frac{\partial}{\partial x_1} (\mathbf{U} \times \boldsymbol{\Omega})_3 + \frac{\partial}{\partial x_3} (\mathbf{U} \times \boldsymbol{\Omega})_1 \right), \quad (1)$$

and a second order equation for the vertical vorticity,  $\Omega_2$  :

$$\left( \frac{\partial}{\partial t} - \frac{\nabla^2}{Re_h} \right) \Omega_2 = \frac{\partial}{\partial x_3} (\mathbf{U} \times \boldsymbol{\Omega})_1 - \frac{\partial}{\partial x_1} (\mathbf{U} \times \boldsymbol{\Omega})_3, \quad (2)$$

where all variables are made non-dimensional by  $h$  and the initial value of  $\bar{U}_s$ . Here, the instantaneous velocity vector is given by  $\mathbf{U}$  and the instantaneous vorticity vector is defined by  $\boldsymbol{\Omega} = (\nabla \times \mathbf{U})$ . Following the solution of equations 1 and 2, the streamwise and spanwise velocity components,  $U_1$  and  $U_3$ , are recovered from the incompressibility condition.

The equations of motion are solved in Fourier-Chebyshev space where Fourier modes are employed in the horizontal plane and Chebyshev modes in the wall normal direction. The calculations are performed on a  $64 \times 65 \times 48$  grid in  $x_1$ ,  $x_2$ ,  $x_3$  respectively. With the geometry scaled by the channel height, the streamwise, vertical, and transverse dimensions of the channel are  $4\pi$ , 1, and  $3\pi/2$  respectively. In terms of the viscous parameters consisting of the friction velocity,  $u_r$ , and the kinematic viscosity,  $\nu$ , the domain is  $1684\ell^* \times 134\ell^* \times 632\ell^*$  and the Reynolds number,  $R^*$ , is 134. To facilitate substantive qualitative comparisons with the wall-bounded turbulence problem, a companion calculation for a closed channel flow is utilized. For reasons of economy, this calculation is at half the wall-normal resolution of the open channel case and is at a somewhat lower Reynolds number,  $R^* = 125$ . Nevertheless the behavior of these data for all aspects examined is identical to that reported by KMM.

The boundary conditions utilized are periodic on all dependent variables in the streamwise and spanwise directions. No-slip conditions are used at the channel bottom while the free surface is approximated as a rigid, free-slip surface with vanishing shear. The shear-free rigid lid condition is an approximation to the exact free surface condition which is valid at low Froude number for a surface free of any contaminants. Leighton *et al.*<sup>8</sup> have estimated the surface displacement *a posteriori* from the results of the simulation using the channel height,  $h = 0.04m$ , from the experiments of Komori *et al.*<sup>9</sup>. For these conditions the rms surface deflections are expected to be approximately  $1.6 \times 10^{-4}m$  ( $0.004h$ ) and are clearly negligible as observed in the laboratory experiments. The boundary conditions at the solid wall ( $x_2 = 0$ ) and the free surface ( $x_2 = 1$ ) are:

$$U_1 = U_2 = U_3 = 0; x_2 = 0, \quad (3)$$

and

$$\frac{\partial U_1}{\partial x_2} = \frac{\partial U_3}{\partial x_2} = U_2 = 0; x_2 = 1. \quad (4)$$

The code developed for the simulation is designed to run on the CRAY X-MP/24 computer at the Naval Research Laboratory and requires approximately  $10^{-5}$  CPU seconds per timestep per grid point. After the wall shear stress achieved a statistically steady behavior, 42 realizations of the instantaneous velocity data were saved during a time interval of approximately  $4000t^*$  where  $t^* = \nu/u_r^2$ . Statistics were obtained by averaging in the streamwise and spanwise directions as well as over all realizations. Swean *et al.*<sup>10</sup> find good agreement between these simulations and open channel flow experiments.

### 3. TWO-POINT CORRELATIONS AND ENERGY SPECTRA

The turbulent structure near the free surface is revealed in some detail by examining the two-point correlations and energy spectra at different depths below the surface. The two-point correlation function,  $R_{ij}$ , is defined by:

$$R_{ij}(\Delta x_1, \Delta x_3, x_2, x_2') = \frac{u_i(x_1, x_3, x_2)u_j(x_1', x_3', x_2')}{\sqrt{u_i^2 u_j^2}}, \quad (5)$$

where,  $x_j' = x_j + \Delta x_j$ ,  $j=1,3$ . Here, only the properties of  $R_{ij}$  for which  $x_2 = x_2'$  and  $i = j$  will be described. These correlations were computed by averaging over all flow realizations and all flow symmetries (see Sirovich<sup>11</sup>). Figure 1 shows a comparison of the streamwise correlations for open and closed channel flows at several  $x_2$  locations. Note that in each figure a secondary axis is given showing the correlation length in terms of wall variables, i.e.  $\Delta x_1^+$  for this case. In the region close to the bottom solid wall ( $0 < x_2 < 0.5$ ;  $0 < x_2^+ < 68$ ) the streamwise correlations are virtually identical for all three velocity components. As an example, note the similarity between the correlations at  $x_2 = 0.071$  for open channel flow with those of closed channel flow at  $x_2 = 0.076$ . The only notable difference is a somewhat longer streamwise correlation length for  $u_1$  in the open channel case. At distances farther from the wall, however, the differences between the two flows become increasingly more pronounced. As the free surface is approached, two trends are evident. First, the streamwise distance at which  $R_{33}(\Delta x_1, 0, x_2)$ , (subsequently denoted  $R_{33}(\Delta x_1)$ ) attains its minimum value increases as the free surface is approached. For example, at  $x_2 = 0.524$ , the minimum occurs at  $\Delta x_1 \approx 1.34$  and

as the free surface is approached this increases roughly 17% to  $\Delta x_1 \approx 1.57$ . For the closed channel case, however, this distance undergoes virtually no change as  $x_2$  varies from 0.572 to the centerline. Secondly, we observe that the streamwise correlation length of the vertical component of velocity in the open channel case, which may be loosely defined by the first zero crossing, decreases significantly between  $x_2 = 0.524$ , where no zero crossing exists, and  $x_2 = 0.952$  where it attains a value of  $\Delta x_1 \approx 0.75$ . In the closed channel case this scale also decreases, but not nearly as rapidly as in open channel flow where there appears to be a clearer separation between  $R_{22}(\Delta x_1)$  and  $R_{33}(\Delta x_1)$  near the free surface. In Fig. 2 the corresponding results for the spanwise correlations,  $R_{jj}(\Delta x_3)$ , are shown for both cases. As in the streamwise results, close to the wall there appear to be no significant differences between these flows. Farther from the wall ( $x_2 \geq 0.5$ ), it is evident that the correlation length for the  $u_2$  component in the open channel flow is significantly smaller than those for the other two velocity components. This behavior is not evident for the closed channel case in this same region. Again, as with the streamwise correlation length results, there is a clear separation between  $R_{22}(\Delta x_3)$  and  $R_{33}(\Delta x_3)$  as the free surface is approached. One feature of note is the existence of a discernable local minimum in the spanwise correlation of the streamwise velocity component out to normal locations as large as  $x_2 \approx 0.8$  (i.e.,  $\approx 108$  viscous lengths) in the open channel case. This indicates a considerable persistence of a spanwise periodic structure in the flow which will be discussed in more detail in Section 5.

Energy spectra,  $\Phi_{ij}$ , as a function of the streamwise wavenumber,  $\kappa_1$ , are shown in Fig. 3 for two different surface normal locations in close proximity to the free surface boundary ( $x_2 = 0.978$  and 0.952). Additionally, a third energy spectrum at  $x_2 = 0.798$  is given in each plot as a reference condition. Examination of the turbulence intensity profiles (refer to the Fig. 7 discussed later) at this location indicates that free surface effects will be negligible. The  $\Phi_{11}(\kappa_1)$  spectra show that very near the free surface, the energy at low wavenumbers remains unchanged. However, for the intermediate band ( $2 < \kappa_1 < 10$ ) a small increase in energy is evident. There is no change in the spectra at high wavenumbers. These features are quite consistent with the HG predictions. From the  $\Phi_{22}(\kappa_1)$  spectra it is quite evident that, as the free surface is approached, the energy at low wavenumbers decreases more rapidly than at high wavenumbers. This is also consistent with HG. However, it is to be noted that the HG model predicts that the  $\Phi_{22}(\kappa_1)$  spectrum far from the boundary will merge with the spectra near the free surface at a wavenumber of order  $2\pi/\Delta x_2$ , where  $\Delta x_2$  is the vertical distance from

the free surface. This is effectively due to the cutting off of eddies smaller than  $\Delta x_2$  by the presence of the surface. In these calculations, however, the minimum resolvable streamwise length scale dictated by the grid spacing is  $4\pi/64 = 0.196$ , which is in fact of the same order as the source layer. It is evident that higher resolution will be required to resolve these effects. Nevertheless, the basic structure of  $\Phi_{22}(\kappa_1)$  is suggestive of this kind of wavenumber cutoff behavior. The  $\Phi_{33}(\kappa_1)$  spectra show some increase in energy at low wavenumbers as the free surface is approached, but virtually no change for  $\kappa_1 > 3$ . These observations are also qualitatively consistent with HG.

#### 4. MACRO AND MICROSCALES

Turbulent flows are known to contain a wide range of length scales; here we examine both the turbulent macroscales and microscales. The macroscale can be considered the length scale that represents the size of a typical energy containing eddy which is eventually broken up and dissipated by viscosity at smaller scales<sup>12</sup>. The microscale, though not the smallest length scale in the flow, can be thought of as an average length within which most of the energy dissipation occurs. In high Reynolds number flows there is a large separation between these two scales, but in the current computations this separation is not large.

The microscale,  $\lambda$ , corresponding to velocity component  $u_i$  in direction  $x_i$  is defined by:

$$\lambda_{ij}^2 = -2 \left. \frac{\partial^2 R_{jj}(x_i)}{\partial x_i^2} \right|_{x_i=0}. \quad (6)$$

If the turbulence is homogeneous in direction  $x_i$  then it can be shown that an equivalent definition is :

$$\lambda_{ij}^2 = \overline{u_j^2} / \left( \frac{\partial u_j}{\partial x_i} \right)^2. \quad (7)$$

The  $x_1$  and  $x_3$  microscales are computed using both definitions given above and nominally produce identical results. The macroscale  $\Lambda$  is defined by :

$$\Lambda_{ij} = \int_0^\infty R_{jj}(x_i) dx_i. \quad (8)$$

It should be noted that in some circumstances, particularly for the streamwise velocity component, the correlation function  $R_{jj}(\Delta x_1)$  does not decay sufficiently at the end of the computational domain so that the macroscale given by (8) may underestimate the true eddy length scale. Also, since quasi-periodic structures exist close to the wall with their periodicity primarily in the spanwise  $x_3$  direction,  $R_{jj}(\Delta x_3)$  can be negative. This also has the effect of producing a macroscale which underestimates the length of

the largest eddy structures near the wall. For these reasons, the microscales reported below may actually be larger in some cases than the macroscales. This is simply an artifact of the method used here. A better estimate for the macroscales can be had in some cases by using the length associated with the second zero crossing of the correlation function.

Figure 4 shows the results of the calculation of the streamwise macroscale,  $\Lambda_1$  (i.e  $\Lambda_{1j}$ ), and the spanwise macroscale,  $\Lambda_3$ , for both the open and closed channel cases. Recall that the solid wall is at  $x_2 = 0$  and the free surface (or centerline) is at  $x_2 = 1$ . The scales are nominally given in terms of outer units (i.e., channel height) since conversion to wall variables can easily be obtained by multiplying by 135 in the open channel case and 125 for the closed channel. For the streamwise macroscales, significant differences between these two cases are apparent in the rather large region  $0.4 < x_2 < 1.0$ . Here, the most notable observation is that the  $u_3$  velocity component  $\Lambda_1$  length scale changes by a factor of approximately three ( $\approx 0.60$  at the open channel free surface relative to 0.19 at the centerline of the closed channel). For the streamwise velocity component,  $\Lambda_1$  differs only slightly at the free surface from the closed channel centerline value (1.4 vs. 1.14); however, there is a substantially different behavior in how these final values are attained. The closed channel length scale smoothly achieves an asymptotic value of order one at the centerline, whereas the behavior near the free surface resembles that observed near the solid boundary (i.e., a peak at some distance from the boundary indicative of the source layer thickness). The free surface effects on the spanwise macroscales,  $\Lambda_3$ , are confined to a smaller region ( $0.8 < x_2 < 1.0$ ) than those on the streamwise macroscales. Substantial differences are again observed between the values attained at the free surface relative to those at the closed channel centerline. Both the  $u_1$  and  $u_2$  component macroscales differ by a factor of about two with the  $u_1$  scale larger and the  $u_2$  scale correspondingly smaller at the free surface.

In Fig. 5 the microscale results are compared for the open and closed channel flows. Trends similar to those observed for the macroscale results of Fig. 4 are apparent. The streamwise scale,  $\lambda_1$ , of the  $u_3$  component is larger at the free surface than at the closed channel centerline (0.40 vs. 0.29); whereas,  $\lambda_1$  for the  $u_2$  component is somewhat lower (0.21 vs. 0.27). Similar to the spanwise macroscale results, the spanwise microscales differ at the free surface with the  $u_1$  component scale larger and the  $u_2$  component scale smaller by the same amounts than their closed channel centerline values.

The vertical macroscale,  $\Lambda_{2j}$ , is given by:

$$\Lambda_{2j}(x_2) = \int_0^1 R_{jj}(0, 0, x_2, x'_2) dx'_2. \quad (9)$$

At a given vertical location  $x_2$ ,  $\Lambda_2$  gives a measure of the vertical size of a typical eddy that can exist at that depth. These results are shown in Fig. 6. It is observed that  $\Lambda_{21}$  and  $\Lambda_{22}$  increase continuously away from the solid wall until approximately  $x_2 = 0.6$ , where the free surface effects become evident as both decrease. Generally speaking, both the free surface and solid boundaries have similar overall effects in that the eddy size that can exist there is smaller than that existing away from the boundary. However, the lack of viscous dissipation near the free surface apparently allows for a somewhat greater vertical extent than that found near a solid wall, as one would expect. The  $\Lambda_{23}$  macroscale results may not be easily interpreted near the solid boundary since  $R_{33}(x_2, x'_2)$  becomes negative there, presumably due to the presence of the counter-rotating vortex structure typically associated with the wall layer. Near the free surface however,  $R_{33}(x_2, x'_2)$  is strictly positive so that the interpretation of  $\Lambda_{23}$  as a length scale is more meaningful. As with the other two vertical macroscale components, the proximity of the free surface (or perhaps boundary in general) evidences itself as a decrease in the  $\Lambda_{23}$  scale. These results generally tend to confirm the HG model prediction of a strong truncation of the vertical extent of a typical eddy near the free surface.

To summarize, the macroscale results are particularly useful in understanding the change in shape of a typical eddy as it interacts with the free surface. Predominantly, the free surface effects relative to the closed channel centerline behavior are larger spanwise scales associated with the streamwise velocity component  $u_1$ ; generally smaller streamwise and spanwise scales for the wall normal velocity component  $u_2$ ; and larger streamwise scales associated with the spanwise velocity component  $u_3$ . Additionally, the vertical macroscales,  $\Lambda_{2j}$ , associated with all three velocity components decrease on approach to the free surface. This presents a reasonably clear picture of eddies which flatten out or become pancake-like in the horizontal plane as they undergo a reduction in their vertical extent. This is certainly in agreement with one's intuitive expectation of the similar effect of a solid boundary on an impinging eddy. These results indicate a streamwise stretching by a factor of about three and a spanwise elongation of approximately two.

It does not seem possible to make a quantitative comparison of these results with the HG model in its present form, since their model does not account for the strong anisotropy of the open channel flow studied here. Obviously there is some difficulty in defining a far-field integral length scale in this flow,

whereas this scale is well defined for homogeneous turbulence. However, since the source layer of the HG model is generated by the no mass-flux boundary condition, it would seem that the scales of  $u_2$  should give the best indication of the extent of free surface effects. In Fig. 7 the mean-square turbulence intensities scaled by the local turbulent kinetic energy are shown. This demonstrates clearly that all three velocity components show the effects of surface proximity at a distance of about  $\Delta x_2 = 0.3$ . (See Swean *et al.*<sup>10</sup> for a discussion of the redistribution of energy from the vertical velocity component to both the streamwise and spanwise components.) Indeed the vertical velocity component is the only one which has associated macroscales of about this size and which are smaller than the macroscales at the centerline of the closed channel flow. This seems to indicate that the length scales for  $u_2$  also determine the extent of the source layer. This result is certainly consistent with the source layer model of HG as noted above.

### 5. WALL-LAYER STREAK SPACING

In Section 3 the persistence of a spanwise periodic structure at relatively large distance away from the wall was noted for the open channel flow. These streamwise-elongated structures, commonly referred to as wall-layer streaks, appear in flow visualization studies as regions of low-speed fluid close to wall. Though there remains some controversy as to the significance of the streaks, there appears to be increasing evidence that they are indicators of quasi-streamwise oriented vortices. These vortices in turn are thought to play a role in the production of new turbulence and in Reynolds stress production. They were first observed experimentally by Hama (see Corrsin<sup>13</sup>) and later studied in more detail by Kline *et al.*<sup>14</sup>. Their visualization studies showed that the streaks were typically observed below  $x_2^+ = 30$  and that they occurred randomly in space and time. Kline *et al.* also found that the average spanwise spacing between the streaks,  $\bar{\lambda}^+$ , was approximately 100 essentially independent of Reynolds number. The experimental results reported by Nakagawa and Nezu<sup>15</sup> for open channel flow indicate that the mean streak spacing increases with distance from the wall and ultimately approaches a value of  $\bar{\lambda}^+ \approx 2x_2^+$  for  $x_2^+ \geq 50$ . This led them to speculate that the increase in length scale resulted from a coalescence (similar to the pairing interaction observed in free shear flows) of neighboring low-speed streaks as the distance from the wall increases. However, it should be noted that for the locations above  $x_2^+ > 30$  the spanwise length scale they observe is very weak and may not necessarily correspond to well-defined streaks.

More recently, Smith and Metzler<sup>16</sup>, in agreement with the findings of Nakagawa and Nezu, found that the average spanwise wavelength increased from

93 at  $x_2^+ = 1$  to 146 at  $x_2^+ = 30$ . They noted, however, that beyond  $x_2^+ = 30$  that the streaks were not sufficiently well defined to warrant making streak counts and they suggest that  $x_2^+ \approx 40$  is the upper limit for which extended regions of low-speed fluid continue to exist. Also in agreement with Nakagawa and Nezu, they found that streak coalescence in the region  $10 \leq x_2^+ \leq 30$  contributed to the increasingly disrupted streak pattern and overall increase in the spanwise length scale with distance from the wall. They noted that since the most active merging occurs in the region of maximum turbulent energy production, this merging process may very well be important to the turbulence production cycle. The observation of wall-layer streaks has not been confined strictly to experimental studies; various numerical simulations appear to very satisfactorily capture the wall-layer dynamics. As an example, KMM show very good agreement with the experimental determinations of the variation of mean spanwise streak spacing with distance from the wall.

In Fig. 8 the dependence of the mean streak spacing on  $x_2^+$  is presented for both open and closed channel flows along with various experimental and numerical simulation results. Here the mean streak spacing is defined as twice the spanwise distance at which  $R_{11}(\Delta x_3)$  reaches a minimum (note that this definition of  $\lambda^+$  is consistent with KMM). The results indicate clearly that for  $x_2^+ < 12$  there is excellent agreement among all the studies that  $\lambda^+ \approx 100$ . The streak spacing in the open channel case shows a jump from a value of 105 at  $x_2^+ = 12$  to approximately 130 at  $x_2^+ = 15$ . Farther from the wall, the open channel streak spacing increases at a rate which is roughly the same as in the closed channel but always remains larger. Thus, Fig. 8 shows that at  $x_2^+ \approx 65$ ,  $\lambda^+$  has attained a value roughly twice that observed at  $x_2^+ \approx 12$ . It is also clear that, unlike the closed channel case where the streak spacing is apparently only clearly defined out to perhaps  $x_2^+ \approx 50$ , the spanwise periodic streaks can definitely be observed well out to  $x_2^+ \approx 80$  in the open channel flow. This is in fact within the logarithmic layer of the streamwise velocity profile (see Swean *et al.*<sup>10</sup> for the open channel flow mean velocity profile). It is apparent that the streaky structure in open channel turbulence is both larger in scale and persists farther from the wall than in closed channel turbulence.

Though the reasons for these differences are far from evident, a few speculations are now offered to explain this behavior. The only obvious difference between these two flow fields is the boundary condition imposed on the upper boundary. Since the shear-free boundary suppresses the production of new turbulence we can envision that this must in turn suppress the ejection of low momentum fluid that would oth-

erwise occur if the boundary were rigid (i.e no-slip boundary conditions). The suppression of these ejections from the top boundary (free surface) toward the bottom boundary (solid wall) may be responsible for slowing down the production of turbulence by lowering the probability of shear layer formation in the region of the solid wall. Thus, the larger, more coherent streaks near the wall in open channel turbulence are due to the suppression of turbulence production at the free surface. Furthermore, in boundary layer flows the entrainment of outer irrotational fluid may act like ejections from the upper wall of a channel. In this sense, boundary layer flow has a closer resemblance to closed channel flow than to open channel flow. These results suggest that the outer flow does have an effect on the wall region at least at these low Reynolds numbers.

## 6. CONCLUSIONS

The structure of turbulence near a free surface has been studied using the results of a direct simulation. The method employed here to understand this structure is to compare the open channel turbulence results with its well studied closed channel turbulence counterpart. A comparative examination of the turbulent macroscales and microscales in these two cases reveals a significant flattening of a typical eddy near the free surface. This flattening is evidenced by a notably larger streamwise scale associated with the spanwise velocity component and a commensurately larger spanwise scale of the streamwise velocity component. Additionally, the vertical macroscales for all three velocity components are smaller than the companion closed channel values. In this flow, the source layer described by the Hunt-Graham model appears to extend about 0.3 channel heights below the free surface. This source region seems to correlate most strongly with the structure of the vertical component of velocity. All length scales for this component are about the correct size and all are smaller than the macroscales at the centerline of the closed channel flow. A direct quantitative comparison of these results with the HG model is not possible since the model does account for the strong anisotropy of the turbulence present in this flow. The energy spectra for all three components of velocity are in qualitative agreement with the HG model though resolution effects and anisotropy limit direct quantitative comparison.

An interesting phenomenon revealed by the current study is the increase in size and persistence of the spanwise periodic structure near the wall. In open channel turbulence this structure is larger in scale and penetrates farther into the flow than in closed channel turbulent flow. The origin of this effect is not clear but one possible explanation is that the free surface suppresses interactions which would normally occur

between the no-slip boundaries of channel flow. This observation lends support to the possibility that the outer flow has a significant effect on wall layer structure. In future work, a quantitative comparison of these results with a modified form of the HG model will be attempted and higher resolution simulations will be undertaken to further elucidate the structure of the turbulence near the free surface.

#### ACKNOWLEDGEMENTS

This work is supported by the Naval Research Laboratory under the Fluid Dynamics Task Area and the Office of Naval Research under the Surface Ship Wake Detection Program. Many of the calculations were performed under an NRL Cray Grant. The authors acknowledge the many fruitful discussions with Dr. J.D. Crouch.

#### REFERENCES

- <sup>1</sup>Uzkan, T. and Reynolds, W.C., "A Shear-Free Turbulent Boundary Layer," *Journal of Fluid Mechanics*, Vol. 28, 1967, pp. 803-821.
- <sup>2</sup>Thomas, N.H. and Hancock, P.E., "Grid Turbulence Near a Moving Wall," *Journal of Fluid Mechanics*, Vol. 82, 1977, pp. 481-496.
- <sup>3</sup>Hunt, J.C.R. and Graham, J.M.R., "Free Stream Turbulence Near Plane Boundaries," *Journal of Fluid Mechanics*, Vol. 84, 1978, pp. 209-235.
- <sup>4</sup>Biringen, S. and Reynolds, W.C., "Large-Eddy Simulation of the Shear-Free Turbulent Boundary Layer," *Journal of Fluid Mechanics*, Vol. 103, 1981, pp. 53-63.
- <sup>5</sup>Brumley, B.H. and Jirka, G.H., "Near-Surface Turbulence in a Grid-Stirred Tank," *Journal of Fluid Mechanics*, Vol. 183, 1987, pp. 235-263.
- <sup>6</sup>Orszag, S.A. and Patera, A.T., "Subcritical Transition to Turbulence in Planar Shear Flows," in *Transition and Turbulence*, ed. by R.E. Myer, Academic, 1981, pp. 127-146.
- <sup>7</sup>Kim, J., Moin, P., and Moser, R., "Turbulence Statistics in a Fully Developed Channel Flow at Low Reynolds Number," *Journal of Fluid Mechanics*, Vol. 177, 1987, pp. 133-166.
- <sup>8</sup>Leighton, R.I., Swean, T.F., Jr., Handler, R.A., and Swearingen, J.D., "Direct Simulation of Low Reynolds Number Open Channel Flow," NRL Memorandum Report, 1991.
- <sup>9</sup>Komori, S., Ueda H., Ogino, F., and Mizushima, T., "Turbulence Structure and Transport Mechanism at the Free Surface in an Open Channel Flow," *International Journal of Heat and Mass Transfer*, Vol. 25, 1982, pp. 513-521.
- <sup>10</sup>Swean, T.F., Jr., Leighton, R.I., Handler, R.A., and Swearingen, J.D., "Turbulence Modeling Near the Free Surface in an Open Channel Flow," AIAA Paper 91-0613, 29th Aerospace Sciences Meeting, Jan. 7-10, 1991, Reno, Nevada.
- <sup>11</sup>Sirovich, L. "Turbulence and the Dynamics Coherent Structures: Part II: Symmetries and Transformations," *Quarterly of Applied Mathematics*, Vol. 45, 1987, pp. 573-582.
- <sup>12</sup>Hinze, J.O., *Turbulence*, McGraw-Hill, New York, 1975.
- <sup>13</sup>Corrsin, S., "Some Current Problems in Turbulent Shear Flows," *Symposium on Naval Hydrodynamics*, Publication 515, National Academy of Sciences-National Research Council, 1957, pp. 373-407.
- <sup>14</sup>Kline, S.J., Reynolds, W.C., Schraub, F.A., and Runstadler, P.W., "The Structure of Turbulent Boundary Layers," *Journal of Fluid Mechanics*, Vol. 30, 1967, pp. 741-773.
- <sup>15</sup>Nakagawa, H. and Nezu, I., "Structure of Space-Time Correlations of Bursting Phenomena in an Open-Channel Flow," *Journal of Fluid Mechanics*, Vol. 104, 1981, pp. 1-43.
- <sup>16</sup>Smith, C.R. and Metzler, S.P., "The Characteristics of Low-Speed Streaks in the Near-Wall Region of a Turbulent Boundary Layer," *Journal of Fluid Mechanics*, Vol. 129, 1983, pp. 27-54.
- <sup>17</sup>Schraub, F.A. and Kline, S.J., "A Study of the Structure of the Turbulent Boundary Layer With and Without Longitudinal Pressure Gradients," *Department of Mechanical Engineering Report MD-12*, 1965, Stanford University.

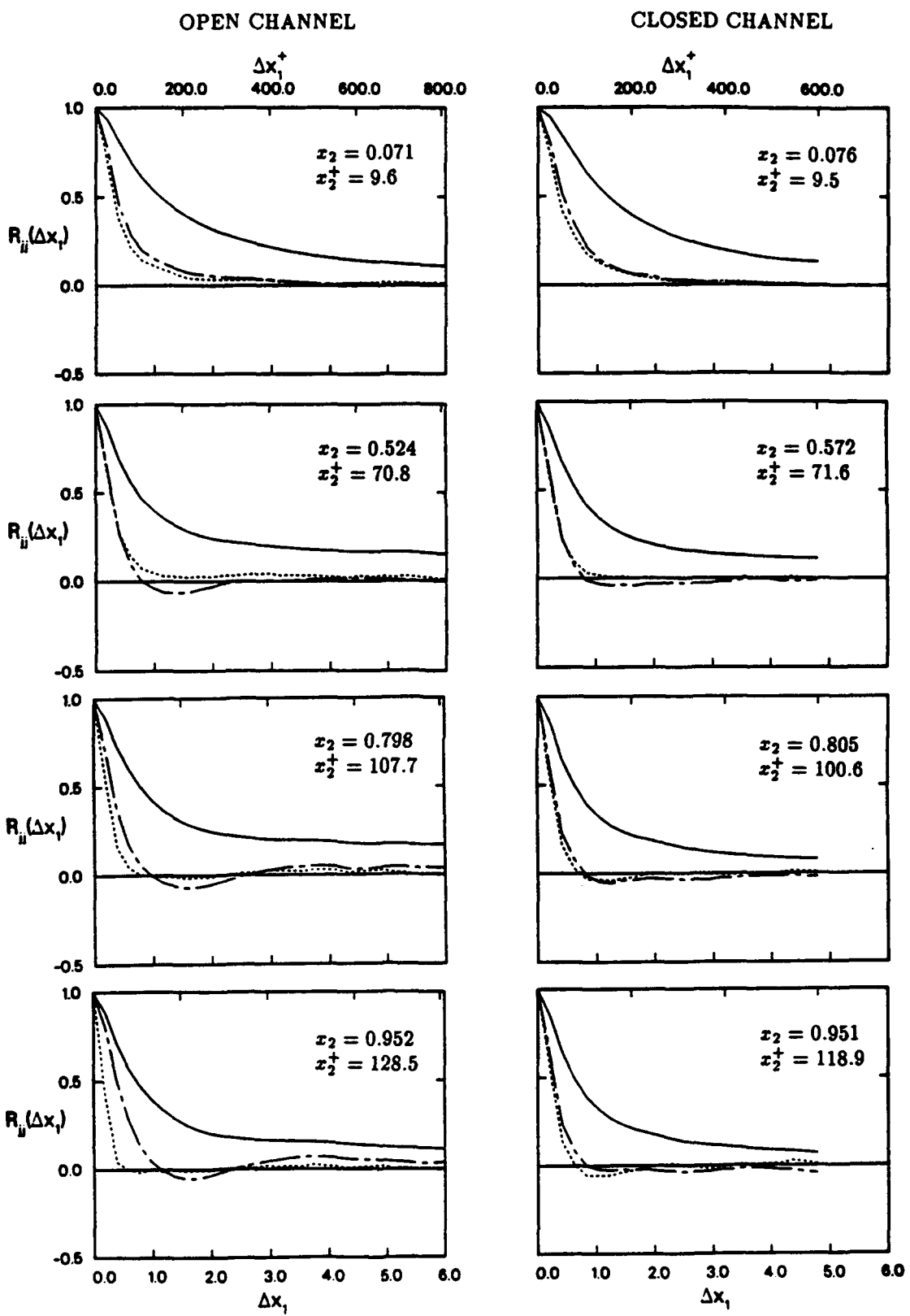


Fig. 1 Streamwise two-point correlations: —,  $R_{11}$ ; - - - ,  $R_{22}$ ; - - - - ,  $R_{33}$ .

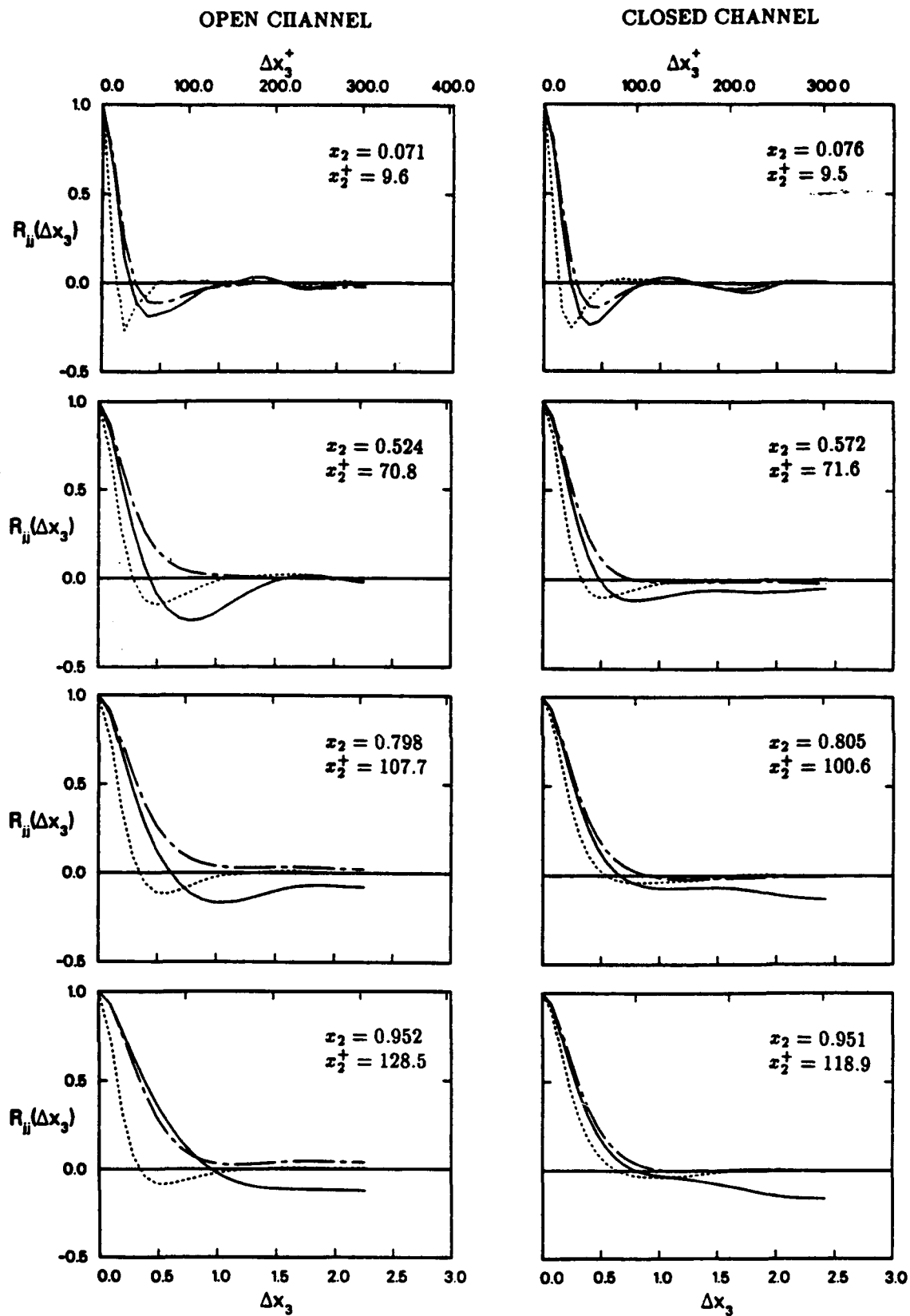


Fig. 2 Spanwise two-point correlations: —,  $R_{11}$ ; - - - - ,  $R_{22}$ ; - - - - - ,  $R_{33}$ .

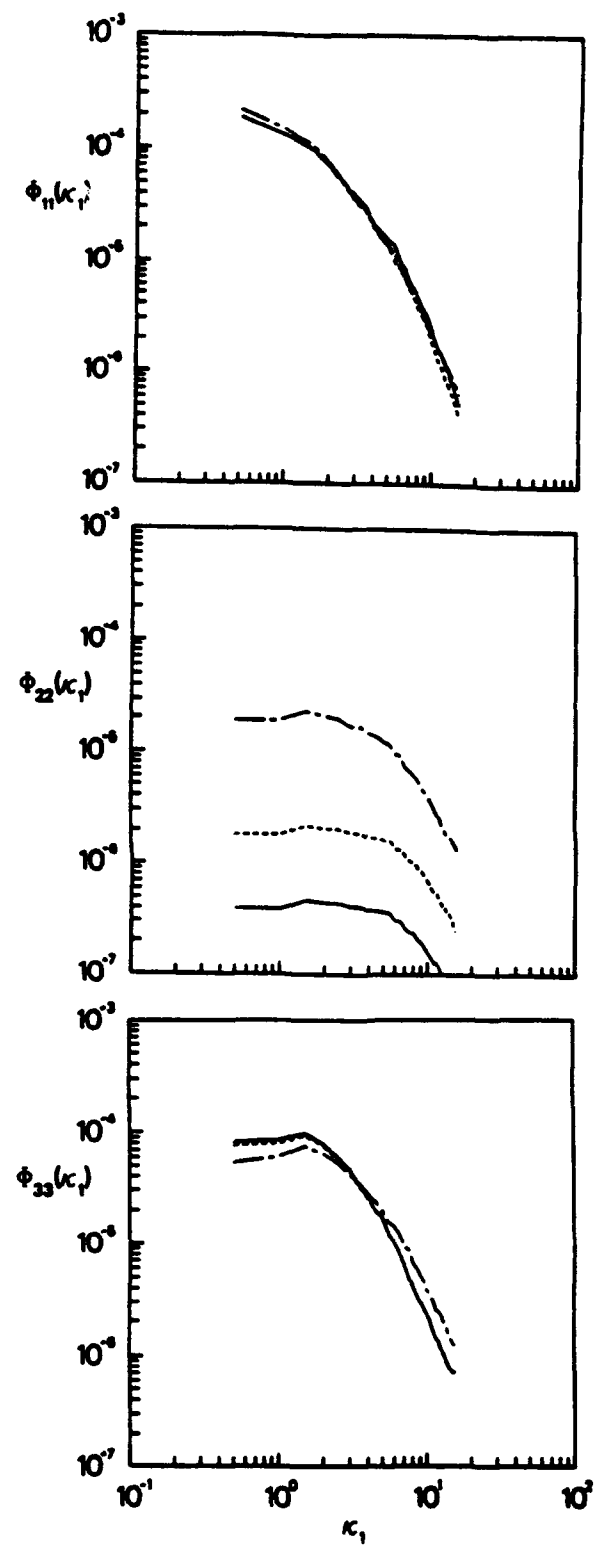


Fig. 3 Velocity spectra near the free surface: —,  $x_2 = 0.978$ ; - - -,  $x_2 = 0.952$ ; - - - - ,  $x_2 = 0.798$ .

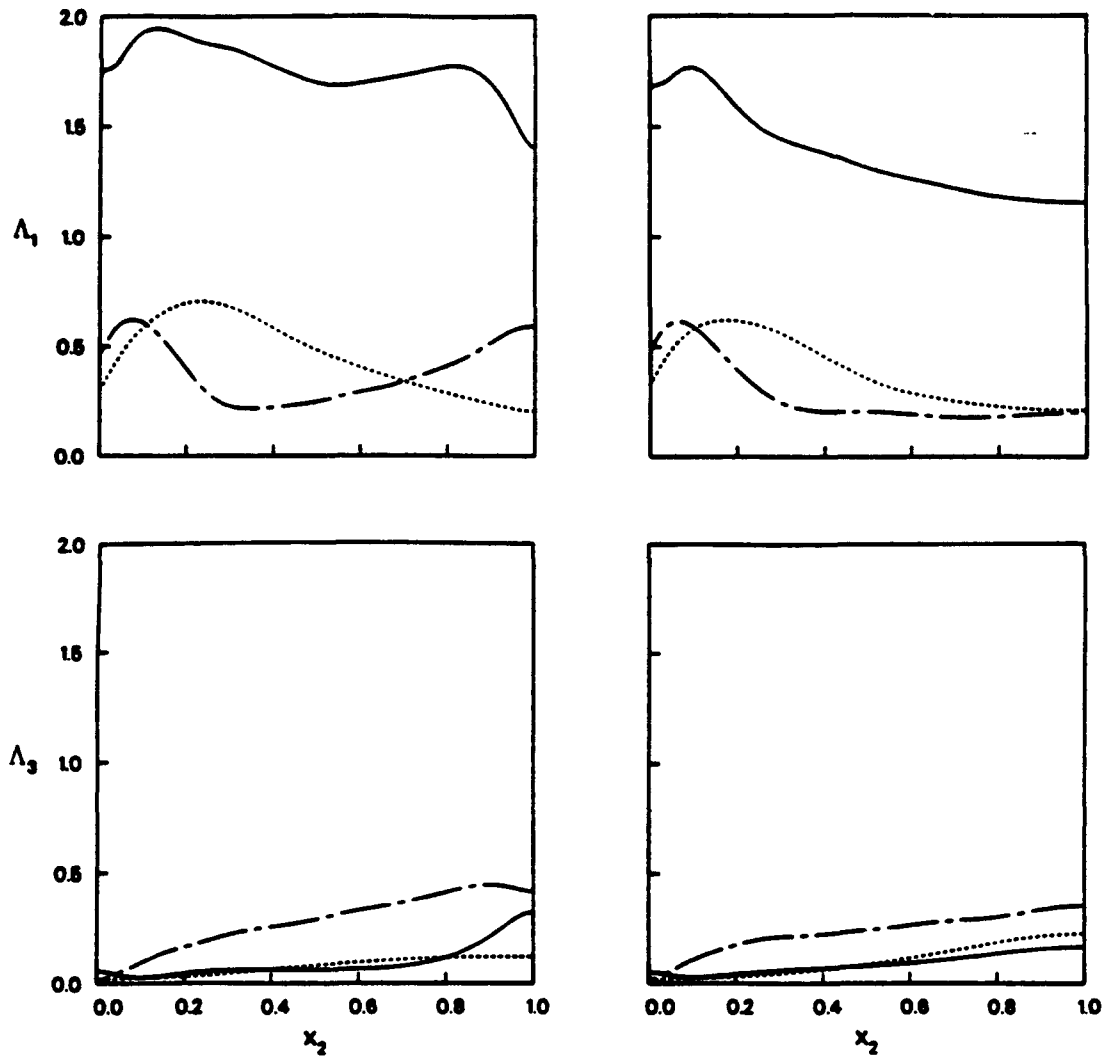


Fig. 4 Streamwise and spanwise macroscales: —,  $\Lambda_{i1}$ ; - - -,  $\Lambda_{i2}$ ; - - - - ,  $\Lambda_{i3}$ .

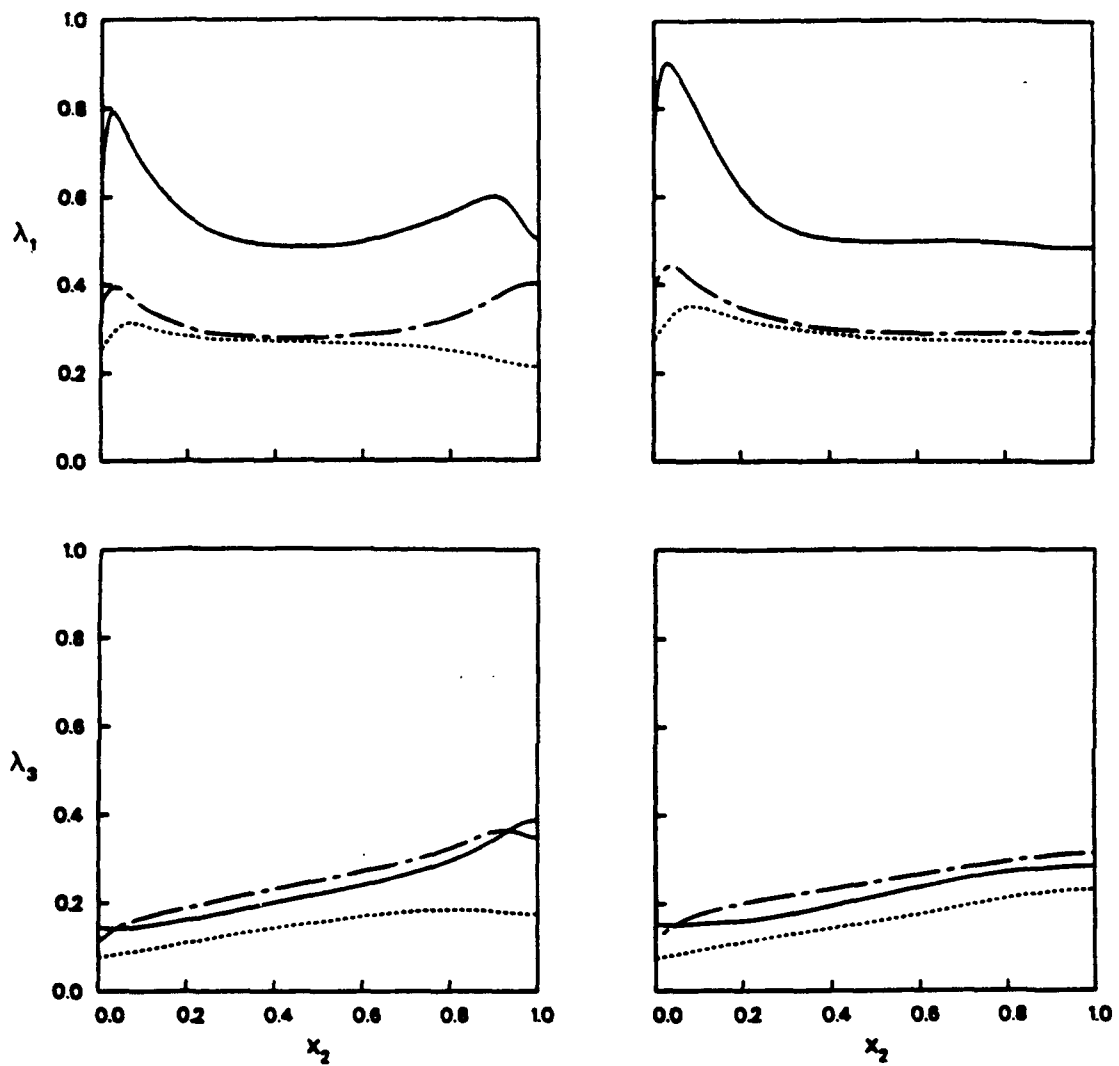


Fig. 5 Streamwise and spanwise microscales: —,  $\lambda_{i1}$ ; - - -,  $\lambda_{i2}$ ; - - - - ,  $\lambda_{i3}$ .

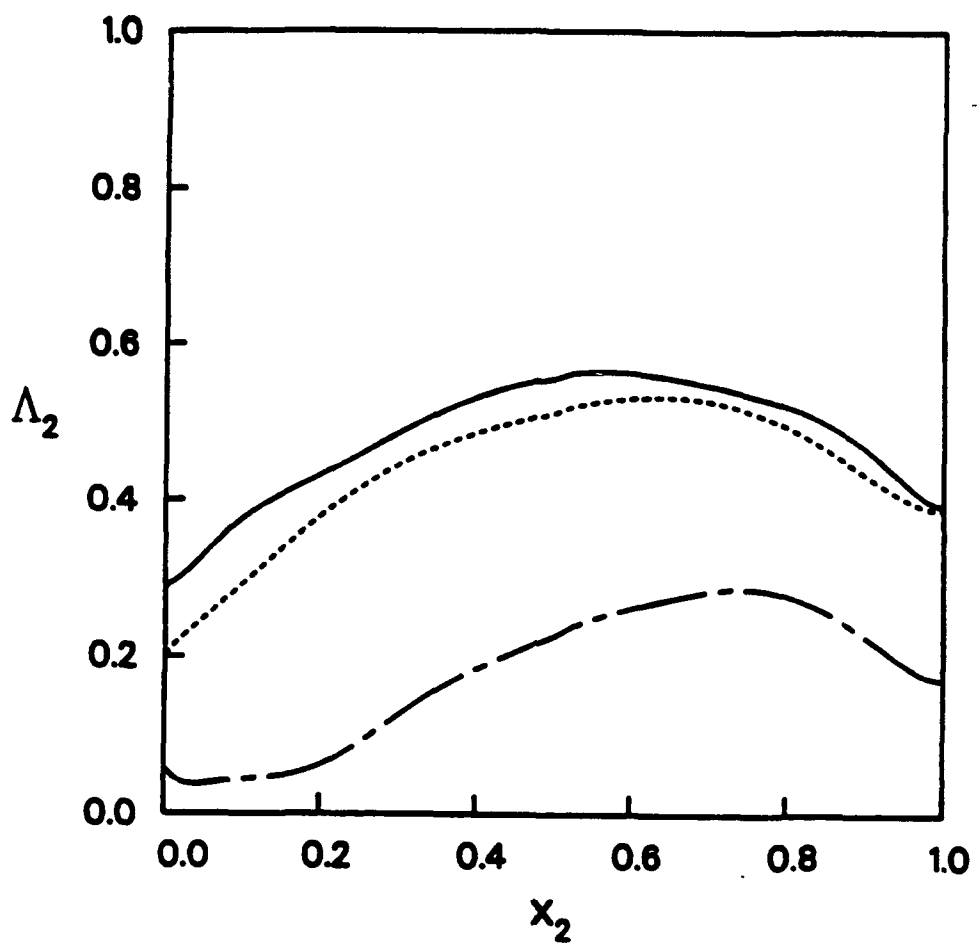


Fig. 6 Vertical macroscales: —,  $\Lambda_{21}$ ; - - -,  $\Lambda_{22}$ ; - - - - ,  $\Lambda_{23}$ .

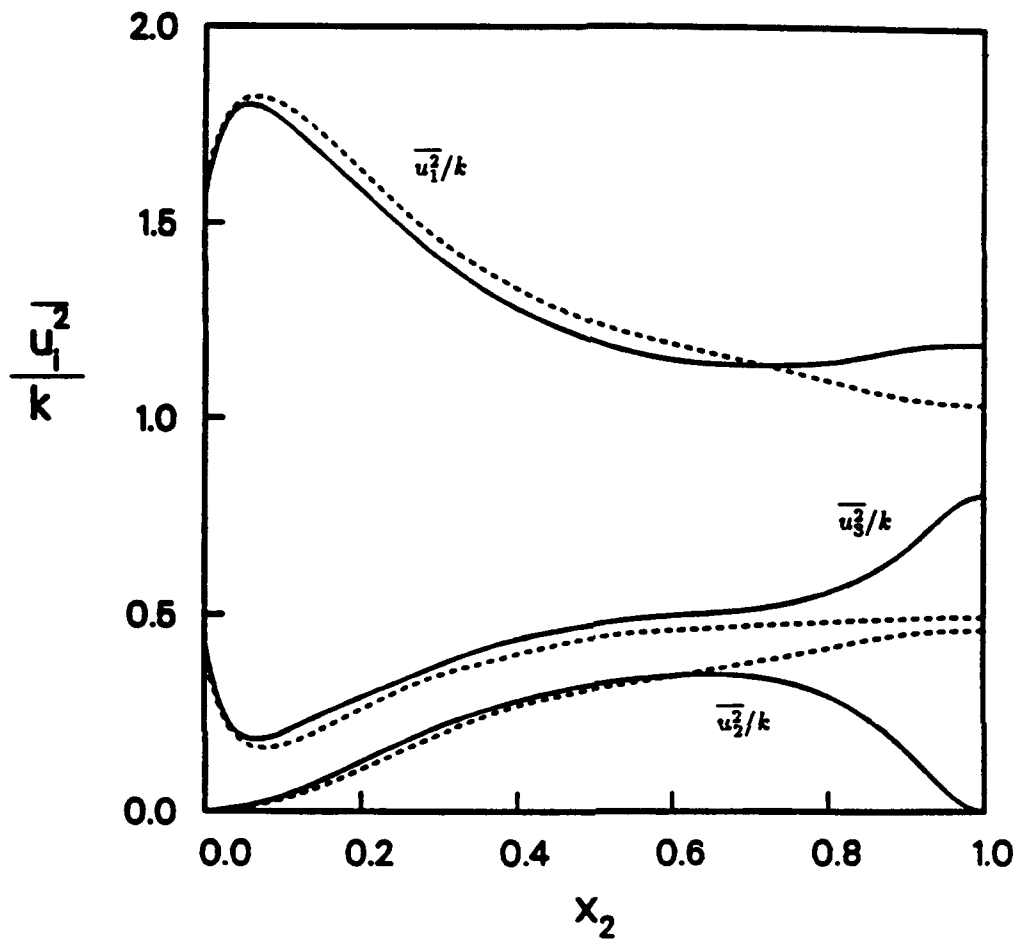


Fig. 7 Profiles of normal stresses scaled by the local value of turbulence kinetic energy. Dashed lines are for the closed channel simulation.

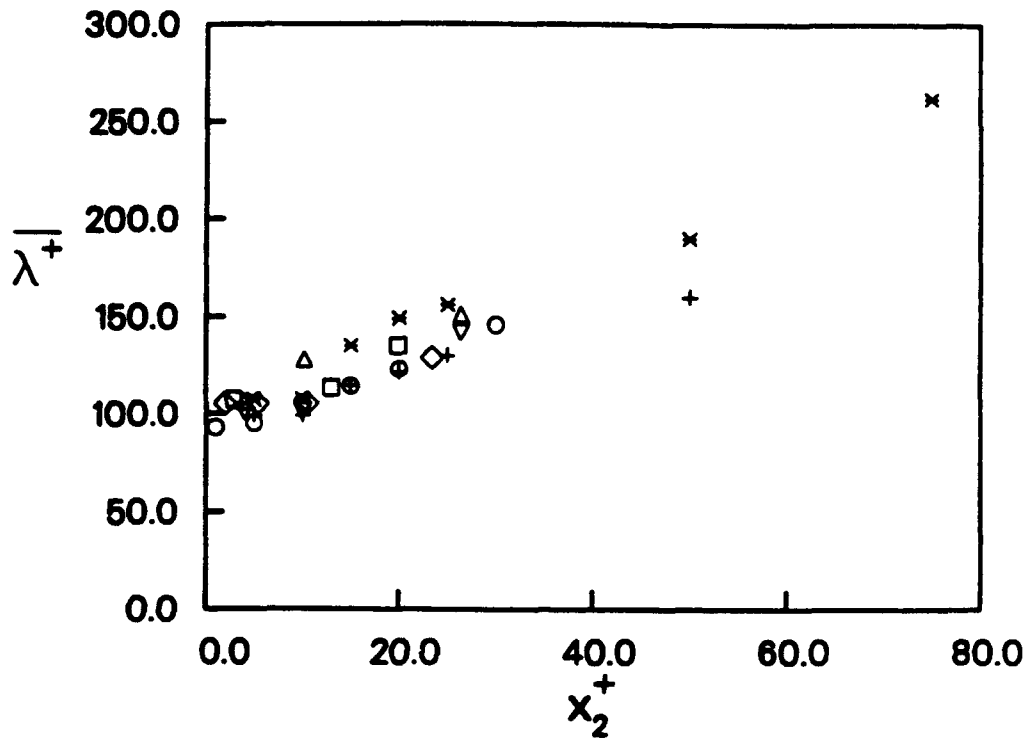


Fig. 8 Variation of mean spanwise streak spacing with wall normal distance. Present study:  $\times$ , open channel,  $R^* = 135$ ;  $+$ , closed channel,  $R^* = 125$ . Smith and Metzler<sup>16</sup>:  $\circ$ , boundary layer expt.,  $R_\theta = 2030$ . Schraub and Kline<sup>17</sup>:  $\square$ , boundary layer expt.,  $R_\theta = 1325$ . Nakagawa and Nezu<sup>15</sup>: open channel expt.,  $\nabla$ ,  $R^* = 248$ ;  $\Delta$ ,  $R^* = 378$ . Kim, Moin, and Moser<sup>7</sup>:  $\diamond$ , closed channel simulation,  $R^* = 180$ .

## **Appendix H**

### **The Enstrophy Balance During the Interaction of a Vortex Ring with a Shear-Free Boundary**

## THE ENSTROPY BALANCE DURING THE INTERACTION OF A VORTEX RING WITH A SHEAR-FREE BOUNDARY

R. I. Leighton\* and T. F. Bawden, Jr.  
Center for Advanced Space Sensing  
Naval Research Laboratory  
Washington, D.C.

### Abstract

The results of a numerical simulation of the interaction of a vortex ring with a shear-free boundary are presented. The Reynolds number is 1000, based on the circulation and viscosity, and the ratio of the core diameter to the ring diameter is 0.4. In this simulation the vortex ring interacts with the shear-free boundary through the primary and secondary reconnection events resulting in a pair of vortex half rings attached to the boundary. The terms of the enstrophy balance equation are calculated and presented. The dynamics of the reconnection process are discussed using the enstrophy balance and an enstrophy model of the diffusion of a strained vortex pair. Based on these results, a physical description of the reconnection events was developed.

### Nomenclature

$a$	Ring radius
$Q = \frac{1}{2} \sum_i \omega_i^2$	Instantaneous enstrophy
$Q_i = \frac{1}{2} \omega_i \omega_i$	$i^{\text{th}}$ component of enstrophy
$Re = \Gamma_0 / \nu$	Reynolds number
$R_0, T_0, P_0, D_0, E_0$	Terms of Enstrophy Balance
$R_0, T_0, P_0, D_0, E_0$	Terms of Enstrophy Balance for $i^{\text{th}}$ component
$t^* = (t \Gamma_0 / a^2)$	Non-dimensional time
$u_i$	Instantaneous velocity
$\Gamma_0$	Initial circulation
$\omega_i$	Instantaneous vorticity
$\nu$	Kinematic viscosity
$\sigma$	Core radius

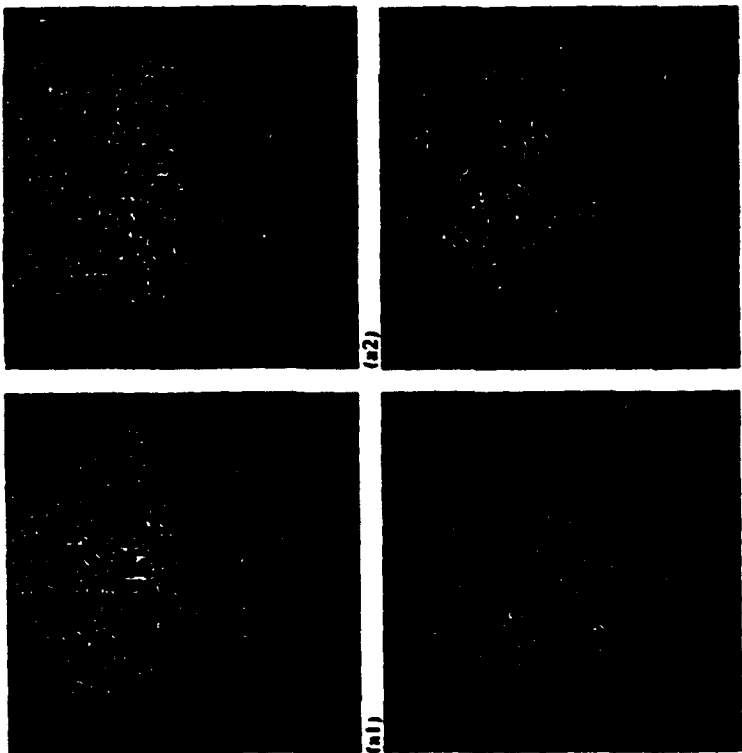


Fig. 6 Shadowgraph images of the free-surface turbulent wake at velocity  $w=2.3$  and  $w=4.0 L/2$ .  
(a1) and (a2) at distances (1) and (4); (b1) and (b2) at distances (2) and (4).

\*Presently with Science Applications International Corp., McLean, VA.

## 1 Introduction

The vortex reconnection process, whereby a pair of vortex elements, such as rings or perturbed vortex pairs, interact, break and reconnect, has been studied by several researchers. Aspects of this problem have been studied experimentally by Fohl and Turner [1], Lim [2], Kwon [3], Schatzle [4] and others. The work of Fohl and Turner and of Schatzle involved interacting vortices in free space. In the work of Kwon a vortex ring was generated below a free surface and allowed to interact with the surface.

Recent numerical studies of the reconnection process include those of Kerr and Hussain [5] and Buntine and Pullin [6]. Kerr and Hussain considered the interaction of a pair of perturbed viscous line vortices in a three-dimensional periodic domain. The work of Buntine and Pullin involved the evolution of a parallel (or anti-parallel) line-vortex pair in a specified strain field. Their work indicates that the local strain field is important to the understanding of the relationship between vorticity distribution and flow kinetic energy during the reconnection process.

In this paper we will describe the results of a direct numerical simulation of the interaction of a vortex ring with a shear-free boundary, with particular attention to the terms of the enstrophy balance equations. This should allow clear identification of the relevant physical processes involved in the reconnection event.

Buntine and Pullin [6] and Kambe [7] indicate that the local straining field is important in understanding the vorticity enhancement and kinetic energy dissipation. Kambe noted that the integral of the enstrophy (or the scalar product of vorticity) is related to the decay rate of the kinetic energy of the flow. The local straining field aligned with the vorticity of the ring enhances the enstrophy via the enstrophy production term. The increased enstrophy is responsible for an increase in the turbulent kinetic energy decay rate.

## 2 The Numerical Simulation

This simulation is an idealization of the experiments of Kwon. In that experiment, vortex rings, generated below the free surface, propagate towards the surface at some angle relative to the direction normal to the free surface. A variety of angles and circulation strengths were tried, resulting in several classes of reconnection events at the surface. In the simulation, the ring is inclined to propagate at an angle of 75 degrees to the free-surface normal direction. The space coordinates are non-dimensionalized by the initial ring diameter,  $a$ , which is assumed to be unity. The vorticity distribution across the core of the ring was initialized with a gaussian distribution,

$$\omega = \frac{\Gamma_0}{\pi a^2} \exp(-r^2/a^2), \quad (1)$$

with a core radius of  $\sigma = 0.2$ . The problem is nondimensionalized by the free-space circulation and the non-dimensional time is defined as  $t^* = t\Gamma_0/a^2$ . The Reynolds number of the simulation ( $R_e = \Gamma_0/\nu$ ) is 1000.

**Numerical Methods** The computer code used in the simulation was designed and developed to run on the Cray X-MP at the Naval Research Laboratory. The code solves the Navier-Stokes equations using the spectral method discussed in Kim, Moin and Moser [8]. The governing equations are recast into a 4th order equation for the vertical velocity and a 2nd order equation for the vertical vorticity and the continuity equation is solved explicitly in the recovery of the streamwise velocity. The equation system is transformed using Fourier expansions in the periodic axial ( $x_1$ ) and transverse ( $x_2$ ) directions and Chebyshev expansions

in the inhomogeneous vertical ( $x_3$ ) direction. The  $x_2$  axis has its origin at the free surface. The calculations are performed on a grid of  $96 \times 97 \times 96$  nodes in  $x_1, x_2, x_3$ . With the geometry scaled by the ring diameter,  $a$ , the height, length and width of the channel are  $4 \times 6 \times 6$ , respectively.

The elevation of the free surface can be described by a coupled set of nonlinear time-dependent partial differential equation. Application of these equations as boundary conditions can be simplified considerably if the surface is not allowed to deflect. The rigid lid approximation is equivalent to

$$u_3 = 0 \text{ at } x_3 = 0. \quad (2)$$

To further simplify the boundary conditions, the usual balance of normal stresses is replaced by

$$\frac{\partial^2 u_3}{\partial x_1^2} = 0 \text{ at } x_3 = 0. \quad (3)$$

Equation (3) can be derived from the zero tangential stress conditions, the continuity equation, and the rigid lid assumption. These conditions and the definition of vorticity can also be combined to form the remaining free-surface boundary condition,

$$\frac{\partial u_2}{\partial x_2} = 0 \text{ at } x_3 = 0, \quad (4)$$

where the vorticity is non-dimensionalized by  $\Gamma_0/a^2$ . Zero shear boundary conditions are imposed at the lower boundary to minimize the effects of a finite domain. The boundary conditions are periodic on all dependent variables in the streamwise and spanwise directions.

**The Evolution of the Vortex Ring** The simulation was started with the axis of the vortex ring 1.5 ring diameters below the top boundary. The trajectory of the vortex ring on the vertical centerplane ( $x_3 = 0$ ) of the domain is shown in Fig. 1a. The closed (open) symbols are the location of the maximum (minimum) vorticity for the upper (lower) portion of the vortex ring. The dashed line at  $x_1 = 0$  indicates the limit of the periodic domain. Fig. 2b shows the trajectories of the attached vorticity on the top boundary. The open symbols are the trajectories of the first or primary reconnections arising from the interaction of the leading (upper) portion of the ring with the boundary. The closed symbols are the trajectories of the maximum and minimum normal vorticity arising from the second interaction of the trailing (lower) portion of the ring with the surface. The markers a, b and c correspond to Figs. 2a-c.

For purposes of discussion the evolution of the ring can be broken into several phases. From  $t^* = 0$  to  $t^* \approx 6$  the ring is propagating, essentially free from the influence of the boundaries. Since the gaussian distribution of vorticity is not an equilibrium solution, the core of the ring evolves rapidly. The ring then enters a vorticity intensification phase ( $6 < t^* < 7.5$ ). During this time, the ring interacts with the shear free boundary and the maximum vorticity increases by approximately a third. The primary vortex reconnection event occurs during the interval  $6.5 < t^* < 10.0$ . The broken primary ring evolves as a half ring connected to the top boundary and propagates in the positive  $x$  direction. By  $t^* \approx 15$ , the bottom of the ring has risen and begins to interact with the top boundary. Prior to the second reconnection, the vorticity does not intensity significantly ( $\sim 5\%$  increase). The secondary vortex reconnection event occurs during the interval  $20 < t^* < 30$ , after which there exists two secondary half rings connected by a vertical structure. Various aspects of the processes are discussed below, and in [9,10].

Figures 2 a-c show the surfaces of constant vorticity magnitude on the right hand-side of the figure and normal strain in the transverse direction,  $\frac{\partial u}{\partial x_3}$ , on the left hand side at times  $t^* = 7.5, 20.6$  and  $26.1$ , respectively. By the end of the intensification phase, shown in Fig. 2a, the vorticity and transverse strain have reach a maximum. As a result of the vorticity intensification, the significant strain and vorticity are confined in a thin region near the shear-free surface and are well correlated. The vortex ring is about to undergo reconnection. Several processes are contributing to the strain field. Contributions of a global nature arise from the interaction of the propagating ring with its image. Contributions of a local nature arise from the strain field. Contributions of a local nature arise from the direction normal to the surface [11] or aligned with the vorticity near the surface [12].

The strain and vorticity associated with the second interaction are relatively weaker. As seen in Fig. 2b the strain field at the top surface is trailing behind the vortex ring, and is stretching only a portion of the interacting vorticity. This weaker less correlated interaction results in a longer time scale and the more complicated vortical structure shown in Figs. 2b-c. As will be described further in section 4, the positive transverse strain will promote the breaking of the vorticity at the trailing edge. As the ring evolves, the reconnected vorticity forms into two small appendages or 'legs' in front of the ring. These appendages evolve into the interior positions of the secondary ring\*, as seen in Fig. 2c. As the reconnection continues, the transverse strain becomes increasingly correlated with the vorticity of the connecting bridge. In the next section, the enstrophy balance equations will be introduced. They will be used to qualify the events during the reconnection process.

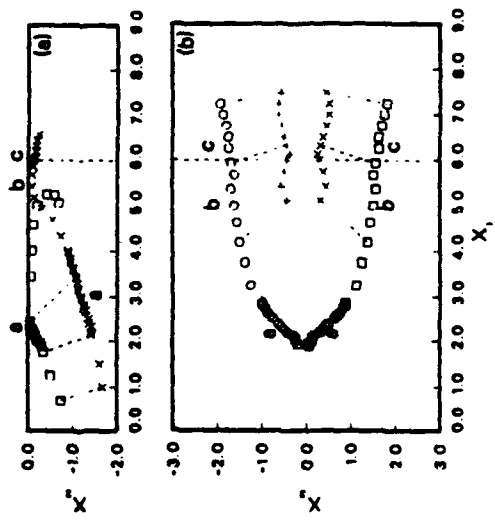


Fig. 1. The trajectories of the vortex ring on (a) the centerplane  $x_3 = 0$ , and (b) the shear free boundary,  $x_3 = 0$ . The labels a, b, and c correspond the Figs. 2 a-c, respectively.

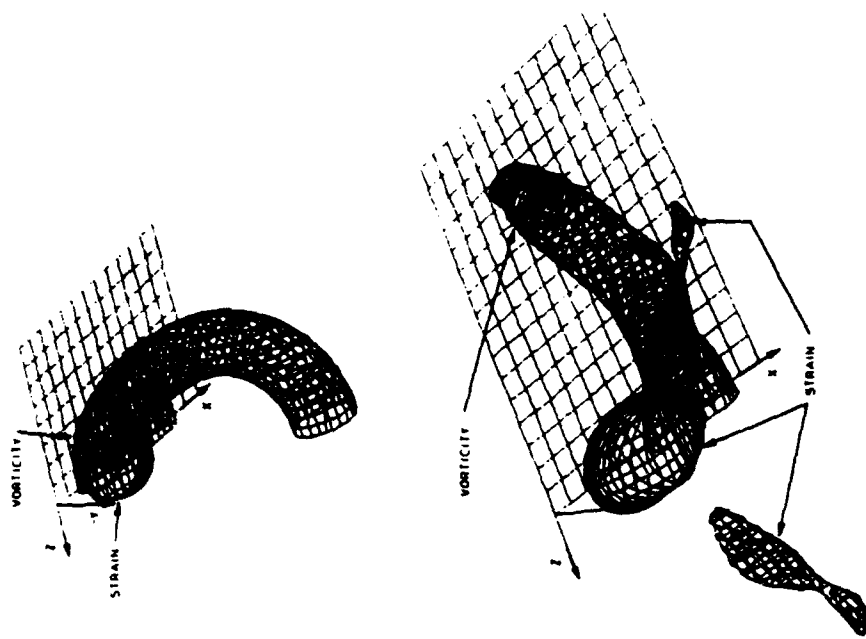


Fig. 2. Iso-surfaces of vorticity magnitude and normal strain in the transverse direction. The vorticity iso-surface is only shown for  $x_3 < 0$ . The flow is symmetric with respect to  $x_3 = 0$ . For (a) and (b), the iso-surface of strain is shown for all  $x_3$ , while for (c) it is shown for  $x_3 > 0$  only. The direction of propagation is from upper left to lower right and the ring is viewed from above, looking down through the free surface. Where the iso-surfaces intersect the free surface, they form closed contours. (a)  $t^* = 7.5$ ,  $|\omega| = 3.0$ ,  $\frac{\partial u}{\partial x_3} = 1.0$ , (b)  $t^* = 20.625$ ,  $|\omega| = 1.25$ ,  $\frac{\partial u}{\partial x_3} = 0.3$ , (c)  $t^* = 26.125$ ,  $|\omega| = 1.0$ ,  $\frac{\partial u}{\partial x_3} = 0.3$ .

### 3 The Enstrophy Balance

Enstrophy is a scalar measure of the magnitude of vorticity in the fluid. The balance equations are derived in the same manner as the balance equations for the components of the Reynolds stress tensor. In this paper the mean flow is zero and the enstrophy,  $Q = \frac{1}{2} \sum \omega_i \omega_i$ , is the instantaneous enstrophy. The instantaneous balance equations are:

$$\frac{\partial}{\partial t} \left( \frac{1}{2} \omega_i \omega_i \right) = -u_i \frac{\partial}{\partial x_j} \left( \frac{1}{2} \omega_i \omega_j \right) + \omega_i \frac{\partial u_i}{\partial x_j} + \nu \frac{\partial^2 \frac{1}{2} \omega_i \omega_i}{\partial x_j \partial x_j} - \nu \frac{\partial u_i}{\partial x_j} \frac{\partial \omega_i}{\partial x_j}, \quad (5)$$

with  $i = 1, 2$ , or,  $3$  for the component equations and an implied summation for the total instantaneous enstrophy.

Following to Tennekes and Lumley [13] and Balint [14], et al., the terms of equation (5) have the following interpretation:

$RQ : \frac{\partial}{\partial t} \left( \frac{1}{2} \omega_i \omega_i \right)$ : The rate of change of enstrophy.

$TQ : -u_i \frac{\partial}{\partial x_j} \left( \frac{1}{2} \omega_i \omega_j \right)$ : The rate of change due to transport,

$PQ : \omega_i \frac{\partial u_i}{\partial x_j}$ : The rate of change due to production,

$DQ : \nu \frac{\partial^2 \frac{1}{2} \omega_i \omega_i}{\partial x_j \partial x_j}$ : The rate of change due to viscous diffusion,

$Eq : \nu \frac{\partial u_i}{\partial x_j} \frac{\partial \omega_i}{\partial x_j}$ : The rate of change due to viscous dissipation.

The production of enstrophy,  $PQ$  accounts for the change in the enstrophy due to the stretching/compression/rotation of the vorticity field by the velocity field. For example, the term  $\omega_3 \frac{\partial u_3}{\partial x_2}$  accounts for the production of  $Q_3$  due to  $\frac{\partial u_3}{\partial x_2}$  and is of dominant importance in this work.

The rate of change of enstrophy due to transport,  $TQ$  is significant during both the propagation phase and the intensification phase. The large strain responsible for the production of  $Q_3$  during the vorticity intensification phase is the result of a positive vertical velocity.

This velocity will transport the high enstrophy fluid in the production region to the shear-free boundary. Further discussion of the terms of equation (5) is given in Leighton, et al. [15].

While it is convenient to consider the components of enstrophy to be independent of each other, the vorticity from which they are derived is bound by certain vector relations, such as  $\nabla \cdot \omega = 0$  and the related Helmholtz theorem. These additional constraints are important considerations when trying to develop a sequential model for the reconnection process. At the free-surface, the individual balance equations have a simple form. At the surface the equations for the horizontal components are:

$$\frac{\partial}{\partial t} \left( \frac{1}{2} \omega_i \omega_i \right) \equiv 0 \equiv \nu \frac{\partial^2 \frac{1}{2} \omega_i \omega_i}{\partial x_j \partial x_j} - \nu \frac{\partial u_i}{\partial x_j} \frac{\partial \omega_i}{\partial x_j} = 0; i = 1 \text{ and } 3. \quad (6)$$

These components of enstrophy are diffused to the surface and must dissipate there. The equation for the vertical component of enstrophy allows for the production of  $Q_3$  by  $\frac{\partial u_3}{\partial x_2}$  and transport of enstrophy at the shear-free boundary:

$$\frac{\partial}{\partial t} \left( \frac{1}{2} \omega_3 \omega_3 \right) = -u_1 \frac{\partial}{\partial x_1} \left( \frac{1}{2} \omega_3 \omega_3 \right) - u_2 \frac{\partial}{\partial x_2} \left( \frac{1}{2} \omega_3 \omega_3 \right) + \omega_2 \omega_3 \frac{\partial u_3}{\partial x_2} + \nu \frac{\partial^2 \frac{1}{2} \omega_3 \omega_3}{\partial x_j \partial x_j} - \nu \frac{\partial u_3}{\partial x_j} \frac{\partial \omega_3}{\partial x_j}. \quad (7)$$

As enstrophy diffuses to the shear-free boundary,  $Q_1$  and  $Q_3$  dissipate, while  $Q_2$  diffuses into the boundary. The transport and production processes are responsible for the intensification of  $Q_3$ .

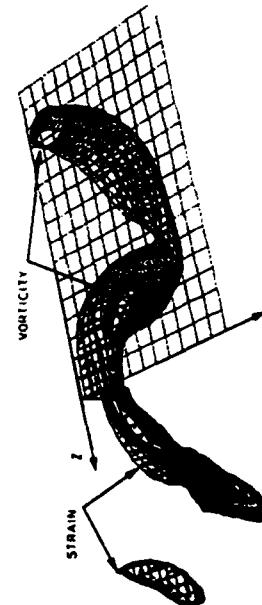
An analytical model of the vorticity diffusion (or enstrophy dissipation) process has been presented by Kambe. The vorticity distribution and its image are modeled as a two-dimensional shear layer under the influence of a three-dimensional strain field. The modeled straining field, which is similar to that observed during the simulated reconnection, causes the vorticity to diffuse into its image at a rate proportional to  $e^{-\alpha t}$ , where  $\alpha$  is the positive strain aligned with the vorticity. The simulation data shows that during the early stages of the primary reconnection event the strain is locally two dimensional ( $1/\frac{\partial x_1}{\partial x_2}, 1/\frac{\partial x_2}{\partial x_1}, 1/\frac{\partial x_3}{\partial x_1}$ ) and the circulation decays exponentially at a rate proportional to the transverse strain. Kambe's model is in qualitative agreement with the simulation data for the early stages of the primary reconnection. However, due to the decrease in the transverse strain during the simulated reconnection, the circulation in the ring exhibits a different decay behavior than that predicted by the model.

### 4 Time Evolution of Planar Averages

In section 2, the major episodes in the evolution of the ring as it interacts with the shear-free boundary were outlined and discussed. This section expands the discussion of the primary and secondary reconnection events by considering planar averages ( $z = z$ ) of the terms of equation (5). For each time chosen, the balances for the normal and transverse components of enstrophy are presented. The axial component of enstrophy,  $Q_1$ , plays only a minor role in the break and reconnect process, and will not be considered below. All of the terms in equation (5), in addition to the components of the production of enstrophy have been calculated, and a full discussion of the results are contained in [10].

**Results** The times chosen for presenting the data bracket the primary and secondary reconnection events. Fig. 3,6 are the data at times  $t^* = 6.625, 7.125, 7.875$ , and  $11.25$ , respectively, and correspond to the primary reconnection event,  $6.5 < t^* < 10$ .

The near equality of the rate of change of  $Q_3$ ,  $RQ_3$ , and the transport rate of  $Q_3$ ,  $TQ_3$ , shown in Fig. 3a, indicates that the ring is in the transport or propagation phase. The decomposition of production into its various terms shows that the only significant contribution



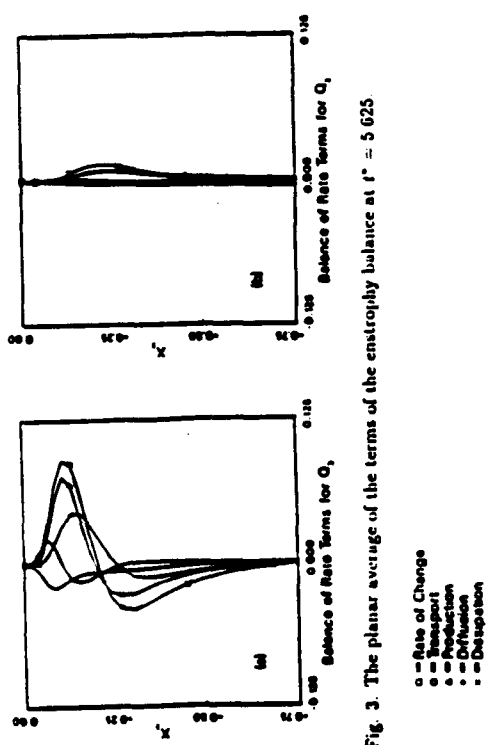


Fig. 3. The planar average of the terms of the enstrophy balance at  $t^* = 5.625$ . Note the change in scale. See Fig. 3 for symbol definitions.

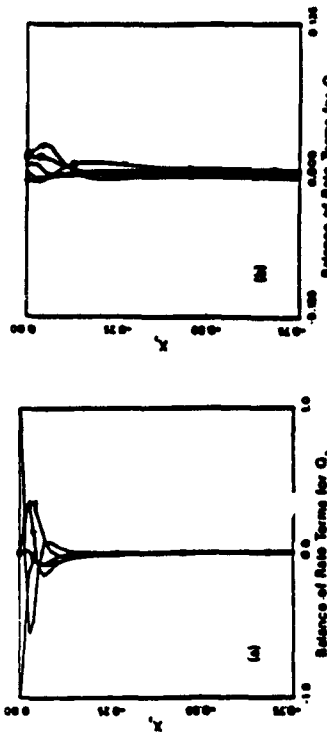


Fig. 5. The planar average of the terms of the enstrophy balance at  $t^* = 7.875$ . Note the change in scale. See Fig. 3 for symbol definitions.

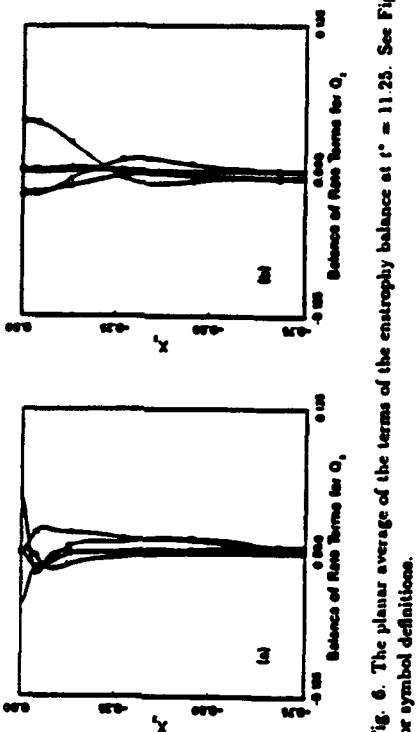


Fig. 6. The planar average of the terms of the enstrophy balance at  $t^* = 11.25$ . See Fig. 3 for symbol definitions.

Fig. 4. The planar average of the terms of the enstrophy balance at  $t^* = 7.125$ . Note the change in scale. See Fig. 3 for symbol definitions.

The production is the transverse stretching of transverse vorticity [10]. This is evidence that the interaction of the ring with the boundary has started. Although other components of production are not small, they tend to cancel. This is apparent in Fig. 3b for the normal component of enstrophy.

The characteristics of the balance for the transverse component of enstrophy change very little between  $t^* = 7.125$  and 7.875 (Fig. 4a and 5a). Near the boundary, the dominant contribution to  $Q_2$  is due to the transverse stretching of enstrophy. The transport of  $Q_2$  is also large and contributes significantly to the increase of enstrophy near the bounding surface.

The rates of dissipation and diffusion of transverse component of enstrophy are very large during this time interval. During this time interval, the rate of change of  $Q_2$  peaks near the shear-free boundary and by the end ( $t^* = 7.875$ ) has almost returned to zero. The enstrophy intensification phase is complete. For the horizontal components, the production and transport processes are superseded by diffusion and dissipation at times later than  $t^* = 7.875$ . Contrary to the above description significant differences are apparent between the balances of the normal component of enstrophy for these two time steps (Figs. 4b and 5b). The shear-free character of the boundary permits normal vorticity to terminate on the boundary. Without anti-parallel image vorticity, the rates of diffusion and dissipation of  $Q_2$  near the boundary is limited [18]. The enstrophy must be compressed into a thin region near the boundary for gradients of  $Q_2$  to become large enough to permit sufficient diffusion for the

remnant is diffusing away. The trajectory of the remnant is apparent in Fig. 1a. Near the surface,  $RQ_1$  is approximately zero. The normal vorticity near the surface has settled to a steady state. The rates of transport and dissipation are almost equal to the rate of production of  $Q_1$ .

The rate terms at  $t^* = 20.625$  (Fig. 7) and  $t^* = 28.125$  (Fig. 8) are less smooth and much smaller than during the primary reconnection. At  $t^* = 20.625$  the rates of production and transport of enstrophy are sufficient to overcome the viscous diffusion, causing an increase in  $Q_3$ . The growth in enstrophy leads to increased diffusion and dissipation of  $Q_3$  at the upper surface. As noted earlier, the strain rate is small, and the time scales are large relative to those characteristic of the primary reconnection. By  $t^* = 28.125$  the vorticity responsible for the production has moved away from the surface. (See Fig. 2a.) After  $t^* = 28.125$  the rate of decay increases as the dissipative and diffusive processes become increasingly more important relative to production.

As in the primary reconnection, the production of normal enstrophy shown in Fig. 7b and 8b is due to the combined effects of normal stretching and rotation from the transverse direction to the normal. Between  $t^* = 20.625$  and  $t^* = 28.125$ , the vorticity associated with this production moves closer to the bounding surface, and at  $t^* = 27$  is significantly attached to the surface. The attached vorticity is transported and dissipated as it is produced.

**Discussion** In this section a simple descriptive model is presented which explains some of the features of the primary and secondary reconnection events. As indicated in Figs. 3a and 4a, the initial growth of enstrophy is due to transport and production by transverse stretching, resulting in a thin layer of vorticity below the shear-free boundary. Following Kambe, the thin vortex layer and its image can be considered as a shear layer. Although the transverse strain within the shear layer,  $\dot{\gamma}_{12}$ , is not a strong function of  $z_3$  the strain will achieve a maximum on the plane of symmetry. According to Kambe's model, the rate of diffusion of the vorticity into its image will also be greatest on the plane of symmetry. As the compressed transverse vorticity diffuses, the magnitude of the axial velocity,  $|u_1|$  on the shear-free boundary decreases. The decrease in  $|u_1|$  increases the circulation through both half planes of the top boundary ( $z_2 = 0, z_3 > 0$ ) and ( $z_2 = 0, z_3 < 0$ ). The vorticity attached to the top surface is convected to the trailing edge of upper portion of the ring. The distribution of the attached vorticity immediately after reconnection resembles an arc-shaped shear layer (Fig. 9). This arc rolls up into the circular distribution vorticity seen intersecting the top surface in Fig. 2b.

The increased complexity of the vorticity and induced strain field of the secondary reconnection event makes the interpretation of the enstrophy balances more difficult, but the sequence is largely the same as that occurring in the primary reconnection. Initially there is a positive transverse strain and vertical velocity near the trailing edge of the bottom of the vortex ring as it approaches the upper boundary. The data of Figs. 2b, 2c, 7 and 8, support the following sequence of events. The induced transport and production of enstrophy enhance the diffusion and dissipation. As the transverse enstrophy decreases on the centerplane, with losses occurring mainly at the trailing edge, the normal enstrophy diffuses to the surface. The secondary reconnection begins. The secondary event requires a much longer time than the primary reconnection. This additional time is enough for the transverse components of the balance near the shear-free boundary in Fig. 6a to be convected forward of the leading edge of the ring by the induced velocity on the top surface. There the vorticity is concentrated and intensified to form the vertical appendages appearing in Fig. 2c. As

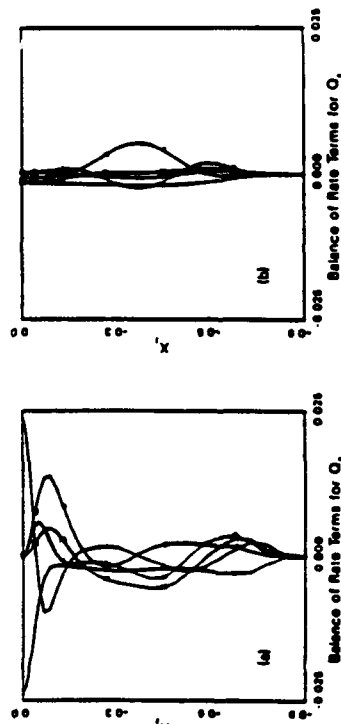


Fig. 7. The planar average of the terms of the enstrophy balance at  $t^* = 20.625$ . Note the change in scale. See Fig. 3 for symbol definitions.

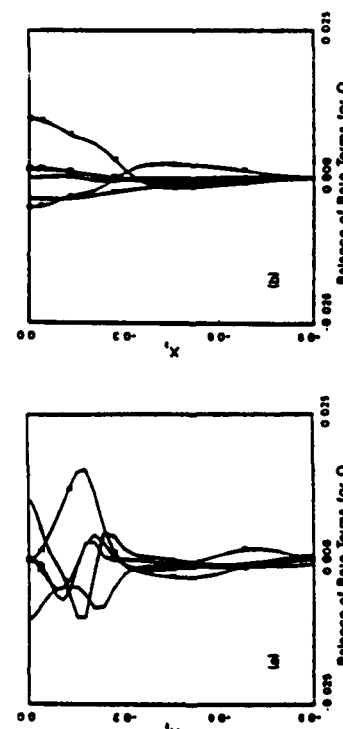


Fig. 8. The planar average of the terms of the enstrophy balance at  $t^* = 28.125$ . See Fig. 3 for symbol definitions.

reconnection to occur. The diffusion of this component of enstrophy reaches a maximum at  $t^* = 7.5$  and has returned to zero by  $t^* = 9$ . After the enstrophy has diffused to the surface, a positive vertical velocity gradient,  $\frac{\partial u_3}{\partial z_2}$ , intensifies the enstrophy at the surface. In Fig. 5b there is a local maximum in the production of enstrophy at  $z \approx -0.15$ . The maximum is due to the rotation of the transverse vorticity,  $\omega_3$  into the normal direction as vorticity is compressed to the surface. At the surface, the rotation term must be zero.

Figure 6 shows that by  $t^* = 11.25$  the primary reconnection is complete and the behavior of the ring at the boundary is quasi steady. The vorticity responsible for the transverse components of the balance near the shear-free boundary in Fig. 6a is mainly associated with a remnant of the top portion of the ring which has not diffused into the boundary during the primary reconnection. Fig. 6a indicates that at this time  $RQ_1$  is negative and the ring

responding increase in the isotropic dissipation function and the dissipation rate of kinetic energy. Evidence of this relation can be found in the simulation data. Prior the primary reconnection, the enstrophy achieves a maximum near the surface. There exists a local minimum in the kinetic energy at the same location in space and in time. The minimum in kinetic energy persists until after the primary reconnection is complete. Clear understanding of this phenomenon, which is only a precursor to reconnection is important in the context of turbulence modeling.

#### Acknowledgements

The authors thank Louis Bernal for several helpful discussions. This work is supported by the Naval Research Laboratory as part of the Fluid Dynamics Task Area. The simulations were performed at the Naval Research Laboratory.

#### References

- [1] Fohi, T. and Turner, J.S., 1975 Colliding vortex rings. *Physics of Fluids* **18**, 433.
- [2] Lim, T.T., 1989 An experimental study of a vortex ring interacting with an inclined wall. *Experiments in Fluids* **7**, 453.
- [3] Kwon, J.T., 1989 Experimental Study of Vortex Ring Interaction with a Free Surface. The University of Michigan Program in Ship Hydrodynamics Technical Report 89-06.
- [4] Schatzle, P.R., 1987 An experimental study of fusion of vortex rings. Ph. D. Thesis, California Institute of Technology.
- [5] Kerr, R. and Hueran, F., 1989 Simulation of vortex reconnection. *Physics of Fluids* **31**, 474.
- [6] Buntine, J.D. and Pullin, D.I., 1989 Merger and cancellation of strained vortices. *J. Fluid Mech.* **205**, 283.
- [7] Kambe, S., 1984 Some dissipation mechanisms in vortex systems. In: *Turbulence and Chaotic Phenomena* (ed. T. Tatsumi), pp 239-244. IUTAM.
- [8] Kim, J., Moin, P., and Moser, R., 1987 Turbulence statistics in a fully developed channel flow at low Reynolds number. *J. Fluid Mech.* **177**, 153.
- [9] Leighton, R.I. and Sreen, Jr., T.F., 1991 The interaction of a vortex ring with a shear-free boundary. In preparation for submittal to *Physics of Fluids*.
- [10] Leighton, R.I. and Sreen, Jr., T.F., 1991 The interaction of a vortex ring with a shear-free boundary. NPL Memorandum Report, *under review*.
- [11] Ashurst, W.T. and Meiron, D.I., 1987 Numerical Study of Vortex Reconnection. *Phys. Rev. Lett.* **58**, 1632-1635.
- [12] Saffman, 1989 A Model of the Vortex Reconnection. *J. Fluid Mech.* **212**, 395-402.
- [13] Tennekes, H. and Lumley, J.L., 1972 *A First Course in Turbulence*. The MIT Press, Cambridge, Mass.
- [14] Balint, J.I., Vukoslavcevic, P. and Wallace, J.M., 1988 The transport of enstrophy in a turbulent boundary layer. In *Proceedings of the Zavod Memorial International Seminar on Wall Turbulence*.

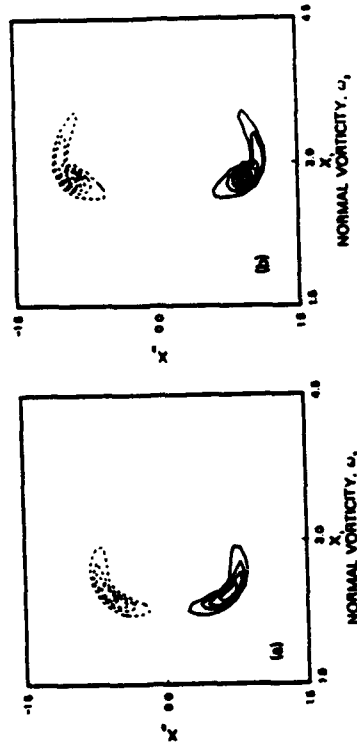


Fig. 9. Contours of normal vorticity on the shear-free boundary. Solid contours indicate positive vorticity. (a)  $\epsilon^* = 7.5$ , (b)  $\epsilon^* = 9.375$ .

more vorticity is reconnected in these appendages, they will induce a strain on the remaining portion of the ring, resulting in increased rates of production, diffusion and dissipation. There finally results two half-ring structures connected by a bridge of vorticity. As mentioned above this bridge is the remnant of the bottom of the ring after the secondary reconnection and will eventually dissipate.

#### 5 Conclusions

The terms of the enstrophy balance equation have been calculated and used to study the dynamics of the reconnection event. From the analysis, a physical description has been developed which relates the vortex reconnection process with the dynamics of enstrophy. The salient features of this description are that as the vortex ring interacts with the surface, the processes of transport and production act to increase the level of enstrophy. The majority of the increase in enstrophy is associated with the increased transverse vorticity. The concentrated enstrophy leads to increased rates of diffusion and dissipation of enstrophy. While the transverse and axial vorticity dissipates at the surface, the enstrophy due to the vertical vorticity accumulates. This is the reconnection event. After the enstrophy is at the surface the processes of transport and production act to concentrate and intensify the enstrophy. What is initially a diffuse region of attached vorticity quickly forms into the compact half-ring apparent in the flow visualization data of Kwon [3] and Leighton, et al. [10]. The interaction between vorticity and a shear-free boundary has been shown to result in the significant production of enstrophy near the boundary. Similar behavior has been when seen random, or turbulent vorticity interacts with a shear-free surface [15]. The increase in enstrophy is an important mechanism for the dissipation of kinetic energy near the surface.

There exists a relationship between enstrophy and the isotropic dissipation function, which has been discussed by Hinze [16] in the context of turbulent flows and by Kamhr [7] for colliding vortex rings. Although this relation holds only in integral form, the largest single term in the enstrophy, in the isotropic dissipation function and in the dissipation of kinetic energy is  $(\frac{\partial \omega}{\partial x})^2$ . Therefore if the dynamics of the flow increase the level of  $Q_3$ , there will be a cor-

[15] Leighton, R.L. and Sween, Jr., T.F., 1991. Interaction of Vorticity with a Free Surface in Turbulent Open Channel Flow. AIAA Paper AIAA-91-0236, presented at the AIAA 29th Aerospace Sciences Meeting and Exhibit, Reno, Nevada, January, 1991.

[16] Hinze, J.O., 1975. *Turbulence*. McGraw-Hill, New York

## REDISTRIBUTION OF SURFACE-ACTIVE MATERIALS IN A SHIP WAKE

R. D. Petter, O. M. Griffin, J. A. C. Katter, and W. R. Berger  
Naval Research Laboratory  
Washington, D.C.

### ABSTRACT

Surface-active films are found in all parts of the ocean. They are easily detected (visually) on the ocean surface when the wind speed is less than 5 m/s. They are generally of biological origin and consist mainly of folic and humic acids, carbohydrates, proteins and lipids. Their molecules have hydrophilic (partially water soluble) heads and hydrophobic (inert-like carbon chain) tails. Surface-active films that have been concentrated at the edges of the centaurine wake generated by the passage of the ship strongly influence the propagation of the short gravity and capillary waves which interact with electromagnetic waves at both radar and visible wavelengths. A highly accurate method for detecting the presence of surface films and measuring the fine-scale surface film pressure and surface elasticity distributions on a water surface was developed at NRL. These measurements have allowed us to develop a clearer understanding of the role these ship-generated surface-active film distributions play in the formation of the dark centaurae and "railroad track" (dark lines aligned at some narrow angle to the ship's track) features in synthetic aperture radar (SAR) signature of ship wakes.

### NOMENCLATURE

$A$	free surface area of surfactant film
$a$	surface wave height
$C$	constant
$E$	surface elasticity
$F$	Froude number, $V/(gL)^{1/2}$
$g$	gravitational acceleration
$h$	measurable
$L$	ship length
$n$	logarithmic slope of pressure-area curve
$V$	ship speed
L-band	SAR operating frequency, 1.2 GHz
C-band	SAR operating frequency, 5.3 GHz
X-band	SAR operating frequency, 9.4 GHz
$\sigma$	surface tension of clean water
$\Pi$	surface film pressure
$T_{meas}$	measured surface tension

**Appendix I**

**Three-Dimensional Vortex Interactions with a Free Surface**

# **RECENT ADVANCES AND APPLICATIONS IN COMPUTATIONAL FLUID DYNAMICS**

*presented at*

THE WINTER ANNUAL MEETING OF  
THE AMERICAN SOCIETY OF MECHANICAL ENGINEERS  
DALLAS, TEXAS  
NOVEMBER 25-30, 1990

*sponsored by*

THE FLUIDS ENGINEERING DIVISION, ASME

*edited by*

OKTAY BAYSAL  
OLD DOMINION UNIVERSITY

THE AMERICAN SOCIETY OF MECHANICAL ENGINEERS  
United Engineering Center  345 East 47th Street  New York, N.Y. 10017

## THREE-DIMENSIONAL VORTEX INTERACTIONS WITH A FREE SURFACE

Henry T. Wang

Laboratory for Computational Physics and Fluid Dynamics  
Naval Research Laboratory  
Washington, D. C.

Richard I. Leighton

Science Applications International Corporation  
McLean, Virginia

### ABSTRACT

This paper presents a numerical calculation of the three-dimensional flow due to a pair of vortices rising toward a shear-free surface. A spectral method with transforms in Fourier-Chebyshev space is used to solve a vertical velocity-vertical vorticity formulation of the Navier-Stokes equations which eliminates the pressure term and implicitly satisfies the equation of continuity. The method is used to study the subsequent evolution of various initial three-dimensional perturbations to the two-dimensional case. It is shown that this evolution leads to flows which range from being negligibly different from the two-dimensional case to being numerically unstable, depending on the type, magnitude, and wavelengths of the initial perturbations. It is also shown that an approximate calculation for the surface elevation is in good qualitative agreement with experimental results for weak vortices corresponding to low values of the Froude number.

### INTRODUCTION

The flow field around a pair of counter-rotating vortices in the vicinity of a bounding surface is of interest in a number of applications. These vortices naturally arise behind lifting surfaces such as airplane wings and underwater hydrofoils. In aerodynamic applications involving the landing or take-off of aircraft, it is of interest to ascertain the characteristics and persistence of the vortices near the runway left behind by previous aircraft. In marine applications, it is important to assess the presence of the nearby free surface on the lift performance of the submerged hydrofoils. More recently, the use of modern remote sensing techniques makes it of interest to ascertain the small surface elevations caused by the subsurface vortices since they change the reflection and refraction characteristics and hence are detectable. In this connection, it is now realized that even small amounts of surface contaminant can have large effects on both the free surface perturbation and the underwater vortices.

Representative of recent experimental studies on vortex pairs are those by Barker and Crow[1], Sarpkaya[2], Sarpkaya,

Elnitsky, and Leeker[3], and Bernal, Hirsa, Kwon, and Willmarth[4]. In these experiments, care must be taken to not only generate the required vorticity but also enough fluid to fill the vortex recirculation cell enclosing both vortices; otherwise, the generated vortices quickly dissipate[1]. To this end, flap mechanisms are used in [1,2,4], while underwater wings are used in [3]. In these and related studies, it is usually observed that there is a tendency for the vortices to rebound away from the surface, the tendency being stronger for no-slip[1] and contaminant surface conditions[4] than for the shear-free case. Barker and Crow postulate that this rebound phenomenon is due to the effect of finite vortex core, which tends to deform in the vicinity of the bounding surface. However, Saffman[5] shows that this effect must be due to viscosity, since the integration of the inviscid Euler equations always predicts a monotonic asymptotic approach of the vortices to the bounding surface. By using a finite-difference approach to solve the Navier-Stokes equations, Peace and Riley[6] support this argument by showing that even for the shear-free case some vorticity is lost to the surface due to viscous diffusion. In [2] and [3], it is shown that the surface perturbation due to the vortex pair consists of three-dimensional ridges or scarifications perpendicular to the axis of the vortices, and depressions or scars which are parallel to the axis.

Recent numerical studies have largely focused on the iterative solution for the underwater vortex flow field and the unknown position of the free surface. Sarpkaya, Elnitsky, and Leeker[3], Marcus and Berger[7], Telste[8], and Yu and Tryggvason[9] assume the fluid to be inviscid while Ohring and Lugi[10] consider the more general case of a viscous fluid. The generalized vortex/boundary integral technique proposed by Baker, Meiron, and Orszag[11] is used in [3,8,9]. The basic technique consists of placing a number of vortices on the free surface, and at each time step iterating on the strength and location of these vortices until the dynamic and kinematic free surface conditions are satisfied. The approaches differ on the number and initial location of the vortices, the desingularization of the velocities near the individual vortices, and the filtering or damping techniques needed for numerical stability. Marcus and Berger use a finite

difference approach to model the Laplace equation and the free surface conditions. Ohring and Lüttgen use a finite difference approach to model the spatial derivatives in the Navier-Stokes and free surface equations. In all of these studies, it is observed that the vortex trajectories vary as a function of the Froude number  $Fr = V_0/\sqrt{ga}$ , where  $V_0$  is the initial translational velocity of the vortex pair,  $g$  is the gravity constant, and  $a$  is the initial vortex spacing. For high values of  $Fr \geq 1$ , approximately, the vortex trajectories are little affected by the presence of the free surface and tend to burst through the interface. As the value of  $Fr$  decreases, the trajectories increasingly approximate those for a rigid wall until there is little difference between these cases for  $Fr \leq 0.15$ , approximately[3].

In a related study, the present authors[12] consider the case of the vortices rising to a surface with various types of contaminant. Here, the unknown free surface condition is not the elevation but the variable shear due to the surface tension gradient caused by the spatially varying contaminant concentration. A spectral method, with transforms in Fourier-Chebyshev space, is used to model the spatial derivatives in the Navier-Stokes equations.

All of the above studies assume two-dimensional flow where the axes of the vortices are assumed to be straight lines parallel to the bounding surface. It is well known that these vortices usually do not conform to this approximation. Crow[13] shows that the exponential growth of certain eigenmodes eventually causes the initially straight cores to break up and form uncorrelated vortex rings. Also, the ambient flow field contains perturbations due to turbulence or irregularities in the forward speed of the lifting surface. Finally, since the vortices are being continuously generated by the lifting surface traveling at forward velocity  $U$ , and the vortices have a finite rise velocity  $V_0$ , the vortex line is inclined at the angle  $\gamma = \tan^{-1}(V_0/U)$  with the horizontal.

In the present paper we investigate the effect of various types of initial three-dimensional perturbations on the subsequent development of the vortex cores rising to a shear-free surface. We present results for three sets of cases. The first set is the previous two-dimensional case to verify the accuracy and stability of our three-dimensional approach. The second set consists of various sinusoidal variations in the axial direction of the horizontal locations of the vortex centers. The third set consists of various random three-dimensional perturbations to the initial two-dimensional flow field. Our numerical approach is essentially a generalization to three dimensions of our previous two-dimensional spectral approach[12]. The resulting basic equations and solution procedure are similar to those given in Kim, Moin, and Moser[14] or Handler, Hendricks, and Leighton[15]. However, the formulation given in these references is for no-slip boundary conditions appropriate for channel flow while we consider shear-free surface conditions. Also, we calculate the free surface elevation from the computed flow field.

We first give a brief outline of those equations and solution procedures which are described more fully in [12,14,15]. However, we give a more detailed description of our boundary and perturbed initial conditions which differ from those given in these references. We also describe our a posteriori calculation of the surface wave elevation and discuss its accuracy. We present and discuss our results which are given in terms of three-dimensional plots for the surface elevation and line and contour plots for the subsurface vorticity and velocity fields. We pay particular attention to the growth or decay of the initial three-dimensional perturbations. We conclude by briefly summarizing the principal

findings.

## THEORETICAL APPROACH

### Basic Equations

Figure 1 shows the coordinate system and the dimensions of the computation domain, while Fig. 2 shows the initial vortex configuration. We nondimensionalize our approach by taking the initial vortex spacing  $a$ , the initial translational velocity of the vortex pair  $V_0$ , and the fluid density  $\rho$ , as reference variables. Figure 1 shows that our computation domain is 2 units in the vertical  $y$  direction where nonperiodic boundary conditions are applied, and 10 units in the horizontal  $x$  and  $z$  directions where periodic boundary conditions apply. The  $z$  direction coincides with the axis of the vortex cores and vortex motion takes place in the  $yz$  plane in the two-dimensional motion considered in previous studies. In terms of dimensionless variables, the Navier-Stokes equations in the so-called rotational form is given by

$$\frac{\partial \mathbf{u}}{\partial t} + \boldsymbol{\omega} \times \mathbf{u} = -\nabla P + \frac{1}{Re} \nabla^2 \mathbf{u} \quad (1)$$

where  $\mathbf{u}$  is the fluid velocity,  $t$  is the time,  $\boldsymbol{\omega} = \nabla \times \mathbf{u}$  is the vorticity,  $P = p + \mathbf{u} \cdot \mathbf{u}/2$  is the dynamic pressure head,  $p$  is the pressure,  $Re = \rho a V_0 / \mu$  is the Reynolds number, and  $\mu$  is the fluid dynamic viscosity. As noted by Hussaini and Zang[16], the use of this form in Fourier collocation methods, as in our study, conserves kinetic energy and hence tends to minimize the effect of nonlinear instabilities. For an incompressible fluid, conservation of mass takes the form

$$\nabla \cdot \mathbf{u} = 0 \quad (2)$$

The troublesome term involving  $P$  may be eliminated and the incompressibility condition implicitly satisfied by writing Eq. (1)

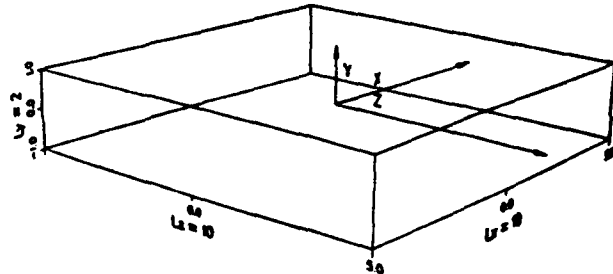


Fig. 1—Coordinate System and Computation Domain

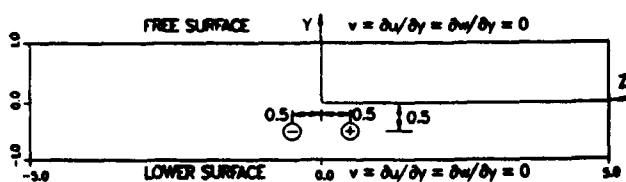


Fig. 2—Initial Vortex Configuration

in component form for the velocities  $(u, v, w)$  in the  $(x, y, z)$  directions, taking second order spatial derivatives of these equations, and using Eq. (2). This results in a fourth order equation for the velocity  $v$  and second order equation for the vorticity component  $\omega_y$ , as follows[14,15]

$$\frac{\partial}{\partial t} \nabla^2 v = H_v + \frac{1}{Re} \nabla^4 v \quad (3)$$

$$\frac{\partial}{\partial t} \omega_y = H_\omega + \frac{1}{Re} \nabla^2 \omega_y, \quad (4)$$

where  $H_v$  and  $H_\omega$  are the nonlinear terms arising from  $\omega \times u$ .

#### Numerical Solution Procedure

We advance Eqs.(3) and (4) in time by using the weighted implicit Crank-Nicholson method for the linear term and the weighted explicit Adams-Basforth method for the nonlinear term. In the case of Eq.(4), this results in the following equation for the value of  $\omega_y$  at the new  $n+1$  time step in terms of values at the previous  $n$  and  $n-1$  time steps

$$(1 - \frac{\Delta t}{2Re} \nabla^2) \omega_y^{n+1} = (1 + \frac{\Delta t}{2Re} \nabla^2) \omega_y^n + \frac{\Delta t}{2} (3H_\omega^n - H_\omega^{n-1}) \quad (5)$$

where  $\Delta t$  is the size of the time step. Since we assume the flow to be shear-free at the upper and lower boundaries, i.e.  $\partial u / \partial y = \partial w / \partial y = 0$  on  $y = \pm 1$ , the resulting boundary condition on  $\omega_y$  is

$$\frac{\partial \omega_y}{\partial y} = 0 \text{ on } y = \pm 1 \quad (6)$$

whereas  $\omega_y = 0$  for the no-slip conditions considered in [14,15].

The fourth-order Eq.(3) for  $v$  is split into two second-order equations as follows

$$(1 - \frac{\Delta t}{2Re} \nabla^2) \phi^{n+1} = (1 + \frac{\Delta t}{2Re} \nabla^2) \phi^n + \frac{\Delta t}{2} (3H_v^n - H_v^{n-1}) \quad (7)$$

$$\nabla^2 v^{n+1} = \phi^{n+1} \quad (8)$$

Our boundary conditions of no flow through, and no shear on, the upper and lower surfaces take the following form

$$v = \frac{\partial^2 v}{\partial y^2} = 0 \text{ on } y = \pm 1 \quad (9)$$

Again we note that for the no-slip case[14,15] the second-order derivative in the above equation is replaced by a first-order derivative.

We do not solve the above formulation directly in physical space but in Fourier-Chebyshev transform space, where the unknowns  $v, \phi, \omega_y$  are expanded as exponential functions in the periodic  $x$  and  $z$  directions, and in Chebyshev polynomials  $T_n$  in the  $y$  direction. For example, in the case of  $v$ , this series takes the form

$$v(x, y, z, t) = \sum_{l=0}^{L/2-1} \sum_{m=-M/2}^{M/2-1} \sum_{n=0}^N \tilde{v}(l, m, n, t) \exp(i\alpha_l x + i\beta_m z) T_n(y) \quad (10)$$

where  $L, M, N + 1$  are the number of grid points in the  $x, z, y$  directions, respectively,  $\alpha_l = 2\pi l / L_z$  and  $\beta_m = 2\pi m / L_z$  are respectively the  $l$ th and  $m$ th wavenumbers in the  $x$  and  $z$  directions, and  $L_z = 10$  and  $L_z = 10$  are respectively the lengths of the computation domain in the  $x$  and  $z$  directions. The grid points  $z_l$  and  $z_m$  are evenly spaced while the  $y_n$  points are cosine-spaced so as to have the highest density near  $y = \pm 1$ .

By noting that the spatial derivatives  $\partial / \partial x$  and  $\partial / \partial z$  respectively correspond to multiplications by  $i\alpha_l$  and  $i\beta_m$  in transform space, it can be seen that the three-dimensional Poisson Equations (5), (7), and (8) reduce to three sets of  $L/2 \times M$  Poisson equations in the  $y$  direction at each time step. For example, the equation for  $\phi$  takes the form

$$\frac{\partial^2 \tilde{\phi}_{lm}^{n+1}}{\partial y^2} - (\alpha_l^2 + \beta_m^2 + \frac{2Re}{\Delta t}) \tilde{\phi}_{lm}^{n+1} = G(y, \alpha_l, \beta_m, \tilde{\phi}_{lm}^n, \tilde{H}_{lm}^n, \tilde{H}_{lm}^{n-1}) \quad (11)$$

Due to the presence of the nonlinear terms  $\tilde{H}_{lm}^n$  and  $\tilde{H}_{lm}^{n-1}$  we must, at each time step, inverse transform to physical space, perform the operations required to obtain  $H_v^n$ , and then transform  $H_v^n$  to get  $\tilde{H}_v^n$ . We perform these transforms by using standard Fast Fourier Transform techniques. Also, to avoid aliasing errors, whereby energy from modes outside our range of consideration is placed into lower modes, we use the well known de-aliasing technique whereby we consider  $(3/2)(L \times M)$  physical points but use only the modes corresponding to  $L \times M$  points.

The Poisson Equation (11) effectively reduces to the inversion of a  $N+1 \times N+1$  matrix for the coefficients of the Chebyshev polynomials. By using recursion relations which relate derivatives of a Chebyshev function of order  $n$  to neighboring orders, the second derivative in Eq. (11) for the  $N+1$  grid points gives rise to two quasi-tridiagonal matrices for the coefficients of the even and odd Chebyshev polynomials (see, for example, Chapter 5 of [17]). Inversion of these matrices is considerably less time consuming than full matrices of the same order.

Our use of the implicit Crank-Nicholson scheme to advance in time the linear terms of our solution assures their stability, regardless of the size of the time step  $\Delta t$ . However, our use of the explicit Adams-Basforth scheme for the troublesome nonlinear terms requires that  $\Delta t$  not exceed the criterion given by the Courant-Friedrichs-Lowy condition, which basically states that  $\Delta t$  should be sufficiently small so that the solution does not completely propagate across any grid cell in the computation domain. The strictly correct manner of implementing this is to evaluate the ratio of grid size to speed of propagation throughout the computation domain at each time step and use the minimum value of this ratio as the new value of  $\Delta t$ . Instead, we find that the following approximate approach yields stable solutions for the present calculations. We take  $2/N$ , the average in the  $y$  direction, as the representative grid dimension and the initial velocity of the vortex pair (which is unity in dimensionless coordinates) as the typical speed of propagation. Our time step is then approximated by

$$\Delta t \doteq \delta \frac{2}{N} \quad (12)$$

where  $\delta \doteq 0.2/12$ .

Once  $\tilde{v}$  and  $\tilde{\omega}_y$  have been computed, the remaining two components of velocity in transform space,  $\tilde{u}$  and  $\tilde{w}$ , may be conveniently obtained by solving the following two simultaneous algebraic equations which arise by using the continuity Eq. (2) and the definition of  $\tilde{\omega}_y = \partial \tilde{u} / \partial z - \partial \tilde{w} / \partial x$

$$\frac{\partial^2 \bar{u}}{\partial x^2} + \frac{\partial^2 \bar{u}}{\partial z^2} = -\frac{\partial \bar{v}}{\partial x} \frac{\partial \bar{v}}{\partial y} + \frac{\partial \bar{\omega}_y}{\partial z} \quad (13a)$$

$$\frac{\partial^2 \bar{v}}{\partial x^2} + \frac{\partial^2 \bar{v}}{\partial z^2} = -\frac{\partial \bar{v}}{\partial z} \frac{\partial \bar{v}}{\partial y} - \frac{\partial \bar{\omega}_y}{\partial x} \quad (13b)$$

The remaining two components of vorticity,  $\bar{\omega}_x$  and  $\bar{\omega}_z$ , are then obtained algebraically from the definition  $\omega = \nabla \times u$ .

The dynamic pressure head  $P$  is then calculated by the following Poisson equation which results from taking the divergence of Eq. (1) and again using the continuity Eq. (2)

$$\nabla^2 P = \nabla \cdot (u \times \omega) \quad (14)$$

The boundary conditions for  $P$  at  $y = \pm 1$  may be conveniently obtained by considering the momentum equation in the  $y$  direction. For our case of shear-free surfaces, the condition is

$$\frac{\partial P}{\partial y} = 0 \text{ on } y = \pm 1 \quad (15)$$

From  $P$  we can conveniently calculate  $p = P - u \cdot u$ . By then considering the continuity of stress in the  $y$  direction at the free surface (see, for example Skop[18]) we can calculate the first order elevation  $\eta$  as follows

$$\eta = Fr^2(p - \frac{2}{Re} \frac{\partial v}{\partial y}) \text{ on } y = \pm 1 \quad (16)$$

We note that the above calculation of the elevation is a posteriori and hence only approximate since by assuming the free surface to be flat, i.e.  $v(y = \pm 1) = 0$ , we have neglected the mutual influence of vortex motion and surface elevation. However, the results of previous studies tend to show that this approximation becomes more accurate with decreasing  $Fr$ , and may give reasonable results for values of  $Fr \leq 0.15$ , approximately[3].

#### Initial Conditions

The initial position of our vortices is as shown in Fig. 2. For the case of two-dimensional Gaussian vortices, the vorticity components  $\omega_{xi}, \omega_{yi}, \omega_{zi}$ ,  $i = 1, 2$ , of each vortex are given by

$$\omega_{xi}(x, y, z) = \frac{\Gamma_i}{\pi \sigma^2} \exp - [(z - z_i)^2 + (y - y_i)^2] / \sigma^2 \quad (17a)$$

$$\omega_{yi}(x, y, z) = \omega_{zi}(x, y, z) = 0 \quad (17b)$$

where  $z_1 = -0.5$ ,  $z_2 = +0.5$ ,  $y_1 = y_2 = -0.50$ ,  $\Gamma_1 = -2\pi$ ,  $\Gamma_2 = +2\pi$ , and  $\sigma = 0.25$  is a measure of the core size. Hereafter, this case is referred to as CTWOD. We consider two series of three-dimensional perturbations. In the first series, we allow the  $z$  spacing of the vortex centers to sinusoidally vary in the axial  $x$  direction. We report results for the case where the amplitude of variation is  $\pm 20\%$ , with period  $L_x$ , and refer to this case as CZ1CY. We considered other values of amplitude and period, and found that halving the amplitude leads to only small differences from the two-dimensional case, while consideration of shorter periods usually leads to numerical instability before the end of the calculations. In the second series, we perturb all three components of  $\omega$  throughout the computation domain by random values in the range  $\pm \epsilon \omega_{max}$  where  $\omega_{max} = \Gamma / (\pi \sigma^2)$ . We consider values of  $\epsilon$  equal 0.010, 0.030, and 0.050, and refer to these cases as CO010, CO030, and CO050, respectively.

We can in principle sum the vorticity contribution from both vortices to obtain the total vorticity field  $\omega$  and then obtain the velocity  $u$  by using the following vector identity and boundary conditions

$$\nabla^2 u = -\nabla \times \omega \quad (18)$$

$$\frac{\partial u}{\partial y} = \frac{\partial v}{\partial y} = v = 0 \text{ on } y = \pm 1 \quad (19)$$

We note, however, that due to the finite size of our computation domain, the velocities induced by our vortex pair will not conform to the prescribed boundary conditions, leading to possible highly oscillatory behavior of the resultant velocities near  $y = \pm 1$ . This in turn may lead to numerical instabilities in our time marching scheme. To minimize this oscillatory behavior, we introduce the following three pairs of image vortices which tend to render the velocity field compatible with the prescribed boundary conditions:

$$\Gamma_{1i} = -\Gamma_i, y_{1i} = -2 - y_i$$

$$\Gamma_{2i} = -\Gamma_i, y_{2i} = +2 - y_i$$

$$\Gamma_{3i} = +\Gamma_i, y_{3i} = +4 + y_i$$

where  $i = 1, 2$ . We then apply Eqs. (18) and (19) to the vorticity field due to all four pairs of vortices.

## NUMERICAL RESULTS

### Calculation Parameters

We performed our calculations on a Cray X-MP/24 mainframe computer. We used a calculation grid of  $16 \times 49 \times 48$  in the  $x, y, z$  directions for the two-dimensional CTWOD and low perturbation CO010 cases, and a finer grid of  $16 \times 65 \times 48$  for the remaining higher perturbation cases. The time steps were taken to be respectively 0.0008 and 0.0005 for the coarse and fine grids, as approximated by Eq. (12). The calculations were carried out for a total time of 6 dimensionless units for the coarse grid cases, and 5 for the finer grid cases, resulting in 7500 and 10000 time steps for the coarse and fine grids, respectively. Computer execution times for one time step are approximately 0.52 seconds for the coarse grid and 0.59 seconds for the finer grid, resulting in total execution times of 3900 and 5900 seconds for the coarse and fine grids, respectively. Assuming the vortices to be nominally propagating at unit velocity at all times, the nonphysical boundaries at  $z = \pm L_z/2$  begin to be strongly felt by the vortices for  $t > 5$ , approximately. The main reason for calculating the coarse grid cases beyond this point is to investigate their numerical stability even under these nonphysical conditions. The value of  $Re$  is taken to be 1000. This is approximately one order of magnitude higher than that considered in those studies which solve the Navier-Stokes equations[6,10] and is close to the range of 3000 to 4000 considered in experimental studies[1,2,4]. This is largely due to our use of the spectral approach which more accurately models spatial variation than the finite-difference approach used in [6,10].

We present our results in three forms. First, we present line plots showing the variation of the velocity  $v$  and vorticity  $\omega_z$  in the  $z$  and  $y$  directions at the  $yz$  plane containing the maximum vorticity, and the velocity  $u$  in the  $x$  and  $y$  directions at the  $xy$  plane containing this same maximum vorticity. These plots show in convenient form the stability of our calculation procedure and the amount of amplification of the initial perturbations. We then present contour plots of the vorticity to show in greater detail the differences between the various cases. Finally, we present three-dimensional plots of the surface elevation to qualitatively show

the degree of agreement with previous studies and the effect of the three-dimensional perturbation in this case.

#### Line Plots of Subsurface Flow

Figure 3 shows six line plots which give the variation of  $u$  in the  $xy$  plane, and  $v$  and  $\omega_z$  in the  $yz$  plane at  $t = 3$  for Case CTWOD. Figures 4-9 show, in the following order, corresponding line plots for Case CTWOD at  $t = 6$ , Case CO010 at  $t = 6$ , Case CZ1CY at  $t = 3$ , Case CO030 at  $t = 0$  and 3, and Case O050 at  $t = 3$ .

Figures 3-4 show the stability of our calculations for the two-dimensional case. The axial velocity  $u$  remains identically zero at all times. Also, even at  $t = 6$  when the vortices have propagated to near the end of the periodic computation domain and are experiencing strong influence from the image vortices across these nonphysical boundaries, the calculated results continue to be smooth and free from numerical instabilities. On the other hand, Figure 5 shows that the low level perturbations for the CO010 case are sufficient to cause the corresponding line plots to exhibit the high frequency noise characteristic of numerical instability, specially noticeable in the variation of  $\omega_z$  with  $y$ . At earlier times, the calculated results are stable and differ little from those for CTWOD.

Figure 6 shows that the calculated results for Case CZ1CY are stable and differ moderately from those for the two-dimensional case. Figure 7 shows that for Case CO030, where the initial vorticity is given a random perturbation in the range  $\pm 0.03\omega_{max}$ , the high frequency content in the initial conditions is substantial for the vorticity but relatively little (though noticeable) in the case of the velocities  $u$  and  $v$ . Figure 8 shows

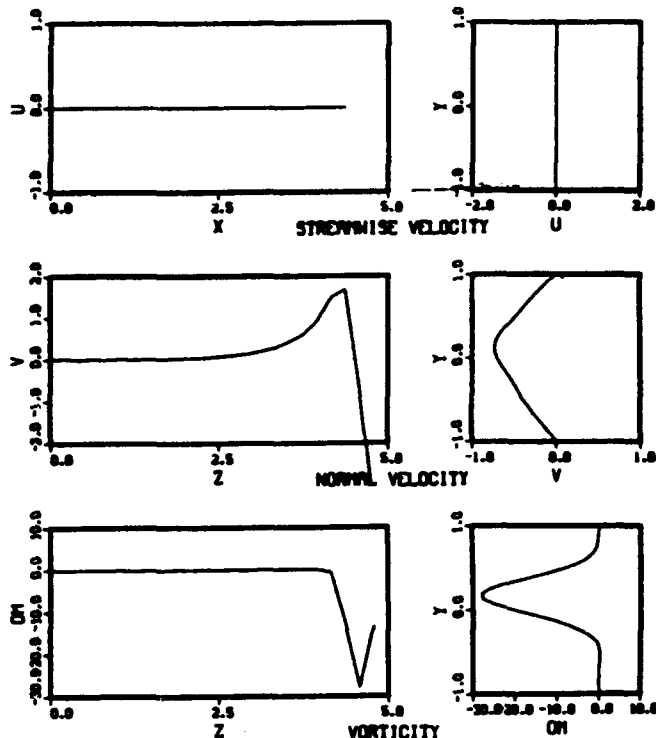


Fig. 4-Flow Variables  $u, v, \omega_z$  for Case CTWOD at  $t = 6$

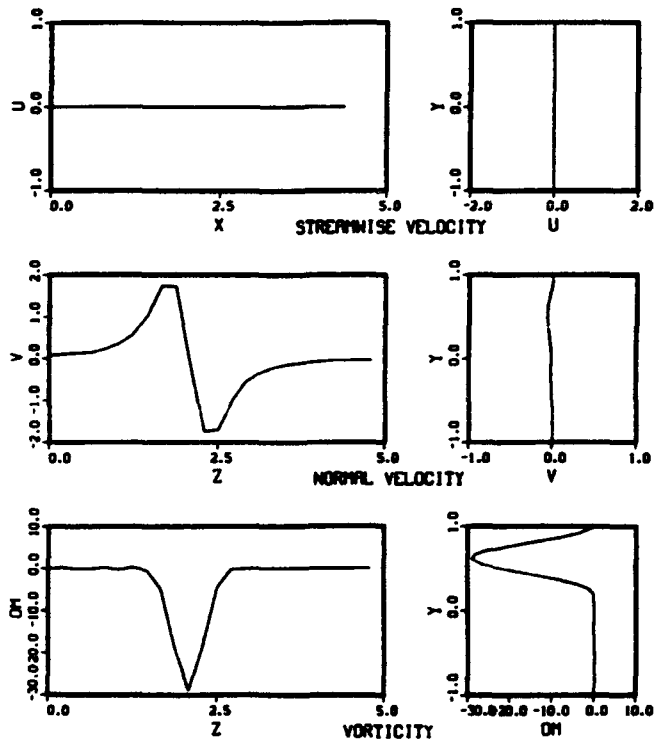


Fig. 3-Flow Variables  $u, v, \omega_z$  for Case CTWOD at  $t = 3$

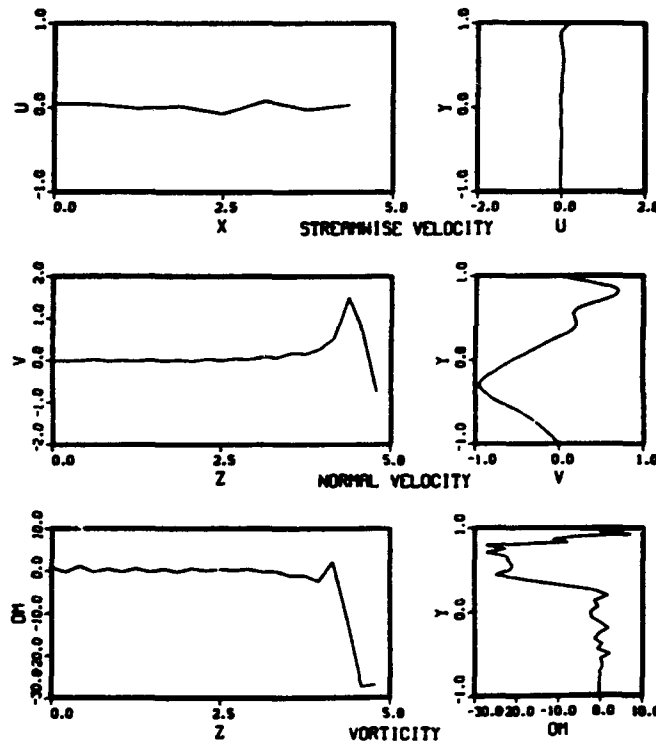


Fig. 5-Flow Variables  $u, v, \omega_z$  for Case CO010 at  $t = 6$

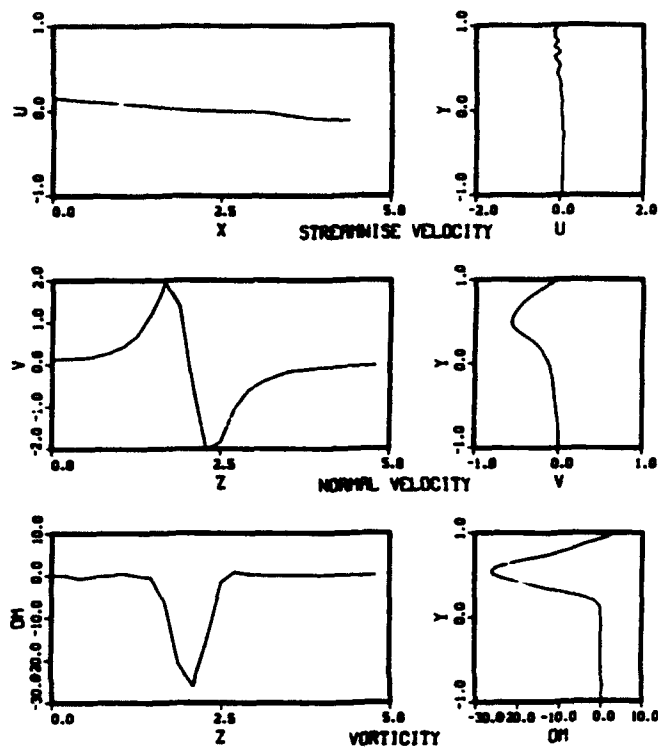


Fig. 6-Flow Variables  $u, v, \omega_z$  for Case CZ1CY at  $t = 3$

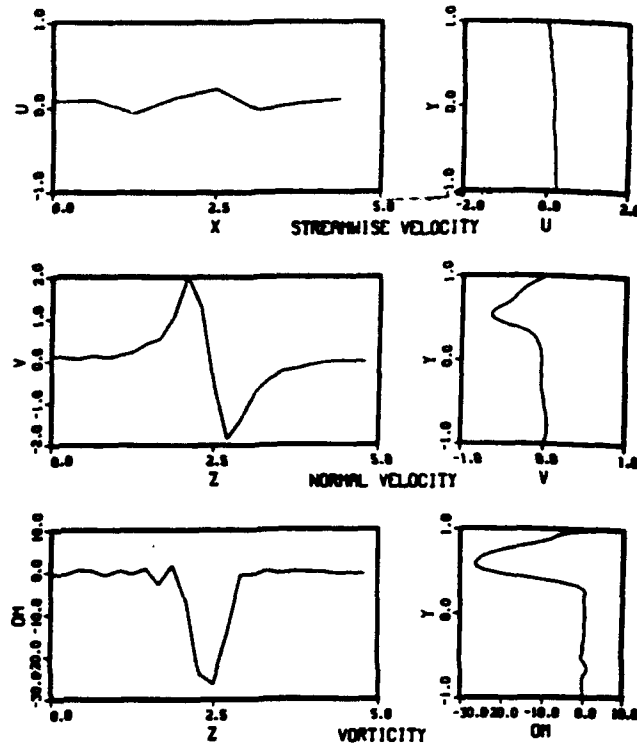


Fig. 8-Flow Variables  $u, v, \omega_z$  for Case CO030 at  $t = 3$

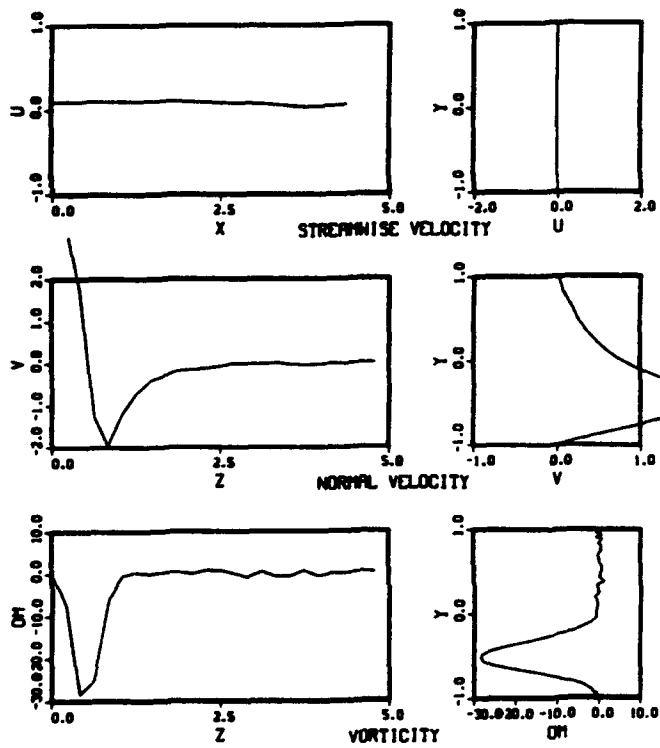


Fig. 7-Flow Variables  $u, v, \omega_z$  for Case CO030 at  $t = 0$

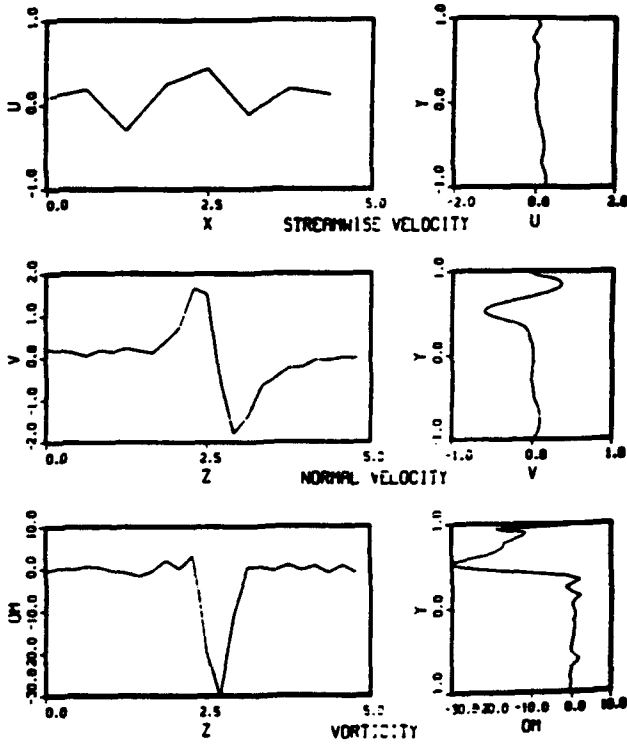


Fig. 9-Flow Variables  $u, v, \omega_z$  for Case CO050 at  $t = 3$

that at  $t = 3$  the calculation for Case CO030 is approaching numerical breakdown while Figure 9 shows that the corresponding plots for Case CO030 are already slightly in the instability region. Figure 8 also shows that the initial perturbations which are largely confined to the vorticity at  $t = 0$  are now also evident in the velocities.

#### Contour Plots of Subsurface Flow

Figure 10 shows the contour plot of the vorticity  $\omega_z$  at the midplane  $z = 0$  and  $t = 3$  for Case CTWOD. Figures 11a-c show these plots for Case CZ1CY at  $t = 3$  for  $z = -L_z/4, 0, +L_z/4$ , respectively. Figures 12a-c show corresponding plots for Case CO030. Figures 11a-c show the expected trend that the vertical distance of the vortex pair below the free surface varies with  $z$  due to the unequal rise velocities caused by the initial axial variation of the  $z$  spacing of the vortex pair. As a result, the vortex contours show different stages of interaction with the free surface. Figure 11a, corresponding to the case of the vortices being closest to, and hence interacting most strongly with, the free surface, suggests the formation of a ribbon-like structure, similar to that observed by Pumir and Kerr[19]. They point out that the calculation of its subsequent evolution is usually limited by grid resolution. It is also of interest to note that Figure 11b, which corresponds to the  $z$  location where the initial vortex spacing is identical to the two-dimensional case, exhibits contours which are similar to those shown in Figure 10 for Case CTWOD. Figures 12a-c show that the contours due to the random vorticity perturbation case CO030 are no longer symmetric about the plane  $z = 0$ .

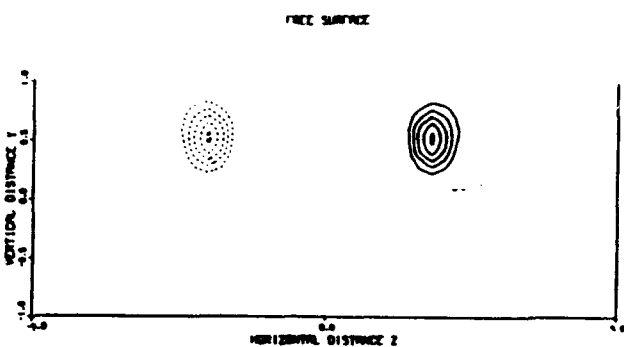


Fig. 11b-Vorticity  $\omega_z$  for Case CZ1CY at  $z = 0, t = 3$

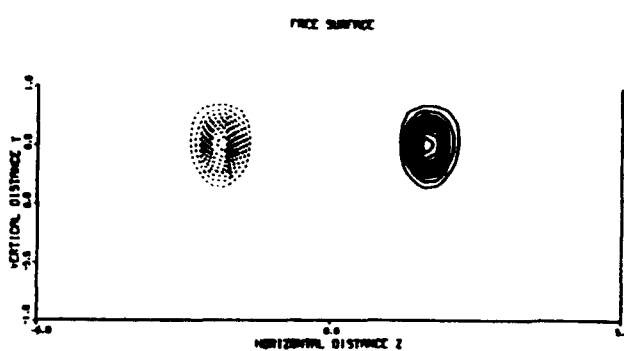


Fig. 11c-Vorticity  $\omega_z$  for Case CZ1CY at  $z = +L_z/4, t = 3$

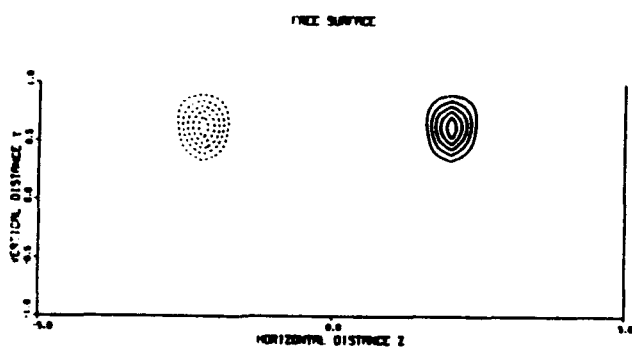


Fig. 10-Vorticity  $\omega_z$  for Case CTWOD at  $z = 0, t = 3$

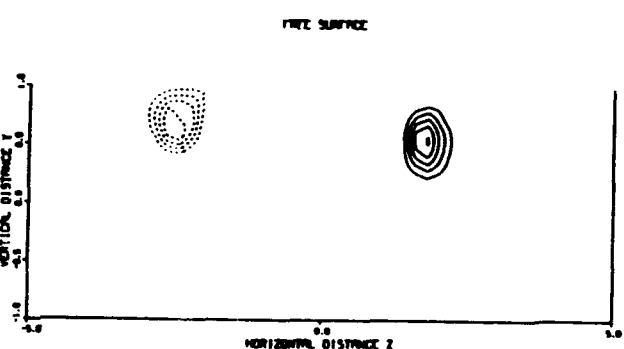


Fig. 12a-Vorticity  $\omega_z$  for Case CO030 at  $z = -L_z/4, t = 3$

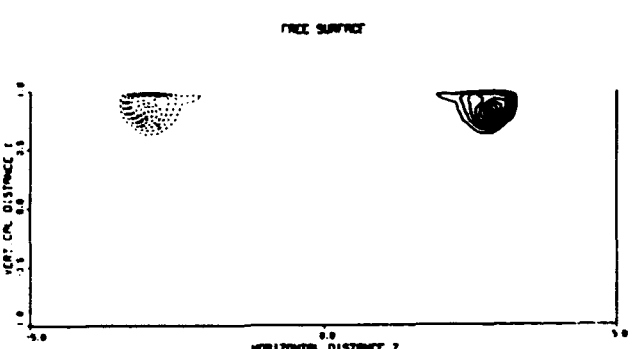


Fig. 11a-Vorticity  $\omega_z$  for Case CZ1CY at  $z = -L_z/4, t = 3$

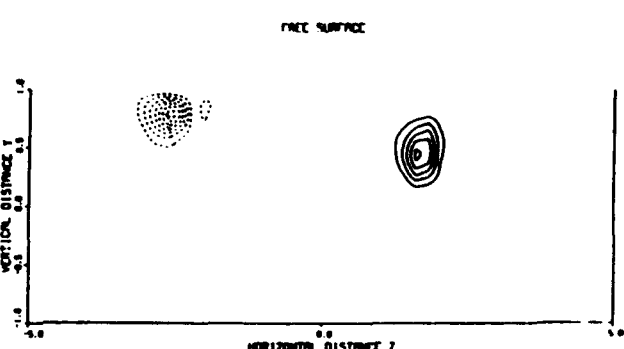


Fig. 12b-Vorticity  $\omega_z$  for Case CO030 at  $z = 0, t = 3$

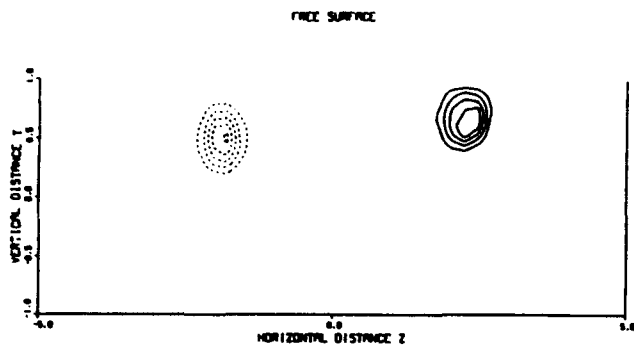


Fig. 12c-Vorticity  $\omega_z$  for Case CO030 at  $x = +L_z/4, t = 3$

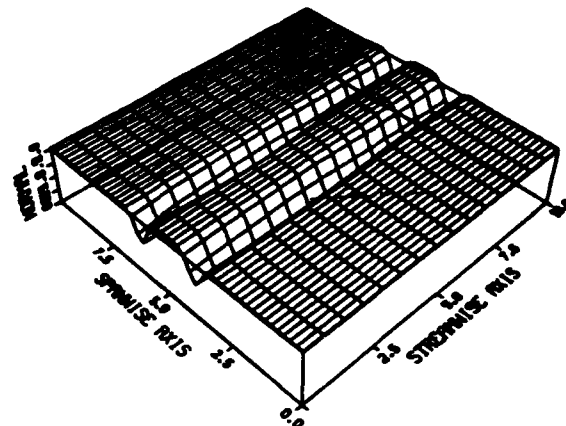


Fig. 13b-Surface Elevation  $\eta$  for Case CO010 at  $t = 2$

#### Three-Dimensional Plots of Surface Elevation

Figures 13a-c show three-dimensional plots of the surface elevation  $\eta$  for Case CO010 at  $t = 0, 2$ , and  $3$ , respectively. Figures 14-16 show corresponding plots at  $t = 3$  for Cases CO030, CO050, and CZ1CY, respectively. Figures 13a-c qualitatively confirm the observed numerical and experimental trends at low  $Fr$ . Thus, Figure 13a shows that there is a mound above the rising vortex pair surrounded by an extensive depression. Figure 13b shows that at  $t = 2$  the depressions on either side of the mound have become sharper and resemble the scars described in [2,3]. Figure 13c shows that at  $t = 3$  the vortices are essentially moving parallel to the free surface, resulting in a wider lower mound above the vortices. Similar to the trends observed in [2], the scars are fixed or "slaved" relative to the vortices and appear slightly ahead of them. The figure also shows that at this value of  $t$  the initial three-dimensional perturbations are now amplified to the point of being noticeable. Figures 14 and 15 show how the general shape remains largely the same but is more pronounced as the amplitude of the (otherwise identical) random perturbation is increased in amplitude. It appears that these perturbations excite a dominant mode in the axial direction. Figure 16 shows the expected trend that the vortices are furthest apart at  $x = -L_z/4$  and closest at  $x = +L_z/4$ .

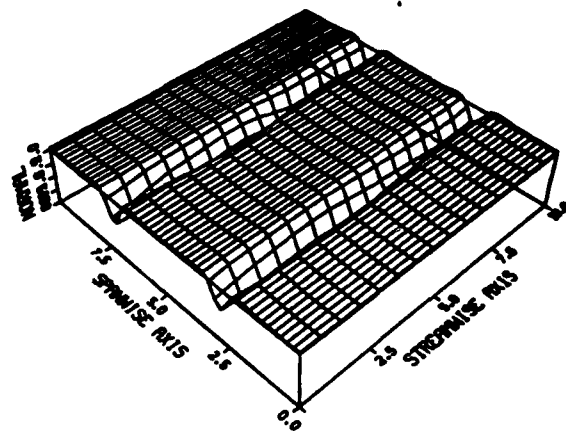


Fig. 13c-Surface Elevation  $\eta$  for Case CO010 at  $t = 3$

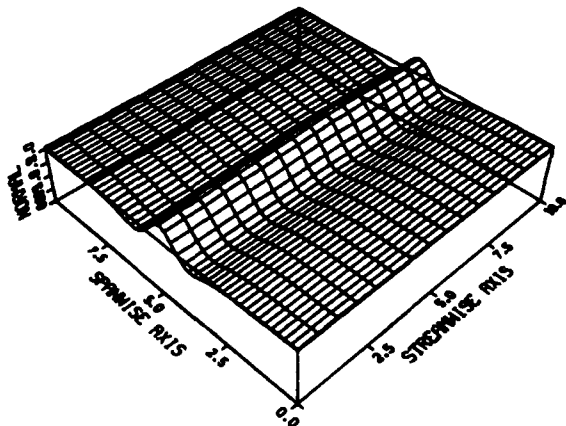


Fig. 13a-Surface Elevation  $\eta$  for Case CO010 at  $t = 0$

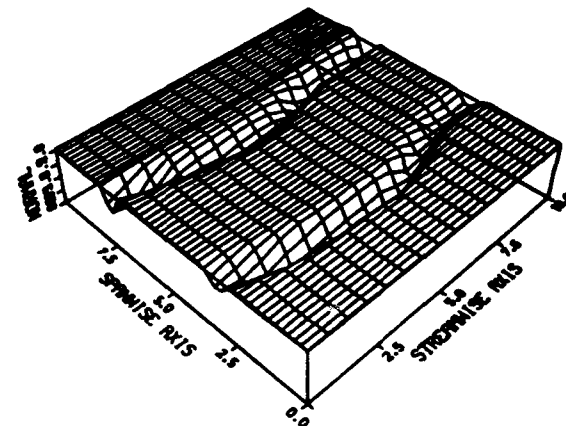


Fig. 14-Surface Elevation  $\eta$  for Case CO030 at  $t = 3$

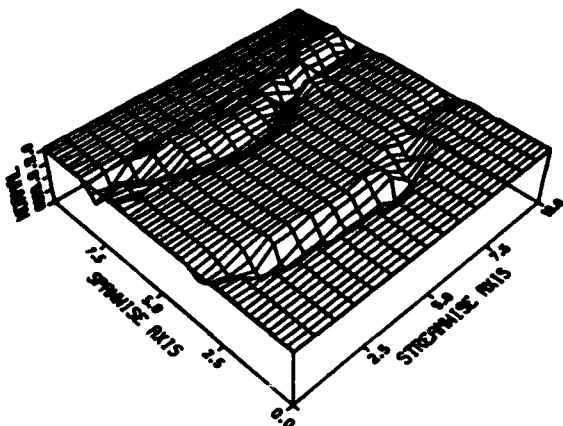


Fig. 15-Surface Elevation  $\eta$  for Case CO050 at  $t = 3$

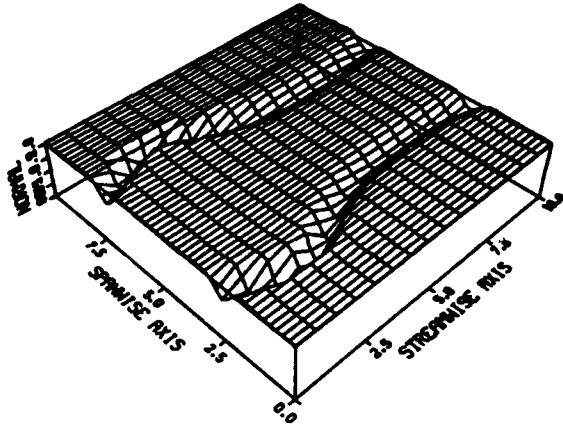


Fig. 16-Surface Elevation  $\eta$  for Case CZ1CY at  $t = 3$

## CONCLUSIONS

We have presented a spectral approach for solving the three-dimensional incompressible Navier-Stokes equations where we expand our solutions as triple series involving exponential functions in the periodic  $x$  and  $z$  directions and Chebyshev polynomials in the nonperiodic  $y$  direction. We eliminate the troublesome pressure term and implicitly satisfy the continuity condition by going to a fourth order equation for the  $y$  component of velocity and a second order equation for the  $y$  component of vorticity.

We apply this method to study the flow due to a pair of counter-rotating Gaussian vortices rising to a shear-free surface. We consider the two-dimensional case as well as two series of three-dimensional perturbations to the initial conditions. In one series, we consider the horizontal  $z$  spacing of the vortex centers to undergo a one-cycle sinusoidal variation in the axial direction and in the second series, we randomly perturb the three components of vorticity by 0.01, 0.03, and 0.05  $\omega_{max}$ . We find that our

computation scheme is stable for the two-dimensional case even at  $t = 6$  when the vortices are interacting strongly with the non-physical boundaries of our computation domain. We present our results in terms of line and contour plots for the subsurface flow and three-dimensional plots for the surface elevation. In terms of differences from the two-dimensional case, they are small for the  $0.01\omega_{max}$  case and moderate for the other cases. The two largest random perturbation cases eventually become numerically unstable before the vortices are influenced by the nonphysical boundaries of our computation domain, at which point the calculations are physically meaningless. The surface elevations show the same mound and depression pattern obtained in previous experimental and numerical studies. In addition, we show the effect of the three-dimensional perturbations.

## ACKNOWLEDGMENT

This study was conducted as part of the Fluid Dynamics Task Area at the Naval Research Laboratory.

## REFERENCES

1. Barker, S.J. and Crow, S.C., "The Motion of Two-Dimensional Vortex Pairs in a Ground Effect," *Journal of Fluid Mechanics*, Vol. 182, Part 4, 1977, pp. 659-671.
2. Sarpkaya, T., "Trailing-Vortex Wakes on the Free Surface," *16th Symposium on Naval Hydrodynamics*, 1986, pp. 38-50.
3. Sarpkaya, T., Elnitsky II, J., and Leeker, Jr., R.E., "Wake of a Vortex Pair on the Free Surface," *17th Symposium on Naval Hydrodynamics*, 1988, pp. 53-60.
4. Bernal, L.P., Hirsa, A., Kwon, J.T., and Willmarth, W.W., "On the Interaction of Vortex Rings and Pairs with a Free Surface for Varying Amounts of Surface Active Agent," *Physics of Fluids*, Vol. A1, No. 12, 1989, pp. 2001-2004.
5. Saffman, P.G., "The Approach of a Vortex Pair to a Plane Surface in Inviscid Fluid," *Journal of Fluid Mechanics*, Vol. 92, Part 3, 1979, pp. 497-503.
6. Peace, A.J. and Riley, N., "A Viscous Vortex Pair in Ground Effect," *Journal of Fluid Mechanics*, Vol. 129, 1983, pp. 409-426.
7. Marcus, D.L. and Berger, S.A., "The Interaction Between a Counter-Rotating Vortex Pair in Vertical Ascent and a Free Surface," *Physics of Fluids*, Vol. A1, No. 12, 1989, pp. 1988-2000.
8. Telste, J.G., "Potential Flow about Two Counter-Rotating Vortices Approaching a Free Surface," *Journal of Fluid Mechanics*, Vol. 201, 1989, pp. 259-278.
9. Yu, D. and Tryggvason, G., "The Free Surface Signature of Unsteady, Two-Dimensional Vortex Flows," University of Michigan Program in Ship Hydrodynamics Report 89-03, 1989.
10. Ohring, S. and Lutg, H.J., "Two Counter-Rotating Vortices Approaching a Free Surface in a Viscous Fluid," David Taylor Research Center Report DTRC-89/013, 1989.
11. Baker, G.R., Meiron, D.I., and Orszag, S.A., "Applications of a Generalized Vortex Method to Nonlinear Free Surface Flows," *Third International Conference on Numerical Ship Hydrodynamics*, 1981, pp. 179-191.

12. Wang, H.T. and Leighton, R.I., "Direct Calculation of the Interaction Between Subsurface Vortices and Surface Contaminants," Ninth International Conference on Offshore Mechanics and Arctic Engineering, Vol. I, Part A, 1990, pp. 271-277.
13. Crow, S.C., "Stability Theory for a Pair of Trailing Vortices," AIAA Journal, Vol. 8, No. 12, 1970, pp. 2172-2179.
14. Kim, J., Moin, P., and Moser, R., "Turbulence Statistics in Fully Developed Channel Flow at Low Reynolds Number," Journal of Fluid Mechanics, Vol. 177, 1987, pp. 133-166.
15. Handler, R.A., Hendricks, E.W., and Leighton, R.I., "Low Reynolds Number Calculation of Turbulent Channel Flow: A General Discussion," Naval Research Laboratory Memorandum Report 6410, 1989.
16. Hussaini, M.Y. and Zang, T.A., "Spectral Methods in Fluid Dynamics," Annual Review of Fluid Mechanics, Vol. 19, 1987, pp. 339-367.
17. Canuto, C., Hussaini, M.Y., Quarteroni, A., and Zang, T.A., Spectral Methods in Fluid Dynamics, Springer-Verlag, New York, NY, 1987.
18. Skop, R.A., "The Hydrodynamic Wake of a Surface Ship: Theoretical Foundations," Naval Research Laboratory Report 8833, 1984.
19. Pumir, A. and Kerr, R.M., "Numerical Simulation of Interacting Vortex Tubes," Physical Review Letters, Vol. 58, No. 16, 1987, pp. 1636-1639.

## **Appendix J**

### **Requirements Definition by Numerical Simulation**

**CONTRABAND DETECTION TRACE CHEMICAL  
PHENOMENOLOGY WORKSHOP  
June 10-11, 1993**

**"Requirements Definition by Numerical Simulation"**

**James Hickman, Chris Kostas, Kang Tsang  
Science Applications International Corporation**

**Abstract:**

We have been investigating the issues involved in requirements definition for narcotics interdiction for the past six months. Our approach has been to simulate numerically the conditions that arise during vapor particulate transport. The advantages of this approach are that: (1) a broad range of scenarios can be rapidly and inexpensively analyzed by simulation and (2) simulations can display quantities that are difficult or impossible to measure. The drawback of this approach is that simulations cannot include all of the phenomena present in a real measurement, and therefore the fidelity of the simulation results is always an issue.

We will discuss these issues and how they apply to the current problems. We will show preliminary data on numerical simulations of simple configurations. We will also show the results of a 1D numerical simulation and compare these results with the analytical solution to the same problem to demonstrate that the model is at least verifiable at its most basic level.

**Requirements Definition By  
Numerical Simulation**

Contract Number N00014-89-C-2106

Presented at

Contraband Detection Trace Chemical  
Phenomenology Invitational Workshop

Submitted from

Science Applications International Corporation  
Applied Physics Operation  
1710 Goodridge Drive  
McLean, Virginia 22102

June 10, 1993

## Requirements Definition for Narcotics Interdiction

1. What do you want to detect?
  - actual narcotics
  - contaminants or residuals
  - decomposition products
2. How much of a particular signature *could* be there?
  - assume best case (i.e., no wrappings, infinite time)
3. How does this amount change as you change conditions?
  - different interdiction situations exist
  - many types of wrappings or transport vehicles
  - atmospheric conditions may change
4. If the best case is within detection limits, how long does it take to reach detectable levels?
  - different scenarios will have drastically different time requirements

# Methods of Requirements Definition

- A. Direct measurement of levels of vapor, aerosol, or particulates
  - model general conditions one may encounter in various scenarios using real system
  - do field testing to obtain real parameters

## Advantages

- direct observation of levels of vapor, aerosol, or particulates generated

## Disadvantages

- can't duplicate even a fraction of conditions to be faced
- condition of samples affects results, so disagreement from lab to lab

- B. Computer simulation of vapor, aerosol, or particulates
  - total simulation of propagation in various scenarios
  - use data already generated as inputs into model

## Advantages

- can vary parameters for a wide variety of situations
- low cost

## Disadvantages

- dependent on experimentally determined values
- can get very complicated with large numbers of variables

## Methods of Requirements Definition

- C. Combination of A and B
  - use real inputs from a few selected scenarios to generate data on propagation
    - cargo container
    - room in customs
    - large scale field test
  - can use one system to check the other

### Advantages

- lower overall cost
- can be interactive
- test most situations with reasonable reliability

### Disadvantages

?

# Numerical Simulation

## Why

### Analytical solution too complex

- non-linear problem
- complex geometry
- complex or unsolvable boundary conditions

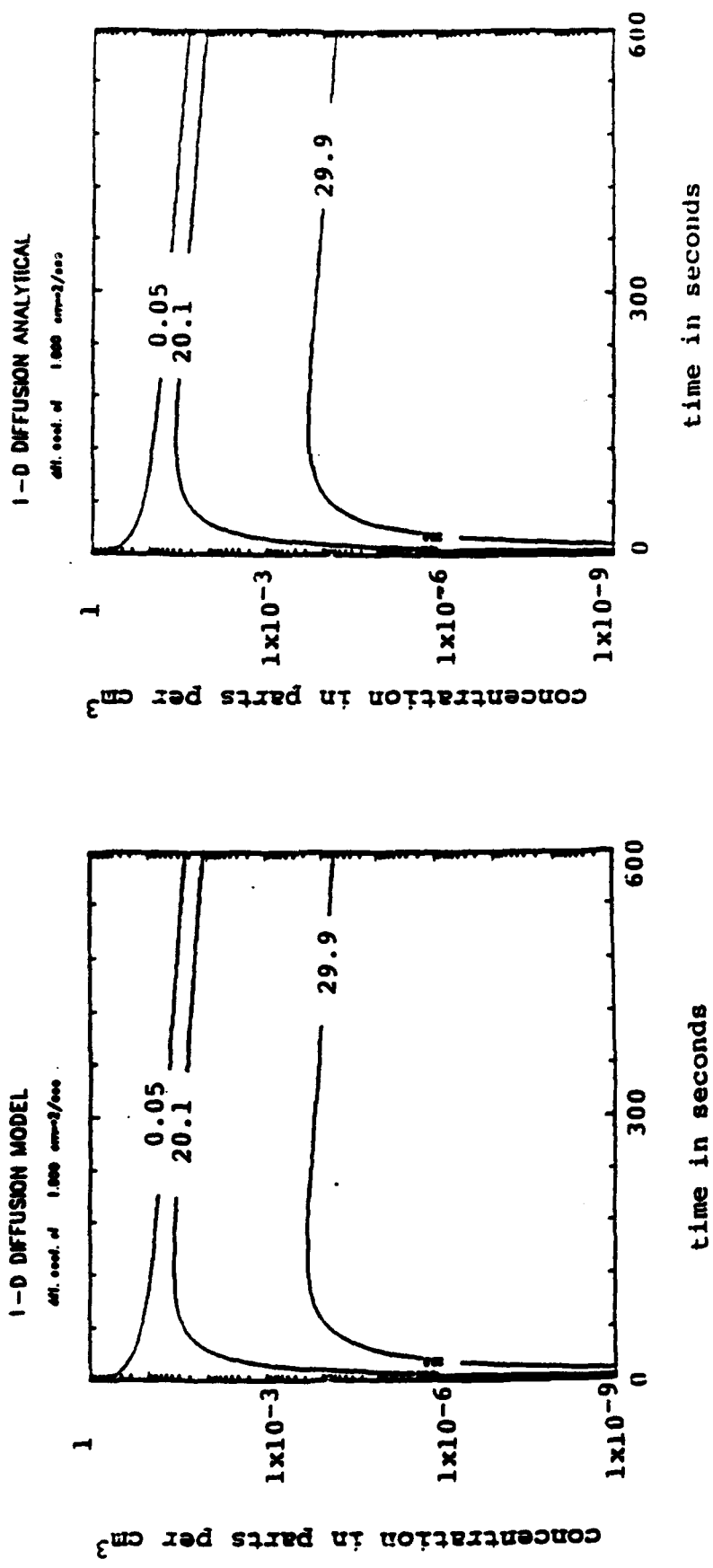
## How

- make a grid that conforms to the specific geometry
- solve just the equations across the boundaries of this grid
- use the computing power to do it fast

## Approach

- 1D model
- Compare 1D model with analytical solutions for test cases
- 3D model
  - any geometry possible
  - diffusion based, variable source
  - impact of various packaging agents
    - diffusion coefficients barriers can be different for each wrapping
    - can do multiple wrappings in one simulation
  - convection included as average modification to diffusion coefficient
    - flow fields can be input from separate calculation
  - absorbing and reflecting walls and topological features
  - effects of environment

## Results of Analytical and Numerical Simulation



At this point in the original presentation a video was shown depicting three simple test cases of vapor propagation.

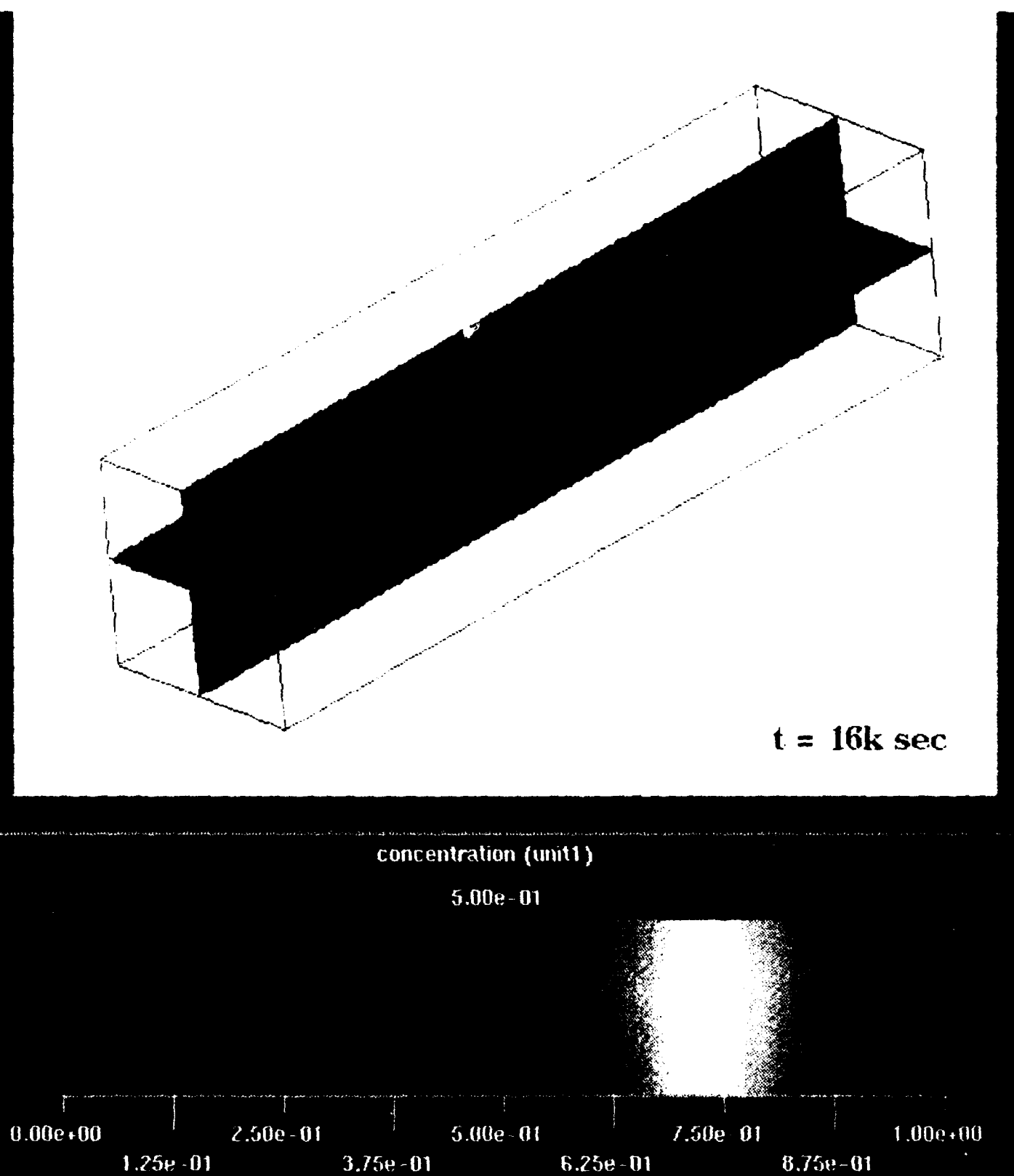
- 1 Point source in center of a  $40' \times 10' \times 10'$  room
- 2 Point source at end of a  $40' \times 10' \times 10'$  room
- 3 Point source at center of a  $40' \times 10' \times 10'$  room with adsorbing box at one end

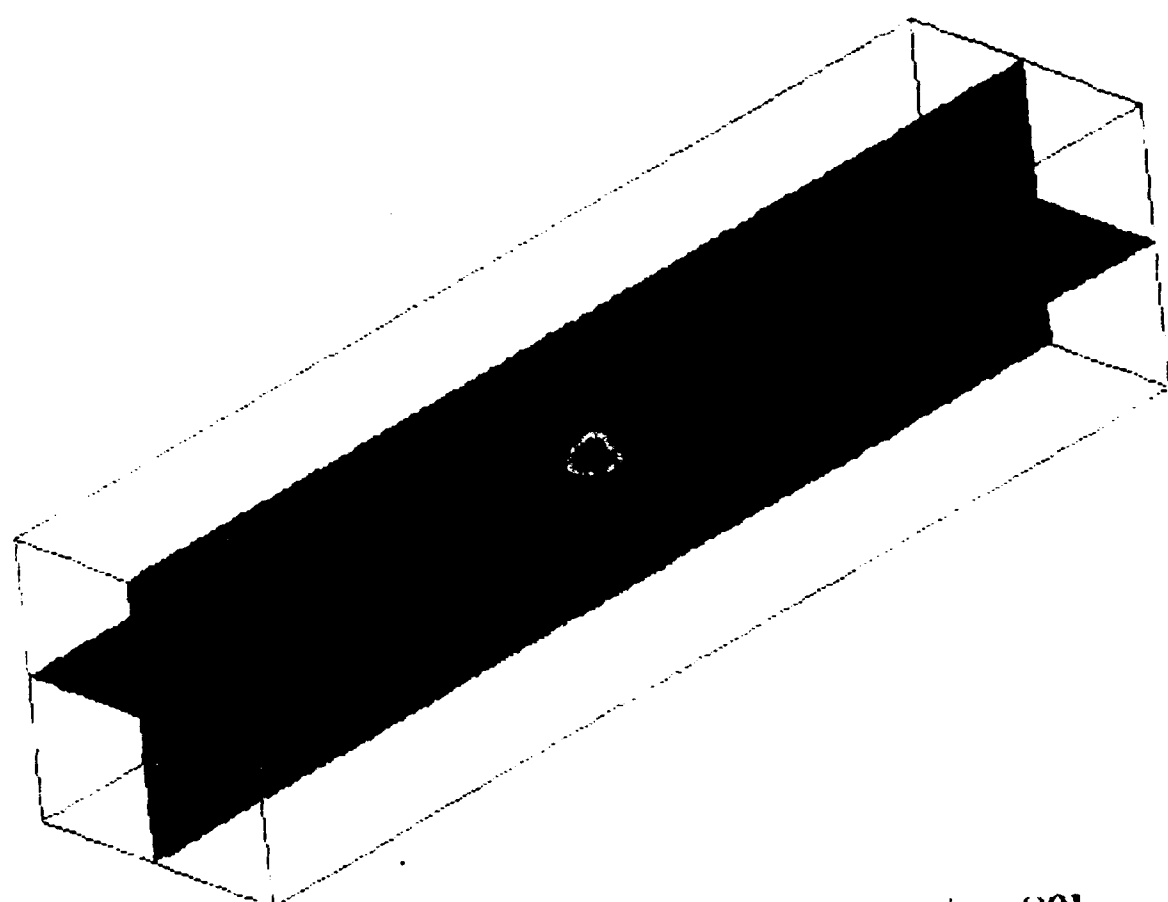
We are including here three frames in time from the first scenario.

The *apparent* diffusion coefficient (combination of molecular diffusion, convection, and other times) was varied between  $1 \text{ cm}^2/\text{s}$  (approximately molecular diffusion) to  $10,000 \text{ cm}^2/\text{s}$  (which approximates a fan in the room on high). The numerical simulations that are shown in the following color graphs were run with  $D = 1 \text{ cm}^2/\text{s}$ . To convert to  $D = 10,000 \text{ cm}^2/\text{s}$  divide the time in the lower right hand corner by 10,000.

The different colors represent different concentrations. An arbitrary concentration scale is shown at the bottom where the extreme right is the equilibrium vapor pressure of the test vapor and the extreme left represents 0 concentration.

These test cases are representations of the most basic numerical simulation. Many levels of complexity can be added to this basic framework.



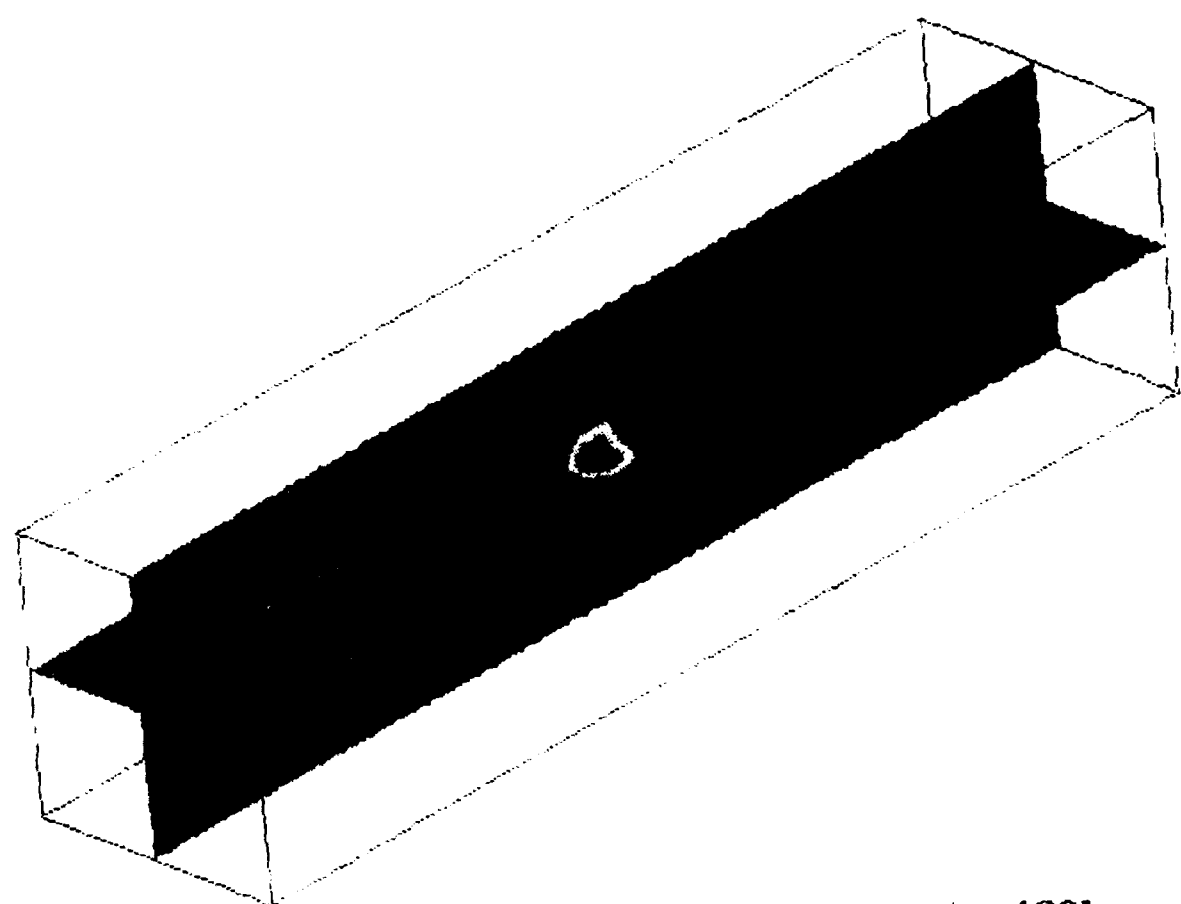


**$t = 80k \text{ sec}$**

**concentration (unit1)**

**5.00e-01**

0.00e+00 1.25e-01 2.50e-01 3.75e-01 5.00e-01 6.25e-01 7.50e-01 8.75e-01 1.00e+00



**$t = 160k \text{ sec}$**

**concentration (unit1)**

**5.00e-01**

0.00e+00    1.25e-01    2.50e-01    3.75e-01    5.00e-01    6.25e-01    7.50e-01    8.75e-01    1.00e+00